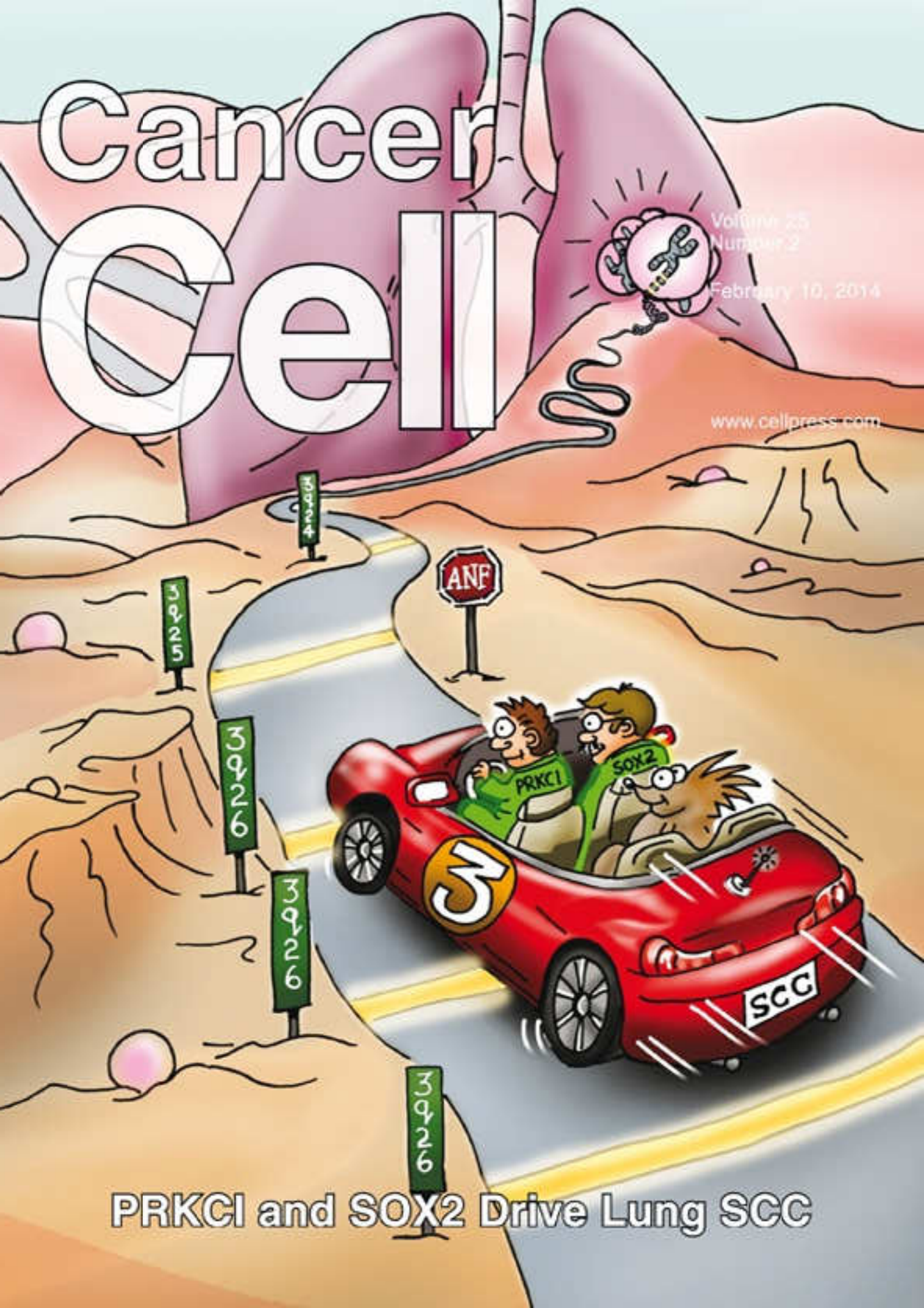
Cancer Cell
Volume 25
Number 2
February 10, 2014
www.cellpress.com
3q25
ANF
3q26
3q26
3q26
PRKCI
SOX2
3
SCC
PRKCI and SOX2 Drive Lung SCC

"Atypical" Regulation of Hedgehog-Dependent Cancers

Scott X. Atwood[1] and Anthony E. Oro[1,*]
[1]Program in Epithelial Biology, Stanford University School of Medicine, Stanford, CA 94305, USA
*Correspondence: oro@stanford.edu
http://dx.doi.org/10.1016/j.ccr.2014.01.027

Growing evidence indicates targeting PKCι may be effective in treating Hedgehog-dependent cancers. In this issue of *Cancer Cell*, Justilien and colleagues present the surprising finding that PKCι promotes Hedgehog ligand production and lung squamous cell carcinoma growth through SOX2, rather than the canonical transcription factor GLI.

Hedgehog (HH) signaling controls the morphogenesis of a panoply of organs by regulating the proliferation and differentiation of stem cells (Briscoe and Thérond, 2013). Because HH regulates key pluripotency and growth genes such as MYC, Cyclin D1, Nanog, and BMI1, it comes as no surprise that alteration of the HH pathway drives tumor growth. Although current HH pathway antagonists are quite effective in certain tumor contexts, recent advances in cancer-associated signaling pathways show a complex and incomplete picture as to the potential for "typical" pathway inhibitors (Atwood et al., 2012).

Tumorigenic HH signaling operates through cell-intrinsic mutations that cause inappropriate pathway activation or by autocrine/paracrine events where the tumor produces HH ligand to feed itself or adjacent growth factor-producing stroma (Figure 1). Before HH is competent to act, the ligand undergoes autoproteolytic cleavage and dual lipid modifications to convert to its active form (Briscoe and Thérond, 2013). HH acyl transferase (HHAT) partly controls production of active HH by adding a palmitoyl moiety to the amino-terminus of the ligand after cleavage, whereas a separate enzyme adds a cholesterol moiety to the C terminus. The dual lipid modified HH is transported to the cell surface where Dispatched1 (DISP1) regulates its release. After activation and secretion, HH binds to its target cell and inhibits the transmembrane receptor Patched1, catalyzing the activation of signal transducer Smoothened (SMO) and translocation of GLI transcription factors to the nucleus to amplify oncogenic gene expression.

Therapeutic inhibition of SMO effectively suppresses tumors driven by cell-intrinsic mutations, such as basal cell carcinoma (BCC) and medulloblastoma (Atwood et al., 2012). Vismodegib, a recently approved SMO antagonist, commands a high response rate in patients with basal cell nevus syndrome that predisposes them to develop hundreds of BCCs, whereas patients with locally advanced or metastatic BCCs show a lower response rate. Patients with more invasive paracrine-driven HH tumors, such as small cell lung or pancreatic cancer, show little to no responsiveness despite evidence of pathway inhibition. Why targeting the HH pathway would lead to such disparate outcomes remains unclear; however, identifying new targets that can act in both cell-intrinsic and autocrine/paracrine tumor proliferation may provide novel therapeutic strategies to treat both tumor types.

Atypical Protein Kinase C lambda/iota (PKCι) plays a central role in determining cell polarity, a fundamental property of cells and tissues that results from the differential distribution of cellular components (proteins, lipids, RNA, and organelles) by promoting asymmetric functions including oriented cell division, cell recognition, and cellular adhesion (Roignot et al., 2013). Apico-basolateral polarity stems from PKCι-dependent regulation of vesicle movements through asymmetric control of the actin cytoskeleton, resulting in vectorial transport of nutrients and signals that play critical roles in the morphogenesis of most multicellular organisms. Loss of PKCι, or the polarity pathways it interacts with, can lead to abnormalities in cell polarity, epithelial-to-mesenchymal transition, and cancer invasiveness.

Apart from polarity signaling, a distinct role for PKCι as an oncogenic kinase in HH signaling has emerged. PKCι has been implicated in tumors with cell-intrinsic HH signaling, such as BCCs, where it phosphorylates the zinc finger domain of GLI1 to activate DNA binding and transcriptional activity (Figure 1A) (Atwood et al., 2013). Because *PRKCI* (the gene that encodes PKCι) is a GLI target gene, higher GLI1 activity produces more PKCι, which feeds back into the system to amplify HH pathway activation independently of SMO to feed tumor growth. BCCs that have become addicted to PKCι are vulnerable to pharmacological inhibition of kinase activity, which results in pathway suppression and the blockade of tumor growth. PKCι has also been implicated as an oncogene in non-small cell lung cancer (NSCLC), although the link between PKCι and HH signaling in this predominantly ligand-driven tumor remained unexplored until now (Regala et al., 2005).

In this issue of *Cancer Cell*, Justilien et al. (2014) show how PKCι maintains cancer stem cell-like properties of lung squamous cell carcinoma (LSCC), an NSCLC subtype (Justilien et al., 2014). LSCC oncospheres displayed increased PKCι activation, which correlated with activation of the HH pathway, as assessed by RNA sequencing from PKCι-deficient oncospheres and pharmacological agents that target either PKCι or SMO suppressed oncosphere growth. Interestingly, the expression of the HH component HHAT was also dependent on PKCι, suggesting a novel regulatory mechanism to control HH ligand production. Both HHAT and DISP1 have been shown to be required for the growth of NCSLC tumor cells and xenografts (Rodriguez-Blanco et al., 2013). Similarly, RNA knockdown of PKCι, GLI1, or HHAT in orthotopic tumors originating from LSCC oncospheres significantly reduced

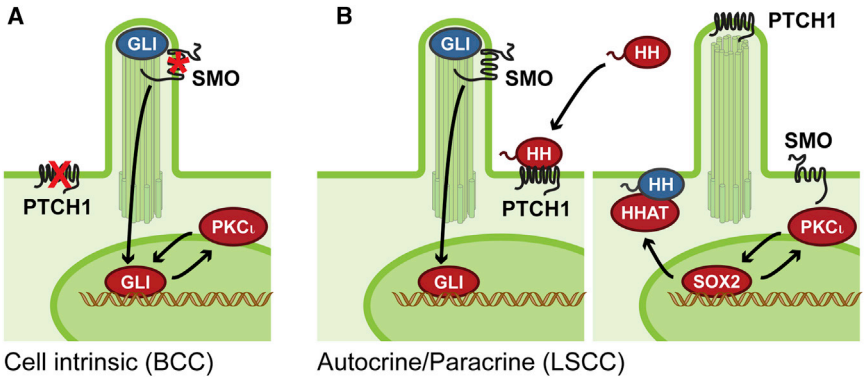

Figure 1. PKCι-Dependent Activation of the HH Pathway

(A) PKCι phosphorylates and activates GLI1 to amplify target gene expression in basal cell carcinoma (BCC), a cell-intrinsic tumor with HH pathway mutations in PTCH1 or SMO. Blue denotes inactive protein, whereas red is active.

(B) PKCι promotes HHAT-mediated HH ligand production by phosphorylating and activating SOX2, which binds to the *HHAT* promoter in HH-driven autocrine/paracrine lung squamous cell carcinoma (LSCC) tumors.

tumor take rate and decreased tumor size.

In addition, the authors found that *PRKCI* is frequently co-amplified and overexpressed in LSCC tumors on the 3q26 amplicon with *SOX2*, a master regulator of stem cell maintenance. Chromatin immunoprecipitation of SOX2 showed occupancy of the *HHAT* promoter and loss of SOX2 significantly decreased HHAT mRNA and protein levels suggesting a novel link between a stem cell gene and HH pathway activation that drives LSCC tumor growth. Surprisingly, SOX2 serves as a substrate for PKCι, with phosphorylation occurring adjacent to the HMG DNA-binding region. SOX2 phosphorylation enhanced binding to the *HHAT* promoter, increased expression of HH target genes, and augmented growth of oncospheres (Figure 1B). Whether PKCι-dependent phosphorylation of SOX2 controls stem cell maintenance or growth of cell-intrinsic HH pathway tumors such as BCCs remains to be determined.

This new work reinforces two new aspects of *PRKCI* biology. First, PKCι has now been implicated in two different HH-driven tumors, because NSCLC growth shows both cell-intrinsic and autocrine/paracrine type signaling (Bermudez et al., 2013; Yuan et al., 2007). This has clinical importance in that targeting SMO appears only to be an effective therapy for cell-intrinsic, but not paracrine, HH-dependent tumors. By contrast, pharmacological inhibition of PKCι may prove useful to treat a variety of HH cancers, because targeting PKCι appears effective in paracrine-driven ovarian cancer (Wang et al., 2013). Second, although PKCι clearly regulates cortical trafficking in polarizing cells, PKCι also operates to regulate nuclear functions by controlling the affinity of specific transcription factors to chromatin. This report adds SOX2 to a growing list of transcription factors regulated by PKCι, which includes GLI1. Whether PKCι-dependent regulation of transcription factors plays similar roles in normal and tumor biology remains to be investigated. In any case, the emerging data implicating "atypical" PKCι in HH cancer biology suggests that PKCι involvement may be the rule rather than the exception.

ACKNOWLEDGMENTS

This work was supported by NIH grants 5ARO54780 and ARO46786.

REFERENCES

Atwood, S.X., Chang, A.L.S., and Oro, A.E. (2012). J. Cell Biol. *199*, 193–197.

Atwood, S.X., Li, M., Lee, A., Tang, J.Y., and Oro, A.E. (2013). Nature *494*, 484–488.

Bermudez, O., Hennen, E., Koch, I., Lindner, M., and Eickelberg, O. (2013). PLoS ONE *8*, e63226.

Briscoe, J., and Thérond, P.P. (2013). Nat. Rev. Mol. Cell Biol. *14*, 416–429.

Justilien, V., Walsh, M.P., Ali, S.A., Thompson, E.A., Murray, N.R., and Fields, A.P. (2014). Cancer Cell *25*, this issue, 139–151.

Regala, R.P., Weems, C., Jamieson, L., Khoor, A., Edell, E.S., Lohse, C.M., and Fields, A.P. (2005). Cancer Res. *65*, 8905–8911.

Rodriguez-Blanco, J., Schilling, N.S., Tokhunts, R., Giambelli, C., Long, J., Liang Fei, D., Singh, S., Black, K.E., Wang, Z., Galimberti, F., et al. (2013). Oncogene *32*, 2335–2345.

Roignot, J., Peng, X., and Mostov, K. (2013). Cold Spring Harb. Perspect. Biol. *5*, 5.

Wang, Y., Hill, K.S., and Fields, A.P. (2013). Mol. Cancer Res. *11*, 1624–1635.

Yuan, Z., Goetz, J.A., Singh, S., Ogden, S.K., Petty, W.J., Black, C.C., Memoli, V.A., Dmitrovsky, E., and Robbins, D.J. (2007). Oncogene *26*, 1046–1055.

Molecular Subtyping of Invasive Bladder Cancer: Time to Divide and Rule?

Carolyn D. Hurst[1] and Margaret A. Knowles[1,*]
[1]Section of Experimental Oncology, Leeds Institute of Cancer and Pathology, University of Leeds, St. James's University Hospital, Beckett Street, Leeds, West Yorkshire LS9 7TF, UK
*Correspondence: m.a.knowles@leeds.ac.uk
http://dx.doi.org/10.1016/j.ccr.2014.01.026

Therapeutic decisions for muscle-invasive bladder cancer (MIBC) are largely based on histopathologic characteristics. In this issue of *Cancer Cell*, Choi and colleagues report three molecular subtypes of MIBC with the potential to guide prognosis, patient stratification, and treatment.

Despite increased molecular understanding, there has not been a significant advance in the treatment of muscle-invasive bladder cancer (MIBC) in recent years. These tumors frequently become metastatic, which is associated with very poor outcome (median survival: approximately 1 year). The standard of care for patients with localized MIBC is radical cystectomy preceded by cisplatin-based chemotherapy (neoadjuvant chemotherapy; NAC), which aims to abolish undetected metastases (Sternberg et al., 2013). However, responses to NAC are recorded in only 40%–60% of cases, and metastatic disease is frequently detected at the time of surgery. Cisplatin-containing combination chemotherapy is also the mainstay of treatment in the metastatic setting, where both de novo and acquired resistance present major problems.

What is needed to improve this dismal situation? Two issues currently under investigation may have an impact. First, predicting the response to chemotherapy may allow selection for NAC responders, avoiding unnecessary toxicity in patients unlikely to respond. Expression signatures associated with sensitivity have been derived from tumors (Takata et al., 2005) and tumor cell lines with known response (Lee et al., 2007), and validation in relevant clinical trials is eagerly awaited. Second, identification of therapeutic targets and development of personalized treatment strategies is urgently needed. Although several druggable targets are present in MIBC, e.g., HER2, EGFR, FGFR1, and FGFR3, adequate biological understanding has been lacking, and few trials with targeted agents have been initiated.

The significant heterogeneity in MIBC clinical behavior suggests more than one disease entity. This is already supported by genome-wide expression and DNA-based analyses, which report distinct molecular subtypes. Encouragingly, the signatures of some of these subtypes show prognostic value (Sjödahl et al., 2012). However, this information has yet to have an impact on clinical management, and predictive information has not been derived from such data.

In this issue of *Cancer Cell*, Choi et al. (2014) used whole-genome gene expression profiling to identify molecular subtypes of MIBC and provided evidence for their biological basis and clinical significance. Their findings have exciting implications for the clinical management of MIBC, because they include not only prognostic information, but also suggestions for subtype-directed targeted therapy and potential to predict response to cisplatin-based chemotherapy.

Choi et al. (2014) initially profiled 73 fresh-frozen MIBCs and, using unsupervised hierarchical cluster analysis, revealed three major clusters, which they term basal, luminal and "p53-like". Basal and luminal designations reflect enrichment for markers previously reported in basal and luminal-type breast cancers, respectively (Sørlie, 2004). Basal MIBCs characteristically expressed CD44, KRT5, KRT6, KRT14, and CDH3 and lacked KRT20 expression. Such differential expression of cytokeratins 5 and 20 is related to urothelial differentiation states, the least differentiated of which characterizes cells in the basal layer of the normal urothelium ($KRT14^{+}KRT5^{+}KRT20^{-}$) (Volkmer et al., 2012) and bladder cancer cells with stem cell-like features (Chan et al., 2009). The basal subtype also expressed "mesenchymal" markers (TWIST1/2, SNAI2, ZEB2, and VIM), low miR-200, which is implicated in mesenchymal marker regulation, and elevated levels of EGFR and its ligands. This subtype was enriched for tumors with sarcomatoid and squamous features, exhibited more aggressive disease at presentation, and had shorter disease-specific and overall survival. The luminal subtype expressed luminal breast cancer biomarkers (CD24, FOXA1, GATA3, ERBB2, ERBB3, XBP1, and KRT20), "epithelial" biomarkers, E-cadherin and the miR-200 family and showed both expression and mutation of FGFR3. The "p53-like" subtype also expressed luminal biomarkers but was distinguished by an activated wild-type p53 gene signature.

Choi et al. (2014) then developed a classifier based on genes differentially expressed between subtypes. Using this, they were able to identify the same three subtypes in a local validation cohort consisting of 57 formalin-fixed paraffin-embedded (FFPE) MIBC samples and in a publically available gene expression data set. As in the initial analysis, these validation cohorts revealed an association between basal subtype and poor survival. A molecular taxonomy for bladder cancer described by Sjödahl et al. (2012) included a subset of squamous cell carcinoma-like (SCCL) MIBCs that expressed basal keratins and showed poor prognosis. Recently, these authors have suggested that the term "basal" is more appropriate for this group (Sjödahl et al., 2013). Choi et al. (2014) applied their classifier to this data set and confirmed that the SCCL group corresponded to

their basal subtype. This analysis also revealed that the luminal and "p53-like" subtypes shared features with the "urobasal A" and "infiltrated" subtypes of Sjödahl et al. (2012), respectively. To investigate the association of squamous features with the basal subtype, Choi et al. (2014) interrogated data from a previous study that reported a "squamous cluster" with KRT5 and KRT14 expression and found a subset of tumors enriched with squamous features that expressed the basal signature. They also examined expression of cytokeratins that were characteristic of basal (CK5/6) or luminal (CK20) tumors in a tissue microarray derived from 332 MIBCs and found an inverse correlation of these markers and association of high CK5/6 with squamous features.

To investigate the biology of the subtypes, a bioinformatics approach was used to seek upstream regulators of basal and luminal gene expression. This implicated transcription factors reportedly active in the basal/stem cell compartment of the normal urothelium (Stat-3, NFkB, Hif1, and p63) (Ho et al., 2012) as potential regulators in basal MIBCs. Activation of PPARγ and estrogen receptor pathways was identified in luminal MIBCs. p63 and PPARγ were then examined in tumor-derived cell lines. p63 knockdown yielded decreased basal marker expression and increased PPAR pathway activation, whereas treatment with a PPARγ-selective agonist activated PPAR and other luminal pathways and decreased basal transcription factor expression, clearly demonstrating the role of these opposing pathways in control of these two major phenotypes. Delineation of these regulators holds promise for improved therapeutic options through the use of pathway-specific targeted agents.

Finally, Choi et al. (2014) noted that all of the NAC-treated "p53-like" MIBCs in their discovery set (n = 7) showed resistance. Strikingly, this pattern was confirmed in an expanded local NAC cohort and 23 archival tumors from a phase III chemotherapy trial. The "p53-like" signature was also identified in cell lines, where it was associated with resistance to cisplatin-induced apoptosis. It should be noted, however, that, although the "p53-like" gene expression signature is characteristic of an activated wild-type p53 gene signature, it was not related to *TP53* mutation status, an observation that is reflected in the long-debated prognostic and predictive value of mutant p53 in bladder cancer. To confirm the link between "p53-like" and chemoresistance, the authors compared gene expression profiles from a cohort of matched pre- and posttreatment samples from a prospective phase II clinical trial of NAC. The lowest response rate was observed in tumors initially classified as "p53-like". A particularly pleasing feature of this study is that FFPE samples were successfully used for validation studies, providing promise for routine clinical application. Intriguingly, enrichment of a p53-like signature in posttreatment tissues from patients whose pretreatment tissue did not express this signature was observed. Whether this reflects global expression changes or selection of resistant subclones remains to be demonstrated. Because not all nonresponding tumors could be identified by this profile, including those exhibiting basal and luminal signatures, it is clear that other biomarkers of resistance remain to be elucidated, as does the possible contribution of intratumor heterogeneity. Nevertheless, these findings represent an important step toward the goal of more rational selection of patients for chemotherapy.

ACKNOWLEDGEMENTS

The authors acknowledge past and current funding from Yorkshire Cancer Research (L346, L362, L367, and L376PA) and Cancer Research UK (C6228/A5433, C6228/A12512, and C37059/A11941).

REFERENCES

Chan, K.S., Espinosa, I., Chao, M., Wong, D., Ailles, L., Diehn, M., Gill, H., Presti, J., Jr., Chang, H.Y., van de Rijn, M., et al. (2009). Proc. Natl. Acad. Sci. USA *106*, 14016–14021.

Choi, W., Porten, S., Kim, S., Willis, D., Plimack, E.R., Hoffman-Censits, J., Roth, B., Cheng, T., Tran, M., Lee, I.-L., et al. (2014). Cancer Cell *25*, this issue, 152–165.

Ho, P.L., Lay, E.J., Jian, W., Parra, D., and Chan, K.S. (2012). Cancer Res. *72*, 3135–3142.

Lee, J.K., Havaleshko, D.M., Cho, H., Weinstein, J.N., Kaldjian, E.P., Karpovich, J., Grimshaw, A., and Theodorescu, D. (2007). Proc. Natl. Acad. Sci. USA *104*, 13086–13091.

Sjödahl, G., Lauss, M., Lövgren, K., Chebil, G., Gudjonsson, S., Veerla, S., Patschan, O., Aine, M., Fernö, M., Ringnér, M., et al. (2012). Clin. Cancer Res. *18*, 3377–3386.

Sjödahl, G., Lövgren, K., Lauss, M., Patschan, O., Gudjonsson, S., Chebil, G., Aine, M., Eriksson, P., Månsson, W., Lindgren, D., et al. (2013). Am. J. Pathol. *183*, 681–691.

Sørlie, T. (2004). Eur. J. Cancer *40*, 2667–2675.

Sternberg, C.N., Bellmunt, J., Sonpavde, G., Siefker-Radtke, A.O., Stadler, W.M., Bajorin, D.F., Dreicer, R., George, D.J., Milowsky, M.I., Theodorescu, D., et al.; International Consultation on Urologic Disease-European Association of Urology Consultation on Bladder Cancer 2012 (2013). Eur. Urol. *63*, 58–66.

Takata, R., Katagiri, T., Kanehira, M., Tsunoda, T., Shuin, T., Miki, T., Namiki, M., Kohri, K., Matsushita, Y., Fujioka, T., and Nakamura, Y. (2005). Clin. Cancer Res. *11*, 2625–2636.

Volkmer, J.P., Sahoo, D., Chin, R.K., Ho, P.L., Tang, C., Kurtova, A.V., Willingham, S.B., Pazhanisamy, S.K., Contreras-Trujillo, H., Storm, T.A., et al. (2012). Proc. Natl. Acad. Sci. USA *109*, 2078–2083.

Wild-Type RAS: Keeping Mutant RAS in CHK

Theonie Anastassiadis[1] and Eric J. Brown[1,*]
[1]Abramson Family Cancer Research Institute, Department of Cancer Biology, Perelman School of Medicine, University of Pennsylvania, 421 Curie Boulevard, Philadelphia, PA 19104, USA
*Correspondence: brownej@upenn.edu
http://dx.doi.org/10.1016/j.ccr.2014.01.029

Mutant RAS-driven tumorigenesis was thought for decades to arise independently of wild-type RAS isoforms, but recent evidence indicates wild-type isoforms are involved. In this issue of *Cancer Cell*, Grabocka and colleagues report how the loss of wild-type RAS alters oncogenic signaling and dampens the DNA-damage response, thereby affecting tumor progression and chemosensitivity.

It has been more than 30 years since constitutively active mutant forms of KRAS, HRAS, and NRAS were shown to transform cells in culture, thus suggesting their ability to drive tumorigenesis autonomously. Indeed, it is now known that mutations in these genes contribute to loss of growth control in approximately 30% of all human cancers (Pylayeva-Gupta et al., 2011). However, detailed analyses of the growth factor signaling pathways impacted by RAS later demonstrated that wild-type (WT) RAS isoforms play a significant role in the transformative abilities of oncogenic RAS mutants (Huang et al., 1993; Lim et al., 2008; Young et al., 2013), but the molecular mechanism remained unknown. In this issue of *Cancer Cell*, Grabocka et al. (2014) provide a major advance in understanding the relationship between oncogenic RAS and WT RAS isoforms in tumorigenesis by elucidating how expression of WT RAS isoforms affect both tumor progression and chemotherapeutic sensitivity by modulating the DNA damage response.

To examine the contribution of WT RAS isoforms in promoting tumorigenesis in KRAS-driven tumors, Grabocka et al. (2014) first use WT KRAS and mutant KRAS (G12D) pancreatic and colon carcinoma cells engineered for inducible suppression of WT HRAS and NRAS expression. They show that silencing of HRAS or NRAS in mutant-KRAS cells increases MAPK-RSK and PI3K-AKT signaling and delays progression through G2/M phase, but has no effect on cells expressing WT KRAS. Furthermore, no substantial change in this delay was observed when both HRAS and NRAS were concurrently depleted, suggesting that HRAS and NRAS function within a single module to regulate oncogenic KRAS signaling. Together with previous studies, these results demonstrate that HRAS and NRAS work to limit oncogenic signaling, which, in turn, leads to cell cycle delays.

The delayed cell cycle progression and mitotic defects observed upon WT RAS isoform suppression are consistent with the well-established effect of oncogenic signaling on genomic instability and cell cycle checkpoint activation. Oncogenic RAS expression, like most oncogenes, causes replication stress, which is defined as the DNA damage response (DDR) associated with perturbed S phase progression, and leads to the activation of the ATR and ATM kinases (Halazonetis et al., 2008). Engagement of the DDR initially acts as a barrier to tumorigenesis by inducing cell cycle arrest, senescence, or apoptosis. However, as tumors evolve, attenuation or loss of specific components of the DDR, such as p53, suppresses these outcomes, thus affording tumor progression. CHK1, a checkpoint kinase operating directly downstream of ATR, has been shown in some cases to be inhibited by growth factor signaling pathways through phosphorylation on S280, which prevents CHK1 activation via phosphorylation of S317 and S345 by ATR (King et al., 2004). Therefore, S280 phosphorylation of CHK1 is one mechanism among many by which the oncogenic stress-induced checkpoint response can be compromised. However, checkpoint abrogation can be a double-edged sword, allowing cell cycle progression but further promoting genomic instability.

Grabocka et al. (2014) demonstrate that depletion of HRAS or NRAS leads to an increase in inhibitory phosphorylation of CHK1 at S280 and a decrease of phospho-CHK1 at S317 and S345 without affecting the ATM-CHK2 signaling pathway. Consistent with checkpoint mitigation after suppression of WT RAS isoforms, KRAS mutant cells failed to block mitotic entry soon after exogenous DNA damage. Because the long-term effects of checkpoint abrogation can be genome destabilizing, these results are in agreement with the observed mitotic defects and increased phosphorylation of the histone variant H2AX (γH2AX) when WT RAS isoforms were suppressed in mutant RAS-transformed cells. These findings indicate that oncogene-enforced limitation of DNA damage checkpoint control may promote additional genomic instability in affected tumors (Figure 1).

Although the analysis described above goes far to explain the mechanism of cell cycle perturbations through CHK1 inhibition, it raises important questions about the mechanism by which WT RAS isoforms promote CHK1 S280 phosphorylation. Previous reports have shown that both the MAPK-RSK and PI3K-AKT pathways can cause CHK1 S280 phosphorylation (King et al., 2004; Ray-David et al., 2013). Grabocka et al. (2014) demonstrate that both of these pathways, MAPK-RSK and PI3K-AKT, are activated and involved in S280 phosphorylation upon suppression of WT RAS isoforms in $KRAS^{G12D}$-expressing cells, and that each pathway contributes to CHK1 S280 phosphorylation. Similar to cultured cells, depletion of WT HRAS in mutant KRAS tumor xenografts also resulted in hyperactivation of the MAPK-RSK and PI3K-AKT pathways as well as repression of CHK1 activity following exposure to DNA-damaging chemotherapeutic agents. Thus, the silencing of WT HRAS and NRAS in

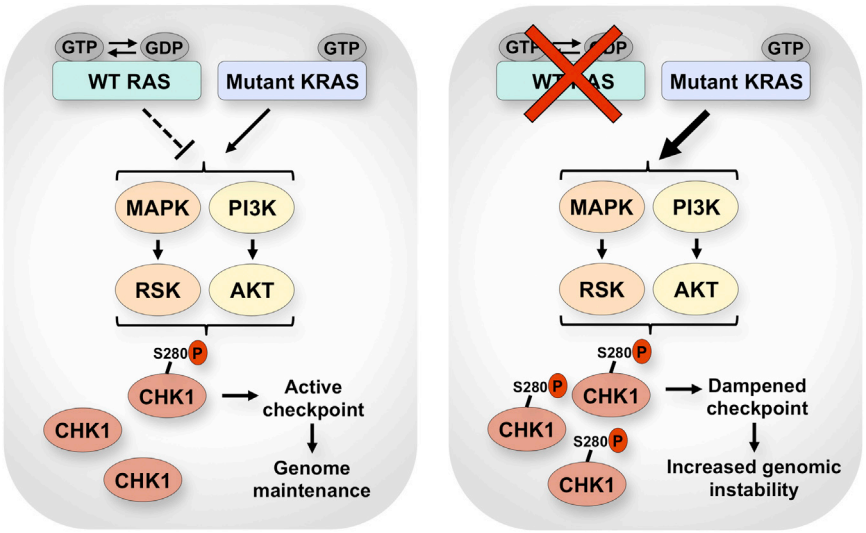

Figure 1. Regulation of the DNA Damage Response by Wild-Type RAS in Mutant KRAS Cells
WT RAS antagonizes mutant KRAS signaling, thereby limiting the inhibitory phosphorylation of CHK1 at S280 from MAPK-RSK and PI3K-AKT signaling. Uninhibited pools of CHK1 afford an active DNA damage checkpoint response and some degree of genome maintenance. Suppressing WT RAS hyperactivates mutant KRAS signaling, which increases inhibitory phosphorylation of CHK1 at S280. CHK1 inhibition dampens the checkpoint and increases genomic instability.

mutant KRAS cells leads to CHK1 S280 phosphorylation through hyperactivation of both the MAPK-RSK and PI3K-AKT pathways (Figure 1).

Mutation or deletion of p53 is well known to confer a survival advantage to cancer cells by hampering induction of apoptosis from DNA-damaging chemotherapy; however, the opposite effect is observed in response to DNA-damaging agents when most other checkpoint genes are compromised. Indeed, genomic instability is exacerbated by checkpoint failure when cells with damaged DNA enter mitosis. With this feature of checkpoint failure in mind, the authors then queried whether cells with dampened checkpoint activity due to CHK1 S280 phosphorylation would be particularly sensitive to DNA damaging chemotherapies. They found that combining knockdown of WT HRAS with irinotecan caused an increase in cell death and tumor regression compared to either treatment alone. Because suppression of WT RAS isoforms sensitized tumors to a standard DNA-damaging treatment, these results may have significant value in the design of novel combinatorial treatments for mutant KRAS-associated cancers. In summary, Grabocka et al. (2014) have now demonstrated that silencing of WT HRAS or NRAS in mutant KRAS cells significantly influences cancer biology in a way that will facilitate the design of individualized treatments.

Although the authors' findings increase our mechanistic understanding of how WT and mutant RAS isoforms interact to promote tumor progression and modulate responses to DNA-damaging chemotherapies, interesting questions remain. For example, the effect of the WT KRAS allele on mutant KRAS-driven tumorigenesis and DDR signaling has not yet been determined. This research area is relevant given that the WT KRAS allele is often downregulated or completely lost in mutant KRAS-driven cancer cells. Because recent findings suggest both tumor-suppressive and promoting roles for expression of the WT KRAS allele (Zhang et al., 2001; Matallanas et al., 2011), it is not immediately apparent how expression of the WT KRAS allele will affect oncogenic KRAS-transformed cells. Furthermore, it is important to note that oncogenic RAS has been associated with increased, not decreased, CHK1 activity (Halazonetis et al., 2008; Gilad et al., 2010). In these cases, CHK1 activity may be slightly stimulated by oncogenic stress, but only to suboptimal levels that are insufficient to counter the frequency of replication abnormalities produced by oncogene expression, leading to increased replication fork collapse and genomic instability (Gilad et al., 2010). Therefore, these studies predict great potential for ATR and CHK1 inhibitors as treatments for KRAS-driven cancers through their ability to further reduce ATR-CHK1 signaling to levels that are toxic (Gilad et al., 2010). Clearly, Grabocka et al. (2014) have provided novel insight into the role of WT RAS isoforms in regulating the DDR, providing a fresh look at a long-standing research question that will undoubtedly stimulate new discoveries for decades to come.

REFERENCES

Gilad, O., Nabet, B.Y., Ragland, R.L., Schoppy, D.W., Smith, K.D., Durham, A.C., and Brown, E.J. (2010). Cancer Res. *70*, 9693–9702.

Grabocka, E., Pylayeva-Gupta, Y., Jones, M.J.K., Lubkov, V., Yemanaberhan, E., Taylor, L., Jeng, H.H., and Bar-Sagi, D. (2014). Cancer Cell *25*, this issue, 243–256.

Halazonetis, T.D., Gorgoulis, V.G., and Bartek, J. (2008). Science *319*, 1352–1355.

Huang, D.C., Marshall, C.J., and Hancock, J.F. (1993). Mol. Cell. Biol. *13*, 2420–2431.

King, F.W., Skeen, J., Hay, N., and Shtivelman, E. (2004). Cell Cycle *3*, 634–637.

Lim, K.H., Ancrile, B.B., Kashatus, D.F., and Counter, C.M. (2008). Nature *452*, 646–649.

Matallanas, D., Romano, D., Al-Mulla, F., O'Neill, E., Al-Ali, W., Crespo, P., Doyle, B., Nixon, C., Sansom, O., Drosten, M., et al. (2011). Mol. Cell *44*, 893–906.

Pylayeva-Gupta, Y., Grabocka, E., and Bar-Sagi, D. (2011). Nat. Rev. Cancer *11*, 761–774.

Ray-David, H., Romeo, Y., Lavoie, G., Déléris, P., Tcherkezian, J., Galan, J.A., and Roux, P.P. (2013). Oncogene *32*, 4480–4489.

Young, A., Lou, D., and McCormick, F. (2013). Cancer Discov *3*, 112–123.

Zhang, Z., Wang, Y., Vikis, H.G., Johnson, L., Liu, G., Li, J., Anderson, M.W., Sills, R.C., Hong, H.L., Devereux, T.R., et al. (2001). Nat. Genet. *29*, 25–33.

Cancer Cell
Article

The *PRKCI* and *SOX2* Oncogenes Are Coamplified and Cooperate to Activate Hedgehog Signaling in Lung Squamous Cell Carcinoma

Verline Justilien,[1] Michael P. Walsh,[1] Syed A. Ali,[1] E. Aubrey Thompson,[1] Nicole R. Murray,[1] and Alan P. Fields[1,*]
[1]Department of Cancer Biology, Mayo Clinic Cancer Center, Jacksonville, FL 32224, USA
*Correspondence: fields.alan@mayo.edu
http://dx.doi.org/10.1016/j.ccr.2014.01.008

SUMMARY

We report that two oncogenes coamplified on chromosome 3q26, *PRKCI* and *SOX2*, cooperate to drive a stem-like phenotype in lung squamous cell carcinoma (LSCC). Protein kinase Cι (PKCι) phosphorylates SOX2, a master transcriptional regulator of stemness, and recruits it to the promoter of Hedgehog (Hh) acyltransferase (*HHAT*) that catalyzes the rate-limiting step in Hh ligand production. PKCι-mediated SOX2 phosphorylation is required for *HHAT* promoter occupancy, *HHAT* expression, and maintenance of a stem-like phenotype. Primary LSCC tumors coordinately overexpress PKCι, SOX2, and HHAT and require PKCι-SOX2-HHAT signaling to maintain a stem-like phenotype. Thus, PKCι and SOX2 are genetically, biochemically, and functionally linked in LSCC, and together they drive tumorigenesis by establishing a cell-autonomous Hh signaling axis.

INTRODUCTION

Lung cancer is the major cause of cancer death, with a 5-year-survival rate of 16% (Siegel et al., 2012). Non-small cell lung cancer (NSCLC) accounts for ~80% of lung cancer cases and is subdivided into adenocarcinoma (LAC), squamous cell carcinoma (LSCC), and large cell carcinoma (LCLC). Distinct histologies, genetic and epigenetic changes, and sites of origin characterize NSCLC subtypes, suggesting they may have unique responses to therapy. Recent therapies targeting pathways active in NSCLC subtypes have resulted in encouraging new treatments for LAC driven by *EGFR* or *EML4-ALK* mutations. However, few advances have resulted in better treatment options for LSCC, a carcinoma that accounts for 30% of all lung cancer cases. Thus, there is a need to better understand molecular mechanisms that drive LSCC and to translate this knowledge into better intervention strategies.

NSCLC tumors contain stem-like cells responsible for lung tumor initiation, maintenance, relapse, and metastasis (Chen et al., 2008; Eramo et al., 2008; Justilien et al., 2012). These cells exhibit resistance to commonly used therapeutic agents (Chen et al., 2008), making them a likely cause of therapeutic failure. Similar cell populations exist in several cancer types (Chen et al., 2012; Driessens et al., 2012; Schepers et al., 2012). Lineage tracing reveals these cells clonally expand to give rise to malignant and nonmalignant, differentiated cell types. These highly tumorigenic cells exhibit self-renewal by activating developmental pathways including Wnt, Hedgehog (Hh), and Notch and by aberrant expression of stem-related genes such as BMI1 (Siddique and Saleem, 2012), OCT3/4 (Chiou et al., 2010), SOX2 (Yuan et al., 2010), and NANOG (Chiou et al., 2010) that participate in their maintenance. As tumorigenic drivers, these stem-like cells must be effectively targeted to elicit long-lasting therapeutic responses.

We previously identified *PRKCI* as an oncogene in LSCC (Regala et al., 2005b). *PRKCI* is overexpressed in LSCC cells and primary tumors due to tumor-specific amplification of a chromosome 3q26 amplicon (Regala et al., 2005b). Tumor protein kinase Cι (PKCι) expression is predictive of poor clinical outcome, and PKCι drives LSCC cell invasion and transformed growth in vitro and in vivo (Frederick et al., 2008; Justilien and Fields, 2009; Regala et al., 2005a, 2008). Genetic disruption of *Prkci* in the *LSL-Kras*^{G12D} mouse LAC model blocks tumor initiation by inhibiting expansion of putative lung cancer stem cells

Significance

Lung cancer is the leading cause of cancer deaths worldwide. LSCC represents 30% of lung cancer diagnoses and is characterized by poor therapeutic response, a high relapse rate, and poor prognosis. Here, we identify a genetic, biochemical, and functional link between two oncogenes on chromosome 3q26, *PRKCI* and *SOX2*, that are coamplified and overexpressed in a majority of LSCC tumors. Our data indicate that chromosome 3q26 copy number gains serve to genetically activate *PRKCI* and *SOX2* that together establish a PKCι-SOX2-HHAT signaling axis that drives a stem-like phenotype. Our results provide a compelling rationale for use of PKCι inhibitors currently in clinical development to target LSCC.

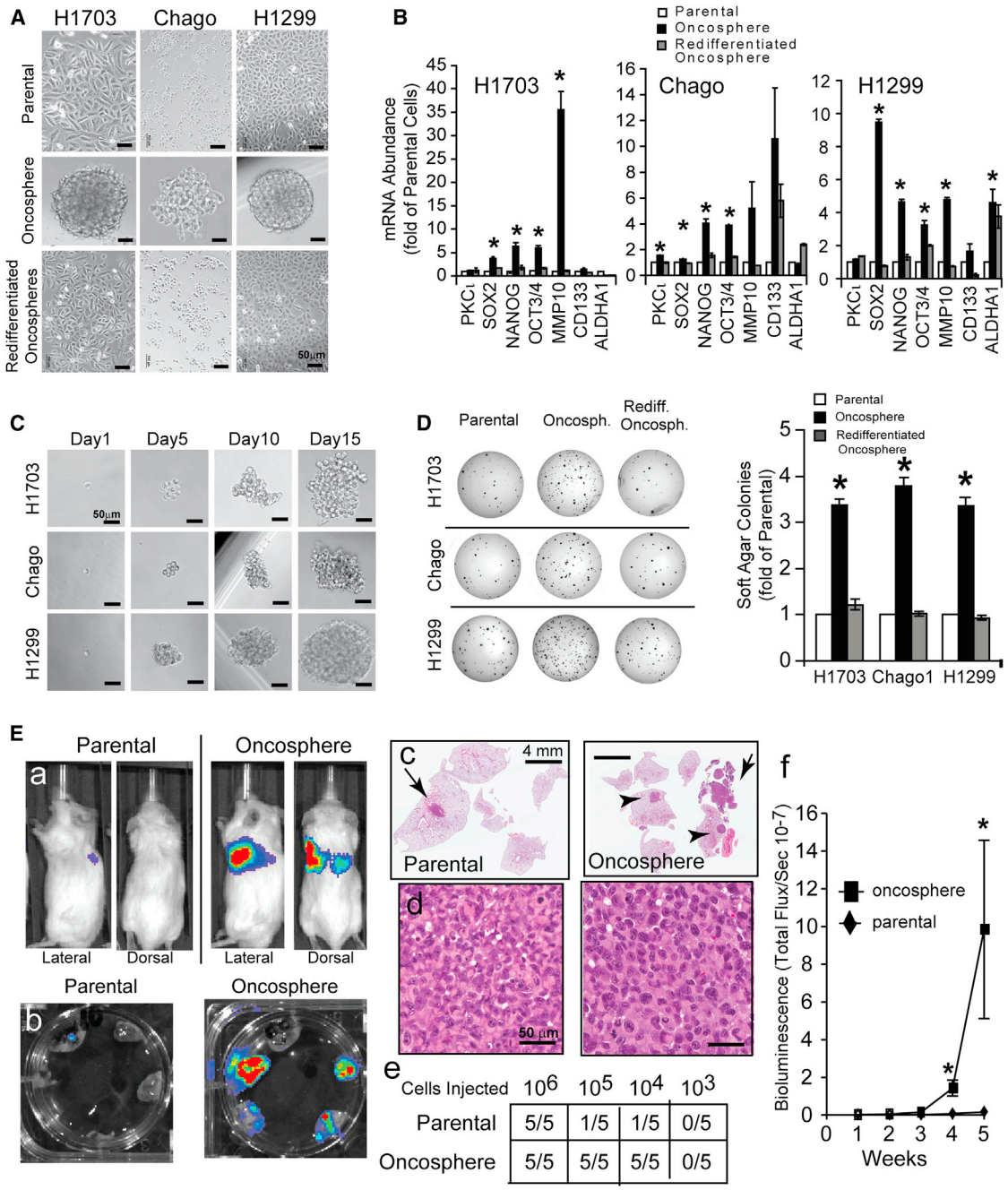

Figure 1. Lung Cancer Oncospheres Exhibit Stem-like Characteristics

(A) Phase contrast photomicrographs of H1703, ChagoK1, and H1299 parental adherent cells (top), oncospheres in low-adherence culture (middle), and redifferentiated oncosphere cells after return to adherent culture (bottom).

(B) qPCR for putative stem cell markers expressed as fold of parental cells ± SEM, n = 3; *p < 0.05 versus NT adherent cells. Results are representative of five independent experiments.

(C) Photomicrographs showing clonal expansion of individual cells into oncospheres over a 15 day period.

(D) Anchorage-independent growth expressed as mean fold-change from parental cells ± SEM, n = 5, *p < 0.05 versus NT adherent cells. Results are representative of five independent experiments.

(E) Formation of lung orthotopic tumors in immunocompromised mice. Ten thousand parental H1299 adherent or oncosphere cells were implanted into the lungs of immune-deficient mice. Lateral and dorsal views of bioluminescent images of a tumor-bearing mouse (a) and corresponding bioluminescence image upon lung dissection (b). Hematoxylin and eosin staining of typical parental and oncosphere tumors (c). Oncospheres develop primary tumors at the site of injection (arrows) and multiple lesions to the ipsilateral and contralateral lobes of the lung (arrowheads); parental cells develop either a single, small tumor at the site of injection

(legend continued on next page)

(Regala et al., 2009). Here, we demonstrate that *PRKCI* maintains a highly tumorigenic phenotype in lung cancer cells harboring *PRKCI* amplification, and in LSCC tumors. Our results reveal a genetic, biochemical, and functional interaction between *PRKCI* and *SOX2* that coordinately drives growth and maintenance of LSCC stem-like cells.

RESULTS

Lung Oncosphere Cells Exhibit Stem-like Properties

Highly malignant tumor cells can be enriched in defined medium at low adherence (Eramo et al., 2008; Justilien et al., 2012). These conditions favor growth of highly tumorigenic stem-like cells, while negatively selecting for less tumorigenic differentiated tumor cells. We isolated stem-like cells from five human lung cancer cell lines harboring 3q26 copy number gains by using established protocols (Eramo et al., 2008; Justilien et al., 2012): H1299, H1703, ChagoK1, H520, and H1869. H1299, H1703, and ChagoK1 grew as cell spheres (oncospheres) that exhibit many stem-like properties (Figure 1A). First, when returned to adherent culture, oncosphere cells redifferentiated and acquired morphology comparable to parental cells (Figure 1A). Second, oncosphere cultures expressed elevated mRNA for genes associated with a stem-like phenotype including SOX2, OCT3/4, NANOG, ALDHA1, PROM1/CD133, and MMP10 that was lost upon redifferentiation (Figure 1B). Third, single oncosphere cells clonally expand with high efficiency (H1703 cells, 91/98 cells [93%]; ChagoK1 cells, 41/44 cells [93%]; and H1299 cells, 125/138 cells [91%]) (Figure 1C). Fourth, oncosphere cultures exhibited enhanced soft agar growth, a property lost upon redifferentiation (Figure 1D). Similar results were obtained in H520 and H1869 LSCC cells (Figures S1A–S1D available online). Finally, oncospheres displayed enhanced tumorigenic potential in vivo. Limiting dilution showed that implantation of as few as 10,000 H1299 oncosphere cells into the lungs of immune-deficient mice resulted in efficient tumor take (5/5), but only occasional tumor take in parental cells (1/5) (Figure 1Ee). A similar increase in tumor take was observed in H520 oncospheres compared with parental H520 cells (Figure S1E). Oncosphere cells developed larger tumors than parental cells and routinely produced lesions in the contralateral lung, whereas parental cells did not. Oncosphere-derived tumors exhibit morphology similar to parental cell tumors (Figure 1Ed), and these tumors express SOX2, OCT3/4, NANOG, ALDHA1, CD133, and MMP10 levels similar to that of parental cells, indicating the ability of oncosphere cells to differentiate in vivo (Figure S1). Finally, H1299 oncosphere cells efficiently generate tumors of similar morphology through three serial passages in mice (data not shown).

PKCι Maintains Oncospheres by Activating a Cell-Autonomous Hh Signaling Axis

PKCι is necessary for transformation and expansion of bronchioalveolar stem cells (BASCs), putative tumor-initiating cells in *Kras*-mediated lung tumorigenesis (Regala et al., 2009). Interestingly, MMP10, a transcriptional target of PKCι in lung cancer cells (Frederick et al., 2008) and transformed BASCs (Regala et al., 2009), is induced in oncospheres (Figure 1B; Figure S1), suggesting that PKCι is activated in these cells. Indeed, oncospheres exhibit an increase in T410 PKCι phosphorylation (Figure S2), an event associated with PKCι activity (Baldwin et al., 2008; Desai et al., 2011; Le Good et al., 1998; Standaert et al., 1999). PKCι RNA interference (RNAi) severely impaired soft agar growth and clonal expansion of H1703, ChagoK1, and H1299 oncospheres (Figures 2A and 2B), indicating that PKCι is required for a stem-like phenotype. Similar results were obtained in H520 and H1869 cells (Figure S2).

To identify PKCι-regulated pathways, we conducted total RNA sequencing on nontarget (NT) and PKCι RNAi parental and oncospheres from H1703, ChagoK1, and H1299 cells to identify genes up- or downregulated in all three oncosphere lines in a PKCι-dependent manner (Tables S1 and S2). We then used MetaCore pathway analysis to determine whether PKCι regulates three main pathways associated with stem maintenance: Wnt, Hh, and Notch. Results revealed that PKCι significantly regulates Hh ($p = 0.025$) but not Wnt ($p = 0.091$) or Notch ($p = 0.354$), suggesting a role for PKCι-dependent Hh signaling in oncospheres. Hh components Hedgehog acyltransferase (*HHAT*), *ADRBK1*, *CDK19*, and *GLI1* were identified as PKCι regulated (raw gene counts are given in Table S3; Hh signaling components are listed in Table S4; and the RNA-seq data are available in the Gene Expression Omnibus [GEO] database [http://www.ncbi.nlm.nih.gov/gds] under the accession number GSE48599), and these genes were validated by quantitative (q) PCR in H1703 and H1299 oncospheres (Figure 2C).

Our data suggest that PKCι regulates Hh pathway activity to stimulate oncosphere growth. Consistent with this notion, auranofin, an antiarthritic gold salt that selectively inhibits PKCι signaling (Erdogan et al., 2006; Stallings-Mann et al., 2006; Wang et al., 2013), led to dose-dependent inhibition of oncosphere proliferation, with half maximal inhibitory concentration values (IC_{50}s) of ~0.5–2.0 μM, and a significant decrease in *HHAT* and *Gli1* expression (Figure S2). Similarly, the Smoothened (SMO) inhibitor LDE225 induced dose-dependent inhibition of oncosphere proliferation, with IC_{50}s in the 10–40 nM range, consistent with the submicromolar IC_{50} for SMO inhibition (Buonamici et al., 2010) (Figure 2D). Interestingly, parental cells were much less sensitive to LDE225 (IC_{50}s > 5 μM; well above the IC_{50} for SMO inhibition) (Figure 2D), consistent with reports that lung progenitor/stem cells exhibit Hh-dependent proliferation, whereas differentiated NSCLC cells do not (Watkins et al., 2003). Interestingly, oncospheres from LAC cell lines (A549, H358, and H1437) are not sensitive to LDE225 (IC_{50}s > 10 μM), suggesting that Hh signaling is not required for LAC oncospheres (Figure S2). Furthermore, neither *HHAT* nor *GLI1* is induced in LAC oncospheres, and PKCι knockdown (KD) does not affect expression of these genes (Figure S2), suggesting that the PKCι-Hh signaling axis is not operative in LAC.

(shown) or no identifiable tumor. The 40× magnification reveals the similar morphology of oncosphere- and parental cell-derived tumors (d). Incidence of tumor formation in limiting dilutions of H1299 oncosphere and parental cells (e). Quantification of tumor growth by in vivo imaging system (IVIS). Data represent mean ± SEM, n = 5; *p < 0.05 versus parental cells (f).
See also Figure S1.

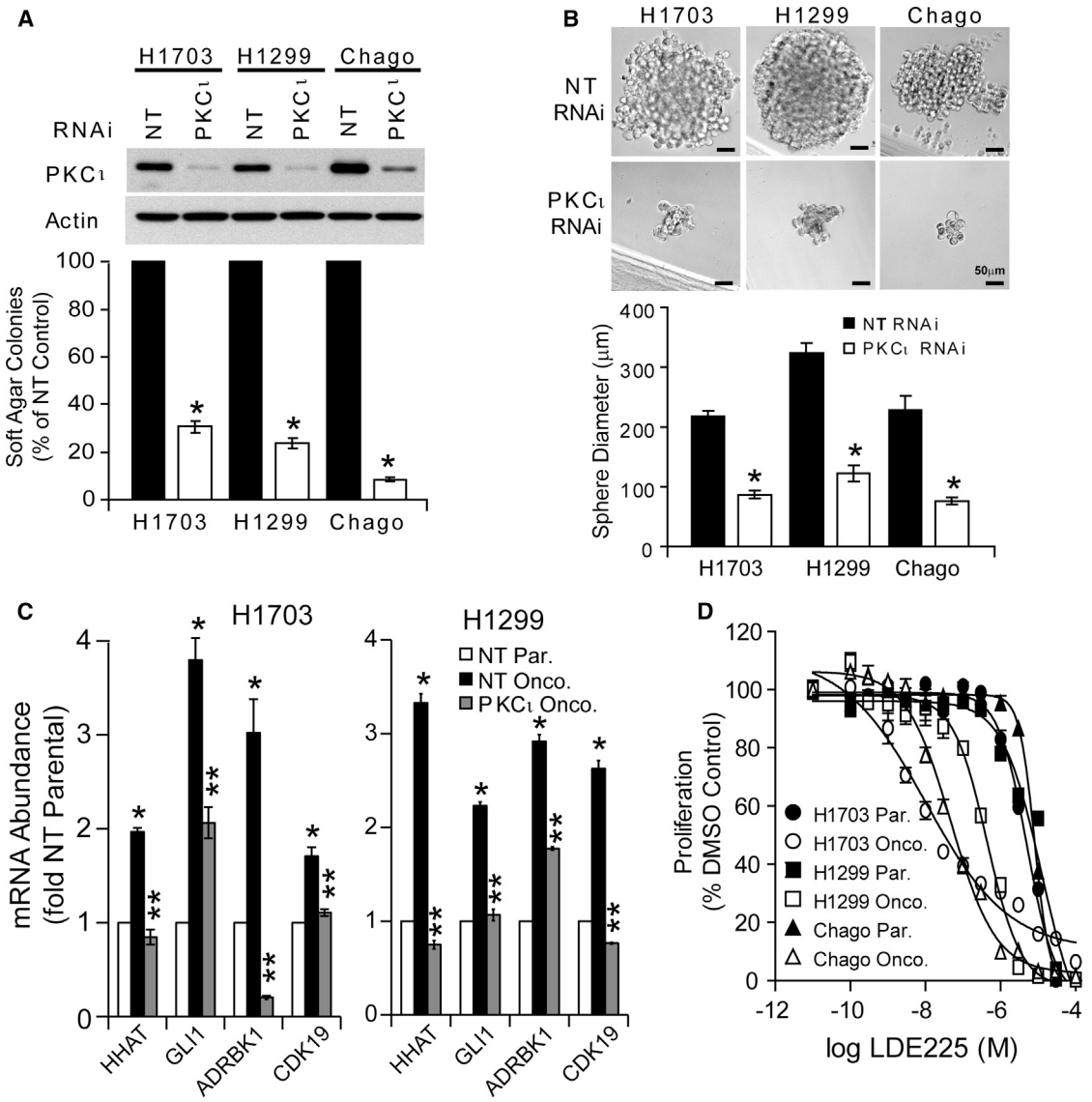

Figure 2. PKCι Is Required for Maintenance of a Stem-like Phenotype in Oncosphere Cells

(A) Effect of RNAi-mediated PKCι KD (immunoblot) on anchorage-independent growth of H1703, H1299, and ChagoK1 oncospheres. Results are expressed relative to NT RNAi control cells ± SEM, n = 5; *p < 0.001. Results are representative of three independent experiments.

(B) Oncosphere size expressed as mean diameter in micrometers ± SEM, n = 98 (H1703), 138 (H1299), and 44 (ChagoK1). *$p < 2 \times 10^{-8}$.

(C) qPCR for HHAT, GLI1, ADRBK1, and CDK19. Results are expressed as fold NT parental cells ± SEM, n = 3; *p < 0.05 compared with NT parental. Results are representative of three independent experiments.

(D) Effect of SMO inhibitor LDE225 on H1703, H1299, and ChagoK1 oncosphere (Onco.) and parental cell (Par.) proliferation. Results expressed as percentage of DMSO control ± SEM, n = 6. Results are representative of three independent experiments.

See also Figure S2 and Tables S1, S2, and S3.

HHAT catalyzes a critical step in Hh ligand processing and can initiate Hh signaling, and GLI1 is a major transcriptional effector of Hh signaling. Therefore, we assessed the effect of genetic inhibition of HHAT and GLI1 on stem-like behavior. HHAT or GLI1 RNAi (Figures 3A and 3B) significantly inhibited clonal expansion and soft agar growth of H1299 oncospheres (Figures 3C and 3D). Similar results were observed in H1703, ChagoK1, H520, and H1869 oncospheres (Figures S3A–S3D). Results were validated by reconstitution using the small-molecule Hh agonist Hh-Ag1.5. PKCι, HHAT, and GLI1 RNAi significantly inhibited (Figure 3E) and Hh-Ag1.5 rescued oncosphere growth in HHAT KD cells, but not PKCι or GLI1 KD cells (Figure 3E). These results are expected because HHAT acts upstream of ligand, PKCι modulates Hh components both upstream (i.e., HHAT) and downstream (i.e., GLI1, ADRBK1, and CDK19) of ligand, and GLI1 activates Hh-mediated transcription downstream of ligand. Because PKCι regulates *HHAT*, an enzyme required for sonic Hedgehog (SHH) palmitoylation, we assessed the effect of PKCι and HHAT KD on palmitolyated SHH production using the palmitic acid analog ω-alkynyl

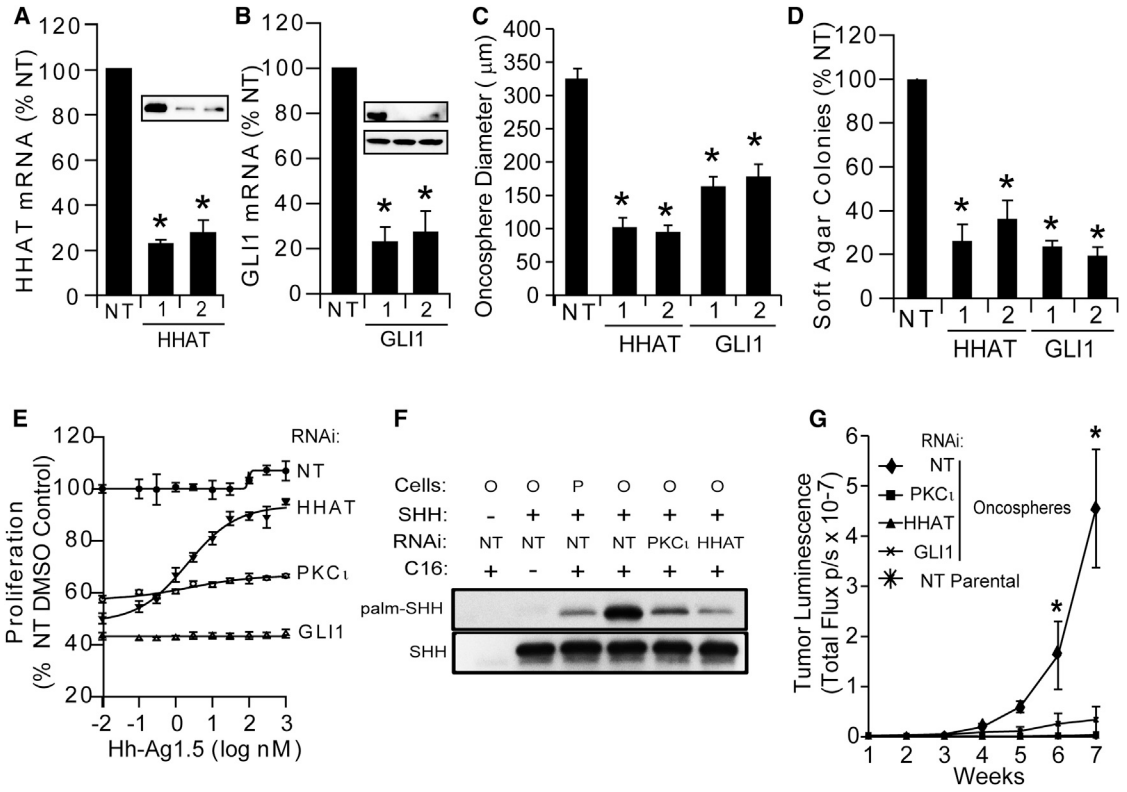

Figure 3. Oncosphere Growth Requires a PKCι-Dependent Hh Signaling Axis

(A and B) RNAi-mediated KD of HHAT (A) and GLI1 (B) in H1299 oncospheres expressed as fold of NT RNAi control ± SEM, n = 3; *p < 0.0005 compared with NT control.

(C) Effect of HHAT or GLI1 RNAi on clonal expansion expressed as oncosphere diameter in micrometers ± SEM, n ≥ 15 per RNAi sample; *p < 1.0×10^{-6}. Data are representative of three independent experiments.

(D) Soft agar growth expressed relative to NT RNAi control cells ± SEM, n = 5; *p < 0.003. Data are representative of three independent experiments.

(E) NT, PKCι, HHAT, and GLI1 oncospheres were treated with the indicated amounts of Hh-Ag1.5, a selective Hh agonist, and cell proliferation was assessed by 3-(4,5-dimethylthiazol-2-yl)-2,5-diphenyltetrazolium (MTT) at 5 days. Results are expressed as percentage of NT DMSO control ± SEM, n = 6.

(F) Detection of palmitoylated SHH in oncospheres. Parental (P) and oncosphere (O) NT, PKCι, and HHAT RNAi cultures expressing FLAG-SHH were metabolically labeled with ω-alkynyl-palmitate (C16), and palmitoylated SHH (palm SHH) and total SHH were detected as described in Experimental Procedures.

(G) Oncosphere growth as lung orthotopic tumors. NT parental and NT, PKCι, HHAT, and GLI1 RNAi oncosphere tumor growth was monitored by bioluminescence detected by IVIS imaging. Data are presented as total flux in photons per second ± SEM, n = 10 per group except for PKCι, where n = 9; *p < 0.05 significantly different from NT RNAi oncosphere tumors.

See also Figure S3.

palmitate as described previously (Yap et al., 2010). Metabolically labeled FLAG-SHH was immunoprecipitated with anti-FLAG antibody, derivatized with azido-biotin using CLICK chemistry, and palmitoylated SHH was detected by immunoblot analysis using horseradish-NeutrAvidin (Figure 3F). NT H1299 oncospheres produce more palmitoylated SHH than NT parental cells, and both PKCι and HHAT KD oncospheres exhibit a striking decrease in palmitoylated SHH. Similar results were obtained in H1703 cells (Figure S3E). Thus, oncospheres use a PKCι-dependent cell-autonomous Hh signaling pathway to maintain their stem-like phenotype.

To assess the importance of PKCι-Hh signaling in oncosphere behavior in vivo, we determined the ability of NT, PKCι, HHAT, and GLI1 RNAi oncospheres, and NT parental cells, to initiate lung orthotopic tumors in immune-deficient mice. As expected, H1299 NT RNAi oncospheres exhibited an increased tumor take rate (10/10 versus 2/10 mice for NT parental cells) and developed significantly larger tumors than NT RNAi parental cells (Figure 3G). PKCι, HHAT, and GLI1 RNAi oncospheres showed a decreased take rate (1/9, 0/10, and 1/10, respectively) and failed to produce large tumors (Figure 3G). These data indicate that cell-autonomous, PKCι-dependent Hh signaling is critical for the tumorigenic growth of oncospheres in vivo.

PKCι can phosphorylate Gli1 and activate its transcriptional activity, and Gli1 can regulate PKCι expression, in basal cell carcinoma cells (Atwood et al., 2013). Thus, we assessed Gli1 phosphorylation status in NT and PKCι KD oncospheres (Figure S3F). We observed a decrease in phospho-(p)Ser/Thr Gli1 commensurate with the decrease in total Gli1 in PKCι KD cells. When normalized to total Gli1, no appreciable change in Gli1 phosphorylation was observed, indicating that the PKCι-Hh signaling axis described here is distinct from that reported in basal cell carcinoma (Figure S3F). Furthermore, neither HHAT nor Gli1 RNAi affected PKCι mRNA abundance in oncospheres,

indicating that PKCι is not a target of Hh-Gli1 signaling in lung cancer stem-like cells (Figure S3G).

PKCι Regulates SOX2-Mediated *HHAT* Expression in Oncospheres

PRKCI is amplified as part of a 3q26 amplicon that drives PKCι expression in LSCC tumors, leading us to explore other possible genetic regulators residing on the 3q26 amplicon. *SOX2*, an SRY-related high mobility group domain (HMG)-box (Sox) transcription factor and master regulator of stem cell maintenance (Sarkar and Hochedlinger, 2013), is consistently induced in our oncosphere cultures (Figure 1B; Figure S1). *SOX2* is an oncogene in LSCC (Bass et al., 2009), and it can maintain cancer stem cells (Basu-Roy et al., 2012; Ikushima et al., 2011; Tian et al., 2012). SOX2 RNAi (Figure 4A) significantly inhibited clonal expansion and anchorage-independent growth of H1299 oncospheres (Figures 4B and 4C), indicating a key role for SOX2 in these cells. Similar results were obtained in H1703, H520, and H1869 oncospheres (Figure S4).

Chromatin immunoprecipitation (ChIP) sequencing analysis of SOX2 revealed that SOX2 can occupy the *HHAT* promoter and regulate *HHAT* expression in glioblastoma cells (Fang et al., 2011). The proximal human *HHAT* promoter contains seven potential SOX2 binding motifs (Figure 4D, inset). Interestingly, SOX2 ChIP assays in NT and PKCι RNAi oncospheres revealed SOX2 occupancy on the HHAT promoter in NT RNAi cells and a significant decrease in occupancy in PKCι RNAi cells without a change in SOX2 protein abundance (Figure 4D). Furthermore, SOX2 KD (Figure 4E) led to a decrease in *HHAT* mRNA and protein (Figure 4F). Similar results were obtained in H1703 oncospheres (Figure S4). Thus, SOX2 regulates *HHAT* promoter activity and expression by a PKCι-dependent mechanism. Not surprisingly, growth of SOX2 RNAi oncospheres cannot be reconstituted by Hh agonist (Figure S4E), indicating that SOX2 regulates genes in addition to *HHAT* that are also required for maintenance of the stem-like phenotype.

Given the functional link between *PRKCI* and *SOX2*, we assessed whether these genes are coordinately amplified and overexpressed in LSCC tumors. Interrogation of a LSCC data set (178 cases) from The Cancer Genome Atlas (TCGA) revealed that *PRKCI* and *SOX2* are frequently coamplified and coordinately overexpressed in primary LSCC tumors (Figure 4G). Analysis also revealed a strong positive correlation between PKCι and SOX2 expression with HHAT and GLI1, two key Hh pathway components regulated by PKCι in oncospheres harboring *PRKCI* copy number gains (Figure 4H). SOX2 and HHAT expression also correlated in LSCC tumors, suggesting that SOX2 regulates HHAT expression in vivo (Table S5) and providing evidence for the PKCι-SOX2-HHAT signaling axis in vivo. We next assessed whether coordinate *PRKCI* and *SOX2* amplification may drive a "stem-like" genotype in primary LSCC tumors. Airway basal cells exhibit stem-like properties (Hajj et al., 2007; Hong et al., 2004; Rock et al., 2009) and are putative stem or progenitor cells for LSCC (Ooi et al., 2010; Wistuba and Gazdar, 2006). Therefore, we tested for an association between *PRKCI* and *SOX2*, and expression of a previously described 13-gene airway basal stem cell signature (Shaykhiev et al., 2013). Analysis revealed a strong positive correlation between *PRKCI*, *SOX2*, and expression of 6 of 13 of the airway basal stem cell signature genes (Table S6). Interestingly, this correlation was not observed in primary LAC tumors, consistent with the proposed role of basal cells as putative cells of origin for LSCC, but not LAC (Wistuba and Gazdar, 2006).

Primary LSCC Cells Require PKCι, SOX2, and HHAT for Oncosphere Formation and Proliferation

To assess whether PKCι-SOX2-Hh signaling regulates behavior of primary LSCC tumors, we established oncosphere cultures from primary LSCCs obtained from individuals undergoing tumor resection. Similarly to established cell lines, primary LSCC tumor cells readily grow as oncospheres in nonadherent stem cell culture (Figure 5A). PKCι, SOX2, or HHAT RNAi led to efficient KD of their respective target (Figure 5B). PKCι and SOX2 RNAi cells also exhibited reduced HHAT and GLI1 expression, whereas HHAT KD had no demonstrable effect on PKCι or SOX2 expression (Figure 5B). PKCι, SOX2, and HHAT RNAi similarly impaired oncosphere proliferation (Figure 5C). Furthermore, PKCι, SOX2, and HHAT RNAi cells produced small, disorganized oncospheres (Figure 5D) exhibiting membrane blebbing and intracellular vacuoles indicative of reduced cell viability (Figure 5E, arrows). Thus, PKCι-SOX2-Hh signaling is important for maintenance and survival of primary human LSCC stem-like cells.

SOX2 Is a PKCι Substrate

Analysis of the SOX2 amino acid sequence indicated that SOX2 may serve as a substrate for atypical PKC. When purified recombinant human PKCι and recombinant human SOX2 were incubated in a kinase reaction, robust incorporation of ^{32}P from ATP into SOX2 was observed that is not observed in the absence of PKCι (Figure 6A). To identify the site(s) phosphorylated by PKCι, phosphorylated SOX2 was subjected to proteolytic digestion and mass spectrometry (MS) analysis as described under Experimental Procedures. MS analysis recovered peptides encompassing all known phosphorylation sites on SOX2 and revealed a single, previously uncharacterized phosphorylation site, T118, that conforms to an atypical PKC consensus recognition motif (Figure 6B).

To assess the importance of T118 phosphorylation we first introduced a silent mutation into a FLAG-tagged SOX2 cDNA to render it resistant to SOX2 RNAi #2 and then mutagenized T118 to either alanine (T118A) or aspartic acid (T118D) to eliminate or mimic T118 phosphorylation. Immunoblot analysis of H1299 oncospheres stably transfected with wild-type (WT)-SOX2, T118A-SOX2, T118D-SOX2, or empty control vector, followed by SOX2 RNAi, revealed efficient loss of endogenous SOX2 and expression of similar levels of WT- and T118-SOX2 mutants (Figure 6C). SOX2 RNAi oncospheres expressing control vector showed reduced HHAT and GLI1 expression as expected (Figure 6D). In contrast, expression of exogenous WT- or T118D-SOX2 significantly restored HHAT and GLI1 expression in SOX2 RNAi cells, whereas T118A-SOX2 did not (Figure 6D). As expected, SOX2 RNAi cells expressing empty control vector showed impaired clonal expansion and soft agar growth (Figures 6E and 6F). Expression of WT- or T118D-SOX2 significantly reconstituted clonal expansion and soft agar growth in SOX2 RNAi oncospheres, whereas

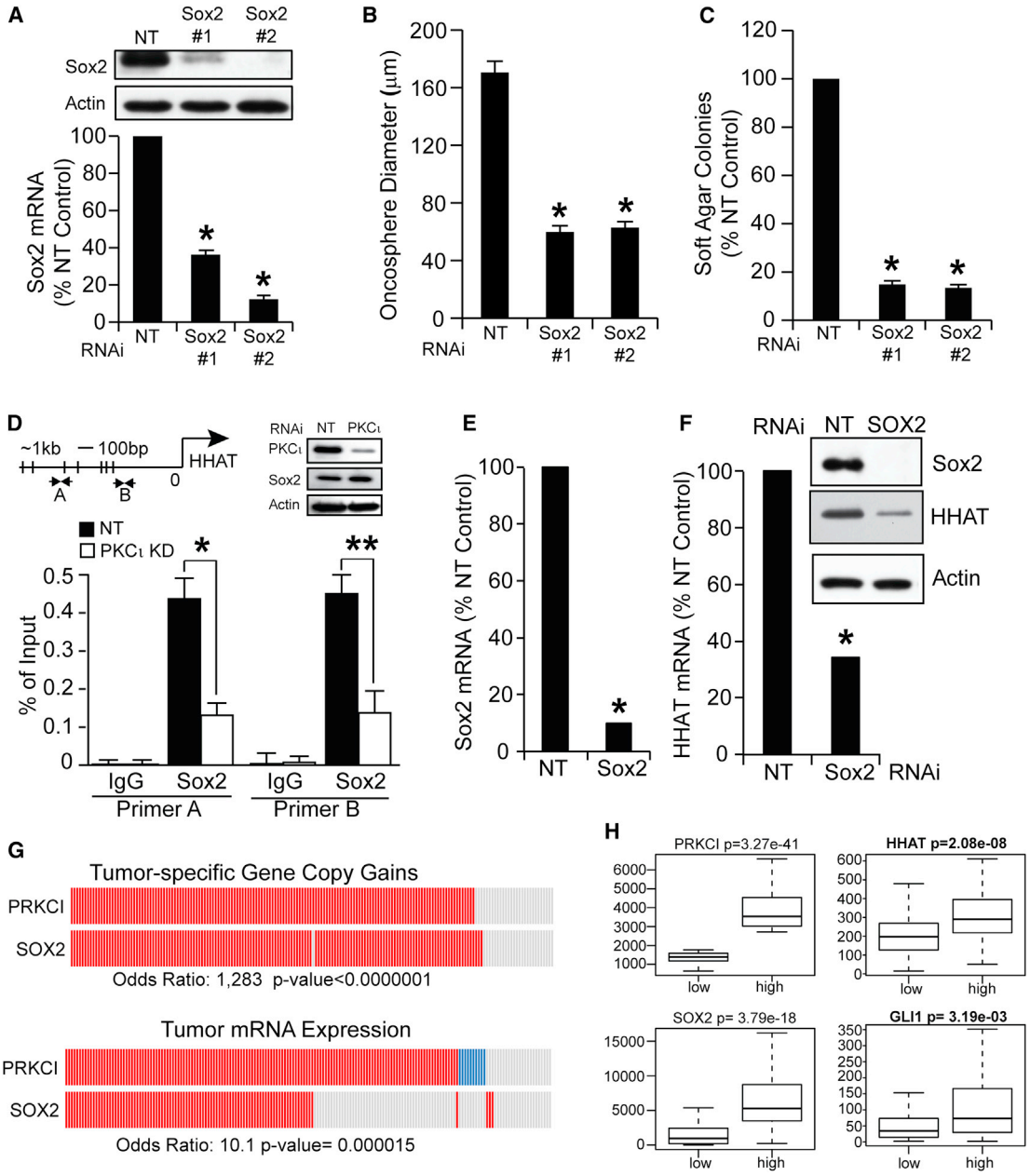

Figure 4. PKCι Regulates HHAT Expression through Control of SOX2 Occupancy of the HHAT Promoter

(A) RNAi-mediated KD of *SOX2* in H1299 oncospheres. Results are expressed as percentage of NT control ± SEM, n = 3; *p < 0.05.

(B) Clonal expansion expressed as oncosphere diameter in micrometers ± SEM, n ≥ 22 per RNAi sample; $p < 3.0 \times 10^{-14}$. Data are representative of three independent experiments.

(C) Anchorage-independent growth relative to NT RNAi control cells ± SEM, n = 5; *$p < 5.0 \times 10^{-9}$. Results are representative of three independent experiments.

(D) ChIP analysis to assess SOX2 occupancy of the HHAT promoter. Schematic depicts the HHAT promoter region; the positions of ChIP probes used are indicated as A and B. Consensus SOX2 binding sites are indicated by vertical slashes. Data are presented as percentage of input ± SEM, n = 3; *p < 0.00002, **p < 0.00003. Data are representative of two independent experiments. IgG, immunoglobulin G.

(E and F) Effect of *SOX2* RNAi (E) on HHAT expression in oncosphere cells (F). Data are expressed relative to NT RNAi control cells ± SEM (*p < 0.0007) and are representative of three independent experiments.

(G) *PRKCI* and *SOX2* amplification (top) and overexpression (bottom) in primary LSCC tumors. Red bars, tumors with amplification (top) or overexpression (bottom); blue bars, tumors with decreased expression; gray bars, tumors with no change in gene copy number (top) or expression (bottom).

(H) Analysis of *PRKCI*, *SOX2*, *HHAT*, and *GLI1* expression in primary LSCC tumors. Primary LSCC tumors were force ranked on *PRKCI* expression and grouped into top and bottom tertiles corresponding to high and low *PRKCI* expression, respectively. Box plots denote the expression of *PRKCI*, *SOX2*, *HHAT*, and *GLI1* in tumors expressing low *PRKCI* (low) and high *PRKCI* (high). Bars represent the median, and boxes denote the 25% and 75% intervals; whiskers represent the 90% confidence intervals.

See also Figure S4 and Tables S4 and S5.

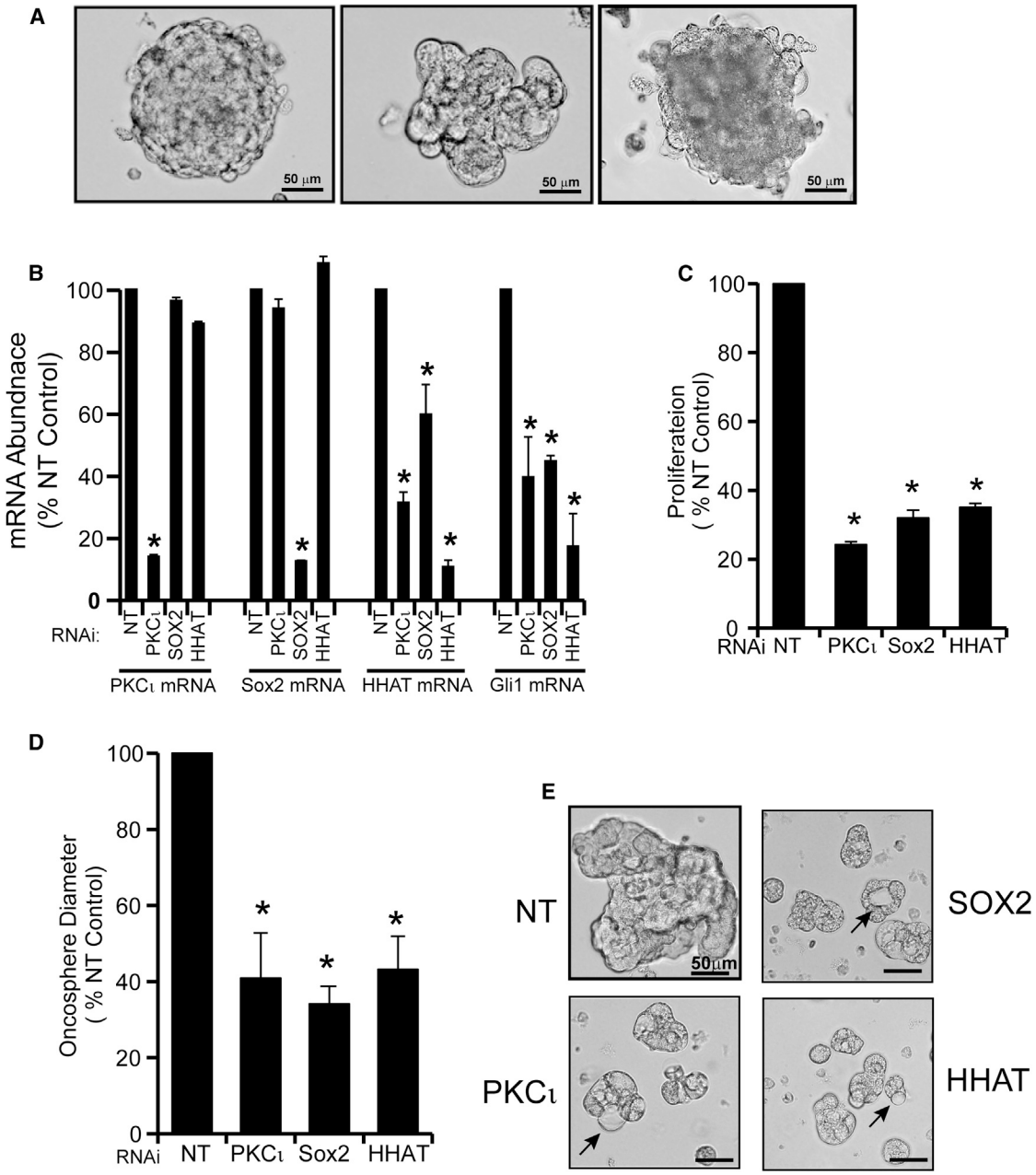

Figure 5. Primary LSCC Cells Require *PRKCI*, *SOX2*, and *HHAT* for Oncosphere Formation and Proliferation

(A) Phase contrast photomicrographs of oncospheres from three surgically resected primary LSCC tumors.

(B) qPCR analysis of *PRKCI*, *SOX2*, *HHAT*, and *GLI1* expressed as percentage of NT RNAi control ± SEM, n = 3; *p < 0.02.

(C) Proliferation of oncospheres by MTT assay expressed as percentage of NT RNAi control ± SEM, n = 3; *p < 4.0×10^{-7}.

(D) Clonal expansion of oncospheres. Results expressed as percentage of NT RNAi control ± SEM, n = 3; *p < 0.0002.

(E) Photomicrographs of NT, *PRKCI*, *SOX2*, and *HHAT* KD oncospheres. Arrows show membrane blebbing indicative of cell death. Results are representative of three independent experiments.

T118A-SOX2 did not (Figures 6E and 6F). SOX2 ChIP assays revealed reduced SOX2 occupancy of the HHAT promoter in SOX2 RNAi oncospheres expressing empty control vector that is significantly restored by expression of either WT- or T118D-SOX2, but not T118A-SOX2 (Figure 6G). T118 resides between the HMG domain and a consensus nuclear localization sequence (NLS) in SOX2, suggesting that T118 phosphorylation could affect SOX2 DNA binding, nuclear localization, or both. Immunoblot analysis revealed that WT-, T118A-, and T118D-SOX2 are predominantly nuclear (Figure 6G, immunoblots). Next, SOX2 RNAi oncospheres expressing WT-, T118A-, or T118D-SOX2 or control empty pCMV vector were transfected with an HHAT promoter luciferase reporter (pGL4-HHAT-luc) and assessed for HHAT promoter

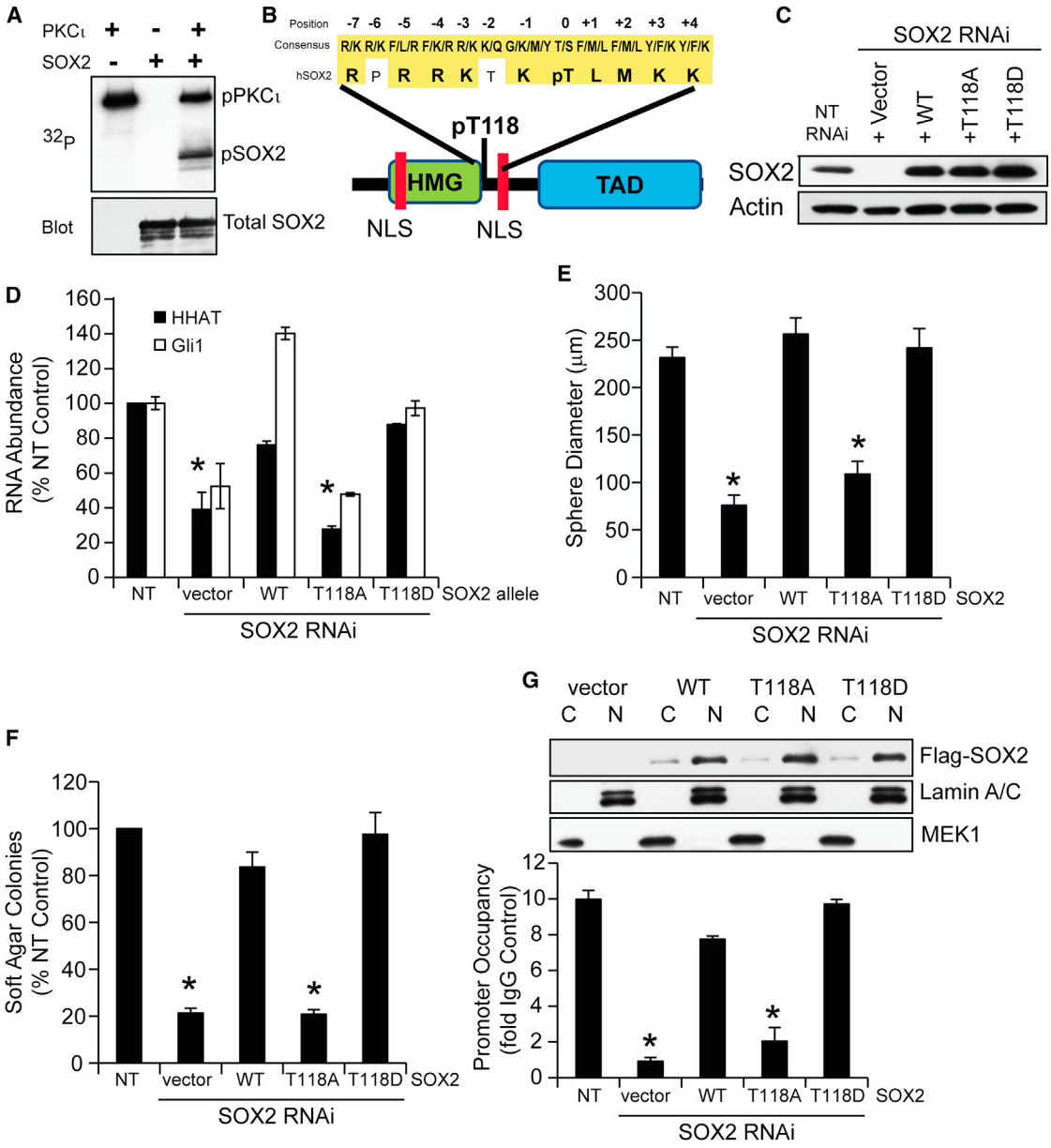

Figure 6. PKCι Directly Phosphorylates SOX2 at a Unique Site, T118, that Is Required for SOX2 Function

(A) Recombinant human SOX2 was incubated in kinase reaction buffer containing [^{32}P]ATP in the absence or presence of recombinant PKCι. Phosphorylated SOX2 was detected by autoradiography, and total SOX2 was detected by immunoblot analysis.

(B) Schematic of SOX2 protein structure. TAD, transactivation domain. MS analysis revealed a single PKCι-mediated phosphorylation site on SOX2 at T118 that conforms to a consensus atypical PKC phosphorylation site motif (insert).

(C) Immunoblot analysis of H1299 oncospheres stably transduced with NT or *SOX2* RNAi and then stably transfected with either empty vector (V) or vector encoding WT-SOX2 (WT), T118A-SOX2 (T118A), or T118D-SOX2 (T118D) mutants.

(D) qPCR analysis for *HHAT* and *GLI1* expressed relative to NT RNAi control cells ± SEM, n = 3; *p < 0.03.

(E) Clonal expansion expressed relative to NT RNAi control cells ± SEM, n > 20 per cell type; *p < 1.0 × 10^{-8}.

(F) Soft agar growth expressed relative to NT RNAi control cells ± SEM, n = 5, *p < 4.0 × 10^{-5}.

(G) Cellular localization and promoter occupancy of T118-SOX2 phosphorylation mutants. Immunoblot analysis of cytoplasmic and nuclear fractions for FLAG, Lamins A/C, and MEK1 (immunoblots). Lamins A/C served as a marker of nuclei and MEK1 as a marker of cytoplasm. *HHAT* promoter occupancy (bar graph) expressed as fold of IgG control ± SEM, n = 3; *p < 0.001. Results in (D)–(G) are representative of three independent experiments.

See also Figure S5.

activity (Figure S5). In all four cell lines tested, WT- and T118D-SOX2 stimulated HHAT promoter activity, whereas T118A did not. Thus, PKCι-mediated T118-SOX2 phosphorylation regulates SOX2 occupancy and HHAT promoter activity to stimulate HHAT expression, thereby driving a PKCι-Hh signaling axis in LSCC oncospheres.

DISCUSSION

Accumulating evidence supports the existence of tumor-initiating or cancer stem cells in human lung tumors that possess the capacity to self-renew, and differentiate into bulk tumor cells. These cells drive tumor initiation, progression, and metastasis, and they may contribute to relapse after chemotherapy. The majority of cancer deaths are caused by tumor metastasis and relapse, making these cells an attractive therapeutic target to achieve lasting therapeutic responses. However, the molecular mechanisms that drive the enhanced tumorigenic potential and stem-like behavior of tumor-initiating cells are poorly understood. We previously demonstrated that PKCι maintains a transformed phenotype in NSCLC cells and is critical for tumor initiation in murine lung cancer models (Regala et al., 2009). *Prkci* is required for tumor initiation and expansion of *Kras*-transformed BASCs, putative lung cancer stem cells in murine LAC models (Regala et al., 2009). Here, we show that PKCι plays a vital and previously unrecognized role in maintenance of stem-like cells isolated from human lung cancer cells harboring *PRKCI* copy number gains, and primary LSCC tumors. We also define a PKCι-SOX2-Hh signaling axis that drives the stem-like phenotype of these cells.

Aberrant Hh signaling has been implicated in the initiation and progression of various cancer subtypes, including lung. In basal cell carcinomas and medulloblastomas, Hh signaling is activated by tumor-specific mutations in the Hh pathway components Patched, SMO, or Suppressor of Fused (Epstein, 2008; Kool et al., 2008). Tumors without activating Hh mutations often use paracrine Hh signaling involving Hh ligand produced by tumor-associated stromal cells (Dierks et al., 2007; Tian et al., 2009; Yauch et al., 2008). Finally, some cancer cells exhibit autocrine Hh signaling, in which Hh ligand is produced and used by the same or neighboring tumor cells (Bar et al., 2007; Berman et al., 2003; Karhadkar et al., 2004; Stecca et al., 2007; Varnat et al., 2009). Autocrine Hh signaling has been described in SCLC and NSCLC (Park et al., 2011; Rodriguez-Blanco et al., 2013; Watkins et al., 2003); however, the factors that regulate and maintain autocrine Hh signaling are largely unknown. We find that PKCι regulates autocrine Hh signaling in oncospheres harboring *PRKCI* copy number gains, and we define a signaling cascade in which PKCι regulates HHAT that catalyzes the rate-limiting step in Hh ligand processing. Our finding that HHAT KD inhibits clonal expansion that can be reconstituted with Hh agonist provides compelling evidence for the importance of this autocrine Hh signaling mechanism in LSCC stem cell maintenance. Finally, our finding that HHAT KD oncospheres fail to generate tumors in vivo indicates that autocrine Hh signaling is vital for tumor initiation.

SOX2 is an oncogene in human LSCC (Bass et al., 2009; Hussenet et al., 2010; Yuan et al., 2010). Sox2 overexpression in mouse lung leads to increased lung epithelial cell proliferation and hyperplasia (Tompkins et al., 2011), whereas Sox2 deletion in mouse bronchiolar Clara cells, a potential lung regional stem cell, results in reduced cell proliferation and loss of airway differentiation markers (Tompkins et al., 2009). SOX2 is required for LSCC cell growth in vitro, and SOX2 overexpression in lung epithelial cells induces migration, transformed growth, and tumor formation in vivo (Hussenet et al., 2010). Consistent with these findings, we demonstrate that SOX2 maintains the tumorigenic potential of human LSCC oncospheres. We also uncover an unexpected link between SOX2 and Hh signaling that is mediated by PKCι. Our findings are consistent with SOX2-mediated regulation of SHH expression in neural stem cells (NSCs) (Favaro et al., 2009) and provide a potential molecular mechanism for SOX2-mediated Hh signaling in NSCs.

Phosphorylation can regulate Sox2 function in mouse embryonic stem cells (Jeong et al., 2010), and phosphoproteome analysis has identified Ser249, Ser250, and Ser251 as potential SOX2 phosphorylation sites (Van Hoof et al., 2009). However, the potential role of SOX2 phosphorylation in human cancer cells has not been investigated. We find that PKCι phosphorylates SOX2 at on a previously uncharacterized site, T118. T118 phosphorylation regulates SOX2 binding to, and activity of, the HHAT promoter. Our MS analysis, which interrogated all known SOX2 phosphorylation sites, detected pThr118 but no other sites in LSCC oncospheres (data not shown). These data indicate that T118 is a major SOX2 phosphorylation site, although we cannot exclude the presence of other low-level phosphorylation sites. Regardless, our functional data demonstrate the importance of T118 phosphorylation in SOX2 function and stem-like behavior.

Chromosome 3q26 amplification is one of the most frequent chromosomal alterations in human cancer and is found in a majority of LSCC (Balsara et al., 1997; Brass et al., 1996), serous ovarian (Sonoda et al., 1997; Sugita et al., 2000), cervical (Sugita et al., 2000), head and neck (Snaddon et al., 2001), oral (Lin et al., 2005), and esophageal tumors (Imoto et al., 2001). Interestingly, a major susceptibility locus for chemically induced mouse LSCC is syntenic with human 3q26 and includes *Prkci* and *Sox2*, suggesting a role for coordinate genetic alteration of *Prkci* and *Sox2* in mouse LSCC (Wang et al., 2004). In this regard, SOX2 overexpression is only weakly transforming (Hussenet et al., 2010), and PKCι overexpression is not sufficient alone to cause cellular transformation (Fields laboratory, unpublished data), suggesting that these oncogenic factors may act in concert to exhibit full tumorigenic potential. Consistent with this idea, *PRKCI* and *SOX2* are frequently coamplified and coordinately overexpressed in LSCC tumors, and these tumors appear to exhibit active PKCι-SOX2-Hh signaling. Based on our data, we propose that in LSCC tumors, and possibly other lung cancer subtypes harboring 3q26 amplification, *PRKCI* and *SOX2* are co-oncogenic drivers activated through a single genetic alteration that cooperatively drives tumorigenesis by maintaining a stem-like phenotype through activation of a PKCι-SOX2-Hh signaling axis. Interestingly, whereas each of the cell lines analyzed here harbor *PRKCI* gene copy number gain and exhibit PKCι-dependent Hh signaling, not all of these cell lines are classified as LSCC. Three cell lines are classified histologically as LSCC (H1703, H520, and H1869), whereas ChagoK1 and H1299 cells are classified as bronchiogenic carcinoma and LCLC, respectively, suggesting that PKCι-SOX2-HHAT signaling may be operative in lung tumor types other than LSCC that harbor *PRKCI* gene copy number gain. Given the prevalence of chromosome 3q26 amplification in human tumors, further studies are warranted to determine whether the PKCι-SOX2-Hh signaling axis elucidated here maintains a stem-like phenotype in other major tumor types harboring these genetic alterations.

Finally, our results have broad implications for development of new therapeutic strategies to target LSCC stem-like cells. SMO inhibitors are in clinical development, but their utility is limited in tumors that acquire Hh mutations that confer resistance. PKCι, which regulates the Hh pathway both upstream and downstream of SMO, may serve as an alternative therapeutic strategy for modulating Hh signaling in tumors harboring such mutations. Our data also provide a rationale for combined use of PKCι and Hh inhibitors for treatment of LSCC tumors. Finally, selective HHAT inhibitors have recently been developed (Petrova et al., 2013). Such inhibitors may exhibit particular potency in tumors harboring chromosome 3q26 amplification and commensurate activation of the autocrine PKCι-SOX2-HHAT signaling axis described here.

EXPERIMENTAL PROCEDURES

Cell Lines, Reagents, and Antibodies

We used the following antibodies: PKCι (BD Biosciences); β-actin, SOX2, GLI1, Lamins A/C, mitogen-activated kinase kinase 1 (MEK1), phospho-atypical PKC Thr-403/410 (Cell Signaling Technology); HHAT (Abgent), pSer/Thr (Abcam), SHH (Santa Cruz Biotechnology), and FLAG (Sigma). Auranofin (Prometheus Pharmaceuticals) and LDE225 and Hh-Ag1.5 (Cellagen) were diluted in dimethyl sulfate (Me_2SO). Cells were treated at concentrations indicated in the figures, and control cells received an equal volume of Me_2SO at 0.1% (v/v). H1703, H1299, H520, H1869, and ChagoK1 lung carcinoma cell lines were obtained from American Type Culture Collection and maintained in low passage culture as recommended. H1299 firefly luciferase cells were established by transducing cells with retroviral firefly luciferase.

Enrichment, Clonal Expansion, and Redifferentiation of Lung Cancer Cell Exhibiting a Stem-like Phenotype

Oncospheres were enriched from H1703, H1299, H520, H1869, and ChagoK1 cells and from primary human LSCC tumors essentially as described previously (Eramo et al., 2008; Justilien et al., 2012). Human tumor tissues were obtained under informed consent, and their collection was approved by the Mayo Clinic Institutional Review Board. Experimental details are provided in Supplemental Experimental Procedures.

Lentiviral RNAi Constructs, Cell Transduction, Plasmids, Transfections, and Immunoblot Analysis

Lentiviral vectors containing small hairpin RNAi against human PKCι, HHAT, GLI1, and SOX2 were obtained from Sigma and packaged into recombinant lentiviruses as described previously (Frederick et al., 2008). The human SOX2 cDNA was cloned into a FLAG mammalian expression vector (QIAGEN catalog no. DAM-105) and rendered RNAi resistant by silent mutation to disrupt the SOX2 RNAi #2 target site as described previously (Frederick et al., 2008). GLI1 was immunoprecipitated from cell lysates using mouse anti-GLI1 and Protein A/G agarose beads (Santa Cruz) according to manufacturer's procedure. Phospho(S/T)-GLI1 was detected in GLI1 immunoprecipitates by immunoblot analysis using pSer/Thr antibody. Detailed protocols are provided in Supplemental Experimental Procedures.

Anchorage-Independent Growth and Orthotopic Implantation Studies

Anchorage-independent growth was assessed as described previously (Justilien et al., 2012). All animal procedures were approved by the Mayo Clinic Institutional Animal Care and Use Committee. Experimental details are provided in Supplemental Experimental Procedures.

Metabolic Labeling and Detection of Palmitoylated SHH

Metabolic labeling and detection of palmitoylated SHH was performed essentially as described previously (Yap et al., 2010). Experimental details are provided in Supplemental Experimental Procedures.

Deep Sequence Analysis of Lung Cancer Cell Transcriptomes

Deep sequencing analysis was performed essentially as described previously (Kalari et al., 2012). Experimental details are provided in Supplemental Experimental Procedures.

Analysis of TCGA Gene Expression Data

Data from TCGA were analyzed using cBIO software (http://www.cbioportal.org/public-portal/) software to correlate gene amplifications and gene expression in 178 human LSCC and 129 LAC tumors. Gene count (reads per kilobase per million) values for these tumors were rank ordered according to *PRKCI* expression and the top and bottom third were compared for differential expression of HHAT, *SOX2*, *GLI1*, and the 13 gene airway basal stem cell gene signature (Shaykhiev et al., 2013).

In Vitro PKCι Kinase Assays

PKCι in vitro kinase assays were performed as described previously (Justilien et al., 2011). Details are provided in Supplemental Experimental Procedures.

ChIP and Analysis

ChIPs were performed to assess *SOX2* occupancy on the HHAT promoter as described in Supplemental Experimental Procedures.

HHAT Promoter Cloning and Luciferase Assays

An ~1 kB fragment of the proximal 5′ promoter region of human HHAT was cloned by PCR from genomic DNA from H1703 cells. The promoter was purified, sequenced to validate a match with the Pub-Med database (NM_001170564), and TA cloned into pGL4-luciferase reporter plasmid using standard techniques. Luciferase assays were conducted as described in Supplemental Experimental Procedures.

MS Analysis of SOX2 Phosphorylation

PKCι phosphorylated SOX2 or SOX2 immunoprecipitated from H1703 cells was isolated and submitted to the Mayo Clinic Cancer Center Protein Chemistry and Proteomics Shared Resource for proteolytic cleavage and phosphorylation site analysis by MS. Details are provided in Supplemental Experimental Procedures.

ACCESSION NUMBERS

The GEO accession number for the RNA-seq data reported in this paper is GSE48599.

SUPPLEMENTAL INFORMATION

Supplemental Information includes Supplemental Experimental Procedures, five figures, and six tables and can be found with this article online at http://dx.doi.org/10.1016/j.ccr.2014.01.008.

ACKNOWLEDGMENTS

We thank Dr. Robert Bergen and Benjamin Madden of the Mayo Clinic Proteomics Research Center for performing MS analysis of SOX2 phosphorylation, Dr. John Odell for consenting individuals and obtaining fresh primary lung tumor tissue, Dr. Al Copland for the retroviral firefly luciferase construct, Ms. Capella Weems and Dr. Lee Jamieson for technical assistance, Ms. Brandy Edenfield for immunohistochemical analysis, the Mayo Clinic Florida Biospecimen Acquisition and Processing laboratory for procurement of primary lung tumor tissues, and the Mayo Clinic Advanced Genomic Technology Center for RNA-seq and data analysis. We also acknowledge Dr. Howard Crawford and members of the Fields laboratory for critical feedback on the manuscript, and Kevin M. Youel for artwork in the graphical abstract. This work was supported by grants from National Institutes of Health/National Cancer Institute (R01 CA081436-16 and R21 CA151250-02), the V Foundation for Cancer Research, the James and Esther King Biomedical Research Program (1KG-05-33971), and the Mayo Clinic Center for Individualized Medicine to A.P.F.; and a National Institutes of Health Research Supplement to Promote Diversity in Health-Related Research Award from the National Cancer Institute

to V.J. A.P.F. is the Monica Flynn Jacoby Professor of Cancer Research, an endowment fund that provides partial support for the investigator's research program.

Received: June 25, 2013
Revised: November 20, 2013
Accepted: January 13, 2014
Published: February 10, 2014

REFERENCES

Atwood, S.X., Li, M., Lee, A., Tang, J.Y., and Oro, A.E. (2013). GLI activation by atypical protein kinase C ι/λ regulates the growth of basal cell carcinomas. Nature *494*, 484–488.

Baldwin, R.M., Parolin, D.A., and Lorimer, I.A. (2008). Regulation of glioblastoma cell invasion by PKC iota and RhoB. Oncogene *27*, 3587–3595.

Balsara, B.R., Sonoda, G., du Manoir, S., Siegfried, J.M., Gabrielson, E., and Testa, J.R. (1997). Comparative genomic hybridization analysis detects frequent, often high-level, overrepresentation of DNA sequences at 3q, 5p, 7p, and 8q in human non-small cell lung carcinomas. Cancer Res. *57*, 2116–2120.

Bar, E.E., Chaudhry, A., Lin, A., Fan, X., Schreck, K., Matsui, W., Piccirillo, S., Vescovi, A.L., DiMeco, F., Olivi, A., and Eberhart, C.G. (2007). Cyclopamine-mediated hedgehog pathway inhibition depletes stem-like cancer cells in glioblastoma. Stem Cells *25*, 2524–2533.

Bass, A.J., Watanabe, H., Mermel, C.H., Yu, S., Perner, S., Verhaak, R.G., Kim, S.Y., Wardwell, L., Tamayo, P., Gat-Viks, I., et al. (2009). SOX2 is an amplified lineage-survival oncogene in lung and esophageal squamous cell carcinomas. Nat. Genet. *41*, 1238–1242.

Basu-Roy, U., Seo, E., Ramanathapuram, L., Rapp, T.B., Perry, J.A., Orkin, S.H., Mansukhani, A., and Basilico, C. (2012). Sox2 maintains self renewal of tumor-initiating cells in osteosarcomas. Oncogene *31*, 2270–2282.

Berman, D.M., Karhadkar, S.S., Maitra, A., Montes De Oca, R., Gerstenblith, M.R., Briggs, K., Parker, A.R., Shimada, Y., Eshleman, J.R., Watkins, D.N., and Beachy, P.A. (2003). Widespread requirement for Hedgehog ligand stimulation in growth of digestive tract tumours. Nature *425*, 846–851.

Brass, N., Ukena, I., Remberger, K., Mack, U., Sybrecht, G.W., and Meese, E.U. (1996). DNA amplification on chromosome 3q26.1-q26.3 in squamous cell carcinoma of the lung detected by reverse chromosome painting. Eur. J. Cancer *32A*, 1205–1208.

Buonamici, S., Williams, J., Morrissey, M., Wang, A., Guo, R., Vattay, A., Hsiao, K., Yuan, J., Green, J., Ospina, B., et al. (2010). Interfering with resistance to smoothened antagonists by inhibition of the PI3K pathway in medulloblastoma. Sci. Transl. Med. *2*, 51ra70.

Chen, Y.-C., Hsu, H.-S., Chen, Y.-W., Tsai, T.-H., How, C.-K., Wang, C.-Y., Hung, S.-C., Chang, Y.-L., Tsai, M.-L., Lee, Y.-Y., et al. (2008). Oct-4 expression maintained cancer stem-like properties in lung cancer-derived CD133-positive cells. PLoS ONE *3*, e2637.

Chen, J., Li, Y., Yu, T.S., McKay, R.M., Burns, D.K., Kernie, S.G., and Parada, L.F. (2012). A restricted cell population propagates glioblastoma growth after chemotherapy. Nature *488*, 522–526.

Chiou, S.H., Wang, M.L., Chou, Y.T., Chen, C.J., Hong, C.F., Hsieh, W.J., Chang, H.T., Chen, Y.S., Lin, T.W., Hsu, H.S., and Wu, C.W. (2010). Coexpression of Oct4 and Nanog enhances malignancy in lung adenocarcinoma by inducing cancer stem cell-like properties and epithelial-mesenchymal transdifferentiation. Cancer Res. *70*, 10433–10444.

Desai, S., Pillai, P., Win-Piazza, H., and Acevedo-Duncan, M. (2011). PKC-ι promotes glioblastoma cell survival by phosphorylating and inhibiting BAD through a phosphatidylinositol 3-kinase pathway. Biochim. Biophys. Acta *1813*, 1190–1197.

Dierks, C., Grbic, J., Zirlik, K., Beigi, R., Englund, N.P., Guo, G.R., Veelken, H., Engelhardt, M., Mertelsmann, R., Kelleher, J.F., et al. (2007). Essential role of stromally induced hedgehog signaling in B-cell malignancies. Nat. Med. *13*, 944–951.

Driessens, G., Beck, B., Caauwe, A., Simons, B.D., and Blanpain, C. (2012). Defining the mode of tumour growth by clonal analysis. Nature *488*, 527–530.

Epstein, E.H. (2008). Basal cell carcinomas: attack of the hedgehog. Nat. Rev. Cancer *8*, 743–754.

Eramo, A., Lotti, F., Sette, G., Pilozzi, E., Biffoni, M., Di Virgilio, A., Conticello, C., Ruco, L., Peschle, C., and De Maria, R. (2008). Identification and expansion of the tumorigenic lung cancer stem cell population. Cell Death Differ. *15*, 504–514.

Erdogan, E., Lamark, T., Stallings-Mann, M., Lee Jamieson, Pellecchia, M., Thompson, E.A., Johansen, T., and Fields, A.P. (2006). Aurothiomalate inhibits transformed growth by targeting the PB1 domain of protein kinase Ciota. J. Biol. Chem. *281*, 28450–28459.

Fang, X., Yoon, J.G., Li, L., Yu, W., Shao, J., Hua, D., Zheng, S., Hood, L., Goodlett, D.R., Foltz, G., and Lin, B. (2011). The SOX2 response program in glioblastoma multiforme: an integrated ChIP-seq, expression microarray, and microRNA analysis. BMC Genomics *12*, 11.

Favaro, R., Valotta, M., Ferri, A.L., Latorre, E., Mariani, J., Giachino, C., Lancini, C., Tosetti, V., Ottolenghi, S., Taylor, V., and Nicolis, S.K. (2009). Hippocampal development and neural stem cell maintenance require Sox2-dependent regulation of Shh. Nat. Neurosci. *12*, 1248–1256.

Frederick, L.A., Matthews, J.A., Jamieson, L., Justilien, V., Thompson, E.A., Radisky, D.C., and Fields, A.P. (2008). Matrix metalloproteinase-10 is a critical effector of protein kinase Ciota-Par6alpha-mediated lung cancer. Oncogene *27*, 4841–4853.

Hajj, R., Baranek, T., Le Naour, R., Lesimple, P., Puchelle, E., and Coraux, C. (2007). Basal cells of the human adult airway surface epithelium retain transit-amplifying cell properties. Stem Cells *25*, 139–148.

Hong, K.U., Reynolds, S.D., Watkins, S., Fuchs, E., and Stripp, B.R. (2004). Basal cells are a multipotent progenitor capable of renewing the bronchial epithelium. Am. J. Pathol. *164*, 577–588.

Hussenet, T., Dali, S., Exinger, J., Monga, B., Jost, B., Dembelé, D., Martinet, N., Thibault, C., Huelsken, J., Brambilla, E., and du Manoir, S. (2010). SOX2 is an oncogene activated by recurrent 3q26.3 amplifications in human lung squamous cell carcinomas. PLoS ONE *5*, e8960.

Ikushima, H., Todo, T., Ino, Y., Takahashi, M., Saito, N., Miyazawa, K., and Miyazono, K. (2011). Glioma-initiating cells retain their tumorigenicity through integration of the Sox axis and Oct4 protein. J. Biol. Chem. *286*, 41434–41441.

Imoto, I., Pimkhaokham, A., Fukuda, Y., Yang, Z.Q., Shimada, Y., Nomura, N., Hirai, H., Imamura, M., and Inazawa, J. (2001). SNO is a probable target for gene amplification at 3q26 in squamous-cell carcinomas of the esophagus. Biochem. Biophys. Res. Commun. *286*, 559–565.

Jeong, C.H., Cho, Y.Y., Kim, M.O., Kim, S.H., Cho, E.J., Lee, S.Y., Jeon, Y.J., Lee, K.Y., Yao, K., Keum, Y.S., et al. (2010). Phosphorylation of Sox2 cooperates in reprogramming to pluripotent stem cells. Stem Cells *28*, 2141–2150.

Justilien, V., and Fields, A.P. (2009). Ect2 links the PKCiota-Par6alpha complex to Rac1 activation and cellular transformation. Oncogene *28*, 3597–3607.

Justilien, V., Jamieson, L., Der, C.J., Rossman, K.L., and Fields, A.P. (2011). Oncogenic activity of Ect2 is regulated through protein kinase C iota-mediated phosphorylation. J. Biol. Chem. *286*, 8149–8157.

Justilien, V., Regala, R.P., Tseng, I.C., Walsh, M.P., Batra, J., Radisky, E.S., Murray, N.R., and Fields, A.P. (2012). Matrix metalloproteinase-10 is required for lung cancer stem cell maintenance, tumor initiation and metastatic potential. PLoS ONE *7*, e35040.

Kalari, K.R., Rossell, D., Necela, B.M., Asmann, Y.W., Nair, A., Baheti, S., Kachergus, J.M., Younkin, C.S., Baker, T., Carr, J.M., et al. (2012). Deep sequence analysis of non-small cell lung cancer: integrated analysis of gene expression, alternative splicing, and single nucleotide variations in lung adenocarcinomas with and without oncogenic KRAS mutations. Front. Oncol. *2*, 12.

Karhadkar, S.S., Bova, G.S., Abdallah, N., Dhara, S., Gardner, D., Maitra, A., Isaacs, J.T., Berman, D.M., and Beachy, P.A. (2004). Hedgehog signalling in prostate regeneration, neoplasia and metastasis. Nature *431*, 707–712.

Kool, M., Koster, J., Bunt, J., Hasselt, N.E., Lakeman, A., van Sluis, P., Troost, D., Meeteren, N.S., Caron, H.N., Cloos, J., et al. (2008). Integrated genomics identifies five medulloblastoma subtypes with distinct genetic profiles, pathway signatures and clinicopathological features. PLoS ONE *3*, e3088.

Le Good, J.A., Ziegler, W.H., Parekh, D.B., Alessi, D.R., Cohen, P., and Parker, P.J. (1998). Protein kinase C isotypes controlled by phosphoinositide 3-kinase through the protein kinase PDK1. Science *281*, 2042–2045.

Lin, S.C., Liu, C.J., Ko, S.Y., Chang, H.C., Liu, T.Y., and Chang, K.W. (2005). Copy number amplification of 3q26-27 oncogenes in microdissected oral squamous cell carcinoma and oral brushed samples from areca chewers. J. Pathol. *206*, 417–422.

Ooi, A.T., Mah, V., Nickerson, D.W., Gilbert, J.L., Ha, V.L., Hegab, A.E., Horvath, S., Alavi, M., Maresh, E.L., Chia, D., et al. (2010). Presence of a putative tumor-initiating progenitor cell population predicts poor prognosis in smokers with non-small cell lung cancer. Cancer Res. *70*, 6639–6648.

Park, K.S., Martelotto, L.G., Peifer, M., Sos, M.L., Karnezis, A.N., Mahjoub, M.R., Bernard, K., Conklin, J.F., Szczepny, A., Yuan, J., et al. (2011). A crucial requirement for Hedgehog signaling in small cell lung cancer. Nat. Med. *17*, 1504–1508.

Petrova, E., Rios-Esteves, J., Ouerfelli, O., Glickman, J.F., and Resh, M.D. (2013). Inhibitors of Hedgehog acyltransferase block Sonic Hedgehog signaling. Nat. Chem. Biol. *9*, 247–249.

Regala, R.P., Weems, C., Jamieson, L., Copland, J.A., Thompson, E.A., and Fields, A.P. (2005a). Atypical protein kinase Ciota plays a critical role in human lung cancer cell growth and tumorigenicity. J. Biol. Chem. *280*, 31109–31115.

Regala, R.P., Weems, C., Jamieson, L., Khoor, A., Edell, E.S., Lohse, C.M., and Fields, A.P. (2005b). Atypical protein kinase C iota is an oncogene in human non-small cell lung cancer. Cancer Res. *65*, 8905–8911.

Regala, R.P., Thompson, E.A., and Fields, A.P. (2008). Atypical protein kinase Cι expression and aurothiomalate sensitivity in human lung cancer cells. Cancer Res. *68*, 5888–5895.

Regala, R.P., Davis, R.K., Kunz, A., Khoor, A., Leitges, M., and Fields, A.P. (2009). Atypical protein kinase Ciota is required for bronchioalveolar stem cell expansion and lung tumorigenesis. Cancer Res. *69*, 7603–7611.

Rock, J.R., Onaitis, M.W., Rawlins, E.L., Lu, Y., Clark, C.P., Xue, Y., Randell, S.H., and Hogan, B.L. (2009). Basal cells as stem cells of the mouse trachea and human airway epithelium. Proc. Natl. Acad. Sci. USA *106*, 12771–12775.

Rodriguez-Blanco, J., Schilling, N.S., Tokhunts, R., Giambelli, C., Long, J., Liang Fei, D., Singh, S., Black, K.E., Wang, Z., Galimberti, F., et al. (2013). The hedgehog processing pathway is required for NSCLC growth and survival. Oncogene *32*, 2335–2345.

Sarkar, A., and Hochedlinger, K. (2013). The sox family of transcription factors: versatile regulators of stem and progenitor cell fate. Cell Stem Cell *12*, 15–30.

Schepers, A.G., Snippert, H.J., Stange, D.E., van den Born, M., van Es, J.H., van de Wetering, M., and Clevers, H. (2012). Lineage tracing reveals Lgr5+ stem cell activity in mouse intestinal adenomas. Science *337*, 730–735.

Shaykhiev, R., Wang, R., Zwick, R.K., Hackett, N.R., Leung, R., Moore, M.A., Sima, C.S., Chao, I.W., Downey, R.J., Strulovici-Barel, Y., et al. (2013). Airway basal cells of healthy smokers express an embryonic stem cell signature relevant to lung cancer. Stem Cells *31*, 1992–2002.

Siddique, H.R., and Saleem, M. (2012). Role of BMI1, a stem cell factor, in cancer recurrence and chemoresistance: preclinical and clinical evidences. Stem Cells *30*, 372–378.

Siegel, R., Naishadham, D., and Jemal, A. (2012). Cancer statistics, 2012. CA Cancer J. Clin. *62*, 10–29.

Snaddon, J., Parkinson, E.K., Craft, J.A., Bartholomew, C., and Fulton, R. (2001). Detection of functional PTEN lipid phosphatase protein and enzyme activity in squamous cell carcinomas of the head and neck, despite loss of heterozygosity at this locus. Br. J. Cancer *84*, 1630–1634.

Sonoda, G., Palazzo, J., du Manoir, S., Godwin, A.K., Feder, M., Yakushiji, M., and Testa, J.R. (1997). Comparative genomic hybridization detects frequent overrepresentation of chromosomal material from 3q26, 8q24, and 20q13 in human ovarian carcinomas. Genes Chromosomes Cancer *20*, 320–328.

Stallings-Mann, M., Jamieson, L., Regala, R.P., Weems, C., Murray, N.R., and Fields, A.P. (2006). A novel small-molecule inhibitor of protein kinase Ciota blocks transformed growth of non-small-cell lung cancer cells. Cancer Res. *66*, 1767–1774.

Standaert, M.L., Bandyopadhyay, G., Perez, L., Price, D., Galloway, L., Poklepovic, A., Sajan, M.P., Cenni, V., Sirri, A., Moscat, J., et al. (1999). Insulin activates protein kinases C-zeta and C-lambda by an autophosphorylation-dependent mechanism and stimulates their translocation to GLUT4 vesicles and other membrane fractions in rat adipocytes. J. Biol. Chem. *274*, 25308–25316.

Stecca, B., Mas, C., Clement, V., Zbinden, M., Correa, R., Piguet, V., Beermann, F., and Ruiz I Altaba, A. (2007). Melanomas require HEDGEHOG-GLI signaling regulated by interactions between GLI1 and the RAS-MEK/AKT pathways. Proc. Natl. Acad. Sci. USA *104*, 5895–5900.

Sugita, M., Tanaka, N., Davidson, S., Sekiya, S., Varella-Garcia, M., West, J., Drabkin, H.A., and Gemmill, R.M. (2000). Molecular definition of a small amplification domain within 3q26 in tumors of cervix, ovary, and lung. Cancer Genet. Cytogenet. *117*, 9–18.

Tian, H., Callahan, C.A., DuPree, K.J., Darbonne, W.C., Ahn, C.P., Scales, S.J., and de Sauvage, F.J. (2009). Hedgehog signaling is restricted to the stromal compartment during pancreatic carcinogenesis. Proc. Natl. Acad. Sci. USA *106*, 4254–4259.

Tian, T., Zhang, Y., Wang, S., Zhou, J., and Xu, S. (2012). Sox2 enhances the tumorigenicity and chemoresistance of cancer stem-like cells derived from gastric cancer. J. Biomed. Res. *26*, 336–345.

Tompkins, D.H., Besnard, V., Lange, A.W., Wert, S.E., Keiser, A.R., Smith, A.N., Lang, R., and Whitsett, J.A. (2009). Sox2 is required for maintenance and differentiation of bronchiolar Clara, ciliated, and goblet cells. PLoS ONE *4*, e8248.

Tompkins, D.H., Besnard, V., Lange, A.W., Keiser, A.R., Wert, S.E., Bruno, M.D., and Whitsett, J.A. (2011). Sox2 activates cell proliferation and differentiation in the respiratory epithelium. Am. J. Respir. Cell Mol. Biol. *45*, 101–110.

Van Hoof, D., Muñoz, J., Braam, S.R., Pinkse, M.W., Linding, R., Heck, A.J., Mummery, C.L., and Krijgsveld, J. (2009). Phosphorylation dynamics during early differentiation of human embryonic stem cells. Cell Stem Cell *5*, 214–226.

Varnat, F., Duquet, A., Malerba, M., Zbinden, M., Mas, C., Gervaz, P., and Ruiz i Altaba, A. (2009). Human colon cancer epithelial cells harbour active HEDGEHOG-GLI signalling that is essential for tumour growth, recurrence, metastasis and stem cell survival and expansion. EMBO Mol. Med. *1*, 338–351.

Wang, Y., Zhang, Z., Yan, Y., Lemon, W.J., LaRegina, M., Morrison, C., Lubet, R., and You, M. (2004). A chemically induced model for squamous cell carcinoma of the lung in mice: histopathology and strain susceptibility. Cancer Res. *64*, 1647–1654.

Wang, Y., Hill, K.S., and Fields, A.P. (2013). Protein kinase Ciota maintains a tumor-initiating cell phenotype that is required for ovarian tumorigenesis. Mol. Cancer Res. *11*, 1636–1638.

Watkins, D.N., Berman, D.M., Burkholder, S.G., Wang, B., Beachy, P.A., and Baylin, S.B. (2003). Hedgehog signalling within airway epithelial progenitors and in small-cell lung cancer. Nature *422*, 313–317.

Wistuba, I.I., and Gazdar, A.F. (2006). Lung cancer preneoplasia. Annu. Rev. Pathol. *1*, 331–348.

Yap, M.C., Kostiuk, M.A., Martin, D.D., Perinpanayagam, M.A., Hak, P.G., Siddam, A., Majjigapu, J.R., Rajaiah, G., Keller, B.O., Prescher, J.A., et al. (2010). Rapid and selective detection of fatty acylated proteins using omega-alkynyl-fatty acids and click chemistry. J. Lipid Res. *51*, 1566–1580.

Yauch, R.L., Gould, S.E., Scales, S.J., Tang, T., Tian, H., Ahn, C.P., Marshall, D., Fu, L., Januario, T., Kallop, D., et al. (2008). A paracrine requirement for hedgehog signalling in cancer. Nature *455*, 406–410.

Yuan, P., Kadara, H., Behrens, C., Tang, X., Woods, D., Solis, L.M., Huang, J., Spinola, M., Dong, W., Yin, G., et al. (2010). Sex determining region Y-Box 2 (SOX2) is a potential cell-lineage gene highly expressed in the pathogenesis of squamous cell carcinomas of the lung. PLoS ONE *5*, e9112.

Cancer Cell
Article

Identification of Distinct Basal and Luminal Subtypes of Muscle-Invasive Bladder Cancer with Different Sensitivities to Frontline Chemotherapy

Woonyoung Choi,[1] Sima Porten,[1] Seungchan Kim,[6] Daniel Willis,[1] Elizabeth R. Plimack,[7] Jean Hoffman-Censits,[8] Beat Roth,[1] Tiewei Cheng,[1,5] Mai Tran,[1,5] I-Ling Lee,[1] Jonathan Melquist,[1] Jolanta Bondaruk,[3] Tadeusz Majewski,[3] Shizhen Zhang,[3] Shanna Pretzsch,[1] Keith Baggerly,[4] Arlene Siefker-Radtke,[2] Bogdan Czerniak,[3] Colin P.N. Dinney,[1] and David J. McConkey[1,5,*]

[1]Department of Urology, University of Texas MD Anderson Cancer Center, Houston, TX 77030, USA
[2]Department of Genitourinary Medical Oncology, University of Texas MD Anderson Cancer Center, Houston, TX 77030, USA
[3]Department of Pathology, University of Texas MD Anderson Cancer Center, Houston, TX 77030, USA
[4]Department of Bioinformatics, University of Texas MD Anderson Cancer Center, Houston, TX 77030, USA
[5]The University of Texas-Graduate School of Biomedical Sciences (GSBS) at Houston, Houston, TX 77030, USA
[6]Computational Biology Division, Translational Genomics Research Institute, 445N, Fifth Street, Phoenix, AZ 85004, USA
[7]Department of Medical Oncology, Fox Chase Cancer Center, 333 Cottman Avenue, Philadelphia, PA 19111-2497, USA
[8]Department of Medical Oncology, Thomas Jefferson University Hospital, 1025 Walnut Street, Suite 700, Philadelphia, PA 19107, USA
*Correspondence: dmcconke@mdanderson.org
http://dx.doi.org/10.1016/j.ccr.2014.01.009

SUMMARY

Muscle-invasive bladder cancers (MIBCs) are biologically heterogeneous and have widely variable clinical outcomes and responses to conventional chemotherapy. We discovered three molecular subtypes of MIBC that resembled established molecular subtypes of breast cancer. Basal MIBCs shared biomarkers with basal breast cancers and were characterized by p63 activation, squamous differentiation, and more aggressive disease at presentation. Luminal MIBCs contained features of active PPARγ and estrogen receptor transcription and were enriched with activating *FGFR3* mutations and potential FGFR inhibitor sensitivity. p53-like MIBCs were consistently resistant to neoadjuvant methotrexate, vinblastine, doxorubicin and cisplatin chemotherapy, and all chemoresistant tumors adopted a p53-like phenotype after therapy. Our observations have important implications for prognostication, the future clinical development of targeted agents, and disease management with conventional chemotherapy.

INTRODUCTION

Bladder cancer progresses along two distinct pathways that pose distinct challenges for clinical management (Dinney et al., 2004). Low-grade non-muscle invasive ("superficial") cancers, which account for 70% of tumor incidence, are not immediately life-threatening, but they have a propensity for recurrence that necessitates costly lifelong surveillance (Botteman et al., 2003). In contrast, high-grade muscle-invasive bladder cancers (MIBCs) progress rapidly to become metastatic and generate the bulk of patient mortality (Shah et al., 2011). Radical cystectomy with perioperative cisplatin-based combination chemotherapy is the current standard of care for high-risk MIBC. Treatment selection depends heavily on clinico-pathologic features, but current staging systems are woefully inaccurate and result in an unacceptably high rate of clinical understaging and consequently inadequate treatment (Svatek et al., 2011). Furthermore, cisplatin-based chemotherapy is only effective in 30%–40% of cases, and it is not yet possible to prospectively identify the patients who are likely to obtain benefit (Shah

Significance

Using whole genome mRNA expression profiling, we identified three molecular subtypes of muscle-invasive bladder cancer (MIBC) that shared molecular features with basal and luminal breast cancers. Tumors in one of them expressed an active p53 gene signature, and these "p53-like" MIBCs were consistently resistant to frontline neoadjuvant cisplatin-based combination chemotherapy. Furthermore, comparison of matched gene expression profiles before and after chemotherapy revealed that all resistant tumors expressed wild-type p53 gene expression signatures. Together, the data indicate that "p53-ness" plays a central role in chemoresistance in bladder cancer and suggest that it should be possible to prospectively identify the patients who most likely will not benefit from neoadjuvant chemotherapy.

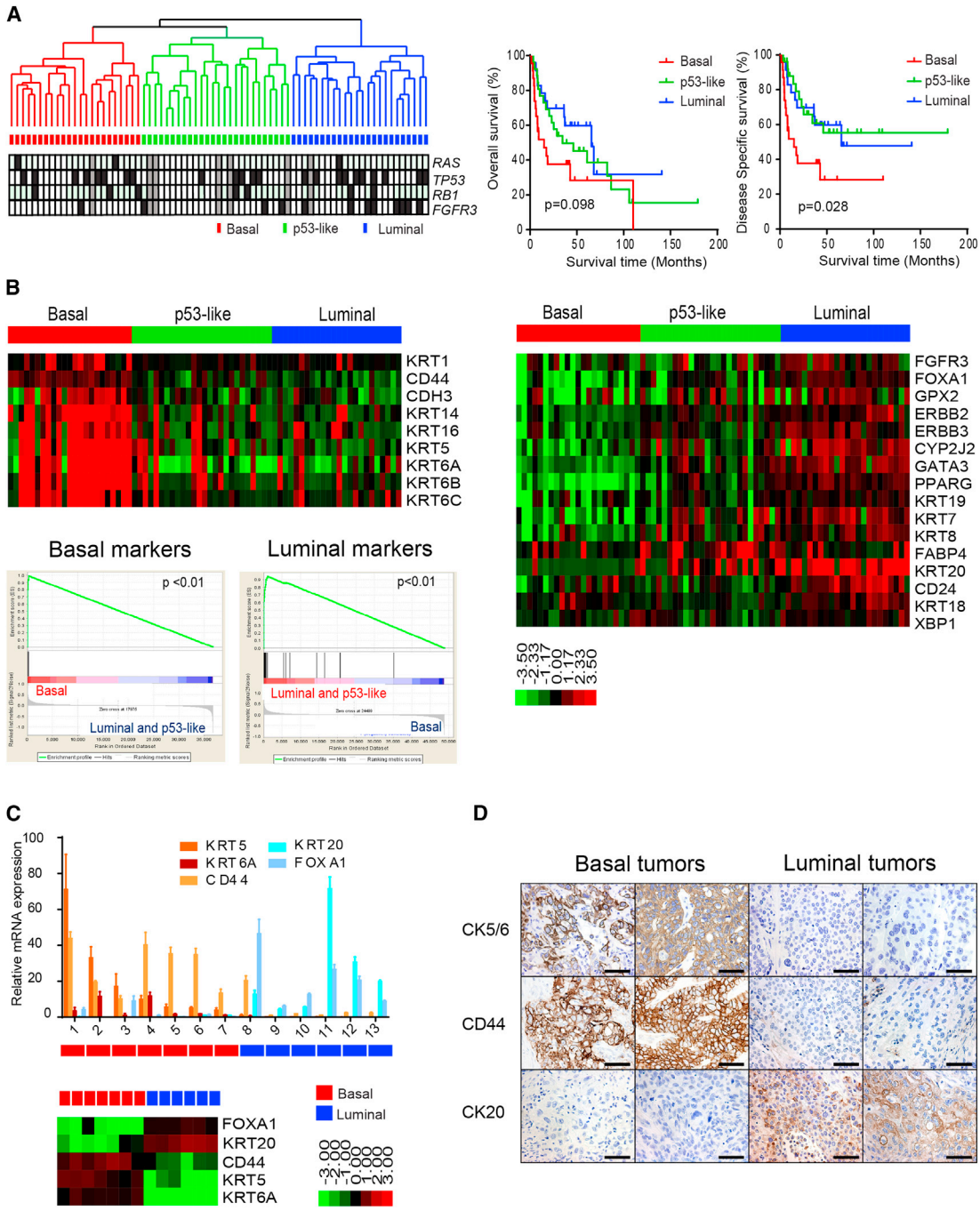

Figure 1. Basal and Luminal Subtypes of Bladder Cancer

(A) Left: whole genome mRNA expression profiling and hierarchical cluster analysis of a cohort of 73 MIBCs. RNA from fresh frozen tumors was analyzed using Illumina arrays. *RAS*, *TP53*, *RB1*, and *FGFR3* mutations were detected by sequencing and are indicated in the color bars below the dendrogram. Black, mutation; white, wild-type; gray, mutation data were unavailable. Right: Kaplan-Meier plots of overall survival ($p = 0.098$) and disease-specific survival ($p = 0.028$) in the three tumor subtypes.

(B) Expression of basal and luminal markers in the three subtypes. The heat maps depict relative expression of basal (left) and luminal (right) biomarkers. GSEA analyses (below, left) were used to determine whether basal and luminal markers were enriched in the subtypes.

(C) Quantitative RT-PCR was used to evaluate the accuracy of the gene expression profiling results. Relative levels of the indicated basal (red shades) and luminal (blue shades) biomarkers measured by RT-PCR were compared to the levels of the same markers measured by gene expression profiling on RNA isolated from macrodissected FFPE sections of the same tumors. Results are presented as relative quantitation (RQ) and the error bars indicate the range of RQ values as defined by 95% confidence level. RT-PCR results are shown on top, DASL gene expression profiling results are shown below.

(D) Analysis of basal and luminal marker expression by immunohistochemistry. Results from two representative basal (left) and luminal (right) tumors as defined by gene expression profiling are displayed. The scale bars correspond to 100 μm.

See also Figure S1.

Table 1. Clinicopathologic Characteristics of the MDACC Discovery Cohort

Characteristic	Total	Basal	p53-like	Luminal	p Value
Cohort size	73	23 (32%)	26 (36%)	24 (33%)	
Mean age (years) ± SD	68.8 ± 10.2	70.1 ± 9.4	69.8 ± 8.9	66.4 ± 12.1	0.371
Gender					
Female	19 (26%)	10 (44%)	6 (23%)	3 (13%)	0.133
Male	54 (74%)	13 (57%)	20 (77%)	21 (88%)	
Race					
Caucasian	54 (74%)	14 (61%)	21 (81%)	19 (79%)	0.352
African American	12 (16%)	6 (26%)	2 (7%)	4 (17%)	
Hispanic	7 (10%)	3 (13%)	3 (12%)	1 (4%)	
Clinical stage at TUR (N0,M0)					
≤cT1	0 (0%)	0 (0%)	0 (0%)	0 (0%)	0.990
cT2	37 (51%)	9 (39%)	16 (62%)	12 (50%)	
cT3	16 (22%)	4 (17%)	7 (27%)	5 (21%)	
cT4	6 (8%)	2 (9%)	2 (8%)	2 (8%)	
Positive clinical lymph nodes, cN+	11 (15%)	5 (22%)	1 (4%)	5 (21%)	0.137
Positive clinical metastasis, cM+	7 (10%)	5 (22%)	0 (0%)	2 (8%)	0.035
Primary treatment					
Cystectomy	57 (78%)	15 (65%)	25 (96%)	17 (71%)	0.019
Other[a]	16 (22%)	8 (35%)	1 (4%)	7 (29%)	
Neoadjuvant Chemotherapy, NAC	18 (25%)	5 (22%)	7 (27%)	6 (25%)	0.910
Response to NAC[b]					
Yes	6 (33%)	2 (40%)	0 (0%)	4 (67%)	0.018
No	12 (67%)	3 (60%)	7 (100%)	2 (33%)	
Pathologic T stage (n = 57)					
pT0	4 (7%)	2 (13%)	0 (0%)	2 (12%)	0.001
pTa, pT1, pTis	6 (11%)	2 (13%)	1 (4%)	3 (18%)	
pT2	10 (18%)	1 (7%)	4 (16%)	5 (29%)	
pT3	25 (44%)	4 (27%)	18 (72%)	3 (18%)	
pT4	12 (21%)	6 (40%)	2 (8%)	4 (22%)	
Positive pathologic lymph nodes	23 (40%)	3 (13%)	14 (54%)	6 (25%)	0.010
Variant histology in specimen					
Squamous differentiation	18 (32%)	13 (57%)	4 (15%)	1 (4%)	<0.001
Sarcomatoid differentiation	3 (5%)	3 (13%)	0 (0%)	0 (0%)	
Other (micropapillary, glandular, adenocarcinoma)	3 (5%)	0 (0%)	3 (12%)	0 (0%)	
Median overall survival (months)	37.2	14.9	34.6	65.6	0.098
Median disease-specific survival (months)	46.3	14.9	not reached	65.6	0.028

The Kruskal-Wallis test was used to compare differences in mean age between groups. Log-rank test was used to compare differences in survival (overall and disease-specific) between groups. For the remainder of categorical variables, Fisher's exact test was used to determine differences between subtypes. p values < 0.05 were considered significant.

[a]Chemotherapy was recommended for all 16 patients, based on available medical records; nine patients had documentation of completion.

[b]Decrease in stage to pT0 or pT1 (for patients with high-risk features at TUR: lymphovascular invasion, variant histology, hydronephrosis, or abnormal exam under anesthesia) at cystectomy.

et al., 2011). To add to the quandary, no effective alternative to cisplatin-based chemotherapy has been identified for resistant tumors. Therefore, there is an urgent need to develop a more precise, biology-based approach to the classification of bladder cancer to inform clinical management.

Gene expression profiling has been used to identify molecular heterogeneity in other human cancers. For example, Perou and coworkers (Perou et al., 2000) used gene expression profiling to identify molecular subtypes of breast cancer (basal/triple negative, HER2$^+$, luminal A, and luminal B) that behave clinically as though they are distinct disease entities—luminal breast cancers respond to estrogen receptor (ER)-targeted therapy, HER2$^+$ tumors to Herceptin and other ErbB2-blocking agents, and basal tumors to chemotherapy only (Rouzier et al., 2005). Previous studies in bladder cancer identified signatures associated with stage and outcomes (Blaveri et al., 2005; Dyrskjøt et al., 2003; Sanchez-Carbayo et al., 2006; Sjodahl et al., 2012) and progression (Kim et al., 2010; Lee et al., 2010), but the biological and

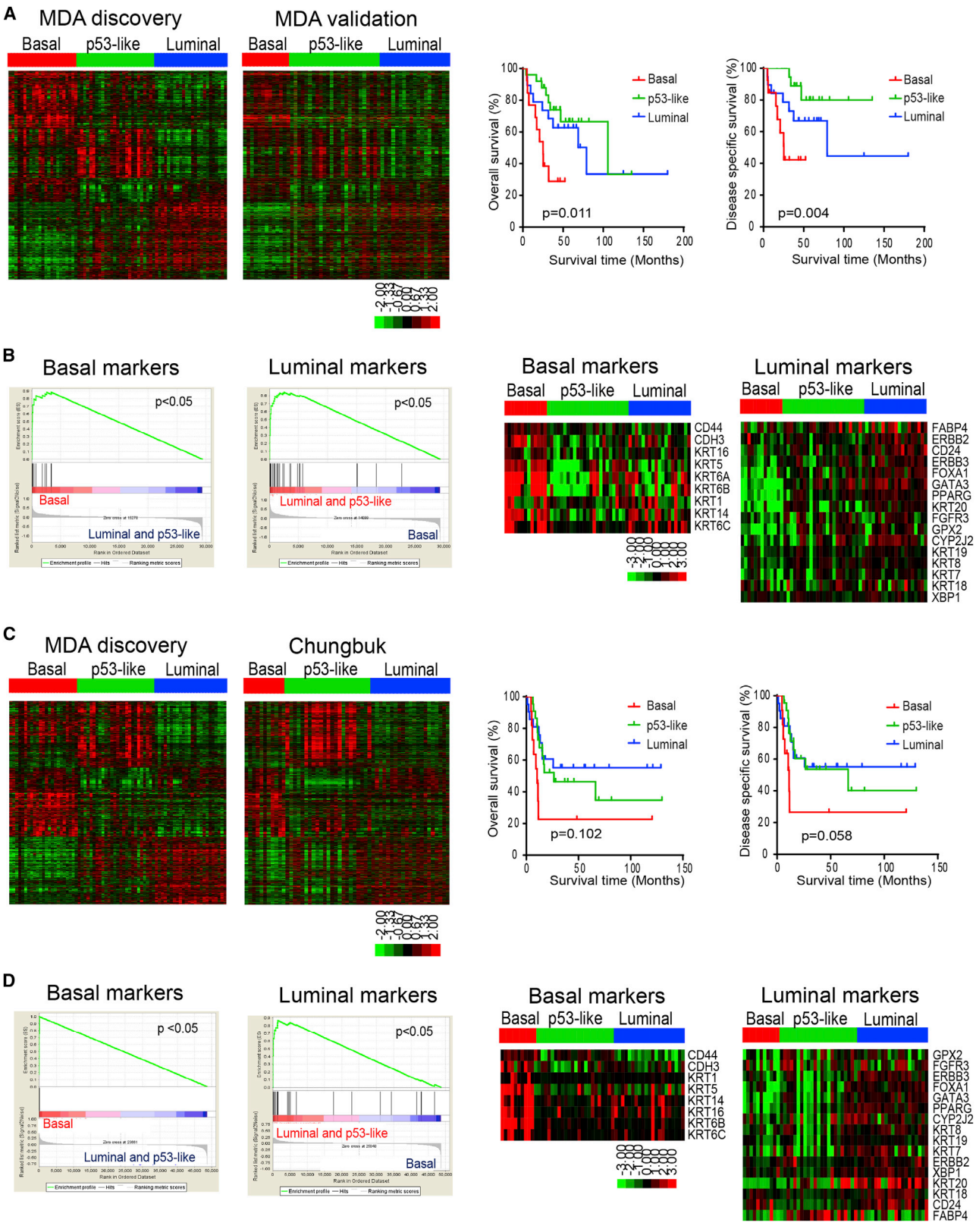

(legend on next page)

clinical significance of these signatures remain unclear. Here we also used gene expression profiling and unsupervised analyses to identify molecular subtypes of MIBC with the goal of defining the biological basis for the molecular heterogeneity that is observed in them.

RESULTS

Muscle-Invasive Bladder Cancers Can Be Grouped into Basal and Luminal Subtypes

We performed whole genome mRNA expression profiling and unsupervised hierarchical cluster analyses on a cohort of 73 primary fresh-frozen MIBCs obtained by transurethral resection at our institution. We identified three distinct molecular subtypes (Figure 1A; Table 1). The upregulated genes (fold changes) that determined subtype assignments contained signature biomarkers for basal (CD44, KRT5, KRT6, KRT14, and CDH3) and luminal (CD24, FOXA1, GATA3, ERBB2, ERBB3, XBP1, and KRT20) breast cancers, respectively (Figure 1B, heat maps; Figure S1A available online; Perou et al., 2000), and formal gene set enrichment analyses (GSEA) confirmed that the subtypes were enriched with basal and luminal markers (Figure 1B, below). In control experiments, we confirmed that the array-based measurements of basal and luminal marker expression correlated well with the results obtained with quantitative RT-PCR (Figure 1C) or immunohistochemistry (Figure 1D) in some of the same tumors. We therefore propose the names "basal" and "luminal" for two of the MIBC subtypes. Although the tumors in the third subtype also expressed luminal biomarkers (Figure 1B; Figure S1A), we have termed this MIBC subtype "p53-like" because its distinguishing feature was an activated wild-type p53 gene expression signature that we will discuss further below.

Table 1 depicts the clinical and pathologic characteristics of the discovery cohort by molecular subtype. Basal tumors were enriched with sarcomatoid features and metastatic disease at presentation (Table 1) and were associated with shorter overall survival (14.9 months, p = 0.098), and disease-specific survival (median 14.9 months, p = 0.028; Figure 1A, right). Although they expressed epithelial cytokeratins, basal tumors also contained "mesenchymal" biomarkers (i.e., TWIST1/2, SNAI2, ZEB2, and VIM; McConkey et al., 2010; Peinado et al., 2007; Figure S1B), as do basal breast cancers (Chaffer et al., 2013). In addition, basal tumors expressed high levels of the epidermal growth factor receptor (EGFR) and several of its ligands (Figure S1B), similar to basal breast and head and neck squamous cell carcinomas (Perou et al., 2000; Romano et al., 2009; Sørlie et al., 2001). On the other hand, luminal tumors were enriched with "epithelial" biomarkers (E-cadherin/CDH1 and members of the miR-200 family; Gregory et al., 2008; Figure S1B), high levels of fibroblast growth factor receptor-3 (FGFR3), and activating *FGFR3* mutations (Figures 1A and 1B; Figure S1C). *TP53* mutation frequencies were similar in all of the subtypes (Figure S1C). To examine cluster stability, we calculated silhouette scores for each subtype. All of the basal and luminal tumors were stable, whereas 9/26 of the p53-like tumors were not (Figure S1D); five of these unstable tumors were most similar to the luminal subtype (data not shown).

We developed a classifier using the differentially expressed genes associated with subtype membership in the discovery cohort and applied it to whole genome mRNA expression data from an independent cohort of formalin-fixed paraffin-embedded MIBCs (n = 57, MD Anderson validation cohort; Figure 2A; Table S1). Like the discovery cohort, basal tumors in the validation cohort were associated with shorter overall survival (median 25.0 months, p = 0.011) and disease-specific survival (median 25.3 months, p = 0.004; Figure 2A, right side) and were enriched with basal biomarkers compared to tumors in the other subtypes (Figure 2B). We then used the classifier to make additional predictions in the MIBCs (n = 55) from a third, publicly available gene expression profiling data set ("Chungbuk cohort"; Kim et al., 2010; Figure 2C; Table S2). The Chungbuk basal tumors were also associated with shorter median disease-specific survival (11.2 months, p = 0.102) and overall survival (10.4 months, p = 0.058; Figure 2C, right side) and were enriched with basal biomarkers (Figure 2D). In addition, GSEA confirmed that luminal biomarkers were enriched in luminal subtypes in both of the validation cohorts (Figures 2B and 2D).

Basal Tumors Are Characterized by Squamous Differentiation

Bladder cancers with squamous histological features are generally considered distinct from conventional urothelial cancers. However, the basal MIBCs in the discovery and validation cohorts were significantly enriched with squamous features (Figure 3A; Table 1; Table S1), and the basal tumors with squamous features also expressed higher basal biomarker mRNA levels than did basal tumors without squamous features (data not shown). The high molecular weight keratins (KRT5, KRT6, and KRT14) that characterized basal MIBCs were also enriched in a lethal "squamous cell carcinoma" MIBC subtype that was

Figure 2. Characterization of Basal and Luminal Subtypes in other MIBC Cohorts

(A) Subtype classification of the MD Anderson validation cohort (n = 57). RNA was isolated from macrodissected FFPE tumor sections and whole genome mRNA expression was measured using Illumina's DASL platform. Kaplan-Meier plots of overall survival (p = 0.011) and disease-specific survival (p = 0.004) associated with the three subtypes are presented on the right.

(B) Expression of basal and luminal markers in the molecular subtypes in the MD Anderson validation cohort. The results of GSEA of basal and luminal marker expression in the subtypes are displayed on the left, and heat maps depicting relative basal and luminal marker levels in the subtypes are displayed on the right.

(C) Subtype classification of the Chungbuk cohort (n = 55). Whole genome mRNA expression profiling (Illumina platform) and clinical data were downloaded from GEO (GSE13507), and the oneNN classifier was used to assign tumors to subtypes. Tumors were assigned to subtypes using the oneNN prediction model (left). Kaplan-Meier plots of overall survival (p = 0.102) and disease-specific survival (p = 0.058) as a function of tumor subtype (right).

(D) Expression of basal and luminal markers in the molecular subtypes in the Chungbuk cohort. The results of GSEA of basal and luminal marker expression in the subtypes are displayed on the left, and heat maps depicting basal and luminal marker expression are displayed on the right.

See also Tables S1 and S2.

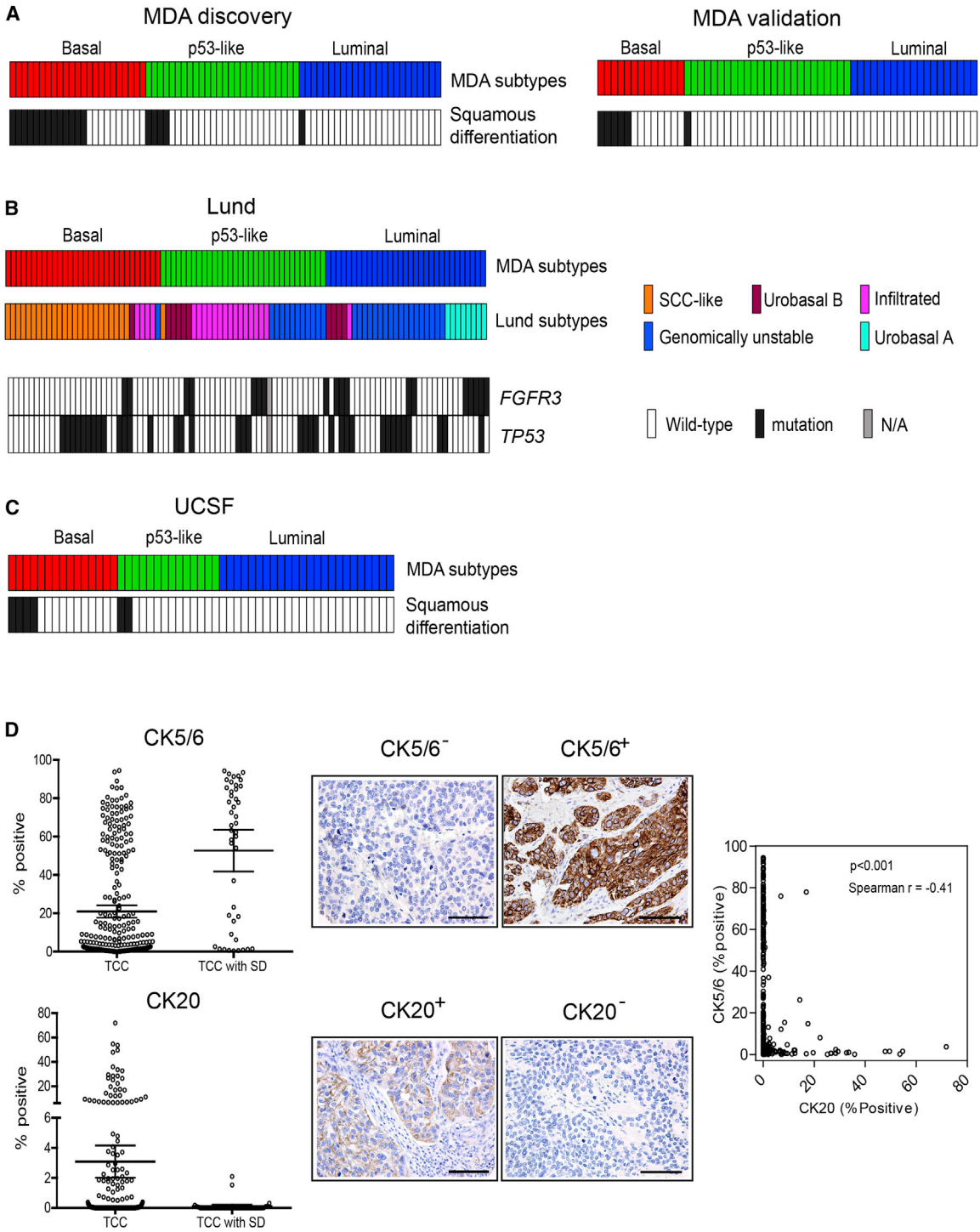

Figure 3. Presence of Squamous Features in the Subtypes

(A) Tumor squamous feature content in the MD Anderson discovery and validation cohorts. Subtype designations are indicated by the top color bars, and the presence of squamous features (in black) is indicated in the color bars below.

(B) Relationship between the MD Anderson subtypes and the molecular taxonomy developed by Sjodahl and colleagues (Sjodahl et al., 2012). Whole genome mRNA expression (Illumina platform) and clinical data were downloaded from GEO (GSE32894), and the oneNN classifier was used to assign the Lund tumors to subtypes. Subtype membership is indicated by the top color bars, and *FGFR3* and *TP53* mutations in the Lund tumors are indicated in color bars below. Black, mutant; white, wild-type; gray (N/A), mutation data were not available.

(C) Presence of squamous features in the UCSF data set. Gene expression profiling (in-house platform) and clinical data were downloaded from GEO (GSE1827), and the oneNN classifier was used to assign the UCSF tumors to the subtypes. Subtype memberships for each tumor are indicated in the top color bars, and the presence of squamous features (in black) is indicated in the color bar below.

(legend continued on next page)

identified recently by another group (Sjodahl et al., 2012). We applied our subtype classifier to the other group's data set ("Lund cohort"; Sjodahl et al., 2012) and confirmed that the Lund squamous cell carcinoma subtype (Sjodahl et al., 2012) corresponded to the basal subtype identified here ("Lund" tumors, Figure 3B; Table S3). Furthermore, like the MD Anderson discovery and validation cohorts, the Lund basal/SCC-like tumors were enriched with squamous differentiation (Sjodahl et al., 2012). Other Lund features also correlated with the subtypes described here—the MD Anderson p53-like subtype and the Lund "infiltrated" (MS2b.1) tumors were enriched with extracellular matrix biomarkers (Figure 3B; also see Figure S2; Sjodahl et al., 2012), and all of the Lund "urobasal A" tumors were confined to the MD Anderson luminal subtype (Figure 3B). In addition, as was the case in the MD Anderson discovery cohort, the Lund luminal tumors were enriched with activating *FGFR3* mutations ($p < 0.05$; Figure 3B; Figure S1C). High molecular weight keratins (KRT5 and KRT14) also characterized a bladder cancer "squamous cluster" (cluster D) identified by a group at the University of California-San Francisco ("UCSF cohort"; Blaveri et al., 2005). We applied our classifier to the UCSF data set and confirmed that the UCSF basal tumors were also enriched with squamous features (Figure 3C; "UCSF," Table S4). Finally, we stained a tissue microarray containing 332 pT3 MIBCs (Table S5) with clinical-grade antibodies specific for basal (CK5/6) or luminal (CK20) cytokeratins, quantified antigen expression across the tissue microarray by image analysis, and correlated cytokeratin levels with the presence of squamous features (Figure 3D). Mean CK5/6 levels were significantly higher in tumors with squamous differentiation, whereas CK20 was expressed at higher levels in conventional MIBCs, and expression of CK5/6 correlated inversely with CK20 across the cohort (Figure 3D). Expression of CK5/6 did not correlate with adverse outcomes (data not shown) because careful stage matching had been performed in the tumor cohort. Together, the results demonstrate that squamous differentiation is a common feature of basal MIBCs and that the subtypes described here are similar to those identified independently by other groups.

p63 and PPARγ Control Basal and Luminal Biomarker Expression

To more clearly define the transcription factors that controlled basal and luminal gene expression, we used the "upstream regulators" function in Ingenuity Pathway Analysis (IPA, Ingenuity Systems; http://www.ingenuity.com) and the gene expression profiling data from the MD Anderson discovery cohort to identify the transcription factors that were responsible for the gene expression signatures observed in the MIBC subtypes (Figure 4; Table S6). Because the silhouette analyses revealed that nine of the p53-like tumors were unstable, we compared the IPA results obtained with (n = 73) and without (n = 64) the unstable tumors (Table S7). Transcription factors that have been implicated in the biology of the basal/stem cell compartment of the normal urothelium (Stat-3, NFκB, Hif-1, and p63; Ho et al., 2012) were predicted to be significantly "activated" in basal MIBCs (Figure 4; Table S6; Figure S3A). TP63 has been identified as a biomarker for lethal MIBCs (Choi et al., 2012; Karni-Schmidt et al., 2011), and we used quantitative RT-PCR to confirm that TP63 levels were elevated in the basal MIBCs in the MD Anderson discovery cohort (Figure S3B). Six of the top ten upregulated basal MIBC biomarkers (KRT5, KRT6A, KRT6C, PI3, KRT14, and S100A7) based on fold changes are known direct ΔNp63α transcriptional targets in other tissues (Boldrup et al., 2007; Celis et al., 1996; Romano et al., 2009; Figure 4, also Figure 1B). Basal tumors were also enriched for MYC expression, which is controlled by p63 in human bladder cancer cells (Marquis et al., 2012).

Luminal MIBCs exhibited strong peroxisome proliferator activator receptor (PPAR) pathway activation as well as high-level expression of PPARG and its direct transcriptional target and coactivator, FABP4 (Figures 1B and 4; Table S6; Ayers et al., 2007). In addition, the estrogen receptor (ER) and its coactivator Trim-24 (Hatakeyama, 2011; Tsai et al., 2010) were among the top "activated" upstream regulators in the luminal MIBCs, whereas the basal Stat-3 and NFκB transcriptional networks were downregulated in them (Table S6; Figures S3C and S3D). Conversely, breast luminal transcriptional pathways (ER, Gata-3, and Trim-24) were all downregulated in the basal MIBCs (Table S6). The p53-like luminal MIBCs could be distinguished from the luminal tumors by their expression of an active p53-associated gene expression signature that was not associated with the presence of wild-type *TP53* (Figure 4; also Figures 1 and 3B; Tables S6 and S7). The p53-like tumors also contained an active p16 (CDKN2A) gene signature (Figure S3E).

To more directly define p63's role in controlling basal gene expression, we stably transduced human UM-UC14 bladder cancer cells with nontargeting or TP63-specific shRNAs and used whole genome mRNA expression profiling to create a bladder cancer p63 pathway gene expression signature. IPA analyses indicated that TP63 knockdown decreased basal (p63 and Myc) pathway gene expression, and interestingly, it also increased PPAR pathway gene expression (Figure 5A; Figure S4A). GSEA analyses in the discovery cohort confirmed that the p63 gene signature was significantly enriched in primary basal MIBCs (Figure 5B).

To determine PPARγ's role in controlling luminal gene expression, we generated PPARγ gene expression signatures using whole genome mRNA expression profiling data collected from two human bladder cancer cell lines (UM-UC7 and UM-UC9) that had been exposed to the PPARγ-selective agonist rosiglitazone. IPA analyses confirmed that rosiglitazone activated PPAR

(D) Tissue microarray analysis of CK5/6 (basal) and CK20 (luminal) cytokeratin expression. Cytokeratin protein expression was measured by immunohistochemistry and optical image analysis in the MD Anderson Pathology Core on a tissue microarray containing 332 high-grade pT3 tumors. The percentages of positive tumor cells as determined by image analysis are shown. Left panels: mean levels of CK5/6 (top) and CK20 (bottom) in tumors without (TCC) or with (TCC with SD) squamous features. Bars indicate mean values with 95% confidence intervals. Middle panels: representative images of stained cores from tumors that expressed high or low levels of CK5/6 or CK20. The scale bars correspond to 100 μm. Right panel: relationship between CK5/6 and CK20 expression across the cohort.
See also Tables S3–S5 and Figure S2.

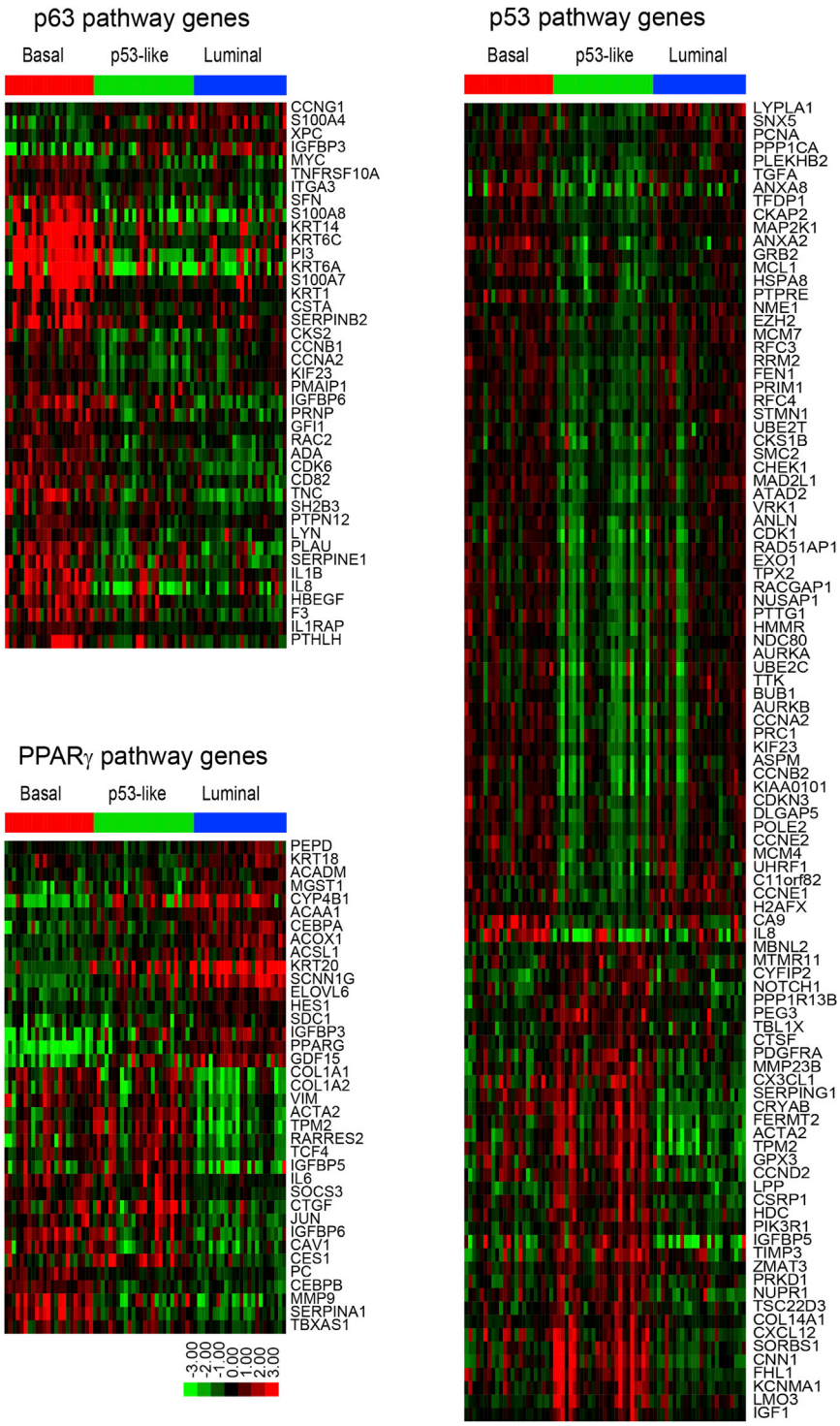

Figure 4. Subtype-Associated Gene Expression Signatures

Signatures were identified using the whole genome mRNA expression profiling data from the MD Anderson discovery cohort and the upstream regulators tool in Ingenuity Pathway Analysis (IPA, Ingenuity Systems; http://www.ingenuity.com). Each heat map displays the expression of the corresponding IPA gene signature as a function of tumor subtype membership; note that genes can be either up- or downregulated by an active transcription factor. Top left: p63-associated gene expression. Bottom left: PPARγ-associated gene expression. Right: p53-associated gene expression.

See also Tables S6 and S7 and Figure S3.

and other luminal transcriptional pathways in both cell lines (Figure 5A; Figures S4B and S4C). GSEA revealed that the UM-UC7 and UM-UC9 PPARγ gene signatures were significantly enriched in primary luminal MIBCs in the discovery cohort (Figure 5B). Interestingly, rosiglitazone also decreased basal transcription factor activation (Figure 5A; Figure S4C). Therefore, PPARγ activation plays an important role in regulating the luminal MIBC gene expression signature, and p63 and PPARγ antagonize each other.

p53-like MIBCs Are Resistant to Neoadjuvant Chemotherapy

Presurgical (neoadjuvant) cisplatin-based chemotherapy (NAC) is the current standard-of-care for high-risk MIBC (Shah et al., 2011), and pathological response to NAC (downstaging to ≤pT1 at cystectomy) is a strong predictor of disease-specific survival (Grossman et al., 2003), as it is in breast cancer (Esserman et al., 2012b). We noticed that all of the p53-like MIBCs from patients treated with NAC in the discovery cohort (n = 7) were resistant to chemotherapy (Table 1). To examine this relationship further, we explored the chemoresistance of p53-like MIBCs in an expanded NAC cohort (n = 34) and in an additional cohort of 23 archival tumors treated uniformly with methotrexate, vinblastine, doxorubicin and cisplatin (MVAC) within the context of a Phase III clinical trial (Millikan et al., 2001). The p53-like MIBCs in both cohorts were resistant to NAC (Figure 6A; Tables S8 and S9). We applied the primary tumor p53 signature to a panel of human bladder cancer cell lines and identified a subset of them that expressed the signature, not all of which retained wild-type *TP53* (Figure 6B). The p53-like cell lines were also resistant to cisplatin-induced apoptosis in vitro (Figure 6C). In addition, four of five of the *TP53* wild-type cell lines that did not contain the "p53-like" signature at baseline were cisplatin-resistant (Figures 6B and 6C).

To further examine whether chemoresistance was a consistent feature of the p53-like subtype, we used gene expression profiling and our classifier to perform molecular subtype

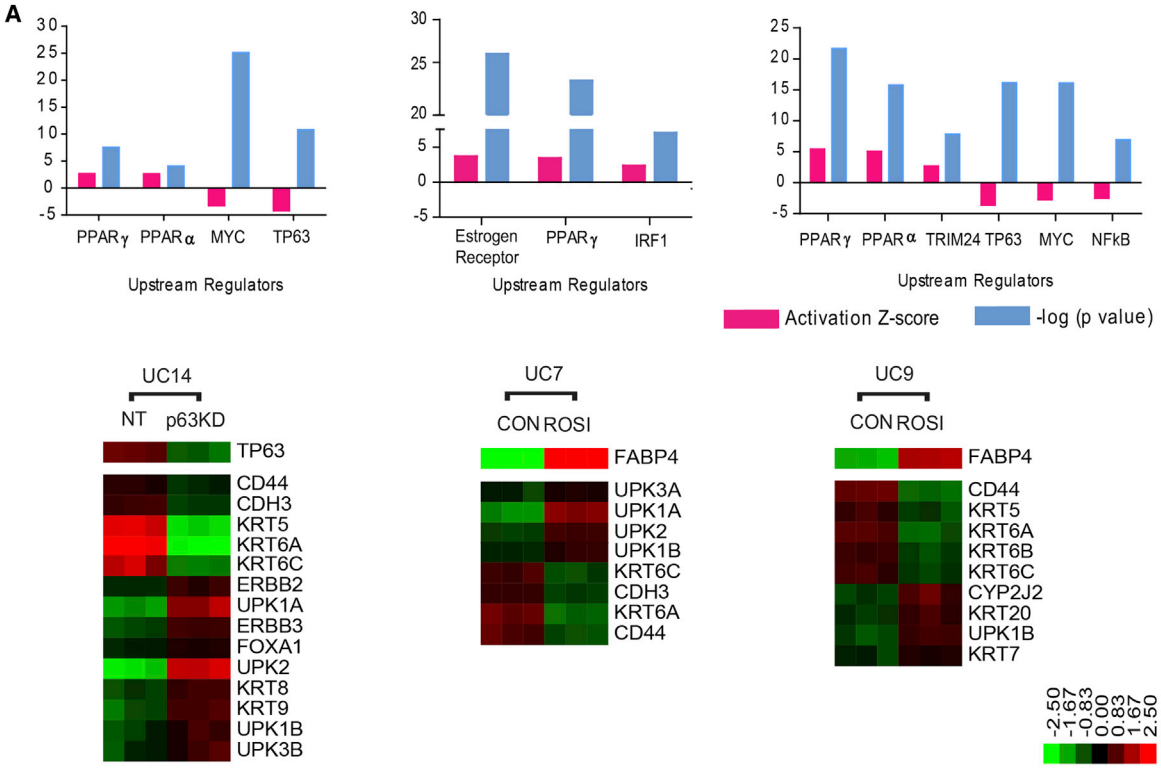

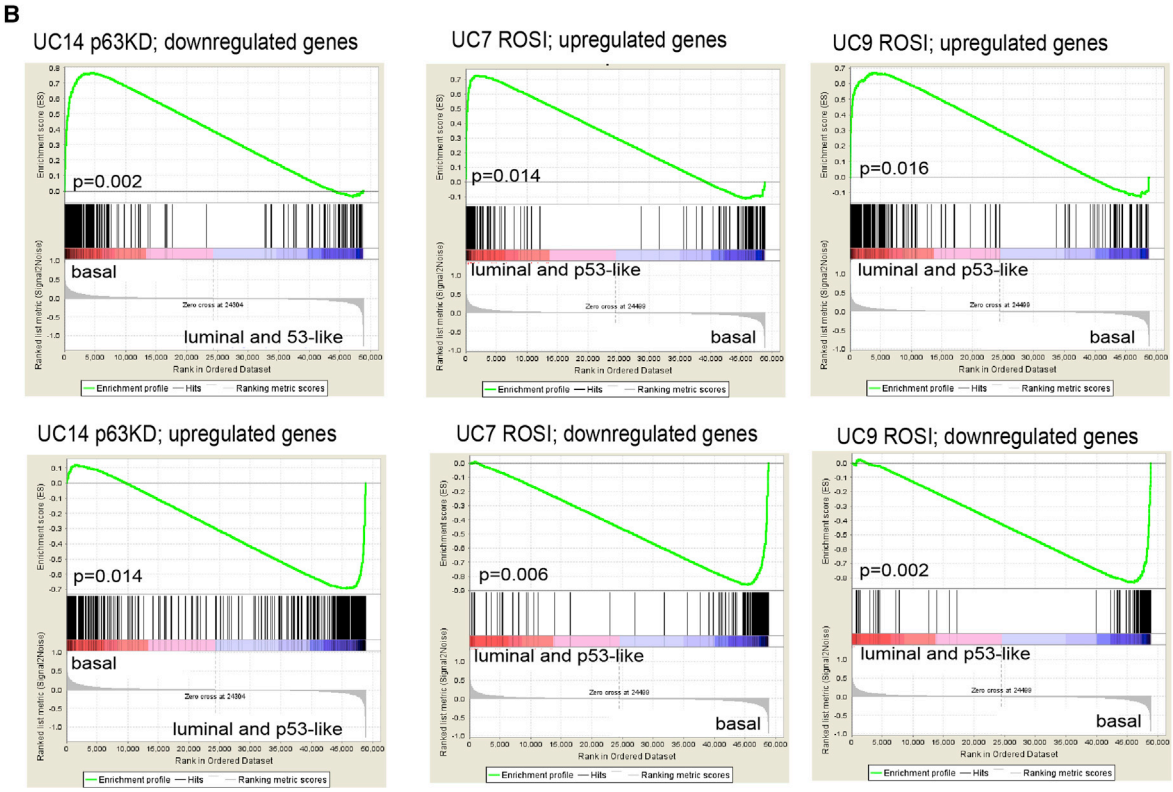

(legend on next page)

assignments on matched pre- and post-treatment MIBCs collected within the context of a prospective Phase II clinical trial of neoadjuvant dose-dense MVAC (DDMVAC), conducted at Fox Chase Cancer Center and Thomas Jefferson University Hospital (Table S10). All of the pretreatment tumors with squamous features in this "Philadelphia" cohort were confined to the basal cluster (Table S10; p = 0.012). In addition, and consistent with what we had observed in the MD Anderson cohorts, many of the Philadelphia basal (7/14) and luminal (12/20) tumors responded to NAC, whereas the response rate in the p53-like tumors was significantly lower at 11% (1/9; Figure 7A). Furthermore, chemoresistant tumors were enriched with the p53-like subtype after NAC (Figure 7B).

To further characterize the molecular mechanisms underlying chemoresistance, we compared the matched pre- and post-treatment gene expression profiles of the chemoresistant Philadelphia tumors using the "upstream regulators" function of IPA (data not shown). The results indicated that chemotherapy caused all of the tumors to express an active p53 pathway gene signature after NAC (Figure 7C; Table S11). Importantly, this chemotherapy-induced p53 signature was not very similar to the one that dictated tumor membership within the p53-like subtype (13 overlapping probes, Table S11).

Finally, we searched for pretreatment gene signatures within the Philadelphia basal and luminal MIBC subtypes that might predict chemosensitivity. We were unable to detect such a signature in the luminal tumors (data not shown), but the chemosensitive Philadelphia basal tumors were enriched for biomarkers reflective of immune infiltration (Figure 7D). Similarly, all of the chemosensitive basal tumors from the MD Anderson MVAC cohort were also enriched with these immune biomarkers (Figure S5).

DISCUSSION

We conclude that MIBCs can be grouped into basal and luminal subtypes reminiscent of those observed in human breast cancers (Perou et al., 2000). Basal MIBCs were associated with shorter disease-specific and overall survival, presumably because patients with these cancers tended to have more invasive and metastatic disease at presentation. The invasive/metastatic phenotype was associated with expression of "mesenchymal" and bladder cancer stem cell (Chan et al., 2009) biomarkers, and the tumors were enriched with sarcomatoid and squamous features (Blaveri et al., 2005; Sjodahl et al., 2012). The link between squamous features and aggressive behavior is consistent with other recent observations (Kim et al., 2012; Mitra et al., 2013), and the presence of EMT and bladder cancer stem cell biomarkers in basal tumors provides a biological explanation for their aggressive behaviors. Transcription factor p63 plays a central role in controlling the basal gene signature, and our preliminary data suggest that the EGFR, Stat-3, NFκB, and Hif-1α are also involved. Importantly, immune-infiltrated basal MIBCs responded to NAC, as do some basal breast cancers (Esserman et al., 2012a, 2012b). Because NAC pathological complete response is associated with excellent long-term survival (Grossman et al., 2003), aggressive early management of basal MIBCs with NAC offers the best chance for improved survival for patients with this potentially deadly form of this disease. It also seems likely that T cell modulators (i.e., anti-CTLA4) and EGFR-, NFκB, Hif-1α/VEGF, and/or Stat-3-targeted agents will also be active within this subtype.

Like luminal breast cancers (Perou et al., 2000; Sørlie et al., 2001), luminal MIBCs displayed active ER/TRIM24 pathway gene expression and were enriched with FOXA1, GATA3, ERBB2, and ERBB3. Agents that target the ER (George et al., 2013; Hoffman et al., 2013; Shen et al., 2006) and/or ErbB2 and -3 may therefore be clinically active in luminal MIBCs. In addition, luminal MIBCs contained active PPAR gene expression and activating *FGFR3* mutations, so PPARγ- and FGFR-3-targeted agents may be active in this subtype. Because many luminal MIBCs responded to NAC, targeted therapies should probably be combined with conventional chemotherapy for maximum efficacy.

The idea that wild-type p53 is required for DNA damage-induced apoptosis is a central tenet in cancer biology (Lowe et al., 1993, 1994). Therefore, it was surprising to us that de novo and induced chemoresistance in MIBCs was associated with wild-type p53 gene expression signatures. Nevertheless, this link between "p53-ness" and chemoresistance is another shared property of MIBCs and luminal breast cancers. The recently completed I-SPY 1 TRIAL ("Investigation of Serial Studies to Predict Your Therapeutic Response With Imaging and Molecular Analysis," CALGB150007/150012) examined the correlation between pathological complete response (pCR) rates and recurrence-free and overall survival in women treated with NAC. One of its main conclusions was that pCR rates varied markedly within the different breast cancer subtypes such that tumors with luminal A and/or wild-type p53-like gene expression signatures responded very poorly to NAC (Esserman et al., 2012a, 2012b). Wild-type p53-induced reversible senescence has also recently been implicated in chemoresistance in a mouse model of breast cancer (Jackson et al., 2012), and more generally, quiescence is considered an important mechanism of chemoresistance. Importantly, *TP53* mutation frequencies

Figure 5. Transcriptional Control of the Basal and Luminal Gene Expression

Whole genome mRNA expression profiling was used to analyze the effects of stable p63 knockdown or rosiglitazone-induced PPARγ activation in human bladder cancer cell lines, and the data were used to generate gene expression signatures characteristic of p63 and PPARγ activation. GSEA was then used to determine whether these signatures were present in the MD Anderson discovery cohort tumor subtypes.

(A) Effects of p63 or PPARγ modulation on basal and luminal transcriptional signatures. Top panels: significantly activated/inhibited transcriptional pathways after p63 knockdown in UM-UC14 cells (top left), PPARγ activation in UM-UC7 (top middle), or PPARγ activation in UM-UC9 (top right) based on IPA analyses. The heat maps below each graph indicate significant changes in basal and luminal marker expression.

(B) p63 and PPARγ gene expression signatures in the subtypes of primary MIBCs. Separate results and p values are shown for the signatures derived from the up- and downregulated genes in each condition. ROSI, rosiglitazone.

See also Figure S4.

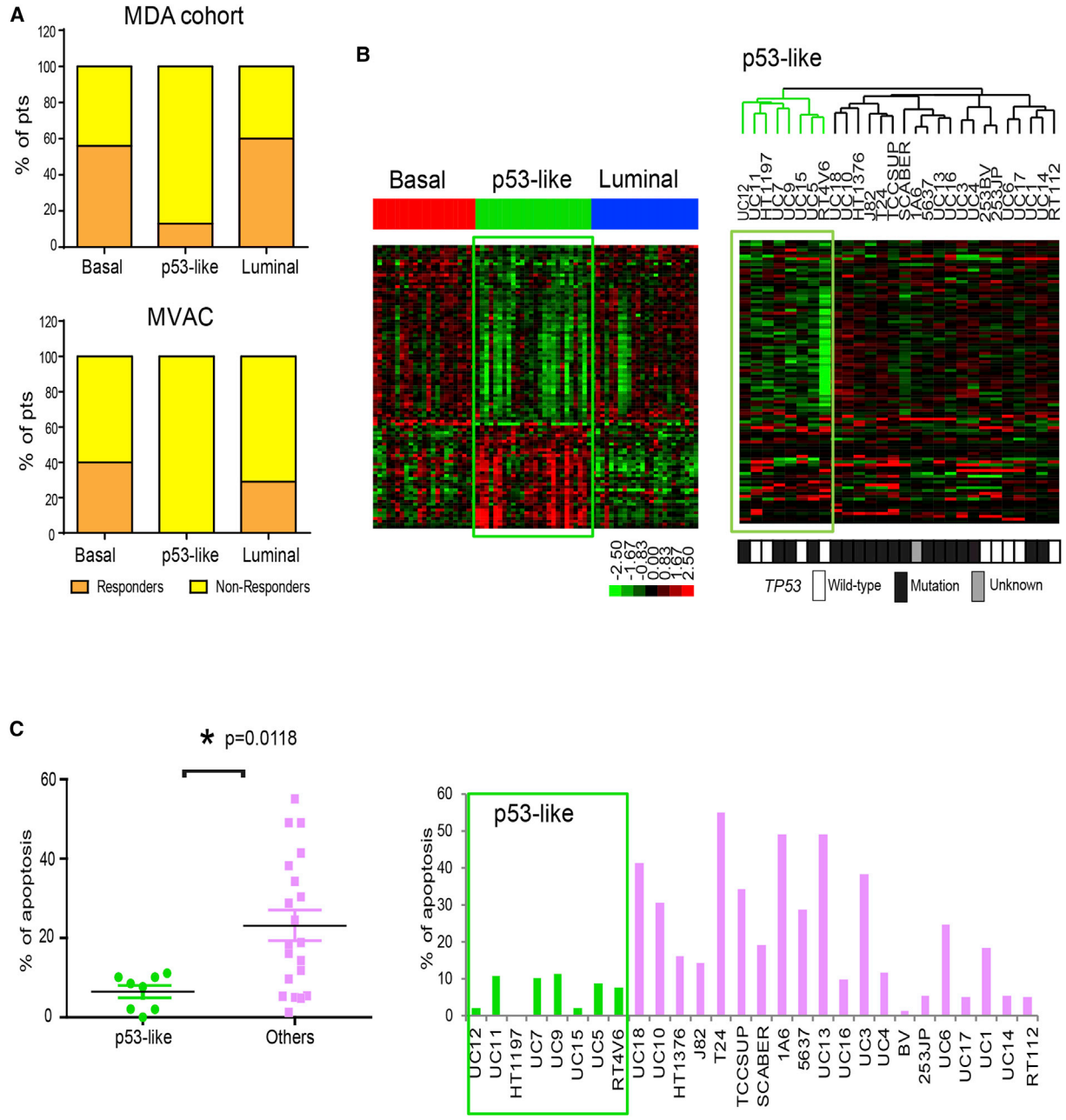

Figure 6. Relationship between Subtype Membership and Chemotherapy Sensitivity

(A) Responses to neoadjuvant chemotherapy in the MD Anderson NAC (n = 34) and MVAC (n = 23) cohorts. Subtype membership was determined using whole genome mRNA expression profiling data obtained from untreated (TURBT) tumors and the oneNN classifier. Pathological response was defined as downstaging to ≤pT1.

(B) The IPA-defined p53 gene expression signature from the p53-like primary MIBCs was used to perform unsupervised hierarchical cluster analysis on whole genome expression data from a panel of human bladder cancer cell lines (n = 28). The green boxes on the heat maps indicate expression of the signature in the MD Anderson discovery cohort (left) or the cell lines (right). *TP53* mutational status was determined by sequencing and is indicated by the color bar below the heat map (black, mutant; white, wild-type; gray, data were not available).

(C) Cells were incubated with or without 10 μM cisplatin for 48 hr and apoptosis-associated DNA fragmentation was quantified by propidium iodide staining and FACS analysis in three independent experiments. The left panel displays a scatter gram comparing the levels within the two subsets of cell lines (mean ± SEM). The right panel displays the mean value of induced apoptosis in each cell line across the entire cohort.

See also Tables S8 and S9.

were similar in all three MIBC subtypes, indicating that wild-type p53 was not responsible for the baseline and chemotherapy-induced p53-like gene expression signatures reported here. We therefore propose that "p53-ness" as measured by mRNA expression would be a more accurate predictor of de novo and induced MIBC chemoresistance than would analyses of *TP53*

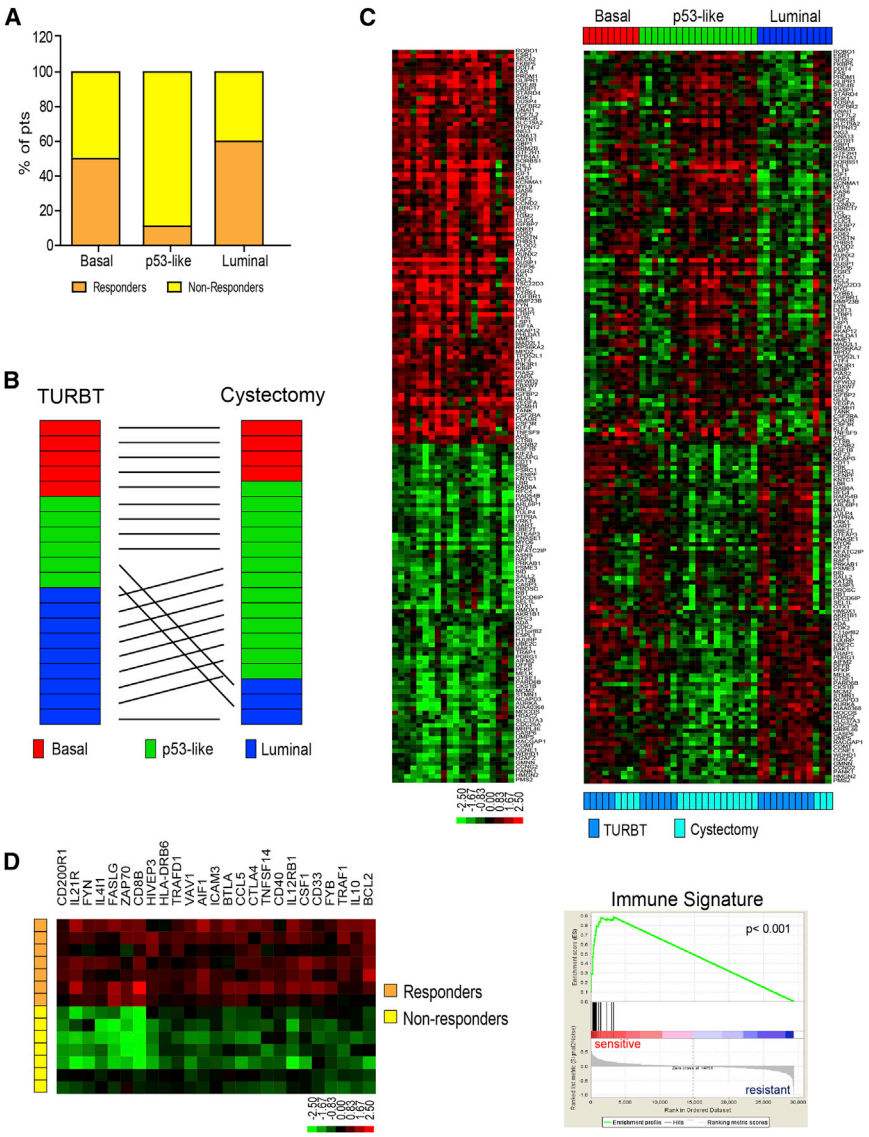

Figure 7. Wild-Type p53 Gene Signatures in Tumors before and after Treatment with NAC

(A) Relationship between subtype membership and response to NAC in the Philadelphia DDMVAC cohort. Subtype membership was determined using pretreatment (TURBT) specimens. Pathological response was defined as downstaging to $\leq$ pT1.

(B) Comparison of subtype membership in the chemoresistant Philadelphia tumors before and after NAC. Whole genome mRNA expression profiling was performed on matched tumors before and after NAC, and the oneNN classifier was used to assign tumors to subtypes. "TURBT" refers to the pretreatment tumors and "cystectomy" to the post-treatment tumors.

(C) Expression of a wild-type p53 gene signature in matched pre- and post-treatment tumors. Left: heat map displaying expression of an active p53 gene signature after NAC (log ratio cystectomy/TURBT of matched tumors). Right: relative expression of the p53 signature in matched pre- and post-treatment tumors arranged according to subtype membership.

(D) Analysis of an immune infiltration signature in basal tumors. A supervised analysis was performed to compare the differences in gene expression between basal tumors that were either sensitive or resistant to neoadjuvant DDMVAC in the Philadelphia cohort. Left: heat map depicting the relative expression of immune signature genes in basal responders and non-responders. Right: GSEA analyses of immune biomarkers in the basal tumors.

See also Tables S10 and S11 and Figure S5.

mutational status. It will be important to determine the molecular basis of these p53-like signatures in future studies so that therapeutic approaches can be developed to overcome de novo and/or prevent acquired chemoresistance. We also plan to prospectively test the relationship between the p53-like phenotype and chemoresistance within the context of a SWOG-sponsored multicenter clinical trial (S1314) that is very similar to I-SPY and was designed to prospectively evaluate another gene expression profiling-based algorithm ("CoXEN"; Lee et al., 2007).

EXPERIMENTAL PROCEDURES

Technical details are provided in the Supplemental Experimental Procedures.

Human Specimens

Clinical data were obtained from the MD Anderson Genitourinary Cancers Research Database, from the Gene Expression Omnibus (GEO), or from patient charts (MVAC and Philadelphia cohorts). All MD Anderson patients signed a "front door" informed consent allowing collection of their tissue and of their clinical data that was approved by the MD Anderson Institutional Review Board (IRB). An additional MD Anderson IRB-approved protocol was obtained specifically for genomics analyses. The Philadelphia tissues were collected and analyzed as part of a Phase II clinical trial that was IRB-approved at the Fox-Chase Cancer Center and Thomas Jefferson University. Unstained tissue sections (10 micron, five slides/tumor) and matched hematoxylin and eosin stained sections from the DDMVAC clinical trial were transferred to MD Anderson under an executed materials transfer agreement between MD Anderson and Fox-Chase. A genitourinary pathologist (Bogdan Czerniak) reviewed all of the tissue samples.

Tumor Cohorts

The Chungbuk (n = 55) (Kim et al., 2010), Lund (n = 93) (Sjodahl et al., 2012), and UCSF (n = 53)(Blaveri et al., 2005) cohort data were downloaded from the GEO (GSE13507, GSE32894, and GSE1827, respectively). The discovery cohort consisted of 73 tumors from transurethral resections (TURs) that had been snap-frozen in liquid nitrogen within 5 min of isolation and transferred to the MD Anderson Bladder SPORE Tissue Core. The MD Anderson validation cohort consisted of 57 randomly selected, formalin-fixed, paraffin-embedded (FFPE) tumors that were obtained from the main MD Anderson Cancer Center CCSG-supported Pathology Tissue Bank. The MD Anderson NAC cohort (n = 34) contained a mixture of 18 tumors from the discovery cohort plus 16 additional FFPE tumors from patients treated with neoadjuvant chemotherapy on- and off-protocol. The MD Anderson MVAC cohort (n = 23) consisted of all available FFPE pretreatment tumors (TURs) from a previously reported Phase

III clinical trial (Millikan et al., 2001). The Philadelphia NAC cohort (n = 43 TURs and 20 cystectomies) consisted of all available pre- and post-treatment FFPE tumors from patients enrolled in a Phase II clinical trial of neodjuvant dose-dense MVAC (DDMVAC) that was conducted at Fox-Chase Cancer Center and The Thomas Jefferson University and will be reported elsewhere. NAC response in all of the cohorts was defined as downstaging to no muscle-invasive disease at cystectomy (≤pT1; Millikan et al., 2001).

Gene Expression Profiling Platforms

The MD Anderson discovery cohort and human bladder cancer cell lines were analyzed by direct hybridization on Illumina HT12v3 and HT12v4 chips, respectively (Illumina). Data from all of the FFPE cohorts were generated using Illumina's DASL platform (WG-DASL HT12v4 chips).

Tumor Cluster Assignments

MIBC clusters (subtypes) were determined in the discovery cohort using unsupervised hierarchical cluster analysis (Eisen et al., 1998). The gene signatures associated with each cluster were then used to generate a one nearest neighbor (oneNN; Dudoit et al., 2002) prediction model that was used in all subsequent analyses to assign tumors to specific subtypes.

Micro RNA Expression

Levels of miR-200b and miR-200c were measured in the discovery cohort by quantitative RT-PCR as described in the Supplemental Experimental Procedures.

Analysis of Cytokeratin Protein Expression

Basal (CK5/6) and luminal (CK20) cytokeratin protein expression was analyzed on a tissue microarray (TMA) consisting of stage-matched (pT3, n = 332) MIBCs collected within the context of the International Bladder Cancer Network's Bladder Cancer Bank initiative (Goebell et al., 2005). Immunohistochemical staining was performed using clinical-grade (CLIA) antibodies and protocols in the MD Anderson Pathology Core, and staining intensities were quantified by image analysis.

Generation of p63 and PPARγ Gene Signatures

UM-UC14 human MIBC cells were stably transduced with TP63-specific or nontargeting lentiviral shRNA constructs in the MD Anderson Vector Core. UM-UC7 and UM-UC9 cells were incubated with or without 1 μM rosiglitazone for 48 hr. Triplicate RNA isolates were prepared on different days for each condition, and global changes in gene expression were determined by whole genome expression profiling. The statistically significant changes in gene expression were used to create signatures that were subsequently used in the IPA and GSEA analyses presented in Figure 5.

Statistical Analyses

Clinicodemographic characteristics were compared using Fisher's exact tests and Kruskal-Wallis tests to assess differences between groups in categorical and continuous variables, respectively. Kaplan-Meier analysis with log-rank statistics was used to characterize survival distributions and associations between subtypes and survival outcomes. Statistical analysis was performed using SPSS (version 19) and a p value less than 0.05 was considered significant.

ACCESSION NUMBERS

The GEO accession numbers for the gene expression profiling data presented in this study are GSE48277 and GSE47993.

SUPPLEMENTAL INFORMATION

Supplemental Information includes Supplemental Experimental Procedures, five figures, and eleven tables and can be found with this article online at http://dx.doi.org/10.1016/j.ccr.2014.01.009.

ACKNOWLEDGMENTS

The authors would like to acknowledge Lyndsay Harris (Southwest Oncology Group, Breast Committee, Case Cancer Center) for her help with the DASL assay and Neema Navai and Matthew Wszolek for sharing their miR-200b and miR-200c PCR data. This work was supported by a grant from the Baker Foundation, the MD Anderson Bladder SPORE (P50 CA91846), grant R01 CA151489 (to B.C.), and the MD Anderson CCSG (P30 016672). E.R.P. is supported by grant no. IRG-92-027-17 from the American Cancer Society. This paper is dedicated to the memory of Dexter Baker. The authors wish to disclose that the MD Anderson Cancer Center has submitted a patent that covers some of the findings reported in this manuscript.

Received: December 19, 2012
Revised: October 17, 2013
Accepted: January 13, 2014
Published: February 10, 2014

REFERENCES

Ayers, S.D., Nedrow, K.L., Gillilan, R.E., and Noy, N. (2007). Continuous nucleocytoplasmic shuttling underlies transcriptional activation of PPARgamma by FABP4. Biochemistry *46*, 6744–6752.

Blaveri, E., Simko, J.P., Korkola, J.E., Brewer, J.L., Baehner, F., Mehta, K., Devries, S., Koppie, T., Pejavar, S., Carroll, P., and Waldman, F.M. (2005). Bladder cancer outcome and subtype classification by gene expression. Clin. Cancer Res. *11*, 4044–4055.

Boldrup, L., Coates, P.J., Gu, X., and Nylander, K. (2007). DeltaNp63 isoforms regulate CD44 and keratins 4, 6, 14 and 19 in squamous cell carcinoma of head and neck. J. Pathol. *213*, 384–391.

Botteman, M.F., Pashos, C.L., Redaelli, A., Laskin, B., and Hauser, R. (2003). The health economics of bladder cancer: a comprehensive review of the published literature. Pharmacoeconomics *21*, 1315–1330.

Celis, J.E., Rasmussen, H.H., Vorum, H., Madsen, P., Honoré, B., Wolf, H., and Orntoft, T.F. (1996). Bladder squamous cell carcinomas express psoriasin and externalize it to the urine. J. Urol. *155*, 2105–2112.

Chaffer, C.L., Marjanovic, N.D., Lee, T., Bell, G., Kleer, C.G., Reinhardt, F., D'Alessio, A.C., Young, R.A., and Weinberg, R.A. (2013). Poised chromatin at the ZEB1 promoter enables breast cancer cell plasticity and enhances tumorigenicity. Cell *154*, 61–74.

Chan, K.S., Espinosa, I., Chao, M., Wong, D., Ailles, L., Diehn, M., Gill, H., Presti, J., Jr., Chang, H.Y., van de Rijn, M., et al. (2009). Identification, molecular characterization, clinical prognosis, and therapeutic targeting of human bladder tumor-initiating cells. Proc. Natl. Acad. Sci. USA *106*, 14016–14021.

Choi, W., Shah, J.B., Tran, M., Svatek, R., Marquis, L., Lee, I.L., Yu, D., Adam, L., Wen, S., Shen, Y., et al. (2012). p63 expression defines a lethal subset of muscle-invasive bladder cancers. PLoS ONE *7*, e30206.

Dinney, C.P., McConkey, D.J., Millikan, R.E., Wu, X., Bar-Eli, M., Adam, L., Kamat, A.M., Siefker-Radtke, A.O., Tuziak, T., Sabichi, A.L., et al. (2004). Focus on bladder cancer. Cancer Cell *6*, 111–116.

Dudoit, S., Fridlyand, J., and Speed, T.P. (2002). Comparison of discrimination methods for classification of tumors using DNA microarrays. J. Am. Stat. Assoc. *97*, 77–87.

Dyrskjøt, L., Thykjaer, T., Kruhøffer, M., Jensen, J.L., Marcussen, N., Hamilton-Dutoit, S., Wolf, H., and Orntoft, T.F. (2003). Identifying distinct classes of bladder carcinoma using microarrays. Nat. Genet. *33*, 90–96.

Eisen, M.B., Spellman, P.T., Brown, P.O., and Botstein, D. (1998). Cluster analysis and display of genome-wide expression patterns. Proc. Natl. Acad. Sci. USA *95*, 14863–14868.

Esserman, L.J., Berry, D.A., Cheang, M.C., Yau, C., Perou, C.M., Carey, L., DeMichele, A., Gray, J.W., Conway-Dorsey, K., Lenburg, M.E., et al.; I-SPY 1 TRIAL Investigators (2012a). Chemotherapy response and recurrence-free survival in neoadjuvant breast cancer depends on biomarker profiles: results from the I-SPY 1 TRIAL (CALGB 150007/150012; ACRIN 6657). Breast Cancer Res. Treat. *132*, 1049–1062.

Esserman, L.J., Berry, D.A., DeMichele, A., Carey, L., Davis, S.E., Buxton, M., Hudis, C., Gray, J.W., Perou, C., Yau, C., et al. (2012b). Pathologic complete response predicts recurrence-free survival more effectively by cancer subset: results from the I-SPY 1 TRIAL–CALGB 150007/150012, ACRIN 6657. J. Clin. Oncol. *30*, 3242–3249.

George, S.K., Tovar-Sepulveda, V., Shen, S.S., Jian, W., Zhang, Y., Hilsenbeck, S.G., Lerner, S.P., and Smith, C.L. (2013). Chemoprevention of BBN-Induced Bladder Carcinogenesis by the Selective Estrogen Receptor Modulator Tamoxifen. Translational oncology *6*, 244–255.

Goebell, P.J., Groshen, S., Schmitz-Drager, B.J., Sylvester, R., Kogevinas, M., Malats, N., Sauter, G., Grossman, H.B., Dinney, C.P., Waldman, F., and Cote, R.J. (2005). Concepts for banking tissue in urologic oncology–the International Bladder Cancer Bank. Clinical cancer research: an official journal of the American Association for Cancer Research *11*, 413–415.

Gregory, P.A., Bert, A.G., Paterson, E.L., Barry, S.C., Tsykin, A., Farshid, G., Vadas, M.A., Khew-Goodall, Y., and Goodall, G.J. (2008). The miR-200 family and miR-205 regulate epithelial to mesenchymal transition by targeting ZEB1 and SIP1. Nat. Cell Biol. *10*, 593–601.

Grossman, H.B., Natale, R.B., Tangen, C.M., Speights, V.O., Vogelzang, N.J., Trump, D.L., deVere White, R.W., Sarosdy, M.F., Wood, D.P., Jr., Raghavan, D., and Crawford, E.D. (2003). Neoadjuvant chemotherapy plus cystectomy compared with cystectomy alone for locally advanced bladder cancer. N. Engl. J. Med. *349*, 859–866.

Hatakeyama, S. (2011). TRIM proteins and cancer. Nat. Rev. Cancer *11*, 792–804.

Ho, P.L., Kurtova, A., and Chan, K.S. (2012). Normal and neoplastic urothelial stem cells: getting to the root of the problem. Nat Rev Urol *9*, 583–594.

Hoffman, K.L., Lerner, S.P., and Smith, C.L. (2013). Raloxifene inhibits growth of RT4 urothelial carcinoma cells via estrogen receptor-dependent induction of apoptosis and inhibition of proliferation. Hormones & cancer *4*, 24–35.

Jackson, J.G., Pant, V., Li, Q., Chang, L.L., Quintás-Cardama, A., Garza, D., Tavana, O., Yang, P., Manshouri, T., Li, Y., et al. (2012). p53-mediated senescence impairs the apoptotic response to chemotherapy and clinical outcome in breast cancer. Cancer Cell *21*, 793–806.

Karni-Schmidt, O., Castillo-Martin, M., Shen, T.H., Gladoun, N., Domingo-Domenech, J., Sanchez-Carbayo, M., Li, Y., Lowe, S., Prives, C., and Cordon-Cardo, C. (2011). Distinct expression profiles of p63 variants during urothelial development and bladder cancer progression. Am. J. Pathol. *178*, 1350–1360.

Kim, W.J., Kim, E.J., Kim, S.K., Kim, Y.J., Ha, Y.S., Jeong, P., Kim, M.J., Yun, S.J., Lee, K.M., Moon, S.K., et al. (2010). Predictive value of progression-related gene classifier in primary non-muscle invasive bladder cancer. Mol. Cancer *9*, 3.

Kim, S.P., Frank, I., Cheville, J.C., Thompson, R.H., Weight, C.J., Thapa, P., and Boorjian, S.A. (2012). The impact of squamous and glandular differentiation on survival after radical cystectomy for urothelial carcinoma. J. Urol. *188*, 405–409.

Lee, J.K., Havaleshko, D.M., Cho, H., Weinstein, J.N., Kaldjian, E.P., Karpovich, J., Grimshaw, A., and Theodorescu, D. (2007). A strategy for predicting the chemosensitivity of human cancers and its application to drug discovery. Proc. Natl. Acad. Sci. USA *104*, 13086–13091.

Lee, J.S., Leem, S.H., Lee, S.Y., Kim, S.C., Park, E.S., Kim, S.B., Kim, S.K., Kim, Y.J., Kim, W.J., and Chu, I.S. (2010). Expression signature of E2F1 and its associated genes predict superficial to invasive progression of bladder tumors. Journal of clinical oncology: official journal of the American Society of Clinical Oncology *28*, 2660–2667.

Lowe, S.W., Ruley, H.E., Jacks, T., and Housman, D.E. (1993). p53-dependent apoptosis modulates the cytotoxicity of anticancer agents. Cell *74*, 957–967.

Lowe, S.W., Bodis, S., McClatchey, A., Remington, L., Ruley, H.E., Fisher, D.E., Housman, D.E., and Jacks, T. (1994). p53 status and the efficacy of cancer therapy in vivo. Science *266*, 807–810.

Marquis, L., Tran, M., Choi, W., Lee, I.L., Huszar, D., Siefker-Radtke, A., Dinney, C., and McConkey, D.J. (2012). p63 expression correlates with sensitivity to the Eg5 inhibitor ZD4877 in bladder cancer cells. Cancer Biol. Ther. *13*, 477–486.

McConkey, D.J., Lee, S., Choi, W., Tran, M., Majewski, T., Lee, S., Siefker-Radtke, A., Dinney, C., and Czerniak, B. (2010). Molecular genetics of bladder cancer: Emerging mechanisms of tumor initiation and progression. Urol. Oncol. *28*, 429–440.

Millikan, R., Dinney, C., Swanson, D., Sweeney, P., Ro, J.Y., Smith, T.L., Williams, D., and Logothetis, C. (2001). Integrated therapy for locally advanced bladder cancer: final report of a randomized trial of cystectomy plus adjuvant M-VAC versus cystectomy with both preoperative and postoperative M-VAC. Journal of clinical oncology: official journal of the American Society of Clinical Oncology *19*, 4005–4013.

Mitra, A.P., Bartsch, C.C., Bartsch, G., Jr., Miranda, G., Skinner, E.C., and Daneshmand, S. (2013). Does presence of squamous and glandular differentiation in urothelial carcinoma of the bladder at cystectomy portend poor prognosis? An intensive case-control analysis. Urol. Oncol. *12*, S1078–S1439.

Peinado, H., Olmeda, D., and Cano, A. (2007). Snail, Zeb and bHLH factors in tumour progression: an alliance against the epithelial phenotype? Nat. Rev. Cancer *7*, 415–428.

Perou, C.M., Sørlie, T., Eisen, M.B., van de Rijn, M., Jeffrey, S.S., Rees, C.A., Pollack, J.R., Ross, D.T., Johnsen, H., Akslen, L.A., et al. (2000). Molecular portraits of human breast tumours. Nature *406*, 747–752.

Romano, R.A., Ortt, K., Birkaya, B., Smalley, K., and Sinha, S. (2009). An active role of the DeltaN isoform of p63 in regulating basal keratin genes K5 and K14 and directing epidermal cell fate. PLoS ONE *4*, e5623.

Rouzier, R., Perou, C.M., Symmans, W.F., Ibrahim, N., Cristofanilli, M., Anderson, K., Hess, K.R., Stec, J., Ayers, M., Wagner, P., et al. (2005). Breast cancer molecular subtypes respond differently to preoperative chemotherapy. Clinical cancer research: an official journal of the American Association for Cancer Research *11*, 5678–5685.

Sanchez-Carbayo, M., Socci, N.D., Lozano, J., Saint, F., and Cordon-Cardo, C. (2006). Defining molecular profiles of poor outcome in patients with invasive bladder cancer using oligonucleotide microarrays. Journal of clinical oncology: official journal of the American Society of Clinical Oncology *24*, 778–789.

Shah, J.B., McConkey, D.J., and Dinney, C.P. (2011). New strategies in muscle-invasive bladder cancer: on the road to personalized medicine. Clinical cancer research: an official journal of the American Association for Cancer Research *17*, 2608–2612.

Shen, S.S., Smith, C.L., Hsieh, J.T., Yu, J., Kim, I.Y., Jian, W., Sonpavde, G., Ayala, G.E., Younes, M., and Lerner, S.P. (2006). Expression of estrogen receptors-alpha and -beta in bladder cancer cell lines and human bladder tumor tissue. Cancer *106*, 2610–2616.

Sjodahl, G., Lauss, M., Lovgren, K., Chebil, G., Gudjonsson, S., Veerla, S., Patschan, O., Aine, M., Ferno, M., Ringner, M., et al. (2012). A molecular taxonomy for urothelial carcinoma. Clinical cancer research: an official journal of the American Association for Cancer Research *18*, 3377–3386.

Sørlie, T., Perou, C.M., Tibshirani, R., Aas, T., Geisler, S., Johnsen, H., Hastie, T., Eisen, M.B., van de Rijn, M., Jeffrey, S.S., et al. (2001). Gene expression patterns of breast carcinomas distinguish tumor subclasses with clinical implications. Proc. Natl. Acad. Sci. USA *98*, 10869–10874.

Svatek, R.S., Shariat, S.F., Novara, G., Skinner, E.C., Fradet, Y., Bastian, P.J., Kamat, A.M., Kassouf, W., Karakiewicz, P.I., Fritsche, H.M., et al. (2011). Discrepancy between clinical and pathological stage: external validation of the impact on prognosis in an international radical cystectomy cohort. BJU Int. *107*, 898–904.

Tsai, W.W., Wang, Z., Yiu, T.T., Akdemir, K.C., Xia, W., Winter, S., Tsai, C.Y., Shi, X., Schwarzer, D., Plunkett, W., et al. (2010). TRIM24 links a non-canonical histone signature to breast cancer. Nature *468*, 927–932.

Cancer Cell
Article

A Peptide Mimicking VGLL4 Function Acts as a YAP Antagonist Therapy against Gastric Cancer

Shi Jiao,[1,3] Huizhen Wang,[1,3] Zhubing Shi,[1,3] Aimei Dong,[2] Wenjing Zhang,[1] Xiaomin Song,[1] Feng He,[1] Yicui Wang,[1] Zhenzhen Zhang,[1] Wenjia Wang,[1] Xin Wang,[1] Tong Guo,[1] Peixue Li,[1] Yun Zhao,[1] Hongbin Ji,[1,*] Lei Zhang,[1,*] and Zhaocai Zhou[1,*]

[1]National Center for Protein Science Shanghai, State Key Laboratory of Cell Biology, Institute of Biochemistry and Cell Biology, Shanghai Institutes for Biological Sciences, Chinese Academy of Sciences, 320 Yue-Yang Road, Shanghai 200031, China
[2]Department of Gastroenterology and Internal Medicine, Nanjing Xiaguan Hospital, Nanjing, Jiangsu 210085, China
[3]These authors contributed equally to this work
*Correspondence: hbji@sibcb.ac.cn (H.J.), rayzhang@sibcb.ac.cn (L.Z.), zczhou@sibcb.ac.cn (Z.Z.)
http://dx.doi.org/10.1016/j.ccr.2014.01.010

SUMMARY

The Hippo pathway has been implicated in suppressing tissue overgrowth and tumor formation by restricting the oncogenic activity of YAP. However, transcriptional regulators that inhibit YAP activity have not been well studied. Here, we uncover clinical importance for VGLL4 in gastric cancer suppression and find that VGLL4 directly competes with YAP for binding TEADs. Importantly, VGLL4's tandem Tondu domains are not only essential but also sufficient for its inhibitory activity toward YAP. A peptide mimicking this function of VGLL4 potently suppressed tumor growth in vitro and in vivo. These findings suggest that disruption of YAP-TEADs interaction by a VGLL4-mimicking peptide may be a promising therapeutic strategy against YAP-driven human cancers.

INTRODUCTION

Hippo pathway controls organ size in diverse species from *Drosophila* to human. This pathway features a central kinase cascade formed by Hippo (Hpo; MST1/2 in mammals) and Warts (Wts; LATS1/2 in mammals) (Huang et al., 2005), whose activations lead to phosphorylation of the downstream transcriptional coactivator Yorkie (Yki; YAP/TAZ in mammals), thus preventing its interaction with and therefore transactivation of the DNA-binding transcriptional factor Scalloped (Sd; TEADs/TEF in mammals) (Goulev et al., 2008; Wu et al., 2008; Zhang et al., 2008; Zhao et al., 2008). Inactivation of the Hippo signaling leads to proproliferation and anti-apoptosis associated with increased cancer risk (Halder and Johnson, 2011; Harvey and Tapon, 2007; Pan, 2010; Zeng and Hong, 2008; Zhao et al., 2010).

As a downstream effector, YAP plays a key role in Hippo pathway to control cell proliferation. Despite a possible suppressor function in some circumstances (Barry et al., 2013), YAP was mostly reported as an oncoprotein and its elevated expression and nuclear localization have been frequently observed in human cancers (i.e., lung cancers, liver cancers, colon cancers, pancreatic cancer, and breast cancers) (Avruch et al., 2012; Cui et al., 2012; Hergovich, 2012; Pan, 2010; Steinhardt et al., 2008; Zender et al., 2006; Zhang et al., 2011; Zhao et al., 2007). The role of YAP as a promising and important therapeutic target has been increasingly recognized. However, research regarding specific YAP inhibitors and their potential therapeutic use in treating cancers remains very limited with only a few reports so far confined to small-molecule inhibitors (Liu-Chittenden et al., 2012).

As a transcriptional coactivator, YAP does not contain any DNA-binding domain but functions through interaction with TEADs, whereby inducing expression of target genes promoting cell proliferation as well as inhibiting apoptosis. Similar to YAP, the mammalian Vestigial-like proteins VGLL1-4 do not contain DNA-binding domain and they also exert their transcriptional

Significance

As an emerging significant player in tumorigenesis, the Hippo pathway has attracted increasing attention for the development of new anticancer drugs. In contrast to targeting upstream regulators such as MST1/2 and LATS, inhibition of YAP, the ultimate downstream effector of Hippo signaling, may provide a more effective and direct way to redress the Hippo pathway. Our findings that VGLL4 is a natural antagonist of YAP, and its TDU region is sufficient for YAP inhibition, allowed for the development of a peptide-based YAP inhibitor. This peptide potently suppresses gastric tumor growth, providing an opportunity for treating gastric cancer that currently lacks effective treatment options. The therapeutic strategy may also be extended to other cancer types driven by hyperactive YAP.

regulatory functions through pairing with TEADs via their Tondu (TDU) domain(s). Specifically, VGLL1-3 proteins share one conserved TDU domain at their N-terminal regions, while VGLL4 has two partially conserved TDU domains at its C terminus (Chen et al., 2004; Maeda et al., 2002; Pobbati et al., 2012; Vaudin et al., 1999). Most studies to date have identified VGLL1-3 as TEADs-related transcriptional coactivators (Faucheux et al., 2010; Günther et al., 2004; Halperin et al., 2013; Maeda et al., 2002). The function of VGLL4 has not been clearly defined, however, although it has been suggested as a candidate tumor suppressor in pancreatic adenocarcinoma (Mann et al., 2012). Recently, we and others have identified VGLL4 in *Drosophila* and human as a transcriptional repressor that inhibits YAP-induced overgrowth and tumorigenesis (Guo et al., 2013; Koontz et al., 2013; Zhang et al., 2014). However, the possible role of VGLL4 in human gastric cancer (GC) has not been defined, and the potential therapeutic application of VGLL4 remains unknown.

Human GC is characteristic of poor prognosis and high death rate, making it the second most common cause of cancer-related death worldwide. Therefore, there is a great need to identify new prognostic markers as well as develop novel therapeutic strategies in GC treatment. In this work, we set out to investigate the clinical relevance of VGLL4 and its regulatory function and mechanism in Hippo pathway, aiming to discover and design a peptide drug candidate against gastric cancer.

RESULTS

VGLL4 Is a Potential Tumor Suppressor in Human Gastric Cancer

To explore a potential role of VGLL4 in gastric tumorigenesis, we first examined its mRNA levels in 84 human gastric tumor clinical specimens. Univariate analysis indicated that the mRNA levels of *VGLL4* were downregulated in 51 out of 84 (61%) GC samples ($p < 0.0087$) (Figure 1A). We collected and preprocessed patients' data by extracting nine available clinical factors in three categories, i.e., the clinical background (age, gender), immunohistochemistry data (Lauren's classification, tumor differentiation, lymphatic invasion), and the cancer's stage information (tumor size, lymph node metastasis, distant metastasis, tumor stage) (Table 1). Considering the important role of *Helicobacter pylori* infection in gastric tumorigenesis, we also included *H. pylori* infectious status for patient analysis. These data indicated that aberrant levels of *VGLL4* mRNA were inversely correlated not only with tumor size and tumor stage, but also with lymphatic invasion and lymph node metastasis. Downregulation of *VGLL4* was found in 5 of 14 grade I (35.7%), 10 of 19 grade II (52.6%), 16 of 26 grade III (61.5%), and 20 of 25 grade IV (80%) ($p = 0.044$) GC samples. Consistent with our observations at mRNA level, VGLL4 expression at protein level also showed an inverse correlation with GC progression (Figure 1B and Figure S1A available online). Semiquantitative immunoblot analysis undertaken for 24 pairs of gastric tumor samples showed that protein levels of VGLL4 in grades I and II were much higher than those in grades III and IV ($p = 0.026$). To further determine the potential association of VGLL4 expression with clinical outcomes, we performed immunohistochemical (IHC) staining of VGLL4 on tissue microarrays containing 91 GC specimens that have a long-term clinical follow-up record (four lost to follow-up). VGLL4 staining was significantly associated with tumor size, lymph node metastasis, and TNM stage ($p < 0.05$), but not significantly correlated to age, gender, and tumor metabasis (Table S1). The positive rates of VGLL4 in both dysplasia (abnormal growth of gastric mucosa) and GC samples were significantly lower than that in normal tissues ($p < 0.05$) (Figure 1C). Subsequent Kaplan-Meier survival analysis showed that expression levels of VGLL4 were inversely correlated with 5 year survival rate of GC patients ($p = 0.0416$) (Figure 1D). Together, these results suggested that VGLL4 is a potential tumor suppressor as well as an independent prognostic marker for overall survival of GC patients (relative risk: 0.2110, 95% confidence interval [CI]: 0.1932–0.6315, $p = 0.0215$) (Table S2).

Previously, it has been reported that increased *YAP* mRNA levels in GC samples are correlated with lymphatic metastasis and tumor TNM stage (Zhou et al., 2013). In our study, we found that *YAP* mRNA levels were not only associated with tumor size, differentiation, and stage, but also with *H. pylori* infectious status ($p < 0.05$) (Table S3). *YAP*-positive rates in GC and dysplasia were much higher than that in normal tissues ($p < 0.01$) (Figure S1B). Consistently, the protein levels of YAP also tend to increase in higher tumor grade (Figure S1A). Notably, we found that the average ratio of *YAP* to *VGLL4* at mRNA levels in higher grade tumor samples is significantly higher than in lower grade tumor samples ($p < 0.05$) (Table S4). Moreover, the *YAP*/*VGLL4* ratio at mRNA level is strongly correlated with GC clinical factors including lymphatic invasion, tumor size, TNM stage, and *H. pylori* infectious status (Table S5). Consistently, the average ratio of YAP to VGLL4 at protein levels increases from 2.7 ± 0.4 in tumor tissues of stage I to 9.1 ± 1.6 in GC samples of stage IV (Table S3). IHC analysis showed that among YAP-positive GC patients, those with VGLL4-positive expression have a better clinical outcome (survival time: 39 months) when compared with VGLL4 negative expression (survival time: 16 months) (Figure 1D). Taken together, these results indicate that YAP/VGLL4 ratio could be considered as an important clinical factor for GC classification and diagnosis.

Overexpression of YAP target genes *CTGF*, *CYR61*, and *CDX2* have been suggested to correlate with GC progression (Da et al., 2009; Jacobson and Cunningham, 2012; Jiang et al., 2011; Kang et al., 2011; Lin et al., 2005; Maeta et al., 2007; Zhao et al., 2011; Zhou et al., 2013). Consistent with these reports, we observed an elevated expression of *YAP* (Figure S1C) and its target genes *CTGF* and *CYR61* in GC tissues than those in paired control tissues (Figure 1E). In our experiment, upregulation of *CDX2* was not statistically significant, despite of their increasing tendency (Figure 1E). Importantly, we found that downregulation of *VGLL4* mRNA was correlated with upregulation of YAP target genes *CTGF*, *CYR61*, and *CDX2* (Figure 1F). Moreover, hierarchical cluster analysis showed that during the early stage of GC (stage I and II), mRNA levels of YAP target genes *CTGF* and *CYR61* in high *VGLL4* expression group was obviously lower than those in normal and low *VGLL4* expression group (Figure S1D). Further tumor stage analysis found that *VGLL4* expression in high tumor stage was lower than that in low tumor stage, while the expressions of *CTGF* and *YAP* were significantly upregulated along tumor progression (Figure S1E). Patients with higher *YAP*/*VGLL4* ratio also have higher expressions of YAP target genes *CTGF*, *CYR61*, and *CDX2* (Figure S1F). Together,

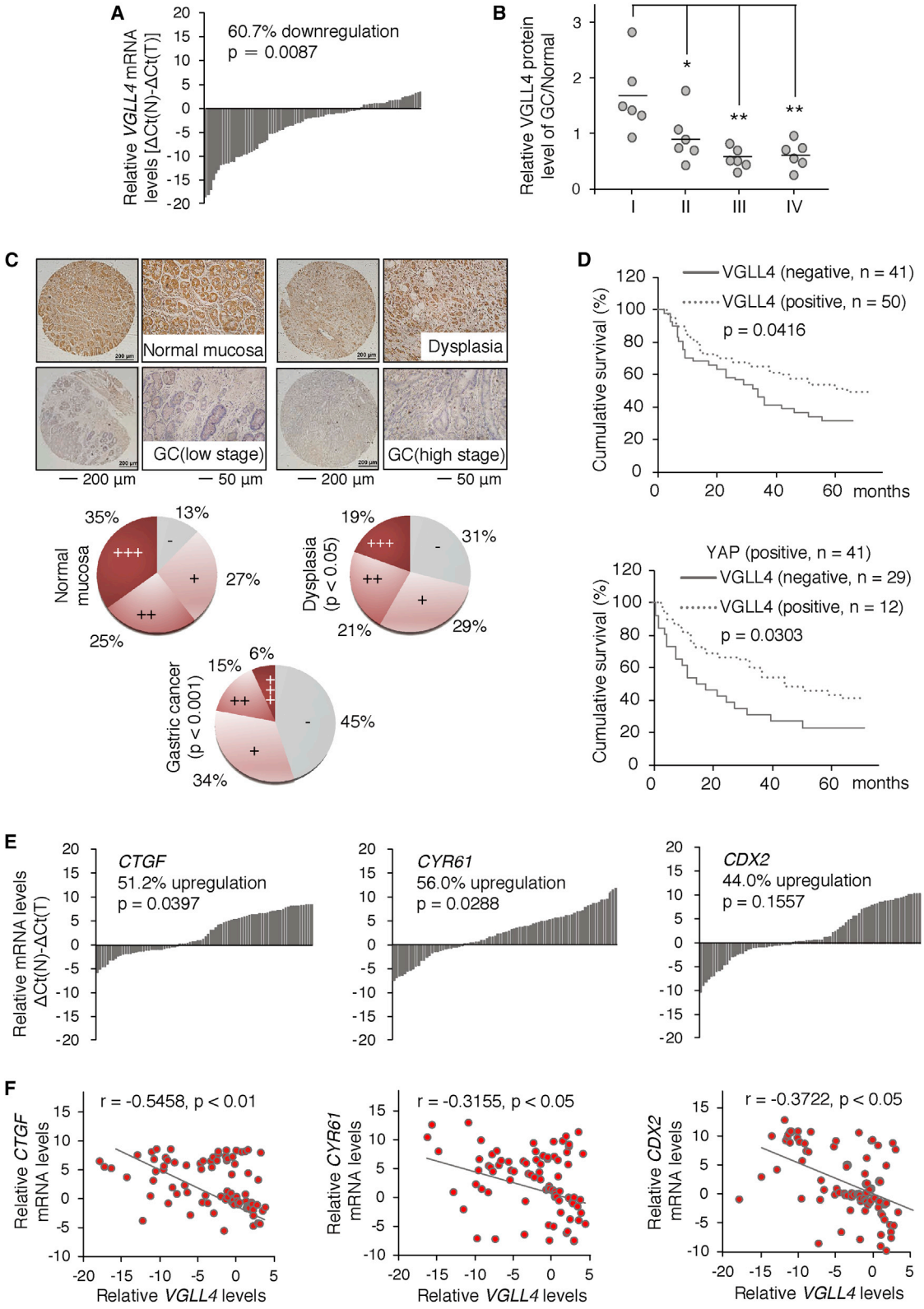

Figure 1. Downregulation of *VGLL4* Was Associated with Upregulation of YAP Target Genes and GC Prognosis

(A) *VGLL4* mRNA levels in GC. mRNA levels of *VGLL4* in 84 paired human GC and normal tissues were examined by real-time PCR, using *GAPDH* as an internal control. Bar value (ΔCt(N)-ΔCt(T)) represents the difference of *VGLL4* mRNA levels between normal tissue and tumor. Bar value > 1 indicates that *VGLL4* mRNA

(legend continued on next page)

these results indicated that VGLL4 may affect YAP-TEADs transcriptional activity in GC.

VGLL4 Suppresses GC Growth in Vitro by Targeting YAP-TEADs

To confirm a biological role of VGLL4 in GC, we first checked the effect of VGLL4 on the growth of several GC cell lines with different differentiation states including BGC-823, HGC-27, MGC-803, and MKN-45. First, we analyzed the expression profiles of YAP and VGLL4, as well as YAP/VGLL4 protein ratio in these cells (Figure S2A). Except MKN-45, all other three GC cell lines appear to have increased YAP levels and decreased VGLL4 levels. As a result, the YAP/VGLL4 ratios are much higher in BGC-823, HGC-27, and MGC-803 cells than those in MKN-45 and HEK293 cells. Next, we found that overexpression of VGLL4 in MGC-803 cells (YAP/VGLL4 ratio: 3.6) not only induced apoptosis, but also inhibited cell viability on plate and anchorage-independent cell growth in soft agar (Figures 2A–2C). To examine whether VGLL4's function is related to a potential inhibition against YAP-TEADs transcriptional activity, we performed TEAD4 reporter assay and analyzed downstream target genes' expression. As shown in Figures 2D and 2E, both TEAD4 reporter activity and expressions of YAP-TEADs target genes *CTGF*, *CYR61*, and *CDX2* were reduced upon transfection of VGLL4 in MGC-803 cells. Similar results were observed for BGC-823 (YAP/VGLL4 ratio: 2.2) and HGC-27 (YAP/VGLL4 ratio: 4.0) cells (Figures S2B–S2F). By contrast, overexpression of VGLL4 in MKN-45 cells (YAP/VGLL4 ratio: 0.1) did not significantly promote apoptosis or inhibit cell growth and colony formation (Figures S2B–S2D). Meanwhile, TEAD4 reporter activity and the target genes' expression were not significantly altered either in MKN-45 cells (Figures S2E and S2F).

Next, we depleted endogenous VGLL4 by special short hairpin RNA (shRNA) targeting its 5′-UTR. Our results showed that knockdown of VGLL4 in BGC-823, MGC-803, and HGC-27 promoted cell growth and enhanced both TEAD4 reporter activity and target genes' expression (Figures 2F–2H and S2G–S2I). Such effects could be rescued by transfection of VGLL4 back into these cells (Figures 2G and S2H). By contrast, the viability, TEAD4 *trans*-activity, and downstream target genes' expression were not significantly altered by knockdown of VGLL4 in MKN-45 cells (Figures S2G–S2I). Taken together, these results indicated that VGLL4 inhibits GC growth in vitro in a way related to cellular YAP/VGLL4 ratio, and importantly, VGLL4 functions through targeting YAP-TEADs transcriptional activity.

To assess the functional importance of the potential TEADs-binding domain of VGLL4, namely the tandem TDU domains, we generated several deletion mutants of VGLL4 (Figure 2I). Our results showed that deletion of the tandem TDU domains of VGLL4 totally abrogated its inhibitory effect on cell growth (Figure 2J). Moreover, deletion of the first TDU domain (TDU1) only moderately impaired VGLL4's inhibition of cell growth, while deletion of the second TDU domain (TDU2) almost completely abolished such function. Consistently, clonogenic assays showed that introduction of wild-type VGLL4, but not the TDU-deletion mutants inhibited clonogenicity of MGC-803 cells in a dose-dependent manner at both basal and YAP-induced levels (Figure 2K). Meanwhile, deletion of VGLL4 TDU1, TDU2 or the whole tandem TDU region impaired or abolished its inhibitory activity toward YAP-induced TEAD4 reporter activity (Figure 2L). Moreover, VGLL4 TDU deletion mutants failed to inhibit YAP-induced *CDX2* expression (Figure 2M). Taken together, these results indicated that the tandem TDU region, especially TDU2, is functionally essential for VGLL4.

Structural Study Identified Key Residues for VGLL4-TEAD4 Complex Formation

Given the importance of the tandem TDU domains for VGLL4 function, we performed a structural study of the VGLL4-TEAD4 complex. As shown by gel filtration and dynamic light scattering assays, the tandem TDU region of VGLL4 directly interacts with the YAP-binding domain (YBD) of TEAD4 and form a stable complex with a molar ratio of 1:2 (Figures S3A and S3B). We then determined the crystal structure of mouse VGLL4 tandem TDU region in complex with the YBD domain of mouse TEAD4 (Table S6). Consistent with our solution studies, each TDU domain of VGLL4 binds one molecule of TEAD4 (Figures 3A, S3C, and S3D). TDU1 is composed of only one α helix (helix α1), while TDU2 consists of a β strand followed by two short α helices (helices α2 and α3) packed against each other (Figures 3A–3C). Due to its highly extended conformation of the tandem TDUs, the two bound TEAD4 molecules (assigned as A and B) do not contact with each other. Thus, TDU1 and TDU2 appear to function as individual binding units for separate TEADs molecules.

Next, we investigated the details of the VGLL4-TEAD4 complex interface, which is dominated by hydrophobic interactions. Residues V206, H209, F210, R212, and L214 of TDU1 form a hydrophobic core with F330, Y362, F366, K369, L370, L373, M378, and V382 of the TEAD4 molecule A (Figure 3B). A total surface area of 588 $Å^2$ is buried upon TDU1 binding with TEAD4. On the other hand, residues V235, H237, F238, K240, and L242 of TDU2 form a hydrophobic core with TEAD4 molecule B (Figure 3C). In addition, residues W246 and I249 from the extra helix (α3) of TDU2 form additional hydrophobic interactions with

level is increased in tumors. Bar value < −1 indicates that *VGLL4* mRNA level is decreased in tumors. Paired t test (univariate) was used to compare the difference of normal group and cancer group.

(B) VGLL4 protein levels at different tumor grades of GC. VGLL4 expression in GC tissues from 24 patients and paired normal tissues were analyzed by immunoblotting with specific antibodies and plotted as indicated. The horizontal lines in the scatter plot represent group medians. Student's t tests were performed to compare the variation between stage I and other tumor stages. *Versus stage I, $p < 0.05$; **$p < 0.01$.

(C) Representative cores of VGLL4 staining on tissue microarray.

(D) Kaplan-Meier survival curves of overall patients (left) and YAP-positive patients (right) based on VGLL4 expression. Survival analysis was performed using log-rank test.

(E) Relative mRNA levels of YAP target genes *CTGF* (left), *CYR61* (middle), and *CDX2* (right) in GC analyzed by using paired t test.

(F) Scatter plot between *VGLL4* and YAP target genes in GC. Relative mRNA levels of *VGLL4* were compared with those of YAP target genes *CTGF* (left), *CYR61* (middle), and *CDX2* (right) by Spearman's correlation.

See also Figure S1 and Tables S1–S5.

Table 1. Downregulation of VGLL4 Correlates with Gastric Cancer Progression

	VGLL4 mRNA				
Groups	Nondecreased	Decreased	n	Decreased (%)	p Value (Fisher's Test)
Age (years)					
<60	15	22	37	59.4	1.0000
≥60	18	29	47	61.7	
Gender					
Male	18	32	50	68.0	0.5002
Female	15	19	34	55.0	
Helicobacter pylori					
Positive	14	31	45	62.1	0.1201
Negative	19	20	39	51.2	
Lauren					
Intestinal	25	41	66	66.1	0.7860
Nonintestinal	8	10	18	55.6	
Differentiation					
Low	21	29	50	58.0	0.6502
Moderate or high	12	22	34	64.7	
Lymphatic invasion					
Ly0-1	14	10	24	45.4	0.0287[a]
Ly2-3	19	41	60	66.3	
Tumor size					
pT1 + pT2 (≤5 cm)	11	6	17	35.3	0.0251[a]
pT3 (>5 cm) + pT4	22	45	67	67.2	
Lymph node metastasis					
N0 + N1	19	15	34	44.1	0.0130[a]
N2 + N3	14	36	50	72.0	
Distant metastasis					
M0	29	45	74	60.1	1.0000
M1	4	6	10	60.0	
Tumor stage					
Stage I + stage II	18	15	33	45.4	0.0247[a]
Stage III + stage IV	15	36	51	70.6	
Total	**33**	**51**	**84**		

Fisher's exact test was used to test the association between two categorical variables.
[a]Represents statistically significant, $p < 0.05$.

TEAD4. Besides the two short helices, the β strand of the TDU2 forms an intermolecular β sheet with TEAD4 (Figures 3A, S3D, and S3E). The total interface area between TDU2 and TEAD4 is up to 1,048 Å^2, suggesting that TDU2 has much stronger interaction with TEAD4 when compared with TDU1.

According to the structural analysis, we designed a series of mutations based on human VGLL4 and TEAD4 to probe and disturb the complex interface (Figure S3F). In vitro biolayer interferometry (BLI) and pull-down assays were subsequently performed to assess the importance of individual amino acids on the interface (Figures 3D and 3E). In agreement with the structural analysis, we found that the overall contribution of TDU2 is much larger than that of TDU1 during complex formation with TEAD4. Specifically, mutations of V209A, H212A, F213A, R215A, L217A, and H212A/F213A targeting TDU1 did not significantly affect VGLL4-TEAD4 interactions. However, mutations of H240A and H240A/F241A targeting TDU2, or H212A/F213A/H240A/F241A (HF4A) targeting both TDUs dramatically decreased VGLL4-TEAD4 complex formation. Moreover, substitution of the β strand of TDU2 with poly-Glycine only slightly decreased VGLL4's binding to TEAD4 (Figures 3D and 3E), suggesting that this β strand is not essential but may help for VGLL4-TEAD4 interaction. We then used H212A/F213A, H240A/F241A, and HF4A as representative mutants for further studies (Figure 3F) and confirmed their effects by coimmunoprecipitation (coIP) analysis (Figure 3G).

VGLL4 Functions through Competing with YAP for TEAD4 Binding

Structural comparison of VGLL4-TEAD4 with YAP-TEAD4 and VGLL1-TEAD4 suggested that VGLL4 and YAP have partially overlapped binding sites on TEADs, thus probably acting as an inhibitor of each other in terms of binding TEADs (see Supplemental Experimental Procedures and Figures S3F–S3H). To further validate that VGLL4 functions through a direct competition with YAP for TEAD4 binding, we examined whether the mutations disrupting VGLL4-TEAD4 interaction will affect VGLL4 function. As shown in Figure 4A, mutation H212A/F213A in TDU1 slightly blocked the inhibitory effect of VGLL4 on YAP-induced TEAD4 reporter activity, while, strikingly, mutation H240A/F241A in TDU2 almost completely abolished this repression effect, suggesting that TDU2 with a tighter binding to TEAD4 also possesses higher inhibitory activity toward YAP. Similarly, cells transfected with VGLL4 mutant HF4A displayed high TEAD4 reporter activity as did the empty vector. Consistent with the luciferase assay, VGLL4 mutant H212A/F213A only partially impaired its inhibitory function on YAP-induced *CDX2* expression, while mutants H240A/F241A and HF4A completely blocked VGLL4's inhibition on YAP-induced target gene expression (Figure 4B). Moreover, VGLL4 mutant H212A/F213A showed partially reduced inhibitory effect on YAP-induced cell proliferation and colony formation in soft agar, while VGLL4 mutants H240A/F241A and HF4A almost completely lost the inhibitory activity (Figures 4C and 4D), again indicating that VGLL4's binding to TEAD4 is required for its repressor function.

Next, we dissected the interplay between VGLL4, YAP, and TEAD4 using purified recombinant proteins. As shown by pull-down assay in Figure 4E, YAP readily competes with VGLL4 tandem TDUs for TEAD4 binding in a dose-dependent manner. On the other hand, VGLL4 tandem TDUs also competes with YAP for TEAD4 binding, although higher concentration of VGLL4 is required (Figure 4E). However, VGLL4 mutants defective in TEAD4 binding could not compete with YAP (Figure 4F). We then quantified the binding affinities between TEAD4 and YAP/VGLL4 using BLI assay (Figure 4G). Consistently, the binding affinity between TEAD4 and YAP (K_d = 2.1 nM) is higher than that between TEAD4 and VGLL4 (K_d = 6.8 nM), suggesting that higher concentration of VGLL4 would be required to compete with YAP for TEADs binding.

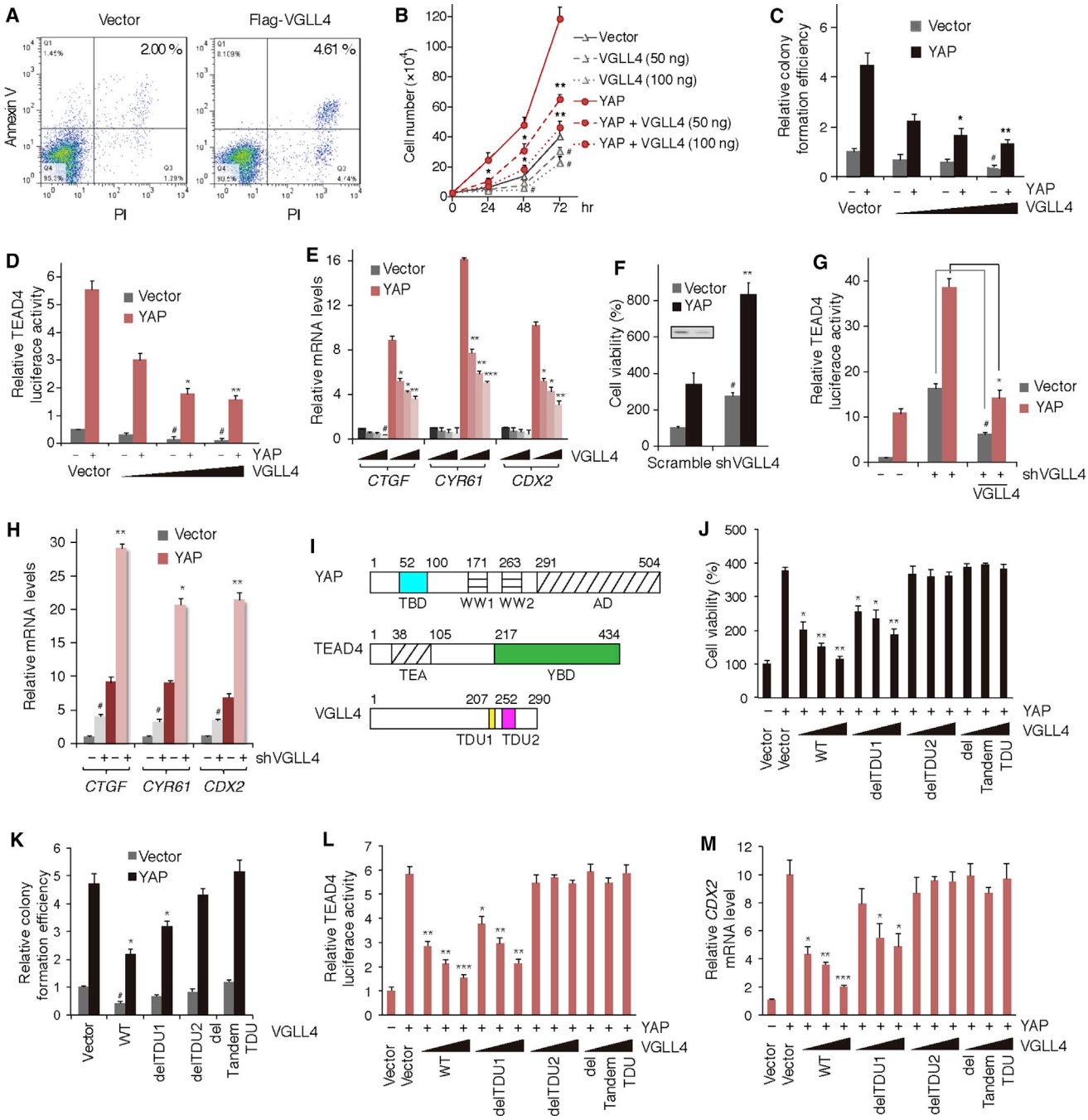

Figure 2. VGLL4 Inhibits Gastric Tumor Cell Growth through Inhibiting YAP-Induced TEAD4 Transactivation

(A) Apoptosis rate in human gastric cancer cell line MGC-803 transfected with VGLL4.

(B–E) Cell viability (B), colony formation (C), TEAD4-relative luciferase activity (D), and YAP target genes levels (E) in MGC-803 cells after transfection with VGLL4 in the absence or presence of YAP.

(F) Cell viability in MGC-803 cells transfected with scramble or shVGLL4 in the absence or presence of YAP.

(G) Rescue assay of VGLL4 on TEAD4-relative luciferase activity in cells after treatment with shVGLL4 targeting its 5′ UTR sequence.

(H) Transcriptional levels of YAP target genes in cells after VGLL4 knockdown.

(I) Schematic illustration of the domain organization for human YAP, TEAD4, and VGLL4. Amino acid numbering is according to human YAP1, TEAD4, and VGLL4.

(J–M) Cell growth (J), colony formation (K), TEAD4 luciferase activity (L), and *CDX2* mRNA levels (M) in MGC-803 cells after transfection with different deletions of VGLL4 tandem TDU sequence in the absence or presence of YAP.

Data were expressed as means ± SD. ANOVA and Student's t test were used; n = 3. #Versus vector-transfected group, $p < 0.05$; *versus YAP-transfected group, $p < 0.05$; ***$p < 0.01$; ***$p < 0.001$. WT represents full-length wild-type VGLL4. delTDU1, delTDU2, and del tandem TDU represent VGLL4 constructs in which TDU1, TDU2, and the whole tandem TDU region were deleted, respectively.

See also Figure S2.

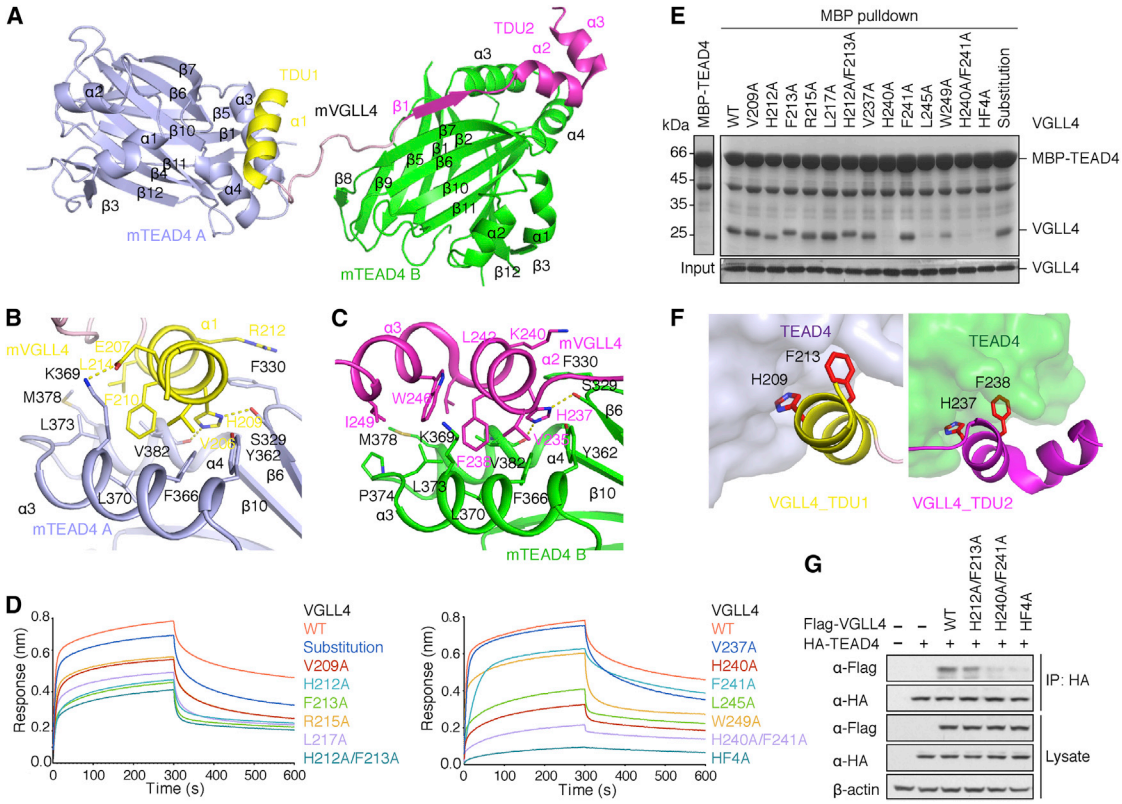

Figure 3. Crystal Structure of VGLL4-TEAD4 Complex

(A) Overall structure of the mouse VGLL4-TEAD4 complex. VGLL4 TDU1 and TDU2 are colored yellow and purple, respectively. One VGLL4 molecule interacts with two TEAD4 molecules with TDU1 bound to TEAD4 A (green) and TDU2 bound to TEAD4 B (blue), respectively.

(B and C) Detailed interface between TEAD4 and TDU1 (B) or TDU2 (C) domains of mouse VGLL4.

(D) BLI analysis of interactions between TEAD4 and various VGLL4 mutants. Colored curves are the experimental traces of BLI experiments for mutations in TDU1 (left) and TDU2 (right), respectively.

(E) Pull-down analysis between TEAD4 and various VGLL4 mutants.

(F) Critical residues in TDU1 and TDU2 for TEAD4 binding.

(G) CoIP between TEAD4 and various VGLL4 mutants.

Substitution represents a VGLL4 construct in which the linker between TDU1 and TDU2 was substituted by a polyglycine linker. All amino acids are numbered according to human VGLL4 except in (A)–(C). HF4A represents VGLL4 mutation H212A/F213A/H240A/F241A.

See also Figure S3 and Table S6.

Taken together, these results clearly demonstrated that VGLL4 and YAP compete with each other for TEADs binding, and thus a ratio between their local concentrations may dictate the function of TEADs as either transcriptional activator or repressor.

TDU Domains Alone Are Sufficient for VGLL4 Function of Inhibiting YAP

We then investigated whether the tandem TDU region alone could be fully competent toward YAP inhibition as is the full-length VGLL4. As shown in Figures 4H and 4I, all the fragments including TDU1, TDU2, and tandem TDU, exerted inhibitory effects on YAP-induced TEAD4 reporter activity, although to different extents. Moreover, TDU2 exhibited a stronger inhibitory activity than TDU1 when used alone, whereas TDU1 and TDU2 mutants with disabled TEAD4-binding showed impaired inhibitory effects on YAP-induced TEAD4 reporter activity. Notably, when compared with the full-length VGLL4, the tandem TDU region alone was fully functional in terms of inhibiting YAP-induced TEAD4 reporter activity. These observations were further confirmed on the levels of YAP-induced *CDX2* expression (Figure 4J), as well as proliferation and colony formation of MGC-803 cells (Figures 4K and 4L). These results demonstrated that the tandem TDU domains of VGLL4, especially TDU2, are not only essential but also sufficient for VGLL4 in inhibiting YAP function, corroborating the conclusion that VGLL4 functions as a competitive inhibitor of YAP.

A Rationally Designed Peptide "Super-TDU" Potently Inhibits GC Growth

Based on our findings that (1) the TDU region of VGLL4 is sufficient for inhibiting YAP activity, and (2) the most important binding sites for VGLL4 and YAP do not overlap on TEAD4, we designed an inhibitor peptide termed "Super-TDU" targeting YAP-TEADs interaction for therapeutic purpose (Figure 5A). As shown by coIP experiment, the Super-TDU reduced endogenous interaction between YAP and TEADs (Figure 5B). As predicted, the Super-TDU inhibited cell viability and colony

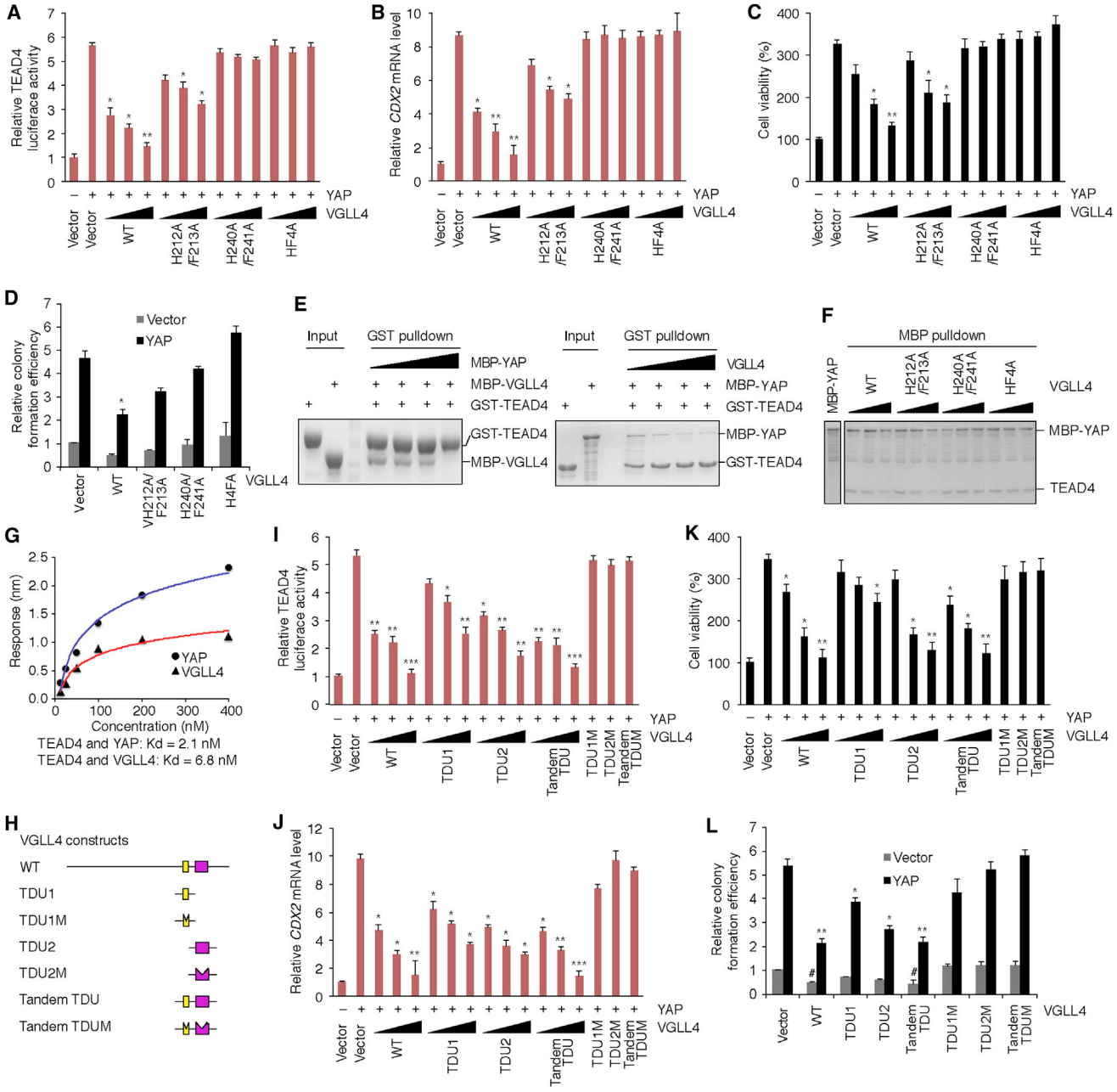

Figure 4. The Tandem TDU Domains of VGLL4 Are Sufficient to Inhibit YAP Activity

(A–D) The functional consequences of mutations H212A/F213A, H240A/F241A, and HF4A were evaluated in the context of full-length VGLL4 by TEAD4 luciferase assay (A), *CDX2* mRNA levels (B), cell viability (C), and clonogenic assay in soft agar (D).

(E) Pull-down assays to detect the effect of YAP (left) or VGLL4 (right) on the interaction between TEAD4 and VGLL4 or YAP, respectively.

(F) Competitive pull-down assay to detect the effect of VGLL4 mutants on YAPs binding to TEAD4.

(G) Binding affinities between TEAD4 and VGLL4/ YAP were determined by BLI experiment.

(H) Diagram of VGLL4 constructs used for functional evaluation.

(I–L) The individual TDU domains or the tandem TDU region of VGLL4, as well as their mutants were evaluated by TEAD4 reporter assay (I), target gene expression (J), cell viability (K), and clonogenic assay (L).

Bar graphs represent means ± SD. ANOVA and Student's t test were used; n = 3. #Versus vector-transfected group, $p < 0.05$. *Versus YAP-transfected group, $p < 0.05$; **$p < 0.01$; ***$p < 0.001$. TDU1, TDU2, and tandem TDU represent individual or tandem TDUs alone, respectively.

formation of GC cell lines MGC-803, BGC-823, and HGC27, but not MKN-45 (Figures 5C, 5D, and S4A). Moreover, the Super-TDU downregulated expression of YAP-TEADs target genes *CTGF*, *CYR61*, and *CDX2* (Figures 5E and S4B). Further chromatin immunoprecipitation (ChIP) assays also showed that the Super-TDU dose-dependently reduced the amount of *CTGF*

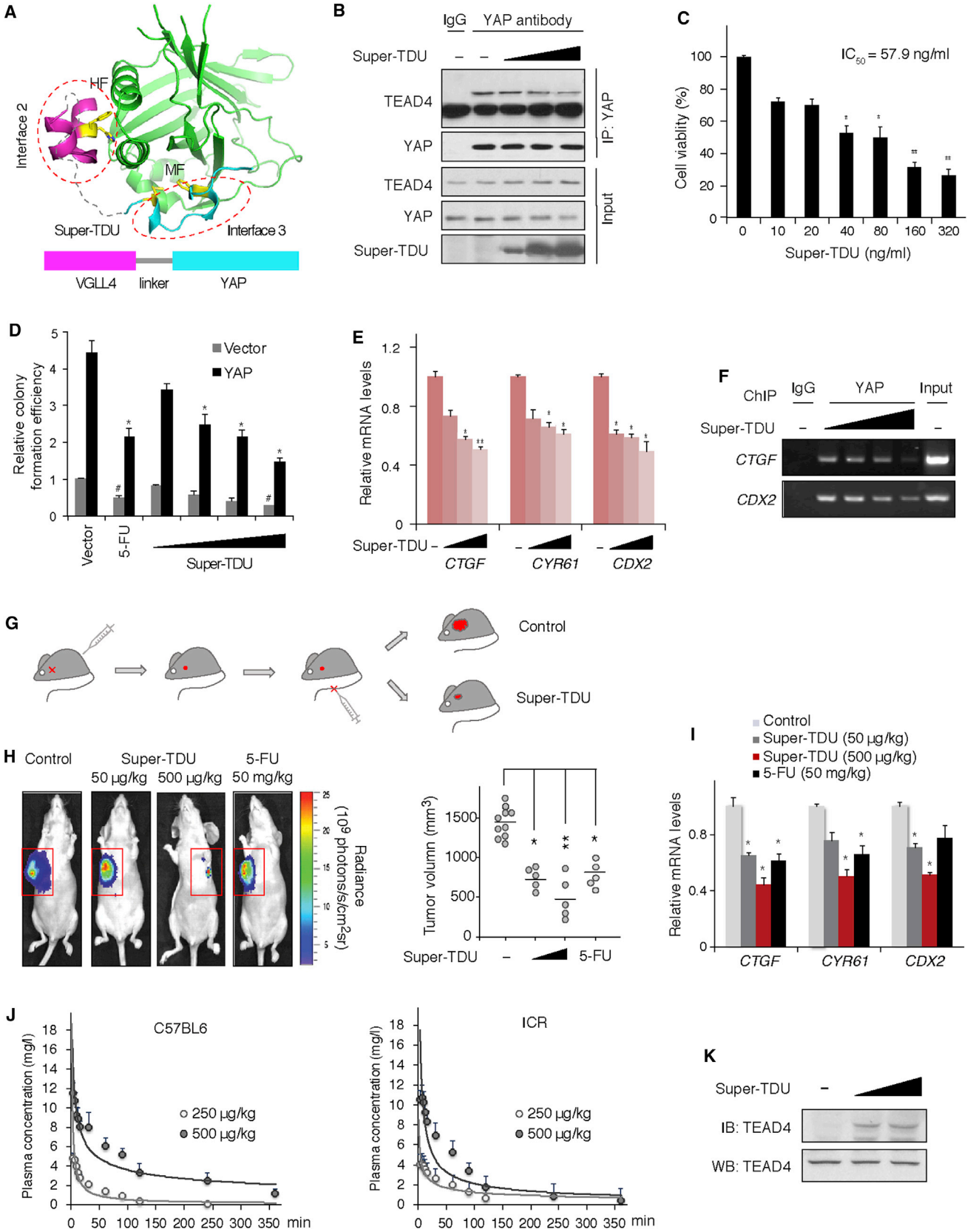

(legend on next page)

and *CDX2* promoter cDNA ChIPed by YAP antibody (Figure 5F). To verify the specificity of the Super-TDU, we created two Super-TDU mutants harboring mutations that disable TEADs binding. As expected, the mutant Super-TDUs failed to interact with TEADs and inhibit cell proliferation (Figures S4C and S4D).

Next, we carried out a preclinical study in which several types of GC cell lines mentioned above were injected into the armpits of BALB/cA nu/nu mice and allowed to form tumors (Figure 5G). Once palpable tumors were detected, pairs of mice were randomized to receive a tail vein injection of either 50 μg/kg (n = 5) or 500 μg/kg (n = 5) per day of the Super-TDU peptide or an irrelevant control peptide (n = 10). In parallel, mice were treated with 50 mg/kg 5-fluorouracil (5-FU), a conventional drug used in GC treatment, intravenously as a positive control (Figure 5H). Consistent with our in vitro observations, not only the sizes and weights of tumors, but also YAP target genes were markedly decreased for the Super-TDU-treated animals in a dose-dependent manner (Figures 5H, 5I, and S4E–S4G).

Pharmacological Evaluation of the Super-TDU

We first determined the acute toxicity of the Super-TDU in ICR mice. Our results in BALB/cA nu/nu mice showed that a dosage of 50 μg/kg Super-TDU was equally effective as 50 mg/kg of 5-FU in terms of reducing tumor mass, tumor volume, and human β2 microglobulin concentration (Figures 5H, S4E, S4G, S4H). However, the Super-TDU exerted no obvious adverse toxic effects in ICR mice at a dosage of 1 mg/kg, while there was a significant decrease of white cell and platelet number in the 5-FU-treated control group (50 mg/kg). The maximum tolerance dose (MTD) of the Super-TDU was >1 mg/kg body weight intravenously in mice (Table S7). We then performed pharmacokinetic analysis of the Super-TDU in ICR and C57BL/6 mice. Representative curves of the Super-TDU concentration versus time were shown in Figure 5J and pharmacokinetic parameters were listed in Table S8 (see Supplemental Experimental Procedures). Moreover, consistent with the downregulation of YAP-TEADs target genes in the Super-TDU-treated mice (Figures 5I and S4F), we found that a biotin-labeled Super-TDU peptide could efficiently pull down the endogenous TEADs, again indicating that the Super-TDU exerts its antitumor activity via directly targeting TEADs (Figure 5K).

Next, we introduced multiple tumor cell lines and evaluated the efficacy of the Super-TDU in these different cellular contexts (Figure S4I; Table S9). The Super-TDU significantly inhibited growth of HeLa, MGC-803, HCT116, A549, and MCF-7 cells, but only marginally inhibited growth of Jurkat and Raji cells, indicating a selectivity of the Super-TDU in inhibiting tumor cell growth. Consistent with our clinical analysis, we found that *YAP*/*VGLL4* ratio correlates well with susceptibility of tumor cells toward the Super-TDU (Figures S4J and S4K). For example, MGC-803 cells (high *YAP*/*VGLL4* ratio) were more susceptible to the Super-TDU than HEK293 cells (low *YAP*/VGLL4 ratio). Thus the Super-TDU may specifically target tumor cells with an elevated YAP/VGLL4 ratio.

Taken together, these results suggested that the Super-TDU is relatively safe and specific as a drug candidate, which may have a broader antitumor activity toward YAP-driven human cancers.

The Super-TDU Inhibits Tumor Growth of Human Primary GC

To further validate the clinical relevance of our findings, we assessed the efficacy of the Super-TDU on primary gastric tumor cells (T1 and T2), which were derived from two individual patients. Paired normal tissue cells (N1 and N2), as well as MGC-803 cells, were used as controls. We found that the cells with a higher ratio of YAP to VGLL4 (sample T1) exhibited an obvious impairment in cell growth and colony formation upon treatment with the Super-TDU, while only a marginal influence was observed for the cells with lower ratio of YAP to VGLL4 (sample T2) (Figures 6A, 6B, S5A, and S5B). By contrast, 5-FU inhibited almost equally the growth and colony formation of all the cells tested (Figures 6B, S5C, and S5D). These observations were further confirmed by tumor formation assay and expression of YAP-TEADs target genes in nude mice (Figures 6C–6E). Taken together, these results indicated a promising therapeutic potential of the Super-TDU in treating GC by directly targeting YAP-TEADs, and importantly, unlike the conventional drug compound 5-FU, its antitumor activity tends to be specific toward tumors with an elevated ratio of YAP to VGLL4.

Figure 5. The Super-TDU Potently Inhibits Gastric Tumor Growth

(A) A structural model of the Super-TDU bound with TEAD4. The purple and cyan regions are derived from VGLL4 and YAP, respectively. Two clusters of residues (HF and MF) critical for TEADs binding are highlighted.

(B) CoIP assay of interactions between TEAD4 and YAP in the presence of the Super-TDU. MGC-803 cells were lysed, and then different doses of the Super-TDU were added into cell lysates. After incubation for 30 min, cell lysates were immunoprecipitated with YAP antibody and analyzed by western blotting.

(C and D) Evaluation of the Super-TDU by ATP cell viability assay (C) and clonogenic assay (D) in MGC-803 cells.

(E) YAP target genes' mRNA levels in MGC-803 cells treated with the Super-TDU.

(F) ChIP assay in MGC-803 cells by YAP antibody in the presence of the Super-TDU.

(G) Flow chart of tumor formation assay in nude mice.

(H) Tumor formation assay to evaluate the effect of the Super-TDU on GC tumor progression. Mice were photographed after sacrifice. Tumors harvested from each mouse were photographed before further processing (left). Tumor volume for each group (eight mice) was plotted (right).

(I) Relative mRNA levels of YAP target genes in samples from (H).

(J) Pharmacokinetic studies of the Super-TDU in different mouse models. Concentration versus time curves of the Super-TDU in C57BL/6 (left) and ICR (right) mice were presented. White and gray circles represent dose levels of 250 and 500 μg/kg, respectively. Results were expressed as means ± SD.

(K) Pull-down of endogenous TEADs by a biotin-labeled Super-TDU in MGC-803 cells.

Bar graphs represent means ± SD. ANOVA and Student's t test were used; n = 3. $^{\#}$Versus vector-transfected group, $p < 0.05$. *Versus YAP-transfected group, $p < 0.05$; **$p < 0.01$.

See also Figure S4 and Tables S7–S9.

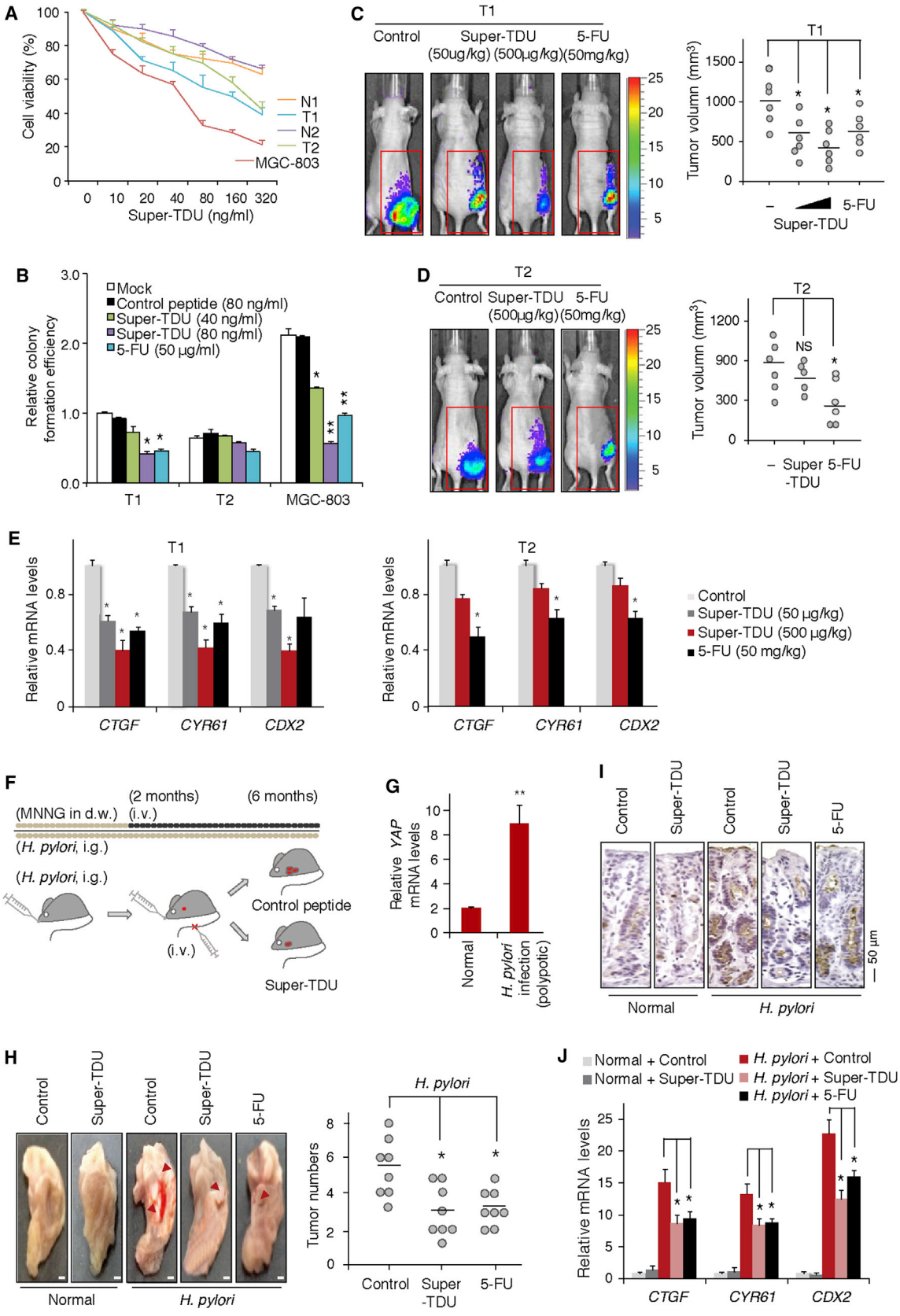

(legend on next page)

The Super-TDU Inhibits GC Tumor Growth in the *H. pylori*-Infected Mouse Model

H. pylori infection is worldwide and once acquired it becomes chronic and probably persists for life if untreated. Multiple lines of evidence demonstrate that *H. pylori* together with cocarcinogens, such as N-methyl-N′-nitro-N-nitrosoguanidine (MNNG), induce gastric carcinogenesis in animals (Danon and Eaton, 1998; Han et al., 2002). Furthermore, previous studies have shown that YAP mRNA levels were increased in mouse mucosa after *H. pylori* infection (Takaishi and Wang, 2007).

To corroborate our observations of the Super-TDU in treating nude mice, we assessed its therapeutic effect in *H. pylori*-infected GC mouse model. Here, we attempted to develop GC mouse models through the administration of *H. pylori* intragastrically with alkylating agent MNNG in drinking water (Figure 6F). C57BL/6 mice were orally gavaged 50 μl of bacterial suspension ($\sim$1 × 10^6 CFU) every day. MNNG (100 mg/ml) was added to the drinking water for a period up to 2 months. After treatment with MNNG, mice were randomized to receive 500 μg/kg per day of the super-TDU (control peptide as negative control, 5-FU as positive control), which persisted for at least 4 months before sacrifice. Consistent with a previous report (Takaishi and Wang, 2007), we found that YAP expression was significantly elevated in *H. pylori*-infected mice (Figure 6G). Tumor numbers in the Super-TDU-treated group displayed a significant decrease, compared with those in the control group, indicating an obvious therapeutic effect of the Super-TDU on gastric carcinogenesis (Figure 6H). These observations were further confirmed by Ki67 IHC staining (Figure 6I). Consistently, we found that expressions of YAP-TEADs target genes (*CTGF*, *CYR61*, and *CDX2*) were downregulated in mice treated with the Super-TDU (Figure 6J). Taken together, these results confirmed our evaluation of the Super-TDU in nude mice, further demonstrating therapeutic potentials of the Super-TDU in treating human cancer with YAP-activation.

DISCUSSION

The Hippo pathway controls multiple cellular processes related to cell proliferation and apoptosis and its dysregulation has been linked to various cancers (Chan et al., 2011; Harvey and Tapon, 2007; Pan, 2010; Steinhardt et al., 2008; Zhao et al., 2010). As a tumor suppressor pathway, therapeutic targeting of the Hippo signaling has recently surfaced (Stanger, 2012; Sudol et al., 2012). Our current work identified the clinical relevance of VGLL4 as a YAP antagonist and found its TDU region is sufficient for inhibiting YAP activity. These findings led to the generation of a peptide-based YAP inhibitor, which exhibits potent antitumor activity against gastric cancer in vitro and in mice.

From a clinical point of view, both YAP and VGLL4 levels should be well confined within a suitable range and thus maintain a concentration balance or ratio to properly control Hippo signaling intensity required for normal development and homeostasis, which, however, may be disrupted under certain disease conditions such as cancers. Consistent with this notion, we found that YAP/VGLL4 ratios in clinical samples were sharply skewed and well correlated with tumor progression in GC. Moreover, we observed an inhibitory effect on a range of different cancer cell lines treated with the Super-TDU, but found that tumor cells with a relatively high YAP/VGLL4 ratio were more susceptible to such treatment. These observations were further confirmed by our clinical study of VGLL4 and therapeutic evaluation of the Super-TDU in colorectal carcinoma (data not shown). Thus the Super-TDU appears to have a broad but specific antitumor activity toward YAP-driven human cancers in which YAP/VGLL4 ratio should be considered as an important prognostic marker for personalized treatment.

The observations that YAP levels, especially in the nucleus, increase specifically under pathological conditions makes it an ideal drug target. Although it has been increasingly revealed that selective inhibition of YAP-induced TEADs transactivation is "a promising and pharmacologically viable strategy" with minimal side effects in treating cancers related to YAP overexpression (Cai et al., 2010; Koontz et al., 2013; Liu-Chittenden et al., 2012), studies regardingYAP inhibitors for therapeutic purposes are still very limited. VGLL4 functions as a physical antagonist of YAP and blocks YAP oncogenic activity at transcriptional level, hence providing a more effective and direct way to correct the consequences caused by excessive YAP.

Our results clearly demonstrated that both VGLL4 and YAP levels were altered in GC samples. Currently, however, the molecular mechanism by which the expressions of YAP and VGLL4 are regulated in cancer remains unknown. There could be multiple pathological reasons accounting for the disruption of YAP-VGLL4 balance. Compared with other pathways correlated with tumorigenesis, DNA mutations are rare in Hippo pathway, while epigenetic silencing of some tumor suppressor

Figure 6. The Super-TDU Inhibits Human Primary GC Growth and GC Tumorigenesis in the *H. pylori*-Infected Mouse Model

(A and B) Evaluation of the Super-TDU by cell viability (A) and colony formation (B) assays in primary gastric cancer cells derived from GC patients. Data are represented as means + SD.

(C and D) Evaluation of the Super-TDU by tumor formation of primary gastric cancer cells T1 (C) and T2 (D) in nude mice.

(E) Relative mRNA levels of YAP target genes in samples from (C) and (D).

(F) Flow chart of treating *H. pylori*-induced GC mice with the Super-TDU. Four-week-old specific-pathogen-free (SPF) C57BL/6-slac mice were used. They were fed sterilized commercial pellet diets and given sterile water ad libitum. A total of 80 mice were reared, including 20 normal controls.

(G) *YAP* mRNA levels in *H. pylori*-infected GC mice.

(H) Pictures of stomach mucosa show gross gastric tumors (left). Arrows indicate adenomas. Average tumor numbers were calculated (right).

(I) Ki-67 staining of adenomas from *H. pylori*-infected GC mice.

(J) Relative mRNA levels of YAP target genes in gastric tissue of *H. pylori*-infected GC mice.

Bar graphs represent means ± SD. ANOVA and Student's t test were used. *Versus control-treated group, $p < 0.05$. NS, no significance. T1 and T2 represent two primary gastric cancer cells; N1 and N2 represent paired control cells.

See also Figure S5.

candidates such as MST1/2 and LATS1/2, have been reported in cancer (Chan et al., 2011, Chen et al., 2012; Zeng and Hong, 2008; Zhou et al., 2009). It is also possible that VGLL4 loss in cancer could be related to epigenetic changes. Recently, it was reported that aberrant Wnt signaling causes YAP upregulation in liver cancer (Wang et al., 2013). In addition, several other tumorigenesis-related pathways have been reported to cross-talk with Hippo pathway (Azzolin et al., 2012; Barry et al., 2013; Fernandez et al., 2009; Konsavage et al., 2012; Varelas et al., 2010). Hence, it is also possible that aberration of these pathways may lead to dysregulation of VGLL4 and YAP in cancer. On the other hand, both negative (Genevet et al., 2010; Hamaratoglu et al., 2006; Neto-Silva et al., 2010) and positive (Jukam et al., 2013) feedback regulation of YAP has been documented, indicating tissue-dependent plasticity and intrinsic complexity of the YAP-related signaling network. Notably, dysregulation of signaling pathways induced by *H. pylori* infection is attributed to ~80% of GC cases (Houghton and Wang, 2005). How such infection may cause malfunction of Hippo pathway in GC remains to be determined. In the future, mechanistic elucidation of VGLL4 and YAP dysregulations in cancer will not only further our understanding of tumorigenesis, but may also help to find new biomarkers and facilitate patient selection.

EXPERIMENTAL PROCEDURES

Collection of Human Gastric Cancer Specimens

All samples used in this research were collected with written informed consent from patients. The use of human tissues was approved by the Institutional Ethics Board of the Shanghai Institutes for Biological Sciences (SIBS) and conforms to the Helsinki Declaration and to local legislation. All patients receiving treatment on this study were treated as part of a clinical protocol. See the Supplemental Experimental Procedures for details.

Tissue Microarray and Immunohistochemical Staining

Gastric cancer and normal tissue microarray sections were prepared by Shanghai Outdo Biotech. This tissue array contains tissues from 31 cases of dysplasia, 91 cases of gastric tumors, and paired normal tissue. The follow-up time of GC patients ranged from 2 to 66 months. This array was used for IHC staining analysis. For details, see the Supplemental Experimental Procedures.

Cell Viability Assay

Cells were transfected with the indicated plasmids of pcDNA3.1 or Flag-VGLL4 wild-type or mutant and/or HA-tagged YAP. ATP cell viability assay was used for detecting cell proliferation. ATP content was measured in accordance with the protocol of the CellTiter-Glo luminescent cell viability assay kit (Promega). Briefly, 100 μl of assay reagent was added to the wells and mixed for 2 min at room temperature. After 10 min, intracellular ATP content was measured using a luminescence multilabel counter (Envision, Perkin Elmer). Cell viability was calculated using the following equation:

$$\%\ \text{Cell viability} = [\text{value(test)} - \text{value(blank)}]/[\text{value(control)} - \text{value(blank)}] \times 100.$$

Protein Purification and Structure Determination

Proteins used in this study were expressed in *Escherichia coli* using pET28a-derived vectors and purified by affinity chromatography and size-exclusive chromatography. Diffraction data were collected at beamline BL17U, Shanghai Synchrotron Radiation Facility (SSRF) of China. See the Supplemental Experimental Procedures for details.

Design and Production of the Super-TDU

The basic rationale for the Super-TDU design lies in that the tandem TDU region of VGLL4 is fully competent in terms of competing with YAP for TEAD binding and therefore inhibiting YAP-mediated TEAD transactivation, and VGLL4 and YAP have overlapped but distinct primary binding sites on TEAD. The amino acid sequence of the Super-TDU contains "SVDD*HF*AK**S**LGDTWLQIGGSGNPKTANVPQTVP*M*RLRKLPDS*F*FKPPE." The Super-TDU was expressed and purified in *E. coli.* For details, see the Supplemental Experimental Procedures. In addition, two Super-TDU mutants were constructed by substitution of underlined residues MF or HFMF with alanines (termed as mutations MF2A and HFMF4A, respectively).

Animal Experiments

Male nude mice (BALB/cA-nu/nu) and C57/BL6 were obtained from Shanghai Experimental Animal Center and maintained in pathogen-free conditions. For animal research, all procedures for animal experimentation were performed in accordance with the Institutional Animal Care and Use Committee guidelines of the Animal Core Facility of the Institutes of Biochemistry and Cell Biology (SIBCB). The approval ID for using the animals was 081 by the Animal Core Facility of SIBCB.

During the tumor formation assay of BALB/c-nu/nu, cancer cell lines were injected at the flank of the mice (1×10^6 to 2×10^6). Tumor volumes were then measured. Once tumors were detected, mice were injected once daily with Super-TDU in saline at the 0.1 ml injection volume via the tail vein. Mice were randomized to receive either 50 μg/kg or 500 μg/kg per day of super-TDU peptide or control peptide. In addition, mice were treated with 50 mg/kg 5-fluorouracil (5-FU) intravenously as a positive control.

For the *H. pylori*-infected mice model, SPF C57BL/6-slac mice were housed in an air-conditioned biohazard room designed for infectious animals, with a 12 hr light/dark cycle. The mice were inoculated with *H. pylori* SS1 grown on solid medium and harvested by swabbing, a single intragastric dose of a 1×10^7 CFU/ml. Normal mice (n = 20) were given same amount of normal saline and were housed in isolators in order to prevent risk of infection.

See the Supplemental Experimental Procedures for details.

Statistical Analysis

Statistical analysis was performed using the SAS statistical software package (9.1.3). Data are presented as means ± SD. ANOVA and Student's t test were used for continuous variables. Fisher's exact test was used for categorical variables. Survival analysis was performed using log-rank test. The Cox proportional hazards model was used for multivariate analysis, and calculation of the hazard ratios and confidence intervals was performed with the ascending step-by-step maximum likelihood method. A p value < 0.05 was considered significantly different.

Other methods are described in the Supplemental Experimental Procedures.

ACCESSION NUMBERS

The Protein Data Bank accession number for the crystal structure of VGLL4-TEAD4 complex reported in this paper is 4LN0.

SUPPLEMENTAL INFORMATION

Supplemental Information includes Supplemental Experimental Procedures, five figures, and nine tables and can be found with this article online at http://dx.doi.org/10.1016/j.ccr.2014.01.010.

ACKNOWLEDGMENTS

We are grateful to Drs. Lin Li and Jinqiu Zhou for generous support and helpful discussion. This work was supported by the 973 program of the Ministry of Science and Technology of China (2012CB910204, 2010CB529701, and 2012CB945001), the National Natural Science Foundation of China (31270808

and 31300734), the Science and Technology Commission of Shanghai Municipality (11JC14140000 and 13ZR1446400), the Strategic Priority Research Program of the Chinese Academy of Sciences (XDA01010406 and XDA01010405), and the "Cross and cooperation in science and technology innovation team" project of the Chinese Academy of Sciences. Z.Z. and L.Z. are scholars of the Hundred Talents Program of the Chinese Academy of Sciences. The Super-TDU-related therapeutic strategy has been patented (201310493193.4).

Received: July 12, 2013
Revised: December 5, 2013
Accepted: January 16, 2014
Published: February 10, 2014

REFERENCES

Avruch, J., Zhou, D., and Bardeesy, N. (2012). YAP oncogene overexpression supercharges colon cancer proliferation. Cell Cycle *11*, 1090–1096.

Azzolin, L., Zanconato, F., Bresolin, S., Forcato, M., Basso, G., Bicciato, S., Cordenonsi, M., and Piccolo, S. (2012). Role of TAZ as mediator of Wnt signaling. Cell *151*, 1443–1456.

Barry, E.R., Morikawa, T., Butler, B.L., Shrestha, K., de la Rosa, R., Yan, K.S., Fuchs, C.S., Magness, S.T., Smits, R., Ogino, S., et al. (2013). Restriction of intestinal stem cell expansion and the regenerative response by YAP. Nature *493*, 106–110.

Cai, J., Zhang, N., Zheng, Y., de Wilde, R.F., Maitra, A., and Pan, D. (2010). The Hippo signaling pathway restricts the oncogenic potential of an intestinal regeneration program. Genes Dev. *24*, 2383–2388.

Chan, S.W., Lim, C.J., Chen, L., Chong, Y.F., Huang, C., Song, H., and Hong, W. (2011). The Hippo pathway in biological control and cancer development. J. Cell. Physiol. *226*, 928–939.

Chen, H.H., Mullett, S.J., and Stewart, A.F. (2004). Vgl-4, a novel member of the vestigial-like family of transcription cofactors, regulates alpha1-adrenergic activation of gene expression in cardiac myocytes. J. Biol. Chem. *279*, 30800–30806.

Chen, L., Qin, F., Deng, X., Avruch, J., and Zhou, D. (2012). Hippo pathway in intestinal homeostasis and tumorigenesis. Protein Cell *3*, 305–310.

Cui, Z.L., Han, F.F., Peng, X.H., Chen, X., Luan, C.Y., Han, R.C., Xu, W.G., and Guo, X.J. (2012). YES-associated protein 1 promotes adenocarcinoma growth and metastasis through activation of the receptor tyrosine kinase Axl. Int. J. Immunopathol. Pharmacol. *25*, 989–1001.

Da, C.L., Xin, Y., Zhao, J., and Luo, X.D. (2009). Significance and relationship between Yes-associated protein and survivin expression in gastric carcinoma and precancerous lesions. World J. Gastroenterol. *15*, 4055–4061.

Danon, S.J., and Eaton, K.A. (1998). The role of gastric Helicobacter and N-methyl-N'-nitro- N-nitrosoguanidine in carcinogenesis of mice. Helicobacter *3*, 260–268.

Faucheux, C., Naye, F., Tréguer, K., Fédou, S., Thiébaud, P., and Théze, N. (2010). Vestigial like gene family expression in Xenopus: common and divergent features with other vertebrates. Int. J. Dev. Biol. *54*, 1375–1382.

Fernandez, L.A., Northcott, P.A., Dalton, J., Fraga, C., Ellison, D., Angers, S., Taylor, M.D., and Kenney, A.M. (2009). YAP1 is amplified and up-regulated in hedgehog-associated medulloblastomas and mediates Sonic hedgehog-driven neural precursor proliferation. Genes Dev. *23*, 2729–2741.

Genevet, A., Wehr, M.C., Brain, R., Thompson, B.J., and Tapon, N. (2010). Kibra is a regulator of the Salvador/Warts/Hippo signaling network. Dev. Cell *18*, 300–308.

Goulev, Y., Fauny, J.D., Gonzalez-Marti, B., Flagiello, D., Silber, J., and Zider, A. (2008). SCALLOPED interacts with YORKIE, the nuclear effector of the hippo tumor-suppressor pathway in Drosophila. Curr. Biol. *18*, 435–441.

Günther, S., Mielcarek, M., Krüger, M., and Braun, T. (2004). VITO-1 is an essential cofactor of TEF1-dependent muscle-specific gene regulation. Nucleic Acids Res. *32*, 791–802.

Guo, T., Lu, Y., Li, P., Yin, M.X., Lv, D., Zhang, W., Wang, H., Zhou, Z., Ji, H., Zhao, Y., and Zhang, L. (2013). A novel partner of Scalloped regulates Hippo signaling via antagonizing Scalloped-Yorkie activity. Cell Res. *23*, 1201–1214.

Halder, G., and Johnson, R.L. (2011). Hippo signaling: growth control and beyond. Development *138*, 9–22.

Halperin, D.S., Pan, C., Lusis, A.J., and Tontonoz, P. (2013). Vestigial-like 3 is an inhibitor of adipocyte differentiation. J. Lipid Res. *54*, 473–481.

Hamaratoglu, F., Willecke, M., Kango-Singh, M., Nolo, R., Hyun, E., Tao, C., Jafar-Nejad, H., and Halder, G. (2006). The tumour-suppressor genes NF2/Merlin and Expanded act through Hippo signalling to regulate cell proliferation and apoptosis. Nat. Cell Biol. *8*, 27–36.

Han, S.U., Kim, Y.B., Joo, H.J., Hahm, K.B., Lee, W.H., Cho, Y.K., Kim, D.Y., and Kim, M.W. (2002). Helicobacter pylori infection promotes gastric carcinogenesis in a mice model. J. Gastroenterol. Hepatol. *17*, 253–261.

Harvey, K., and Tapon, N. (2007). The Salvador-Warts-Hippo pathway - an emerging tumour-suppressor network. Nat. Rev. Cancer *7*, 182–191.

Hergovich, A. (2012). YAP-Hippo signalling downstream of leukemia inhibitory factor receptor: implications for breast cancer. Breast Cancer Res. *14*, 326.

Houghton, J., and Wang, T.C. (2005). Helicobacter pylori and gastric cancer: a new paradigm for inflammation-associated epithelial cancers. Gastroenterology *128*, 1567–1578.

Huang, J., Wu, S., Barrera, J., Matthews, K., and Pan, D. (2005). The Hippo signaling pathway coordinately regulates cell proliferation and apoptosis by inactivating Yorkie, the Drosophila Homolog of YAP. Cell *122*, 421–434.

Jacobson, A., and Cunningham, J.L. (2012). Connective tissue growth factor in tumor pathogenesis. Fibrogenesis Tissue Repair *5* (*Suppl 1*), S8.

Jiang, C.G., Lv, L., Liu, F.R., Wang, Z.N., Liu, F.N., Li, Y.S., Wang, C.Y., Zhang, H.Y., Sun, Z., and Xu, H.M. (2011). Downregulation of connective tissue growth factor inhibits the growth and invasion of gastric cancer cells and attenuates peritoneal dissemination. Mol. Cancer *10*, 122.

Jukam, D., Xie, B., Rister, J., Terrell, D., Charlton-Perkins, M., Pistillo, D., Gebelein, B., Desplan, C., and Cook, T. (2013). Opposite feedbacks in the Hippo pathway for growth control and neural fate. Science *342*, 1238016.

Kang, J.M., Lee, B.H., Kim, N., Lee, H.S., Lee, H.E., Park, J.H., Kim, J.S., Jung, H.C., and Song, I.S. (2011). CDX1 and CDX2 expression in intestinal metaplasia, dysplasia and gastric cancer. J. Korean Med. Sci. *26*, 647–653.

Konsavage, W.M., Jr., Kyler, S.L., Rennoll, S.A., Jin, G., and Yochum, G.S. (2012). Wnt/β-catenin signaling regulates Yes-associated protein (YAP) gene expression in colorectal carcinoma cells. J. Biol. Chem. *287*, 11730–11739.

Koontz, L.M., Liu-Chittenden, Y., Yin, F., Zheng, Y., Yu, J., Huang, B., Chen, Q., Wu, S., and Pan, D. (2013). The Hippo effector Yorkie controls normal tissue growth by antagonizing scalloped-mediated default repression. Dev. Cell *25*, 388–401.

Lin, M.T., Zuon, C.Y., Chang, C.C., Chen, S.T., Chen, C.P., Lin, B.R., Wang, M.Y., Jeng, Y.M., Chang, K.J., Lee, P.H., et al. (2005). Cyr61 induces gastric cancer cell motility/invasion via activation of the integrin/nuclear factor-kappaB/cyclooxygenase-2 signaling pathway. Clin. Cancer Res *11*, 5809–5820.

Liu-Chittenden, Y., Huang, B., Shim, J.S., Chen, Q., Lee, S.J., Anders, R.A., Liu, J.O., and Pan, D.J. (2012). Genetic and pharmacological disruption of the TEAD-YAP complex suppresses the oncogenic activity of YAP. Genes Dev. *26*, 1300–1305.

Maeda, T., Chapman, D.L., and Stewart, A.F. (2002). Mammalian vestigial-like 2, a cofactor of TEF-1 and MEF2 transcription factors that promotes skeletal muscle differentiation. J. Biol. Chem. *277*, 48889–48898.

Maeta, N., Osaki, M., Shomori, K., Inaba, A., Kidani, K., Ikeguchi, M., and Ito, H. (2007). CYR61 downregulation correlates with tumor progression by promoting MMP-7 expression in human gastric carcinoma. Oncology *73*, 118–126.

Mann, K.M., Ward, J.M., Yew, C.C., Kovochich, A., Dawson, D.W., Black, M.A., Brett, B.T., Sheetz, T.E., Dupuy, A.J., Chang, D.K., et al.; Australian Pancreatic Cancer Genome Initiative (2012). Sleeping Beauty mutagenesis reveals cooperating mutations and pathways in pancreatic adenocarcinoma. Proc. Natl. Acad. Sci. USA *109*, 5934–5941.

Neto-Silva, R.M., de Beco, S., and Johnston, L.A. (2010). Evidence for a growth-stabilizing regulatory feedback mechanism between Myc and Yorkie, the Drosophila homolog of Yap. Dev. Cell *19*, 507–520.

Pan, D. (2010). The hippo signaling pathway in development and cancer. Dev. Cell *19*, 491–505.

Pobbati, A.V., Chan, S.W., Lee, I., Song, H., and Hong, W. (2012). Structural and functional similarity between the Vgll1-TEAD and the YAP-TEAD complexes. Structure *20*, 1135–1140.

Stanger, B.Z. (2012). Quit your YAPing: a new target for cancer therapy. Genes Dev. *26*, 1263–1267.

Steinhardt, A.A., Gayyed, M.F., Klein, A.P., Dong, J., Maitra, A., Pan, D., Montgomery, E.A., and Anders, R.A. (2008). Expression of Yes-associated protein in common solid tumors. Hum. Pathol. *39*, 1582–1589.

Sudol, M., Shields, D.C., and Farooq, A. (2012). Structures of YAP protein domains reveal promising targets for development of new cancer drugs. Semin. Cell Dev. Biol. *23*, 827–833.

Takaishi, S., and Wang, T.C. (2007). Gene expression profiling in a mouse model of Helicobacter-induced gastric cancer. Cancer Sci. *98*, 284–293.

Varelas, X., Miller, B.W., Sopko, R., Song, S., Gregorieff, A., Fellouse, F.A., Sakuma, R., Pawson, T., Hunziker, W., McNeill, H., et al. (2010). The Hippo pathway regulates Wnt/beta-catenin signaling. Dev. Cell *18*, 579–591.

Vaudin, P., Delanoue, R., Davidson, I., Silber, J., and Zider, A. (1999). TONDU (TDU), a novel human protein related to the product of vestigial (vg) gene of Drosophila melanogaster interacts with vertebrate TEF factors and substitutes for Vg function in wing formation. Development *126*, 4807–4816.

Wang, J., Park, J.S., Wei, Y., Rajurkar, M., Cotton, J.L., Fan, Q., Lewis, B.C., Ji, H., and Mao, J. (2013). TRIB2 acts downstream of Wnt/TCF in liver cancer cells to regulate YAP and C/EBPα function. Mol. Cell *51*, 211–225.

Wu, S., Liu, Y., Zheng, Y., Dong, J., and Pan, D. (2008). The TEAD/TEF family protein Scalloped mediates transcriptional output of the Hippo growth-regulatory pathway. Dev. Cell *14*, 388–398.

Zender, L., Spector, M.S., Xue, W., Flemming, P., Cordon-Cardo, C., Silke, J., Fan, S.T., Luk, J.M., Wigler, M., Hannon, G.J., et al. (2006). Identification and validation of oncogenes in liver cancer using an integrative oncogenomic approach. Cell *125*, 1253–1267.

Zeng, Q., and Hong, W. (2008). The emerging role of the hippo pathway in cell contact inhibition, organ size control, and cancer development in mammals. Cancer Cell *13*, 188–192.

Zhang, L., Ren, F., Zhang, Q., Chen, Y., Wang, B., and Jiang, J. (2008). The TEAD/TEF family of transcription factor Scalloped mediates Hippo signaling in organ size control. Dev. Cell *14*, 377–387.

Zhang, X., George, J., Deb, S., Degoutin, J.L., Takano, E.A., Fox, S.B., Bowtell, D.D., and Harvey, K.F.; AOCS Study Group (2011). The Hippo pathway transcriptional co-activator, YAP, is an ovarian cancer oncogene. Oncogene *30*, 2810–2822.

Zhang, W., Gao, Y., Li, P., Shi, Z., Guo, T., Li, F., Han, X., Feng, Y., Zheng, C., Wang, Z., et al. (2014). VGLL4 functions as a new tumor suppressor in lung cancer by negatively regulating the YAP-TEAD transcriptional complex. Cell Res. Published online January 24, 2014. http://dx.doi.org/10.1038/cr.2014.10.

Zhao, B., Wei, X., Li, W., Udan, R.S., Yang, Q., Kim, J., Xie, J., Ikenoue, T., Yu, J., Li, L., et al. (2007). Inactivation of YAP oncoprotein by the Hippo pathway is involved in cell contact inhibition and tissue growth control. Genes Dev. *21*, 2747–2761.

Zhao, B., Ye, X., Yu, J., Li, L., Li, W., Li, S., Yu, J., Lin, J.D., Wang, C.Y., Chinnaiyan, A.M., et al. (2008). TEAD mediates YAP-dependent gene induction and growth control. Genes Dev. *22*, 1962–1971.

Zhao, B., Li, L., Lei, Q., and Guan, K.L. (2010). The Hippo-YAP pathway in organ size control and tumorigenesis: an updated version. Genes Dev. *24*, 862–874.

Zhao, Z.S., Li, L., Wang, H.J., and Wang, Y.Y. (2011). Expression and prognostic significance of CEACAM6, ITGB1, and CYR61 in peripheral blood of patients with gastric cancer. J. Surg. Oncol. *104*, 525–529.

Zhou, D., Conrad, C., Xia, F., Park, J.S., Payer, B., Yin, Y., Lauwers, G.Y., Thasler, W., Lee, J.T., Avruch, J., and Bardeesy, N. (2009). Mst1 and Mst2 maintain hepatocyte quiescence and suppress hepatocellular carcinoma development through inactivation of the Yap1 oncogene. Cancer Cell *16*, 425–438.

Zhou, G.X., Li, X.Y., Zhang, Q., Zhao, K., Zhang, C.P., Xue, C.H., Yang, K., and Tian, Z.B. (2013). Effects of the hippo signaling pathway in human gastric cancer. Asian Pac. J. Cancer Prev. *14*, 5199–5205.

Cancer Cell
Article

The RhoGEF GEF-H1 Is Required for Oncogenic RAS Signaling via KSR-1

Jane Cullis,[1,3,10] David Meiri,[1,10] Maria Jose Sandi,[1] Nikolina Radulovich,[1,5] Oliver A. Kent,[1] Mauricio Medrano,[1,3] Daphna Mokady,[1] Josee Normand,[1] Jose Larose,[1] Richard Marcotte,[1] Christopher B. Marshall,[1] Mitsuhiko Ikura,[1,3] Troy Ketela,[6,8] Jason Moffat,[6,8] Benjamin G. Neel,[1,3,5] Anne-Claude Gingras,[6,9] Ming-Sound Tsao,[1,3] and Robert Rottapel[1,2,3,4,7,*]

[1]Princess Margaret Cancer Center, University Health Network, 101 College Street, Room 8-703, Toronto Medical Discovery Tower, University of Toronto, Toronto, ON M5G 1L7, Canada
[2]Department of Medicine, University of Toronto, 1 King's College Circle, Toronto, ON M5S 1A8, Canada
[3]Department of Medical Biophysics, University of Toronto, 1 King's College Circle, Toronto, ON M5S 1A8, Canada
[4]Department of Immunology, University of Toronto, 1 King's College Circle, Toronto, ON M5S 1A8, Canada
[5]Department of Laboratory Medicine and Pathobiology, University of Toronto, 1 King's College Circle, Toronto, ON M5S 1A8, Canada
[6]Department of Molecular Genetics, University of Toronto, 1 King's College Circle, Toronto, ON M5S 1A8, Canada
[7]Division of Rheumatology, St. Michael's Hospital, 30 Bond Street, Toronto, ON M5B 1W8, Canada
[8]Donnelly Centre and Banting and Best Department of Medical Research, 160 College Street, Room 8-804, University of Toronto, Toronto, ON M5S 3E1, Canada
[9]Lunenfeld-Tanenbaum Research Institute, Mount Sinai Hospital, 600 University Avenue, Room 992A, Toronto, ON M5G 1X5, Canada
[10]These authors contributed equally to this work
*Correspondence: rottapel@uhnresearch.ca
http://dx.doi.org/10.1016/j.ccr.2014.01.025

SUMMARY

Cellular transformation by oncogenic RAS engages the MAPK pathway under strict regulation by the scaffold protein KSR-1. Here, we report that the guanine nucleotide exchange factor GEF-H1 plays a critical role in a positive feedback loop for the RAS/MAPK pathway independent of its RhoGEF activity. GEF-H1 acts as an adaptor protein linking the PP2A B' subunits to KSR-1, thereby mediating the dephosphorylation of KSR-1 S392 and activation of MAPK signaling. GEF-H1 is important for the growth and survival of $HRAS^{V12}$-transformed cells and pancreatic tumor xenografts. GEF-H1 expression is induced by oncogenic RAS and is correlated with pancreatic neoplastic progression. Our results, therefore, identify GEF-H1 as an amplifier of MAPK signaling and provide mechanistic insight into the progression of RAS mutant tumors.

INTRODUCTION

The centrality of the RAS/MAPK pathway in promoting tumor formation is underscored by the high frequency of gain-of-function mutations in RAS family members and other components of the pathway in human cancers. KRAS has a particularly high mutation frequency of 30%–50% in colon and greater than 90% in pancreatic adenocarcinomas (Oliveira et al., 2007; Mulcahy et al., 1998). The importance of RAS is a reflection of its essential role in mediating the transduction of signals from growth factor receptors to pathways that regulate transcription, cell cycle progression, cell shape, and cell survival, all of which are commonly disturbed in cancer (Macara et al., 1996). RAS engages diverse signaling pathways, including RAF, PI3K, RAL-GDS, and TIAM-1, each of which are also subject to activating mutations in cancer (Davies et al., 2002; Samuels and Velculescu, 2004; Philp et al., 2001; Sjöblom et al., 2006; Greenman et al., 2007; Engers et al., 2000). RAS activation is coupled to transcription through the activation of the MAPK cascade, involving the sequential phosphorylation and activation of the serine/threonine kinases RAF (MAPKKK), MEK1/2 (MAPKK), and ERK1/2 (MAPK)

Significance

Mutational activation of RAS occurs in over 90% of pancreatic cancers and is required for both the initiation and progression of tumorigenesis. However, the mechanism of RAS-mediated cellular transformation is not fully understood. Here, we find that GEF-H1 is necessary for optimal RAS/MAPK pathway signaling and contributes to the growth and survival of RAS mutant cells. GEF-H1 expression is induced by oncogenic RAS and is elevated in pancreatic tumor samples, thereby providing an amplifying loop for RAS/MAPK signaling. Our results, therefore, extend our understanding of the signaling dependencies of oncogenic RAS, which may ultimately improve the development of RAS-pathway-directed therapeutics.

(Moodie et al., 1993; Warne et al., 1993; Zhang et al., 1993; Vojtek et al., 1993).

The Kinase Suppressor of RAS (KSR-1) was originally identified in genetic screens in *Drosophila* and *Caenorhabditis elegans* designed to isolate mutations in genes that modify the phenotypes associated with oncogenic RAS alleles (Jacobs et al., 1999; Therrien et al., 1995; Sundaram and Han, 1995). In mammalian cells, KSR-1 acts as a molecular scaffold to assemble a macromolecular complex of MAPK pathway components to facilitate efficient signal transmission (Therrien et al., 1996; Michaud et al., 1997; Cacace et al., 1999; Morrison, 2001) and is required for mutant RAS-mediated cellular transformation (Nguyen et al., 2002; Lozano et al., 2003). KSR-1 also functions as a gate to control flux through the MAPK pathway. In quiescent cells, KSR-1 is phosphorylated on S297 and S392 by C-TAK1 and held in an inactive state in the cytosol by 14-3-3 proteins (Ory et al., 2003). RAS activation stimulates the dephosphorylation of KSR-1 on S392, resulting in its translocation to the plasma membrane where it potentiates MAPK signaling (Ory et al., 2003).

Genetic studies performed in model organisms showed that mutations in the PP2A phosphatase phenocopied a loss of KSR-1 function in a RAS mutant background (Wassarman et al., 1996; Sieburth et al., 1999), suggesting that PP2A is a positive regulator of KSR-1. PP2A was subsequently shown to be the critical phosphatase required for dephosphorylation of KSR-1 on S392 in response to activated RAS (Ory et al., 2003). PP2A is a heterotrimeric serine/threonine protein phosphatase composed of a catalytic (C), structural (A), and regulatory (B) subunit. The catalytic and structural subunits are constitutively associated to form a core complex to which one of many B subunits can bind (Janssens and Goris, 2001). Four different B subunits (B, B', B'', and B''') exist in mammals that determine the localization and substrate specificity of the holoenzyme (Janssens and Goris, 2001). The A and C subunits constitutively associate with KSR-1, whereas association of the B' subunit is induced only upon RAS activation (Ory et al., 2003). The mechanism by which the B' subunit is recruited to KSR-1 has yet to be elucidated.

GEF-H1, which is encoded by *ARHGEF2*, is a microtubule-associated guanine nucleotide exchange factor (GEF) for the Rho family of small GTPases (Ren et al., 1998). Several lines of evidence have highlighted the transforming potential of GEF-H1. *ARHGEF2* is amplified in hepatocellular carcinoma (Cheng et al., 2012) and is a transcriptional target of gain-of-function p53 mutants (Mizuarai et al., 2006) and the metastasis-associated hPTTG1 (Liao et al., 2012). Truncated versions of GEF-H1 can transform NIH 3T3 cells (Whitehead et al., 1995) and induce tumor formation in nude mice (Brecht et al., 2005). *ARHGEF2* is one of six genes significantly downregulated in response to imatinib treatment in gastrointestinal tumors (Frolov et al., 2003). In addition, *ARHGEF2* was identified in a genome-wide pooled small hairpin RNA (shRNA) screen designed to identify genes that are required for the survival of human breast, colon, lung, ovarian, and pancreatic cell lines (Marcotte et al., 2012). These data suggest that GEF-H1 may be a marker for and/or contribute to tumorigenesis in multiple contexts.

RESULTS

GEF-H1 Contributes to the Survival of a Subset of Human Cancer Cell Lines, and Its expression Is Regulated by the RAS/MAPK Pathway

GEF-H1 was found to contribute to the competitive growth characteristics of 18 out of 73 cell lines, 13 of which were identified in the original shRNA screen and 5 of which were identified in our secondary screen (Figure 1A and Table S1 available online). For further validation, we selected three of these cell lines and stably infected them with two distinct lentiviral hairpins directed against GEF-H1. Cells depleted of GEF-H1 exhibited decreased growth and increased death relative to control hairpin-expressing cells as assessed by caspase 3 cleavage (Figures 1B and S1A–S1H). These data suggest that GEF-H1 is important for cell growth and survival in several human cell lines derived from different tumor types.

We noted that GEF-H1 dependency was enriched in RAS/BRAF mutant cell lines (13 of 30 [43.3%]) compared to RAS/BRAF wild-type cell lines (5 of 43 [11.6%]). GEF-H1 was found to contribute to cell growth/survival in 10 of 25 (40%) KRAS mutant pancreatic cancer cell lines with little effect on the three wild-type KRAS pancreatic cancer cell lines (Table S1). We therefore explored the possibility that GEF-H1 sensitivity in some cellular contexts is epistatic with gain-of-function mutations in the RAS/MAPK pathway. Because elevated expression of GEF-H1 is transforming in NIH 3T3 cells (Whitehead et al., 1995), we examined the ability of mutant RAS family members to induce GEF-H1 expression in a common isogenic cellular background. We observed that GEF-H1 protein levels were increased in cells transformed by each mutant RAS family member compared to nontransformed cells (Figure 1C). We next determined whether the induction of GEF-H1 expression was a direct result of activated RAS or a secondary consequence of the transformed state. We used a murine embryonic fibroblast (MEF) cell line expressing a hydroxytamoxifen (4-OHT)-inducible form of $HRAS^{V12}$ (ER:$HRAS^{V12}$) (Gupta et al., 2007) and found that GEF-H1 expression increased within 15 min of ER:$HRAS^{V12}$ induction and continued to increase with progressive elevation of ER:$HRAS^{V12}$ expression (Figure 1D, upper panel). Cells treated with vehicle control (EtOH) exhibited no change in GEF-H1 levels (Figure 1D, lower panel). These data show that GEF-H1 is induced acutely in response to expression of $HRAS^{V12}$. MAP kinase pathway activation followed a bimodal distribution, peaking at 15 min and 8 hr after $HRAS^{V12}$ induction, but decreasing over intermediate time points, as has been previously shown (Gupta et al., 2007).

ARHGEF2 Is a Transcriptional Target of the RAS/MAPK Pathway

To assess whether GEF-H1 expression was dependent on MAPK activation, we treated OV-90, HCT116, and Panc 02.03 cells with the MEK1/2 inhibitors PD98059 and UO126 and found that the GEF-H1 protein level decreased following MEK1/2 inhibition (Figure 2A). Similar findings were observed in $HRAS^{V12}$-transformed NIH 3T3 cells (Figure 2B). We noted that the GEF-H1 mRNA level was elevated 2-fold in $HRAS^{V12}$-transformed NIH 3T3 cells relative to wild-type cells (Figure 2C) and sought to determine whether *ARHGEF2* was a direct

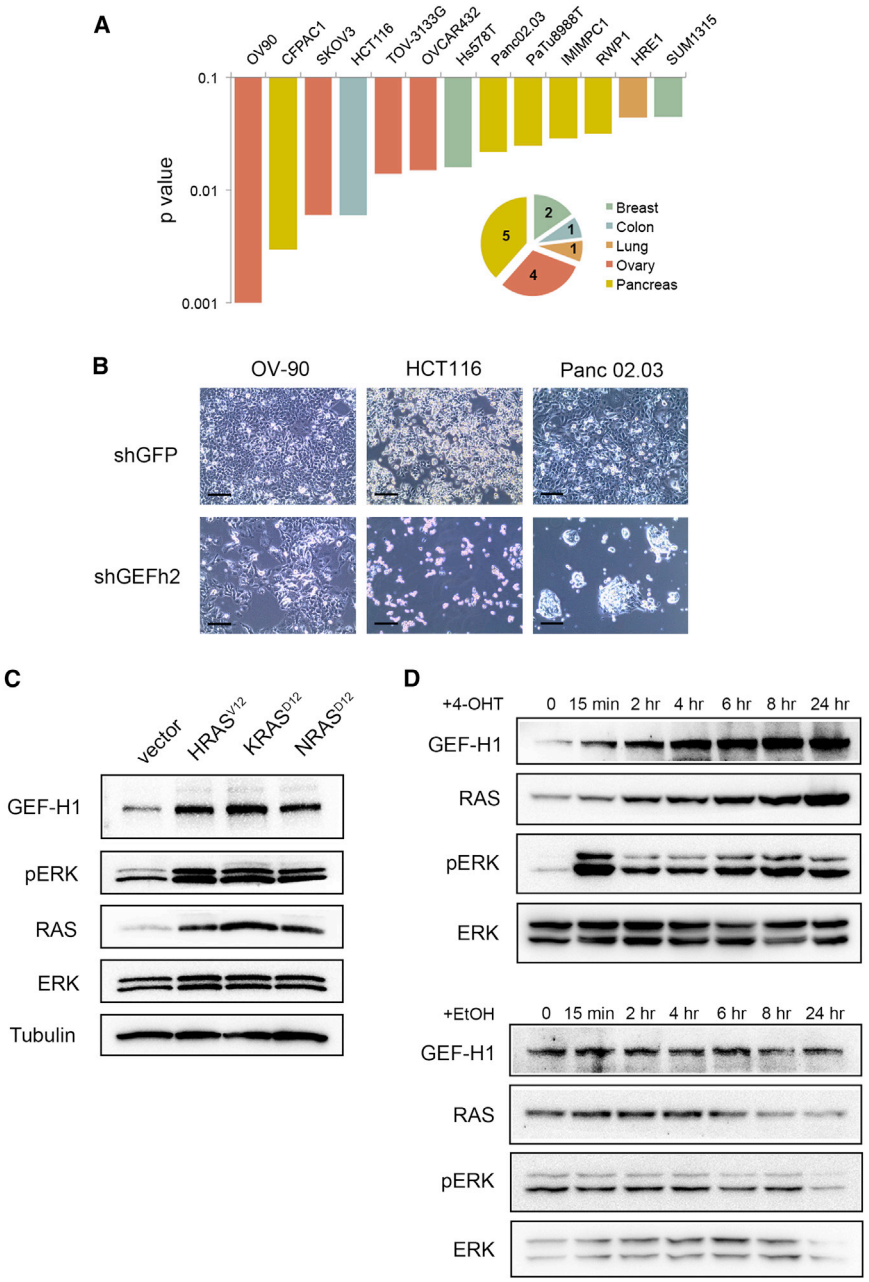

Figure 1. GEF-H1 Contributes to the Survival Fitness of a Subset of Human Cancer Cell Lines, and Its Protein Expression Is Regulated by the RAS/MAPK Pathway

(A) Schematic graphical representation of 13 GEF-H1-sensitive cell lines arranged according to the p values for the normalized Genetic Activity Rank Profile (zGARP) score across 75 cell lines (Marcotte et al., 2012). The fraction of GEF-H1-sensitive cell lines from each tumor type is depicted by the pie chart. The number of cell lines showing GEF-H1 dependency is indicated within the area of each slice.

(B) Bright field images of the indicated cells 6 days following infection and selection with hairpin control (shGFP) or human GEF-H1 shRNA (shGEFh2) lentivirus. Scale bars, 100 μm.

(C) Immunoblot analysis of GEF-H1 and RAS expression in NIH 3T3 cells stably expressing vector, T7-HRAS^{V12}, T7-KRAS^{D12}, or T7-NRAS^{D12}. pERK indicates level of MAPK pathway activation and total ERK and tubulin served as protein loading controls.

(D) Immunoblot analysis of GEF-H1 expression following acute induction of ER:HRAS^{V12} with 100 nM 4-OHT (upper panel) or treatment with vehicle control (lower panel) over the indicated period of time.

See also Figure S1 and Table S1.

GEF-H1 Contributes to Cell Survival and Growth in HRAS^{V12}-Transformed Cells

We next sought to determine whether GEF-H1 was important for HRAS^{V12}-mediated cellular transformation. We stably knocked down murine GEF-H1 in HRAS^{V12}-transformed NIH 3T3 cells using two distinct GEF-H1 lentiviral hairpins (Figure 3A), which resulted in increased apoptosis as measured by caspase 3 cleavage (Figure 3B). We also observed that stable depletion of GEF-H1 suppressed anchorage-independent growth by 90% compared with parental HRAS^{V12}-transformed cells or transformed cells expressing a nontargeting hairpin (Figures 3C and S2A).

transcriptional target of mutant RAS. Based on phylogenetic footprinting and CpG island enrichment, we identified a 1.9 kb region upstream of the first exon of murine *Arhgef2* predicted to contain the putative promoter, and we cloned this region into a luciferase reporter (Figure 2D). Expression of HRAS^{V12} induced a 7-fold increase in the normalized *Arhgef2* promoter-mediated luciferase activity compared to NIH 3T3 cells expressing the *Arhgef2* promoter alone and was quenched following MEK inhibition (Figure 2E). Together, these data show that *Arhgef2* is a transcriptional target of the RAS/MAPK pathway and that the elevated GEF-H1 protein level observed in HRAS^{V12}-transformed cells are, at least in part, due to elevated transcription.

To address the role of GEF-H1 in supporting tumor formation of HRAS^{V12}-transformed NIH 3T3 cells, we generated subcutaneous tumor xenografts in NCr nude mice. Parental and shGFP-expressing cells formed tumors within 10 days of injection, while GEF-H1-depleted cells demonstrated attenuated tumor growth (Figures 3D, 3E and S2B). Moreover, GEF-H1-depleted tumors exhibited increased caspase 3 cleavage relative to parental and hairpin controls (Figure 3F). To further examine the role of GEF-H1 in HRAS^{V12}-mediated cell survival, we monitored the behavior of MEFs derived from *Arhgef2* knockout mice (*Arhgef2*$^{-/-}$) following ectopic expression of HRAS^{V12} (Figure 3G). Extensive cell death was observed in *Arhgef2*$^{-/-}$ compared to wild-type MEFs following HRAS^{V12}

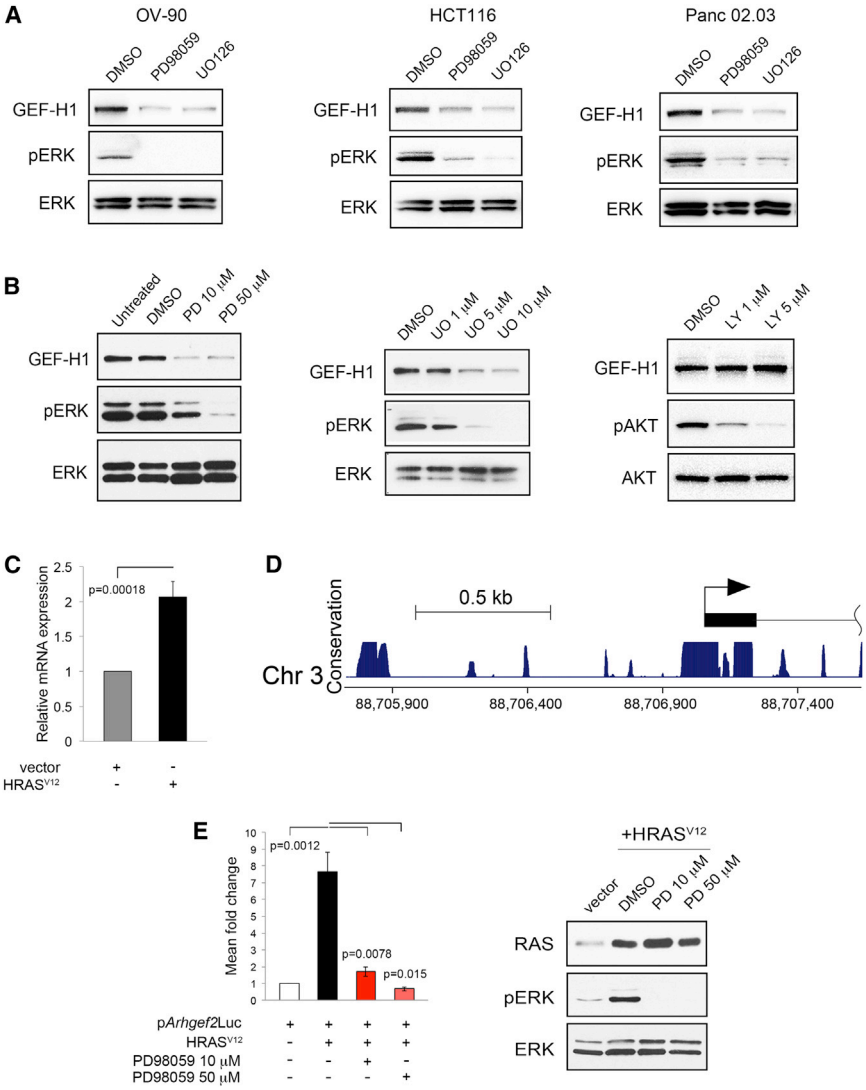

Figure 2. *Arhgef2* Is a Transcriptional Target of the RAS/MAPK Pathway

(A) Immunoblot analysis of GEF-H1 expression in cancer cell lines after treatment with DMSO, PD98059 (30 μM), or UO126 (10 μM) for 48 hr.

(B) $HRAS^{V12}$-transformed NIH 3T3 cells were treated with DMSO, PD98059, UO126, or LY294002 for 48 hr, and GEF-H1 expression was assessed by western blot. pERK and ERK indicate phosphorylated and total ERK, respectively, whereas pAKT and AKT indicate phosphorylated and total AKT, respectively.

(C) The GEF-H1 mRNA level in NIH 3T3 cells expressing vector or T7-$HRAS^{V12}$ was quantified by real-time PCR and normalized to tubulin. Levels are represented as fold change over vector-expressing cells.

(D) Schematic representation of the putative promoter region of murine *Arhgef2* showing the highly conserved transcriptional start site (TSS) from the UCSC genome browser.

(E) p*Arhgef2*Luc was co-transfected with empty vector or T7-$HRAS^{V12}$ expression plasmid and treated with PD98059. Luciferase activity was normalized to renilla expression and is represented as fold change over empty vector-expressing cells (left graph). Lysates were assayed for RAS expression and MAPK activation by western blot (right panel). All data are representative of three independent experiments ± SEM.

expression. Re-expression of GEF-H1 in *Arhgef2*$^{-/-}$ MEFs expressing $HRAS^{V12}$ restored cell viability. These data show that GEF-H1 contributes to $HRAS^{V12}$-mediated cell transformation and cell viability in vitro and in vivo.

GEF-H1 Induction and Dependency in $BRAF^{V600E}$-Expressing Cell Lines

Because OV-90 carries the activating *BRAF*^{V600E} mutation (Estep et al., 2007), we queried whether $BRAF^{V600E}$ similarly induced GEF-H1 protein expression. We found that GEF-H1 protein levels were increased in $BRAF^{V600E}$-transformed NIH 3T3 cells and were sensitive to MEK inhibition (Figures S2C and S2D). Moreover, GEF-H1 expression in the human melanoma cell line A375, which carries an endogenous *BRAF*^{V600E} mutation, was suppressed following MEK inhibition (Figure S2E). $BRAF^{V600E}$ expression also induced a 4.6-fold increase in the normalized *Arhgef2* promoter-mediated reporter expression compared to NIH 3T3 cells expressing the *Arhgef2* promoter alone, which was suppressed with MEK inhibition (Figure S2F). Lastly, knockdown of GEF-H1 induced cell death in $BRAF^{V600E}$-transformed cells (Figures S2G and S2H). These data indicate that the induction of GEF-H1 expression and GEF-H1-dependent cell survival extends to other oncogenes that activate the MAPK pathway.

GEF-H1 Is Necessary for Optimal MAPK Pathway Activation in Response to $HRAS^{V12}$

We next sought to investigate the mechanism underlying the contribution of GEF-H1 to $HRAS^{V12}$-mediated cellular transformation. We compared the levels of Rho-GTP in control and GEF-H1 knockdown cells expressing $HRAS^{V12}$ but found no change in Rho-GTP levels (Figure S3A and S3B), demonstrating that a change in Rho-GTP cannot account for the contribution of GEF-H1 in $HRAS^{V12}$-mediated transformation. We therefore investigated whether elevated levels of GEF-H1 affected the signaling characteristics of upstream components of the RAS/MAPK pathway as part of a potential positive feedback mechanism. We expressed $HRAS^{V12}$ in MEFs harboring stable knockdown of GEF-H1 and probed lysates for phosphorylated forms of MEK1/2 and ERK1/2 to assess MAPK pathway activity. MEK1/2 and ERK1/2 were highly phosphorylated in $HRAS^{V12}$-expressing MEFs (Figure 4A, lane 2), but, surprisingly, MEK1/2 and ERK1/2 phosphorylation was significantly reduced in GEF-H1-depleted cells (Figure 4A, lanes 4 and 6). Expression of an shRNA-resistant GEF-H1 (rGEF-H1) restored MEK1/2 and ERK1/2 phosphorylation in response to $HRAS^{V12}$ expression in GEF-H1 knockdown MEFs (Figure 4A, lane 7). A similar defect in $HRAS^{V12}$-mediated ERK1/2 phosphorylation was seen in

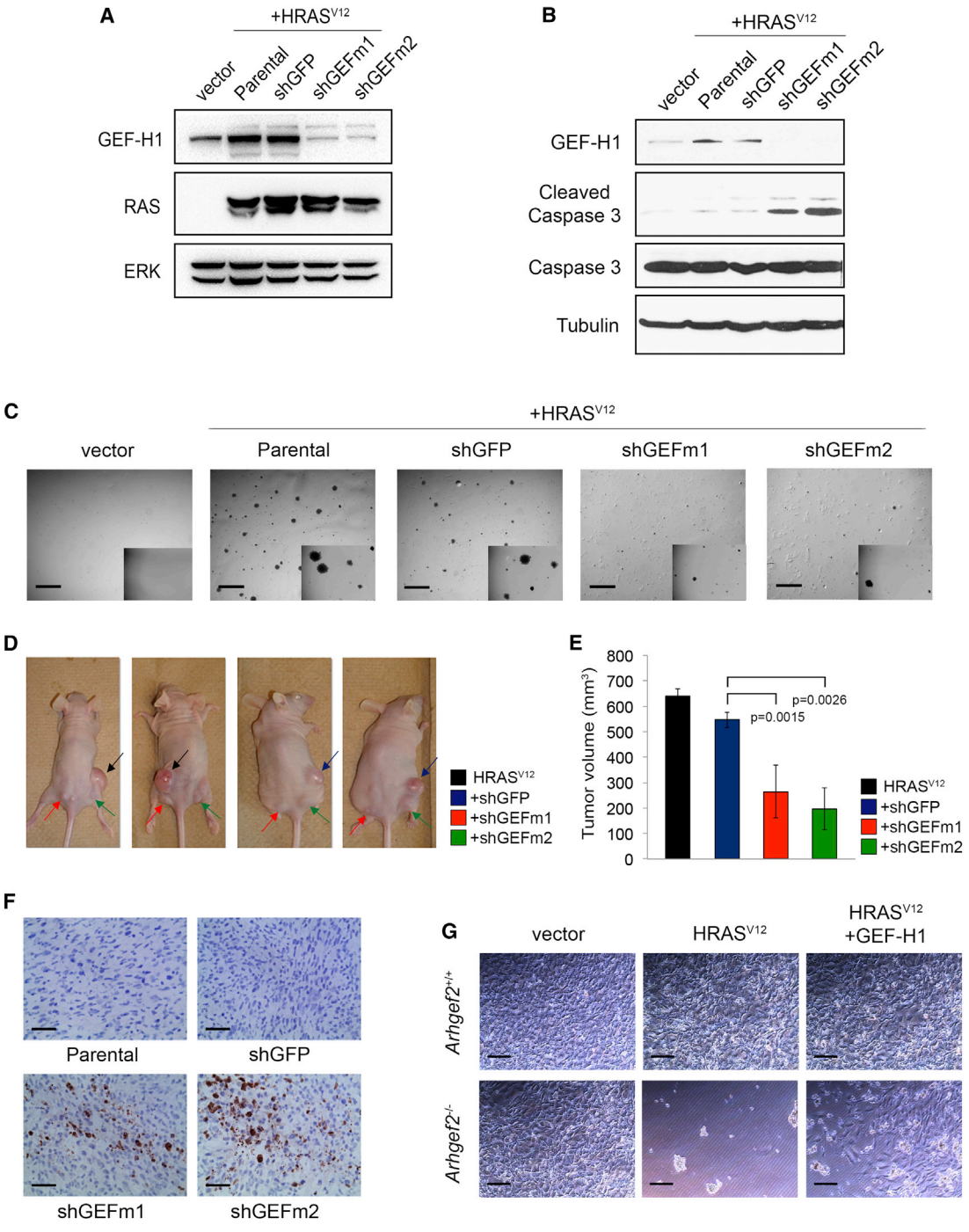

Figure 3. GEF-H1 Contributes to Cell Survival and Growth in HRAS^{V12}-Transformed Cells

(A) GEF-H1 protein levels in NIH 3T3 cells expressing vector, HRAS^{V12}, or HRAS^{V12} with a control hairpin (shGFP) or two distinct murine GEF-H1 shRNAs (shGEFm1 and shGEFm2).

(B) Cells described in (A) were probed for caspase 3 cleavage by western blot 5 days after infection with lentiviral hairpins. Tubulin served as a protein loading control.

(C) Representative images of cell lines described in (A) grown for 10 days in 0.3% agar to form colonies. Scale bars, 200 μm.

(D) Photographs of NCr nude mice 14 days after subcutaneous injection of cells described in (A).

(E) Final mean tumor volumes are shown in (D). Results are the combination of four independent experiments (n = 21 tumors). Error bars indicate ± SEM.

(F) Immunohistochemistry of NIH 3T3-HRAS^{V12} tumor sections stained for cleaved caspase 3. Four tumors were sampled from two independent experiments. Scale bars, 100 μm.

(G) Bright field images of wild-type or *Arhgef2*$^{-/-}$ MEFs expressing eGFP, eGFP-HRAS^{V12}, or eGFP-HRAS^{V12} and Flag-GEF-H1 4 days after transfection and selection. Scale bars, 100 μm.

See also Figure S2.

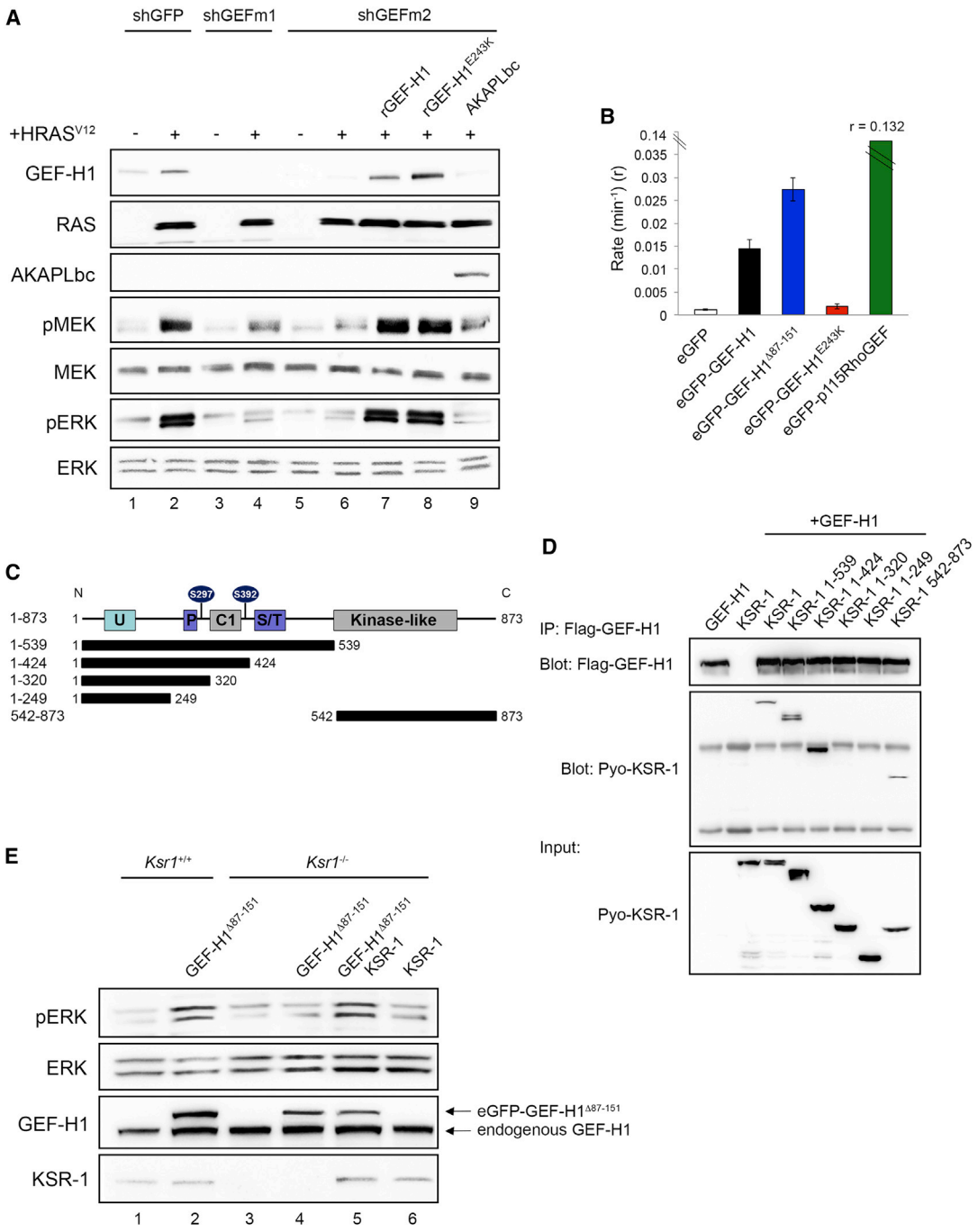

Figure 4. GEF-H1 Is Necessary for Optimal MAPK Pathway Activation in Response to HRAS^{V12}

(A) MEFs stably expressing shGFP, shGEFm1, or shGEFm2 were transfected with empty vector or HRAS^{V12} and probed for pERK or pMEK by western blot. shGEFm2-expressing cells were co-transfected with HRAS^{V12} and Flag-rGEF-H1, Flag-rGEF-H1^{E243K}, or Flag-AKAPLbc. Expression of plasmids was confirmed by immunoblotting with anti-GEF-H1, anti-RAS, or anti-Flag (AKAPLbc) antibodies.

(B) Real-time NMR measurement of RhoA nucleotide exchange rates in lysates from HEK293T cells expressing eGFP, eGFP-GEF-H1, eGFP-GEF-H1$^{\Delta 87–151}$, eGFP-GEF-H1^{E243K}, or eGFP-p115RhoGEF. Graphical representation of eGFP-p115RhoGEF-induced nucleotide exchange rate is not to scale as indicated by breaks in graph, because the rate was 9.4-fold over eGFP-GEF-H1 (r = 0.132 versus r = 0.014). Data are representative of three independent experiments ± SD.

(C) Schematic representation of KSR-1 constructs used in (D).

(D) Pyo-tagged KSR-1 constructs were coexpressed with Flag-GEF-H1 in HEK293T cells. Protein complexes were immunoprecipitated with anti-Flag antibody, and proteins were detected by immunoblotting with anti-KSR-1 or anti-Flag antibodies.

(E) MEFs were transfected with vector or eGFP-GEF-H1$^{\Delta 87–151}$, and *Ksr1*$^{-/-}$ MEFs were transfected with vector, eGFP-GEF-H1$^{\Delta 87–151}$, eGFP-GEF-H1$^{\Delta 87–151}$ and Pyo-KSR-1, or Pyo-KSR-1 alone and assayed for pERK by western blot. GEF-H1 and KSR-1 expression was determined by western blot.

See also Figure S3.

Arhgef2$^{-/-}$ MEFs, which was restored by GEF-H1 expression (Figure S3C, lanes 4 and 5).

To determine the specificity of GEF-H1-dependent MAPK pathway activation, we attempted to rescue the GEF-H1 knockdown phenotype by expressing either AKAP-Lbc, the closest GEF family member to GEF-H1, or p115 RhoGEF, another RhoGEF family member. Neither AKAP-Lbc (Figure 4A, lane 9) nor p115 RhoGEF (Figure S3C, lane 7) rescued MEK1/2 and ERK1/2 phosphorylation in response to acute HRAS^{V12} expression in GEF-H1 knockdown or *Arhgef2*$^{-/-}$ MEFs, respectively, despite 9-fold greater catalytic activity of p115RhoGEF compared to GEF-H1 (Figure 4B). To investigate whether GEF-H1-mediated MAPK pathway activation was dependent on its GEF activity, we coexpressed a catalytically inactive, shRNA-resistant form of GEF-H1 (rGEF-H1^{E243K}, Figure 4B) with HRAS^{V12} in MEFs depleted of endogenous GEF-H1 and found that MEK1/2 and ERK1/2 phosphorylation was fully restored (Figure 4A, lane 8). These findings were confirmed in *Arhgef2*$^{-/-}$ MEFs (Figure S3C, lane 6). These data show that GEF-H1 potentiates the HRAS^{V12}/MAPK pathway in a manner independent of its GEF activity.

GEF-H1 Is a Component of the KSR-1 Complex and Is Required for the Dephosphorylation of the Negative Regulatory Site of KSR-1

Given that GEF-H1 catalytic activity is dispensable for HRAS^{V12}-dependent MAPK pathway activation, we hypothesized that GEF-H1 may be providing a scaffold function for components of the MAPK pathway. We investigated whether GEF-H1 could form a complex with KSR-1, the major scaffold for the MAPK pathway. We detected an interaction between endogenous GEF-H1 and endogenous KSR-1 in GEF-H1 immunoprecipitates from wild-type, but not *Arhgef2*$^{-/-}$, MEFs (Figure S3D). Similarly, in an overexpression system, we detected an interaction between KSR-1 and a mutant of GEF-H1 deleted of the negative regulatory sequences between amino acids 87–151 and unbound from microtubules (GEF-H1$^{\Delta 87-151}$, Meiri et al., 2012) (Figure S3E). To discern which domains of KSR-1 interact with GEF-H1, we analyzed Flag-GEF-H1 immune complexes from cells that expressed full-length or a series of Pyo-tagged KSR-1 deletions (Figure 4C). We found that full-length KSR-1, KSR-1 (1–539), KSR-1(1–424), and KSR-1(542–873) interacted with full-length GEF-H1 (Figure 4D). These data show that KSR-1 can form a complex with GEF-H1 and that both the C1 domain and the kinase domain of KSR-1 contribute to GEF-H1 binding.

We next sought to determine whether ERK1/2 activation by GEF-H1 was dependent on KSR-1. Expression of the active GEF-H1$^{\Delta 87-151}$ mutant (Figure 4B) in wild-type MEFs induced strong ERK1/2 phosphorylation even in the absence of HRAS^{V12} expression (Figure 4E, lane 2), whereas *Ksr1*$^{-/-}$ MEFs were resistant to GEF-H1$^{\Delta 87-151}$-induced ERK1/2 phosphorylation (Figure 4E, lane 3 and 4). Re-expression of KSR-1 restored GEF-H1$^{\Delta 87-151}$-induced ERK1/2 phosphorylation in *Ksr1*$^{-/-}$ cells (Figure 4E, lane 5), whereas re-expression of KSR-1 in the absence of GEF-H1$^{\Delta 87-151}$ alone had little effect on ERK1/2 phosphorylation (Figure 4E, lane 6). These data confirm that GEF-H1 requires KSR-1 to positively regulate ERK1/2 activation.

Platelet-derived growth factor (PDGF) or HRAS^{V12} induce the dephosphorylation of KSR-1 at S392 and its subsequent translocation from the cytoplasm to the plasma membrane (Ory et al., 2003). We therefore examined the requirement of GEF-H1 for PDGF-induced KSR-1 membrane translocation (Figure 5A). In 22% (21 of 97) of wild-type cells, KSR-1 translocated from the cytoplasm to the plasma membrane in a PDGF-dependent manner (Figure 5A, columns 1 and 2; Figure S4A). By contrast, only 3.5% of cells (3 of 87) underwent PDGF-dependent membrane translocation in *Arhgef2*$^{-/-}$ cells (Figure 5A, columns 3 and 4; Figure S4A), a defect that was rescued by the expression of wild-type GEF-H1 (Figure 5A, columns 5 and 6; Figure S4A). Because translocation of KSR-1 to the plasma membrane requires dephosphorylation of S392, we queried whether the S392A point mutant form of KSR-1 could rescue the dependence on GEF-H1 for translocation to the plasma membrane. We expressed wild-type KSR-1 or KSR-1^{S392A} in *Arhgef2*$^{-/-}$ cells and found that, in the absence of growth factor stimulation, wild-type KSR-1 was rarely associated with the plasma membrane (9% or 6 of 69 cells, Figures 5B and S4B), whereas KSR-1^{S392A} efficiently localized to the plasma membrane even in the absence of GEF-H1 (37% or 28 of 76 cells) (Figure 5B, columns 1 and 2; Figure S4B). These data show that GEF-H1 is required for the translocation of KSR-1 to the plasma membrane in a manner that depends on the dephosphorylation of KSR-1 on S392. Re-expression of GEF-H1 and KSR-1 in *Arhgef2*$^{-/-}$ MEFs was insufficient to induce membrane translocation of KSR-1 in the absence of PDGF treatment (6% or 4 of 67 cells) (Figure 5B, column 3; Figure S4B). However, the requirement for growth factor-stimulated KSR-1 translocation to the plasma membrane could be circumvented by the expression of the non-microtubule-associated form of GEF-H1, GEF-H1$^{\Delta 87-151}$ (Meiri et al., 2012), with 30% (21 of 71) of cells exhibiting KSR-1 plasma membrane localization (Figure 5B, column 4; Figure S4B). These data suggest that the growth factor dependence of KSR-1 translocation to the plasma membrane is contingent on the release of GEF-H1 from the microtubule array. Importantly, we found that the endogenous interaction of GEF-H1 and KSR-1 was induced between 5–20 min of PDGF stimulation, correlating with their translocation to the plasma membrane (Figure 5C). These data suggest that endogenous complex formation between GEF-H1 and KSR-1 occurs at the plasma membrane in response to PDGF treatment.

To clarify whether the dependence of HRAS^{V12} on GEF-H1 for cell survival was mediated through KSR-1, we measured cell viability following ectopic expression of wild-type KSR-1 or KSR-1^{S392A} with HRAS^{V12} in *Arhgef2*$^{-/-}$ MEFs and found that only KSR-1^{S392A} restored cellular viability (Figures 5D and 5E). These data provide genetic evidence that dephosphorylation of the negative regulatory site S392 on KSR-1 is the critical target downstream of GEF-H1 that supports cell survival in HRAS^{V12}-transformed cells.

To determine whether GEF-H1 regulation of the HRAS^{V12}/MAPK cascade is coupled to the dephosphorylation of KSR-1, we asked whether wild-type KSR-1 or KSR-1^{S392A} could restore HRAS^{V12}-induced ERK1/2 phosphorylation in the absence of GEF-H1. HRAS^{V12} expression induced ERK1/2 phosphorylation in control hairpin-expressing MEFs, but not in cells depleted of GEF-H1 (Figure 5F, lanes 2 and 4). High expression of rGEF-H1 in GEF-H1-depleted cells greatly enhanced ERK1/2 activation in response to HRAS^{V12}, supporting the model that increased levels of GEF-H1 result in amplification of the MAPK

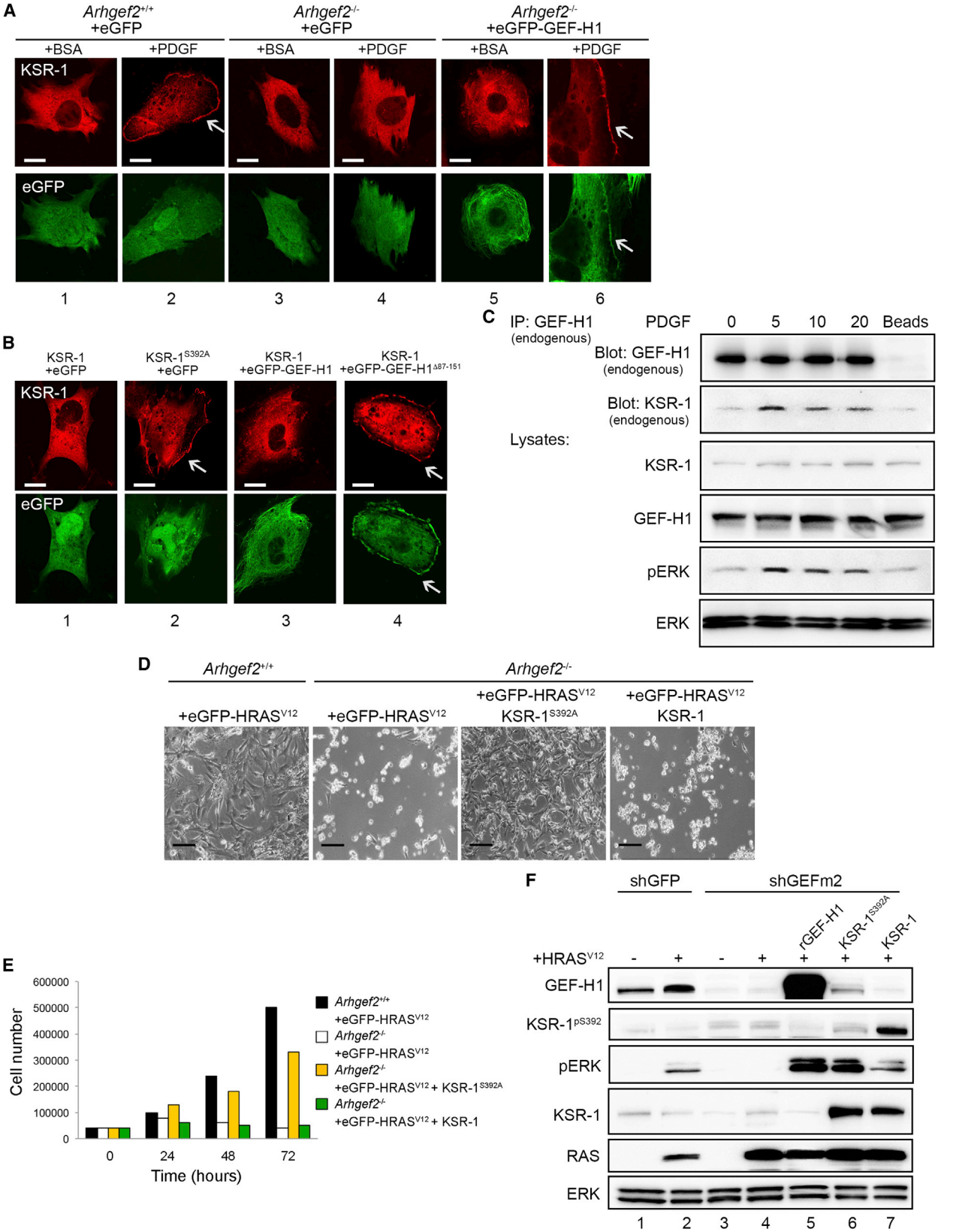

(legend on next page)

cascade (Figure 5F, lane 5). Expression of KSR-1^{S392A} efficiently restored HRAS^{V12}-mediated ERK1/2 phosphorylation in GEF-H1 knockdown cells compared to wild-type KSR-1 (Figure 5F, lanes 6 and 7). These data demonstrate that dephosphorylation of KSR-1 S392 is sufficient to overcome the GEF-H1-dependence of HRAS^{V12}-mediated ERK1/2 activation.

GEF-H1 Is Required for PP2A-Mediated Dephosphorylation of KSR-1

In an independent study, we identified GEF-H1 as a PP2A interacting partner in a proteomic screen designed to probe for proteins that bound to the PP2A catalytic subunit (D.M., C.B.M., J.L., M. Mullin, A.-C.G., M.I., and R.R., unpublished data) and found that GEF-H1 interacts with the B' regulatory PP2A subunits (PPP2R5A, PPP2R5B, and PPP2R5E). We hypothesized that GEF-H1 may function as a bridge between KSR-1 and PP2A to control KSR-1 S392 dephosphorylation. First, we confirmed the previously published data showing an interaction between KSR-1 and the B' regulatory PP2A subunits (Figure 6A) (Ory et al., 2003). We observed that GEF-H1 bound to the same PP2A subunits that interacted with KSR-1 (Figure 6A). We next determined the regions of GEF-H1 involved in PP2A and KSR-1 binding by expressing deletion mutants of GEF-H1 (Figure 6B) and probing for the catalytic subunit of PP2A and KSR-1 in GEF-H1 immune complexes (Figure 6C). Analysis of GEF-H1 immunoprecipitates revealed that endogenous KSR-1 interacted with full-length GEF-H1, GEF-H1(236–572), and GEF-H1(236–433). These results localize the binding site for KSR-1 to the DH domain of GEF-H1, while endogenous PP2Ac binds to the GEF-H1 PH domain (Figure 6C). These data show that KSR-1 and PP2A bind to distinct sites on GEF-H1 and suggest that GEF-H1 may function to bridge PP2A to KSR-1.

To determine whether GEF-H1 acts as a bridge to link KSR-1 to PP2A, we stably infected human embryonic kidney 293T (HEK293T) cells expressing the PP2A B' subunit with an shRNA targeting GEF-H1 and probed PP2A immunoprecipitates for endogenous KSR-1 (Figure 6D). KSR-1 was detected in immune complexes of PP2A B' subunits in shGFP-expressing cells, but not those depleted of GEF-H1. Thus, the interaction between KSR-1 and PP2A is dependent on GEF-H1. These data support a model whereby GEF-H1 provides a bridging function to recruit the PP2A B' subunits required for the dephosphorylation of the negative regulatory S392 site on KSR-1 and activation of the MAPK pathway.

Given that dephosphorylation of KSR-1 on S392 is induced in response to PDGF and oncogenic RAS, we sought to determine whether the interaction between GEF-H1 and KSR-1 was similarly regulated. We isolated Flag-PPP2R5E immune complexes from HEK293T cells and probed them for the presence of GEF-H1 and KSR-1 after PDGF treatment (Figure 6E). Although GEF-H1 and KSR-1 were not detectable in PPP2R5E immune complexes in starved cells, both GEF-H1 and KSR-1 were recruited to PPP2R5E immune complexes after 5 min of PDGF stimulation and disappeared after 15 min (Figure 6E). Moreover, induction of oncogenic HRAS with 4-OHT induced a protein complex composed of endogenous KSR-1, GEF-H1, and PPP2R5E proteins after 20 min and extending to 90 min following RAS activation (Figure S5). These data show that PDGF or HRAS^{V12} induce the formation of a KSR-1, GEF-H1, and PP2A protein complex. Moreover, the complex appears to be temporally regulated, suggesting the presence of feedback mechanisms that attenuate its assembly even with constitutive activation of the pathway.

GEF-H1 Is Important for the Growth of RAS Mutant Pancreatic Tumor Xenografts

Over 90% of human pancreatic ductal adenocarcinomas (PDACs) harbor activating mutations in *KRAS* (Smit et al., 1988). We evaluated whether GEF-H1 expression was increased in PDAC by immunohistochemistry on pancreatic tissue microarrays (TMAs). We probed tissue sections of 14 normal pancreatic ducts, 32 PanIN-1 (A and B) lesions, 9 PanIN-2 and IN-3 lesions, and 14 PDAC tumor samples for GEF-H1 expression using a monoclonal antibody against GEF-H1 (Figure 7A). Normal pancreatic ducts and PanIN-1 lesions did not express GEF-H1, whereas greater than 90% (21 out of 23) of the more advanced histologic grades expressed GEF-H1 (Figures 7A and S6A). These data demonstrate that GEF-H1 expression is positively correlated with neoplastic progression of pancreatic tumors. Treatment of the PDAC cell line PANC-1, harboring a *KRAS*^{D12} mutation, with MEK inhibitors PD98059 or UO126 resulted in reduced GEF-H1 levels (Figure S6B). Together, these data show that GEF-H1 expression is increased in PDAC cells in a manner that is dependent on MAPK pathway activation.

To determine whether GEF-H1 was necessary for MAPK pathway activation in PDAC cells, we knocked down GEF-H1 in PANC-1 cells and observed increased KSR-1 S392 phosphorylation and a corresponding decrease in ERK1/2

Figure 5. KSR-1 Signals through GEF-H1 in Response to PDGF and Oncogenic RAS

(A) Wild-type or *Arhgef2*$^{-/-}$ MEFs were transfected with eGFP or eGFP-GEF-H1 and treated with BSA or 25 ng/ml PDGF for 10 min and fixed and stained for endogenous KSR-1. Arrows indicate KSR-1 plasma membrane localization and eGFP-GEF-H1 localization. Scale bars, 20 μm. Images are representative of four independent experiments.

(B) *Arhgef2*$^{-/-}$ MEFs were co-transfected with KSR-1 or KSR-1^{S392A} and eGFP, eGFP-GEF-H1, or eGFP-GEF-H1$^{\Delta 87–151}$ and stained for endogenous KSR-1. Arrows and scale bars are as in (A), and images are representative of four independent experiments.

(C) HEK293T cells were starved for 12 hr and treated with BSA or 25 ng/ml PDGF for 5, 10, or 20 min. Endogenous GEF-H1 immune complexes were isolated and probed for the presence of endogenous KSR-1. Lysates were probed for total levels of GEF-H1 and KSR-1. pERK and ERK reflect the temporality of MAPK pathway activation and total protein levels, respectively.

(D) Representative bright field images of wild-type or *Arhgef2*$^{-/-}$ MEFs expressing eGFP-HRAS^{V12}, eGFP-HRAS^{V12} + Pyo-KSR-1, or eGFP-HRAS^{V12} + Pyo-KSR-1^{S392A} 72 hr after transfection. Scale bars, 100 μm.

(E) Quantification of the number of viable cells described in (D) 24, 48, and 72 hr after transfection; 4 × 10^4 cells were plated at time 0.

(F) MEFs stably expressing shGFP or shGEFm2 were transfected with vector, HRAS^{V12}, or co-transfected with HRAS^{V12} and Flag-rGEF-H1, Pyo-KSR-1^{S392A}, or Pyo-KSR-1. KSR-1 S392 phosphorylation was assessed with a pS392-specific KSR-1 antibody.

See also Figure S4.

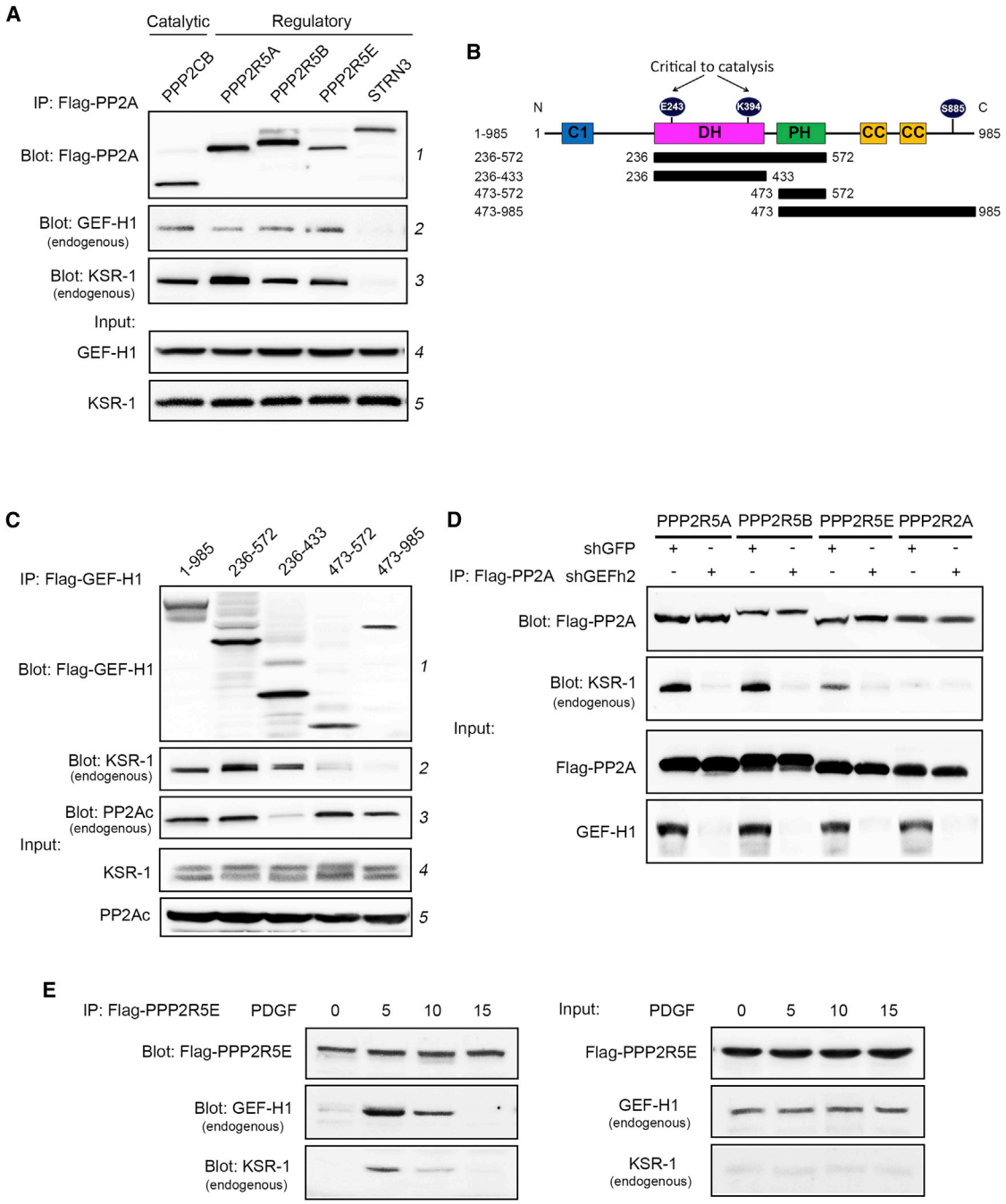

Figure 6. GEF-H1 Is Required for PP2A-Mediated Dephosphorylation of KSR-1 on S392

(A) Flag-PP2A immune complexes were isolated from stable Flag-PP2A catalytic and regulatory subunit-expressing HEK293T cells using anti-Flag antibodies. Flag-PP2A complexes were probed for endogenous GEF-H1 and endogenous KSR-1 (rows 2 and 3). Total expression levels of GEF-H1 and KSR-1 in lysates are shown in rows 4 and 5.

(B) Schematic representation of GEF-H1 constructs used in (C).

(C) Flag-tagged truncated variants of GEF-H1 were expressed in HEK293T cells, and protein complexes were immunoprecipitated with anti-Flag antibodies. Lysates were probed with anti-KSR-1 or anti-PP2Ac antibodies.

(D) HEK293T cells stably expressing Flag-tagged PP2A regulatory subunits were infected with shGFP or shGEFh2 lentiviruses. Flag-PP2A subunits were immunopurified with anti-Flag (row 1) and probed for endogenous KSR-1 (row 2). Flag-PP2A subunit expression (row 3) and GEF-H1 knockdown (row 4) were confirmed by immunoblotting lysates with Flag and GEF-H1 antibodies, respectively.

(E) HEK293T cells stably expressing Flag-PPP2R5E were treated with 25 ng/ml PDGF for 0, 5, 10, or 15 min. Flag-PPP2R5E immune complexes were isolated with anti-Flag antibodies and probed for the presence of endogenous GEF-H1 and KSR-1 (left panel). Lysates were probed for total levels of Flag-PPP2R5E, endogenous GEF-H1 and KSR-1 (right panel).

See also Figure S5.

phosphorylation compared with control hairpin-expressing cells (Figure 7B). Expression of shRNA-resistant GEF-H1$^{\Delta 87-151}$ restored the basal levels of phosphorylated KSR-1 and ERK1/2 in GEF-H1-depleted cells (Figure 7B). These data indicate that GEF-H1 is both necessary and sufficient for KSR-1 S392 dephosphorylation and ERK1/2 activation in PDAC cells harboring endogenous RAS mutations. Expression of KSR-1^{S392A}, but not wild-type KSR-1, corrected the defect in the phosphorylated ERK levels in GEF-H1 knockdown cells, showing that active KSR-1 can circumvent the need for GEF-H1 in PANC-1 cells (Figure 7B).

We tested the contribution of GEF-H1 to the in vitro cell growth of four human KRAS mutant pancreatic cancer derived cell lines including PANC-1 Panc 08.13, Panc 04.03, and PL-45 (Figures S6C–S6F). These cell lines displayed varying sensitivity to GEF-H1 depletion for cell growth (a 50%, 90%, 80%, and 65% reduction, respectively) compared to control hairpin-expressing cells. Of the six pancreatic lines that we had tested, we examined the contribution of GEF-H1 to tumor growth in three of these lines, PANC-1 (*KRAS*^{D12}), HPAF-II (*KRAS*^{D12}), and BxPC3 (wild-type *KRAS*), in immune-deficient mice. PANC-1 and HPAF-II cells exhibited profound attenuation of tumor growth relative to control hairpin cells (Figures 7C, S6G, and S6H). The tumor growth of BxPC3 cells was not affected by depletion of GEF-H1, highlighting the dependency of oncogenic RAS on GEF-H1 (Figures 7C and S6I). In addition, increased tumor-associated caspase 3 cleavage was observed in PANC-1 xenografts (Figure S6J). Collectively, our data demonstrate an amplifying feedback loop involving GEF-H1 in the RAS/MAPK pathway across a variety of cell types expressing different mutant RAS family members. These data support the model that GEF-H1 is important for the growth of tumor cells harboring activating mutations in RAS.

DISCUSSION

Signaling through the RAS/MAPK pathway is gated by KSR-1, a highly conserved scaffold protein that ensures strict spatiotemporal regulation of ERK activation. Genetic studies have demonstrated a critical requirement of KSR-1 for growth factor-mediated signaling through the RAS/MAPK pathway (Sieburth et al., 1999; Lozano et al., 2003) and the formation of HRAS^{V12}-dependent tumors (Xiao et al., 2010). The requirement of KSR-1 in HRAS^{V12}-mediated transformation is strictly dependent on the dephosphorylation of KSR-1 at S392 by PP2A (Razidlo et al., 2004). In this study, we provide a mechanistic explanation of how the B' subunit is recruited to the PP2A/KSR-1 complex and uncover a positive feedback loop involving the RhoGEF GEF-H1 that is necessary for HRAS^{V12}-mediated transformation. We show that *Arhgef2* is a direct transcriptional target of the RAS/MAPK pathway, and its elevated protein expression is similarly responsive to oncogenic BRAF and H-, K-, and NRAS family members. We demonstrate that GEF-H1 contributes to the growth and survival of BRAF^{V600E} and HRAS^{V12}-transformed NIH 3T3 cells and PDAC xenografts. We anticipate that there may be examples of escape mechanisms whereby some RAS mutant tumors no longer depend on the GEF-H1 amplifying loop, which will be an area of future investigation.

The discovery that a RhoGEF is involved in a positive feedback loop for the MAPK pathway suggests a model whereby amplification of the MAPK pathway could be coupled to signal diversification through the activation of RhoA, a known component of the RAS transformation program (Qiu et al., 1995; Prendergast et al., 1995; Sahai et al., 2001; Chen et al., 2003). Our data suggest that oncogenic RAS induces RhoA-GTP independently of GEF-H1, a finding consistent with the previously reported model that a decrease in p190RhoGAP activity, rather than an increase in total cellular RhoGEF activity, controls RhoA-GTP levels in HRAS^{V12}-transformed cells (Chen et al., 2003). The observation that overexpression of GEF-H1 is sufficient to increase MEK1/2 and ERK1/2 phosphorylation raises the possibility that the oncogenic potential of GEF-H1 is mediated through its capacity to increase cellular Rho-GTP levels and/or activate the MAPK pathway.

An important implication that follows from this study is the possibility that mitogenic signals conveyed through the MAPK pathway might be coupled to microtubule function through GEF-H1, thereby coordinating growth signals with changes in cell shape, migration, and/or morphogenesis. We show that the mutant GEF-H1$^{\Delta 87-151}$, unable to interact with the microtubule array, is largely cytoplasmic (Meiri et al., 2012) and is able to induce KSR-1 membrane translocation and ERK1/2 phosphorylation in the absence of either PDGF or oncogenic RAS. These findings suggest that the release of GEF-H1 from microtubules links HRAS^{V12} to KSR-1 function. This idea is supported by the observations that depolymerization of microtubules potently activates components of the MAPK pathway through currently unknown mechanisms (Birukova et al., 2005; Guo et al., 2012; Hayne et al., 2000). Active HRAS contributes to microtubule instability that may promote the invasive behavior of transformed cells and reinforce the GEF-H1 positive feedback loop on the MAPK pathway (Harrison and Turley, 2001). In addition, ERK phosphorylation and activation of GEF-H1 (Fujishiro et al., 2008) might trigger its release from microtubules, where it can interact with cytosolic KSR-1. The signaling events that coordinate the spatial coupling of GEF-H1 with cytosolic KSR-1 remain to be elucidated.

The identification of GEF-H1 as a component of the RAS signaling circuitry is part of an emerging role of RhoGEFs in RAS signaling. TIAM1, a Rac exchange factor, is directly activated by RAS-GTP through a RAS binding motif in its N terminus and is required for RAS-induced skin tumors (Lambert et al., 2002; Malliri et al., 2002). The RhoGEF AKAP-Lbc was shown to couple PKA to KSR-1 through its A-kinase anchoring protein scaffold function (Smith et al., 2010). GEF-H1 may also be important in other genetic contexts, because it has been reported to contribute to the growth and survival of cell lines harboring stabilizing p53 mutations and those expressing the oncogene hPTTG1 (Mizuarai et al., 2006; Liao et al., 2012).

The GEF-H1-mediated feedback loop adds to a growing number of other feedback loops that control flux through the MAPK pathway. ERK1/2-dependent phosphorylation of upstream components SOS, RAF, and EGFR (Buday et al., 1995; Porfiri and McCormick, 1996; Dougherty et al., 2005; Ritt et al., 2010; Heisermann et al., 1990; Li et al., 2008) dampens further pathway activation, and a second, kinetically slower, negative feedback loop involves the induction of DUSP phosphatases that directly

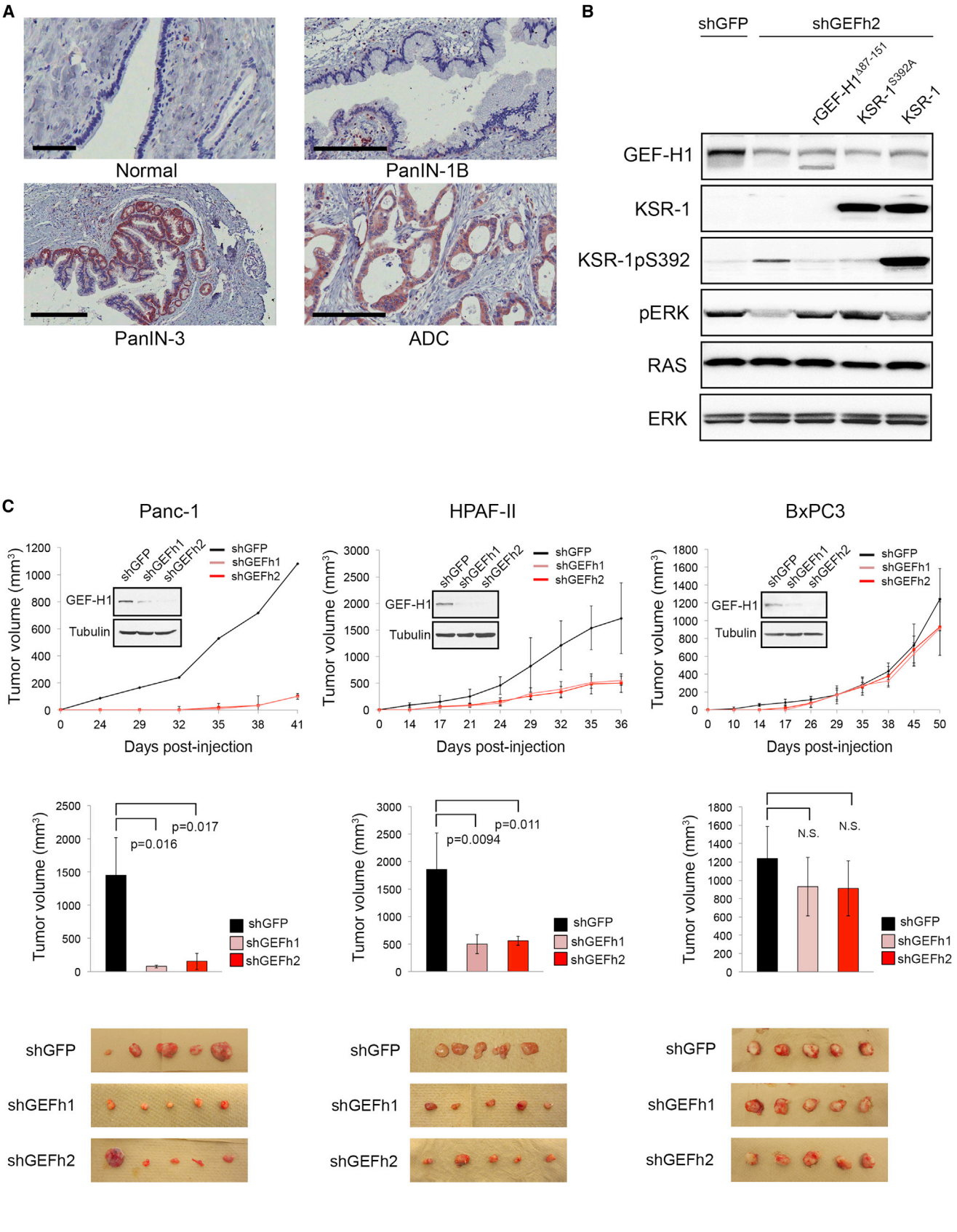

(legend on next page)

dephosphorylate ERK1/2 (Owens and Keyse, 2007). The elaboration of the MAPK pathway with both positive and negative feedback loops ensures that the amplitude and persistence of the MAPK signal is both robust and tunable so as to serve the multiplicity of developmental and mitogenic functions it provides.

In summary, we have found that the induction of GEF-H1 in RAS mutant cells amplifies MAPK signaling and contributes to pancreatic tumor xenograft growth. The identification of GEF-H1 as a component of a positive amplifying loop critical for $HRAS^{V12}$-mediated transformation therefore provides mechanistic insight into the manifold features of the transformation program activated by mutant RAS in human cancers.

EXPERIMENTAL PROCEDURES

Animal Studies

All animal studies were carried out using protocols that have been approved by the University Health Network Animal Care Committee. Detailed experimental procedures are provided in Supplemental Experimental Procedures.

Cell Treatments

ER:$HRAS^{V12}$ MEFs were starved in DMEM containing 0% FBS for 16 hr then treated with 100 nM 4-OHT (Sigma). For MEK and PI3K inhibition experiments, cell lines were cultured in complete medium and incubated with PD98059, UO126, or LY294002 (Sigma) diluted in DMSO (Sigma) for 48 hr. For immunofluorescence studies, MEFs were starved for 24 hr in 0% FBS and treated in DMEM containing 10 mM HEPES and 0.5 mg/ml fatty acid-free BSA (A8806, Sigma). PDGF (Sigma) was suspended in HBSS containing 0.5 mg/ml fatty acid-free BSA and 20 mM HEPES to a stock concentration of 1 μM.

Luciferase Reporter Assays

The regulatory sequence of murine *Arhgef2* (nucleotides 62–1,968 upstream of the transcription start site) was PCR-amplified from mouse BAC clones and inserted into the pGL3 luciferase vector to generate p*Arhgef2*Luc (Promega, E1910). MEFs or NIH 3T3 cells expressing empty vector, $KRAS^{D12}$, or $BRAF^{V600E}$ were plated in a 24-well plate in triplicate at 7×10^4 cells/well. After 16 hr, cells were cotransfected with 50 ng p*Arhgef2*Luc, empty vector, T7-$HRAS^{V12}$, or T7-$KRAS^{D12}$ expression plasmids and 1 ng phRL-SV40 (Promega) using LipoD293 (SignaGen, SL100668) or Lipofectamine 2000 (Invitrogen) according to the manufacturer's instructions. Twenty four hours after transfection, cells were lysed and assayed for firefly and renilla luciferase activity using the Dual-Luciferase Reporter System (Promega). Where indicated, cells were treated with DMSO, PD98059, UO126, or LY294002 for 16 hr prior to cell lysis.

Immunohistochemistry

In this study, we used a human pancreatic TMA generated in a previously published study (Al-Aynati et al., 2004). The use of this TMA in this study was approved by the University Health Network Research Ethics Board (protocol 04-0018T). Immunohistochemistry was performed using the Biotin-Streptavidin-HRP detection system and a human GEF-H1 antibody (14B11 mouse monoclonal antibody) at 1:500 dilution. To evaluate the expression levels of GEF-H1, staining intensity in the ductal cells or lesions were judged by two pathologists and scored as 2 (strong staining), 1 (weak staining), or 0 (absent staining). For NIH 3T3 xenograft studies, tumor sections were fixed in OCT medium, flash frozen in methylbutanol, and stored at −80°C before being sent for immunohistological processing at Toronto General Hospital's Pathology Department. PDAC xenograft tumors were fixed in 10% formalin, paraffin embedded, and sent for immunohistological processing at the Applied Molecular Profiling Lab (Princess Margaret Hospital, Toronto, Canada). Tumor sections were probed for caspase 3 cleavage using anti-cleaved caspase 3 (Asp 175) antibody (CST 9661).

Promoter Analysis of GEF-H1

Phylogenetic footprinting analysis was performed using mouse and human sequences of *ARHGEF2* (NM_1162383.1 and NM_004723.3, respectively) (Zhang and Gerstein, 2003). Sequences were aligned to the genome with BLAT, where the TSS was ascertained, and DNA 1 kb downstream (3′) and 5 kb upstream (5′) were pulled from the database. The 5 kb and 1 kb segments were analyzed separately using Consite (Sandelin et al., 2004), employing all matrices found in the public Jaspar database.

Statistical Analyses

Values are expressed as means ± SD. Paired Student's t tests (Kirkman, 2006) were performed to determine statistical significance between samples. Experiments were performed at least three times, and means with $p < 0.05$ were considered statistically significant.

See Supplemental Experimental Procedures for descriptions of all other experimental procedures.

SUPPLEMENTAL INFORMATION

Supplemental Information includes Supplemental Experimental Procedures, six figures, and one table and can be found with this article online at http://dx.doi.org/10.1016/j.ccr.2014.01.025.

ACKNOWLEDGMENTS

We gratefully acknowledge Marc Therrien (l'IRIC), D. Morrison (National Cancer Institute), J. Scott (Howard Hughes Medical Institute, University of Washington), J. Downward (London Research Institute), G. Mills (The University of Texas MD Anderson Cancer Centre), and D. Bar-Sagi (Langone Medical Centre) for reagents used in this study. R. Agbanay (UHN) assisted with animal studies and A. Daulat (University of Toronto) assisted with luciferase assays. The authors thank Helen Burston for careful reading of the manuscript. This work was supported by the Canadian Institute for Health Research and a joint grant from the Terry Fox Research Institute and the Ontario Institute for Cancer Research.

Received: March 24, 2013
Revised: November 26, 2013
Accepted: January 23, 2014
Published: February 10, 2014

REFERENCES

Al-Aynati, M.M., Radulovich, N., Riddell, R.H., and Tsao, M.S. (2004). Epithelial-cadherin and beta-catenin expression changes in pancreatic intraepithelial neoplasia. Clin. Cancer Res. *10*, 1235–1240.

Figure 7. GEF-H1 Is Important for the Growth of RAS Mutant Pancreatic Tumor Xenografts

(A) GEF-H1 expression in tissue sections of normal pancreatic ducts, PanIN-1B, PanIN-3, or pancreatic adenocarcinoma (ADC) was determined by immunohistochemistry. GEF-H1 staining is represented in brown. Scale bars, 60 μm (Normal); 200 μm (PanIN-1B); 300 μm (PanIN-3); and 200 μm (ADC).

(B) PANC-1 cells were infected with shGFP or shGEFh2 and transfected with Flag-GEF-$H1^{\Delta 87-151}$, Pyo-KSR-1^{S392A}, or Pyo-KSR-1. Lysates were probed for the indicated proteins by immunoblotting.

(C) Indicated cells were infected with shGFP, shGEFh1, or shGEFh2, and GEF-H1 protein expression was assayed by western blot using tubulin as a loading control (insets). Growth curves of xenografts derived from 2×10^5 cells are depicted in the top row. Final mean tumor volumes are depicted in the middle row, and representative images of dissected tumors from one of two experiments performed per cell line are shown in the bottom row. Data are representative of two independent experiments ± SD of n = 5 tumors per condition. N.S. denotes that statistical difference was not significant (p value > 0.05).

See also Figure S6.

Birukova, A.A., Birukov, K.G., Gorshkov, B., Liu, F., Garcia, J.G., and Verin, A.D. (2005). MAP kinases in lung endothelial permeability induced by microtubule disassembly. Am. J. Physiol. Lung Cell. Mol. Physiol. *289*, L75–L84.

Brecht, M., Steenvoorden, A.C., Collard, J.G., Luf, S., Erz, D., Bartram, C.R., and Janssen, J.W. (2005). Activation of gef-h1, a guanine nucleotide exchange factor for RhoA, by DNA transfection. Int. J. Cancer *113*, 533–540.

Buday, L., Warne, P.H., and Downward, J. (1995). Downregulation of the Ras activation pathway by MAP kinase phosphorylation of Sos. Oncogene *11*, 1327–1331.

Cacace, A.M., Michaud, N.R., Therrien, M., Mathes, K., Copeland, T., Rubin, G.M., and Morrison, D.K. (1999). Identification of constitutive and ras-inducible phosphorylation sites of KSR: implications for 14-3-3 binding, mitogen-activated protein kinase binding, and KSR overexpression. Mol. Cell. Biol. *19*, 229–240.

Chen, J.C., Zhuang, S., Nguyen, T.H., Boss, G.R., and Pilz, R.B. (2003). Oncogenic Ras leads to Rho activation by activating the mitogen-activated protein kinase pathway and decreasing Rho-GTPase-activating protein activity. J. Biol. Chem. *278*, 2807–2818.

Cheng, I.K., Tsang, B.C., Lai, K.P., Ching, A.K., Chan, A.W., To, K.F., Lai, P.B., and Wong, N. (2012). GEF-H1 over-expression in hepatocellular carcinoma promotes cell motility via activation of RhoA signalling. J. Pathol. *228*, 575–585.

Davies, H., Bignell, G.R., Cox, C., Stephens, P., Edkins, S., Clegg, S., Teague, J., Woffendin, H., Garnett, M.J., Bottomley, W., et al. (2002). Mutations of the BRAF gene in human cancer. Nature *417*, 949–954.

Dougherty, M.K., Müller, J., Ritt, D.A., Zhou, M., Zhou, X.Z., Copeland, T.D., Conrads, T.P., Veenstra, T.D., Lu, K.P., and Morrison, D.K. (2005). Regulation of Raf-1 by direct feedback phosphorylation. Mol. Cell *17*, 215–224.

Engers, R., Zwaka, T.P., Gohr, L., Weber, A., Gerharz, C.D., and Gabbert, H.E. (2000). Tiam1 mutations in human renal-cell carcinomas. Int. J. Cancer *88*, 369–376.

Estep, A.L., Palmer, C., McCormick, F., and Rauen, K.A. (2007). Mutation analysis of BRAF, MEK1 and MEK2 in 15 ovarian cancer cell lines: implications for therapy. PLoS ONE *2*, e1279.

Frolov, A., Chahwan, S., Ochs, M., Arnoletti, J.P., Pan, Z.Z., Favorova, O., Fletcher, J., von Mehren, M., Eisenberg, B., and Godwin, A.K. (2003). Response markers and the molecular mechanisms of action of Gleevec in gastrointestinal stromal tumors. Mol. Cancer Ther. *2*, 699–709.

Fujishiro, S.H., Tanimura, S., Mure, S., Kashimoto, Y., Watanabe, K., and Kohno, M. (2008). ERK1/2 phosphorylate GEF-H1 to enhance its guanine nucleotide exchange activity toward RhoA. Biochem. Biophys. Res. Commun. *368*, 162–167.

Greenman, C., Stephens, P., Smith, R., Dalgliesh, G.L., Hunter, C., Bignell, G., Davies, H., Teague, J., Butler, A., Stevens, C., et al. (2007). Patterns of somatic mutation in human cancer genomes. Nature *446*, 153–158.

Guo, X., Zhang, X., Li, Y., Guo, Y., Wang, J., Li, Y., Shen, B., Sun, D., and Zhang, J. (2012). Nocodazole increases the ERK activity to enhance MKP-1expression which inhibits p38 activation induced by TNF-α. Mol. Cell. Biochem. *364*, 373–380.

Gupta, S., Ramjaun, A.R., Haiko, P., Wang, Y., Warne, P.H., Nicke, B., Nye, E., Stamp, G., Alitalo, K., and Downward, J. (2007). Binding of ras to phosphoinositide 3-kinase p110alpha is required for ras-driven tumorigenesis in mice. Cell *129*, 957–968.

Harrison, R.E., and Turley, E.A. (2001). Active erk regulates microtubule stability in H-ras-transformed cells. Neoplasia *3*, 385–394.

Hayne, C., Tzivion, G., and Luo, Z. (2000). Raf-1/MEK/MAPK pathway is necessary for the G2/M transition induced by nocodazole. J. Biol. Chem. *275*, 31876–31882.

Heisermann, G.J., Wiley, H.S., Walsh, B.J., Ingraham, H.A., Fiol, C.J., and Gill, G.N. (1990). Mutational removal of the Thr669 and Ser671 phosphorylation sites alters substrate specificity and ligand-induced internalization of the epidermal growth factor receptor. J. Biol. Chem. *265*, 12820–12827.

Jacobs, D., Glossip, D., Xing, H., Muslin, A.J., and Kornfeld, K. (1999). Multiple docking sites on substrate proteins form a modular system that mediates recognition by ERK MAP kinase. Genes Dev. *13*, 163–175.

Janssens, V., and Goris, J. (2001). Protein phosphatase 2A: a highly regulated family of serine/threonine phosphatases implicated in cell growth and signalling. Biochem. J. *353*, 417–439.

Kirkman, T.W. (2006). Statistics to use. http://www.physics.csbsju.edu/stats.

Lambert, J.M., Lambert, Q.T., Reuther, G.W., Malliri, A., Siderovski, D.P., Sondek, J., Collard, J.G., and Der, C.J. (2002). Tiam1 mediates Ras activation of Rac by a PI(3)K-independent mechanism. Nat. Cell Biol. *4*, 621–625.

Li, X., Huang, Y., Jiang, J., and Frank, S.J. (2008). ERK-dependent threonine phosphorylation of EGF receptor modulates receptor downregulation and signaling. Cell. Signal. *20*, 2145–2155.

Liao, Y.C., Ruan, J.W., Lua, I., Li, M.H., Chen, W.L., Wang, J.R., Kao, R.H., and Chen, J.H. (2012). Overexpressed hPTTG1 promotes breast cancer cell invasion and metastasis by regulating GEF-H1/RhoA signalling. Oncogene *31*, 3086–3097.

Lozano, J., Xing, R., Cai, Z., Jensen, H.L., Trempus, C., Mark, W., Cannon, R., and Kolesnick, R. (2003). Deficiency of kinase suppressor of Ras1 prevents oncogenic ras signaling in mice. Cancer Res. *63*, 4232–4238.

Macara, I.G., Lounsbury, K.M., Richards, S.A., McKiernan, C., and Bar-Sagi, D. (1996). The Ras superfamily of GTPases. FASEB J. *10*, 625–630.

Malliri, A., van der Kammen, R.A., Clark, K., van der Valk, M., Michiels, F., and Collard, J.G. (2002). Mice deficient in the Rac activator Tiam1 are resistant to Ras-induced skin tumours. Nature *417*, 867–871.

Marcotte, R., Brown, K.R., Suarez, F., Sayad, A., Karamboulas, K., Krzyzanowski, P.M., Sircoulomb, F., Medrano, M., Fedyshyn, Y., Koh, J.L., et al. (2012). Essential gene profiles in breast, pancreatic, and ovarian cancer cells. Cancer Discov *2*, 172–189.

Meiri, D., Marshall, C.B., Greeve, M.A., Kim, B., Balan, M., Suarez, F., Bakal, C., Wu, C., Larose, J., Fine, N., et al. (2012). Mechanistic insight into the microtubule and actin cytoskeleton coupling through dynein-dependent RhoGEF inhibition. Mol. Cell *45*, 642–655.

Michaud, N.R., Therrien, M., Cacace, A., Edsall, L.C., Spiegel, S., Rubin, G.M., and Morrison, D.K. (1997). KSR stimulates Raf-1 activity in a kinase-independent manner. Proc. Natl. Acad. Sci. USA *94*, 12792–12796.

Mizuarai, S., Yamanaka, K., and Kotani, H. (2006). Mutant p53 induces the GEF-H1 oncogene, a guanine nucleotide exchange factor-H1 for RhoA, resulting in accelerated cell proliferation in tumor cells. Cancer Res. *66*, 6319–6326.

Moodie, S.A., Willumsen, B.M., Weber, M.J., and Wolfman, A. (1993). Complexes of Ras.GTP with Raf-1 and mitogen-activated protein kinase kinase. Science *260*, 1658–1661.

Morrison, D.K. (2001). KSR: a MAPK scaffold of the Ras pathway? J. Cell Sci. *114*, 1609–1612.

Mulcahy, H.E., Lyautey, J., Lederrey, C., qi Chen, X., Anker, P., Alstead, E.M., Ballinger, A., Farthing, M.J., and Stroun, M. (1998). A prospective study of K-ras mutations in the plasma of pancreatic cancer patients. Clin. Cancer Res. *4*, 271–275.

Nguyen, A., Burack, W.R., Stock, J.L., Kortum, R., Chaika, O.V., Afkarian, M., Muller, W.J., Murphy, K.M., Morrison, D.K., Lewis, R.E., et al. (2002). Kinase suppressor of Ras (KSR) is a scaffold which facilitates mitogen-activated protein kinase activation in vivo. Mol. Cell. Biol. *22*, 3035–3045.

Oliveira, C., Velho, S., Moutinho, C., Ferreira, A., Preto, A., Domingo, E., Capelinha, A.F., Duval, A., Hamelin, R., Machado, J.C., et al. (2007). KRAS and BRAF oncogenic mutations in MSS colorectal carcinoma progression. Oncogene *26*, 158–163.

Ory, S., Zhou, M., Conrads, T.P., Veenstra, T.D., and Morrison, D.K. (2003). Protein phosphatase 2A positively regulates Ras signaling by dephosphorylating KSR1 and Raf-1 on critical 14-3-3 binding sites. Curr. Biol. *13*, 1356–1364.

Owens, D.M., and Keyse, S.M. (2007). Differential regulation of MAP kinase signalling by dual-specificity protein phosphatases. Oncogene *26*, 3203–3213.

Philp, A.J., Campbell, I.G., Leet, C., Vincan, E., Rockman, S.P., Whitehead, R.H., Thomas, R.J., and Phillips, W.A. (2001). The phosphatidylinositol

3′-kinase p85alpha gene is an oncogene in human ovarian and colon tumors. Cancer Res. *61*, 7426–7429.

Porfiri, E., and McCormick, F. (1996). Regulation of epidermal growth factor receptor signaling by phosphorylation of the ras exchange factor hSOS1. J. Biol. Chem. *271*, 5871–5877.

Prendergast, G.C., Khosravi-Far, R., Solski, P.A., Kurzawa, H., Lebowitz, P.F., and Der, C.J. (1995). Critical role of Rho in cell transformation by oncogenic Ras. Oncogene *10*, 2289–2296.

Qiu, R.G., Chen, J., Kirn, D., McCormick, F., and Symons, M. (1995). An essential role for Rac in Ras transformation. Nature *374*, 457–459.

Razidlo, G.L., Kortum, R.L., Haferbier, J.L., and Lewis, R.E. (2004). Phosphorylation regulates KSR1 stability, ERK activation, and cell proliferation. J. Biol. Chem. *279*, 47808–47814.

Ren, Y., Li, R., Zheng, Y., and Busch, H. (1998). Cloning and characterization of GEF-H1, a microtubule-associated guanine nucleotide exchange factor for Rac and Rho GTPases. J. Biol. Chem. *273*, 34954–34960.

Ritt, D.A., Monson, D.M., Specht, S.I., and Morrison, D.K. (2010). Impact of feedback phosphorylation and Raf heterodimerization on normal and mutant B-Raf signaling. Mol. Cell. Biol. *30*, 806–819.

Sahai, E., Olson, M.F., and Marshall, C.J. (2001). Cross-talk between Ras and Rho signalling pathways in transformation favours proliferation and increased motility. EMBO J. *20*, 755–766.

Samuels, Y., and Velculescu, V.E. (2004). Oncogenic mutations of PIK3CA in human cancers. Cell Cycle *3*, 1221–1224.

Sandelin, A., Wasserman, W.W., and Lenhard, B. (2004). ConSite: web-based prediction of regulatory elements using cross-species comparison. Nucleic Acids Res. *32*, W249–W252.

Sieburth, D.S., Sundaram, M., Howard, R.M., and Han, M. (1999). A PP2A regulatory subunit positively regulates Ras-mediated signaling during Caenorhabditis elegans vulval induction. Genes Dev. *13*, 2562–2569.

Sjöblom, T., Jones, S., Wood, L.D., Parsons, D.W., Lin, J., Barber, T.D., Mandelker, D., Leary, R.J., Ptak, J., Silliman, N., et al. (2006). The consensus coding sequences of human breast and colorectal cancers. Science *314*, 268–274.

Smit, V.T., Boot, A.J., Smits, A.M., Fleuren, G.J., Cornelisse, C.J., and Bos, J.L. (1988). KRAS codon 12 mutations occur very frequently in pancreatic adenocarcinomas. Nucleic Acids Res. *16*, 7773–7782.

Smith, F.D., Langeberg, L.K., Cellurale, C., Pawson, T., Morrison, D.K., Davis, R.J., and Scott, J.D. (2010). AKAP-Lbc enhances cyclic AMP control of the ERK1/2 cascade. Nat. Cell Biol. *12*, 1242–1249.

Sundaram, M., and Han, M. (1995). The C. elegans ksr-1 gene encodes a novel Raf-related kinase involved in Ras-mediated signal transduction. Cell *83*, 889–901.

Therrien, M., Chang, H.C., Solomon, N.M., Karim, F.D., Wassarman, D.A., and Rubin, G.M. (1995). KSR, a novel protein kinase required for RAS signal transduction. Cell *83*, 879–888.

Therrien, M., Michaud, N.R., Rubin, G.M., and Morrison, D.K. (1996). KSR modulates signal propagation within the MAPK cascade. Genes Dev. *10*, 2684–2695.

Vojtek, A.B., Hollenberg, S.M., and Cooper, J.A. (1993). Mammalian Ras interacts directly with the serine/threonine kinase Raf. Cell *74*, 205–214.

Warne, P.H., Viciana, P.R., and Downward, J. (1993). Direct interaction of Ras and the amino-terminal region of Raf-1 in vitro. Nature *364*, 352–355.

Wassarman, D.A., Solomon, N.M., Chang, H.C., Karim, F.D., Therrien, M., and Rubin, G.M. (1996). Protein phosphatase 2A positively and negatively regulates Ras1-mediated photoreceptor development in Drosophila. Genes Dev. *10*, 272–278.

Whitehead, I., Kirk, H., Tognon, C., Trigo-Gonzalez, G., and Kay, R. (1995). Expression cloning of lfc, a novel oncogene with structural similarities to guanine nucleotide exchange factors and to the regulatory region of protein kinase C. J. Biol. Chem. *270*, 18388–18395.

Xiao, H., Zhang, Q., Shen, J., Bindokas, V., and Xing, H.R. (2010). Pharmacologic inactivation of kinase suppressor of Ras1 sensitizes epidermal growth factor receptor and oncogenic Ras-dependent tumors to ionizing radiation treatment. Mol. Cancer Ther. *9*, 2724–2736.

Zhang, Z., and Gerstein, M. (2003). Of mice and men: phylogenetic footprinting aids the discovery of regulatory elements. J. Biol. *2*, 11.

Zhang, X.F., Settleman, J., Kyriakis, J.M., Takeuchi-Suzuki, E., Elledge, S.J., Marshall, M.S., Bruder, J.T., Rapp, U.R., and Avruch, J. (1993). Normal and oncogenic p21ras proteins bind to the amino-terminal regulatory domain of c-Raf-1. Nature *364*, 308–313.

Cancer Cell
Article

UHRF1 Overexpression Drives DNA Hypomethylation and Hepatocellular Carcinoma

Raksha Mudbhary,[1,2,3] Yujin Hoshida,[1,4] Yelena Chernyavskaya,[1,2] Vinitha Jacob,[1,2,3] Augusto Villanueva,[7,8] M. Isabel Fiel,[5] Xintong Chen,[1,4] Kensuke Kojima,[1,4] Swan Thung,[5] Roderick T. Bronson,[9] Anja Lachenmayer,[4] Kate Revill,[2,4] Clara Alsinet,[7] Ravi Sachidanandam,[6] Anal Desai,[10] Sucharita SenBanerjee,[10] Chinweike Ukomadu,[10] Josep M. Llovet,[1,4,7,11] and Kirsten C. Sadler[1,2,3,4,*]

[1]Division of Liver Diseases, Department of Medicine, Icahn School of Medicine at Mount Sinai, New York, NY 10029, USA
[2]Department of Developmental and Regenerative Biology, Icahn School of Medicine at Mount Sinai, New York, NY 10029, USA
[3]Graduate School of Biological Sciences, Icahn School of Medicine at Mount Sinai, New York, NY 10029, USA
[4]Liver Cancer Program/Tisch Cancer Institute, Icahn School of Medicine at Mount Sinai, New York, NY 10029, USA
[5]Department of Pathology, Icahn School of Medicine at Mount Sinai, New York, NY 10029, USA
[6]Department of Genetics and Genomics, Icahn School of Medicine at Mount Sinai, New York, NY 10029, USA
[7]HCC Translational Research Laboratory, IDIBAPS, CIBEREHD, Hospital Clinic, University of Barcelona, Catalonia 08036, Spain
[8]Institute of Liver Studies, Division of Transplantation Immunology and Mucosal Biology, King's College London, London SE5 9RS, UK
[9]Rodent Histopathology Core Dana Farber/Harvard Cancer Center, Harvard Medical School, Boston, MA 02115, USA
[10]Division of Gastroenterology, Department of Medicine, Brigham and Women's Hospital, Harvard Medical School, Boston, MA 02115, USA
[11]Institució Catalana de Recerca i Estudis Avançats Lluís Companys, Barcelona 08010, Spain
*Correspondence: kirsten.edepli@mssm.edu
http://dx.doi.org/10.1016/j.ccr.2014.01.003

SUMMARY

Ubiquitin-like with PHD and RING finger domains 1 (UHRF1) is an essential regulator of DNA methylation that is highly expressed in many cancers. Here, we use transgenic zebrafish, cultured cells, and human tumors to demonstrate that UHRF1 is an oncogene. UHRF1 overexpression in zebrafish hepatocytes destabilizes and delocalizes Dnmt1 and causes DNA hypomethylation and Tp53-mediated senescence. Hepatocellular carcinoma (HCC) emerges when senescence is bypassed. *tp53* mutation both alleviates senescence and accelerates tumor onset. Human HCCs recapitulate this paradigm, as *UHRF1* overexpression defines a subclass of aggressive HCCs characterized by genomic instability, *TP53* mutation, and abrogation of the TP53-mediated senescence program. We propose that UHRF1 overexpression is a mechanism underlying DNA hypomethylation in cancer cells and that senescence is a primary means of restricting tumorigenesis due to epigenetic disruption.

INTRODUCTION

The expression of genes that encode readers and writers of the epigenetic code are widely deregulated across cancer types (You and Jones, 2012). This contributes to the massive gene-expression changes and remodeling of the epigenetic landscape, a characteristic of many types of cancer. In particular, loss of global DNA methylation is a hallmark of cancer cells.

DNA hypomethylation contributes to oncogenesis through multiple mechanisms, including chromosomal instability (Eden et al., 2003; Karpf and Matsui, 2005), derepression of imprinted genes (Berdasco and Esteller, 2010; Jirtle, 2004; Li et al., 1993), retrotransposon activation (Gaudet et al., 2004; Howard et al., 2008; Jackson-Grusby et al., 2001; Sharif et al., 2007), and aberrant gene expression, including induction of oncogenes (Cheah et al., 1984). Many studies have documented that expression

Significance

Global DNA hypomethylation occurs in most types of cancer and can induce genomic instability and widespread changes in gene expression. UHRF1 is a key regulator of DNA methylation, and here, we show that UHRF1 overexpression causes HCC in zebrafish without any other genetic alteration, demonstrating that it is an oncogene. High UHRF1 expression causes DNA hypomethylation and Tp53-mediated senescence, which serves to restrict transformation of UHRF1-overexpressing cells. High *UHRF1* expression in human HCC correlates with a poor prognosis, genomic instability, *TP53* mutation, and repression of the TP53-mediated senescence program. We conclude that UHRF1 is an oncogene that promotes widespread DNA hypomethylation, an epigenetic hallmark of cancer cells, and that UHRF1 overexpression drives tumorigenesis when senescence is bypassed.

of the core factors required for maintenance DNA methylation—i.e., DNA methyltransferase 1 (DNMT1) and ubiquitin-like with PHD and RING finger domains 1 (UHRF1) (Babbio et al., 2012; Jin et al., 2010; Unoki et al., 2010; Wang et al., 2012)—are significantly altered across cancer types. However, whether changes in the expression of these key factors are sufficient to alter the cancer cell methylome and drive carcinogenesis is unknown. Moreover, the mechanism by which DNA methylation is lost in cancer cells is poorly understood.

The cellular response to DNA hypomethylation varies by cell type, physiological context, and degree of hypomethylation. In some cells, DNA hypomethylation induces tumor-suppressive mechanisms, including apoptosis (Anderson et al., 2009; Biniszkiewicz et al., 2002; Chen et al., 2007; Jackson-Grusby et al., 2001) or senescence (Decottignies and d'Adda di Fagagna, 2011; Fairweather et al., 1987), whereas in other cells it blocks differentiation of progenitor cells (Rai et al., 2010) or causes cancer (Gaudet et al., 2003; Yamada et al., 2005). In part, the cellular response to loss of DNA methylation is dictated by the genomic region affected: hypomethylation of gene regulatory regions, such as promoters, can derepress gene expression, whereas hypomethylation of repetitive elements can reduce heterochromatin formation and promote recombination and genomic instability.

UHRF1 plays an essential role in DNA methylation by recognizing hemimethylated DNA generated during DNA replication and then by recruiting DNMT1 to ensure faithful maintenance of DNA-methylation patterns in daughter cells (Arita et al., 2008; Avvakumov et al., 2008; Bostick et al., 2007; Hashimoto et al., 2008; Liu et al., 2013; Nishiyama et al., 2013; Sharif et al., 2007). Consequently, UHRF1 depletion results in global DNA hypomethylation (Bostick et al., 2007; Feng et al., 2010; Sharif et al., 2007; Tittle et al., 2011). Conversely, UHRF1 may also limit DNA methylation by targeting DNMT1 for ubiquitin-mediated degradation (Du et al., 2010; Qin et al., 2011) or by delocalizing DNMT1 (Sharif et al., 2007). Thus, how UHRF1 overexpression impacts the methylome is unclear.

We previously reported that *uhrf1* mutation in zebrafish blocks liver outgrowth in embryos and regeneration in adults (Sadler et al., 2007) and that depleting UHRF1 from cancer cells induces apoptosis (Tien et al., 2011). Here, we tested the hypothesis that UHRF1 overexpression would alter global DNA methylation and promote hepatocellular carcinoma (HCC).

RESULTS

High UHRF1 Expression Causes DNA Hypomethylation

UHRF1 is required for DNA methylation, as it recruits DNMT1 to hemimethylated DNA during DNA replication (Bostick et al., 2007; Feng et al., 2010; Liu et al., 2013; Nishiyama et al., 2013; Sharif et al., 2007). Paradoxically, UHRF1 also serves as an ubiquitin ligase that targets DNMT1 for degradation (Du et al., 2010; Qin et al., 2011). To determine how UHRF1 overexpression impacts DNA methylation, we generated transgenic zebrafish expressing human UHRF1 fused to GFP (*hsa.UHRF-GFP*) under the hepatocyte-specific *fabp10* promoter (*Tg*(*fabp10:hsa.UHRF1-GFP*); Chu et al., 2012).

Human and zebrafish UHRF1 are 66% identical, and the ability of human UHRF1 to rescue zebrafish embryos depleted of Uhrf1 (V.J. and K.C.S., unpublished data; Chu et al., 2012) indicates they are functional orthologs. Expression is first detected in hepatocytes on 3 days postfertilization (dpf) and by 5 dpf; nuclear UHRF1-GFP is easily detected at variable levels in hepatocytes (Figure S1A available online; Chu et al., 2012). We isolated an allelic series of *Tg*(*fabp10:hsa.UHRF1-GFP*) transgenics expressing a range of *UHRF1* levels (Figures S1A and S1B; hereafter referred to *UHRF1-GFP High*, *Medium* and *Low*).

We probed genomic DNA isolated from the liver of 5 dpf larvae from each line with an antibody specific for 5-methyl cytosine (5MeC) to assess DNA methylation and found significant hypomethylation only in the liver of *UHRF1-GFP High* larvae (38% of controls; $p = 0.007$; Figures 1A and S1C). 5MeC immunofluorescence showed DNA methylation to be uniformly distributed in the nuclei of hepatocytes from control larvae that express nuclear-localized mCherry under the *fabp10* promoter (*Tg*(*fabp10:nls-mCherry*); abbreviated to *nls-mCherry*). Only dim staining was detected in hepatocytes of *UHRF1-GFP High* larvae (Figure 1B). Because equivalent levels of 5MeC were detected in the liverless carcasses (Figure 1A) or cells of the fin where the transgene is not expressed (Figure 1B), we conclude that DNA hypomethylation was specific to the liver of *UHRF1-GFP High* larvae.

We hypothesized that UHRF1-induced DNA hypomethylation could be caused by mislocalization or destabilization of Dnmt1. Immunofluorescence revealed uniform Dnmt1 distribution in the nucleoplasm of *nls-mCherry* hepatocytes (Figure 1C), but in *UHRF1-GFP High* hepatocytes, it was concentrated in nuclear foci that contained UHRF1-GFP (Figure 1C). Interestingly, the range of UHRF1-GFP expression within cells of the same liver revealed that cells with high GFP had dim, puncate Dnmt1 staining, but the Dnmt1 levels and distribution pattern were similar to control hepatocytes in cells with low or no GFPDnmt1 levels, and the distribution pattern was similar to control hepatocytes in cells with low or no GFP (arrows, Figure 1C). Thus, UHRF1 expressed at high levels colocalizes with Dnmt1 and high UHRF1 expression redistributes Dnmt1 to intranuclear structures reminiscent of senescence-associated heterochromatin foci (Di Micco et al., 2011).

Endogenous Dnmt1 in the liver was below the levels detectable by immunoblotting (not shown), so we used a transgenic line expressing UHRF1-GFP under the inducible *hsp70l* promoter (Chu et al., 2012) to quantitatively assess the impact of UHRF1 overexpression on Dnmt1 stability at a developmental time when we could easily detect Dnmt1 levels by immunoblotting. We optimize a heat-shock protocol that maximized UHRF1-GFP expression in *Tg*(*hsp70l:UHRF1-GFP*) larvae (Figure 1D) and found that UHRF1-GFP overexpression reduced Dnmt1 protein by 27% compared to non-heat-shocked transgenics ($p = 0.03$; Figure 1E). Treatment with a nontoxic dose of the proteasome inhibitor, MG132, prevented the decrease in Dnmt1 induced by UHRF1 overexpression ($p = 0.01$; Figure 1E). Neither heat shock nor MG132 significantly affected Dnmt1 protein levels in nontransgenic controls (Figure 1E). Thus, both Dnmt1 delocalization and destabilization could account for DNA hypomethylation caused by UHRF1 overexpression.

DNA Hypomethylation Caused by UHRF1 Overexpression Reduces Liver Size

Uhrf1 in zebrafish is required for hepatic outgrowth and liver regeneration (Sadler et al., 2007). To determine if UHRF1

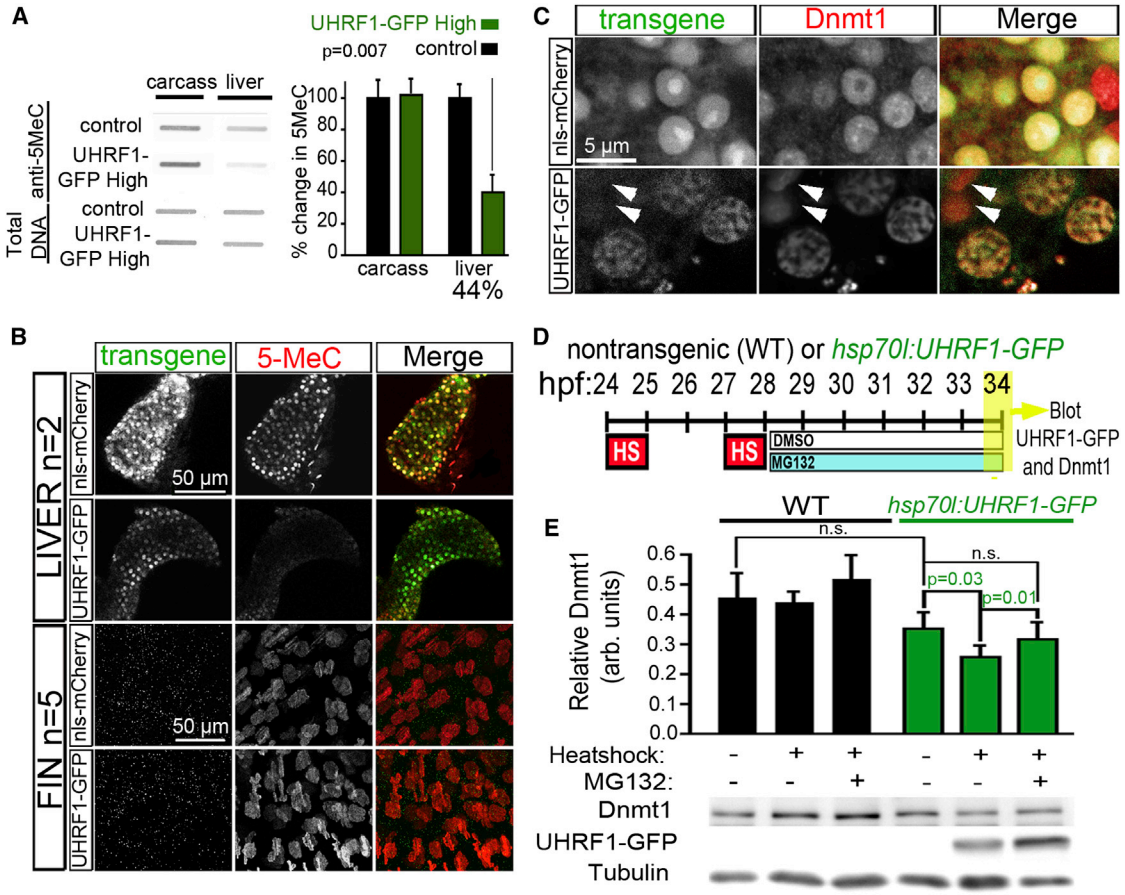

Figure 1. High UHRF1 Expression Causes Global DNA Hypomethylation

(A) 5MeC levels and total DNA stained with methylene blue were measured in 5 dpf control and *UHRF1-GFP High* livers (n = 4) and liverless carcasses (n = 3). The ratio of 5MeC to total DNA was averaged and normalized to controls. Student's t test was used to determine p values.

(B) Confocal stacks of livers (top) and fins (bottom) from 5 dpf *nls-mCherry* and *UHRF1-GFP High* larvae stained with anti-5MeC. Because a hepatocyte-specific promoter was used for transgenesis, there was no transgene expression in the fin.

(C) Dnmt1 is uniform in the hepatocyte nucleus of four dpf *nls-mCherry* larvae but is found in GFP-containing punctae in *UHRF1-GFP High* hepatocytes. Arrows point to cells that do not express GFP and have Dnmt1 distribution pattern similar to controls.

(D) *Tg*(*hsp70l:UHRF1-EGFP*) and nontransgenic controls were heat shocked at 37°C for 1 hr at 24 and 27 hpf, treated with 10 µM MG132 or DMSO at 28 hpf, and collected at 34 hpf for immunoblotting.

(E) Dnmt1 levels normalized to tubulin were averaged from six experiments. Student's t test was used to determine p values; n.s., not significant; error bars represent SD.

See also Figure S1.

overexpression in hepatocytes affected hepatic outgrowth, we assessed liver size in fish from all transgenic lines (Figures 2A–2C and S2A). Low and medium expressing lines had no gross changes in liver size (Figure S2A), but 74% of *UHRF1-GFP High* larvae on 5 dpf had small livers (Figure 2C), with the median area of the left liver lobe reduced by 35% compared to controls ($p < 0.001$; Figures 2D and S2A), without reduction of total fish size (Figure S2B).

Larvae with small livers appeared sick (see 10 dpf larvae in Figure 2A), and only 20% of *UHRF1-GFP High* fish survived to 20 dpf (Figures S2C and 2E). Moreover, *UHRF1-GFP High* larvae with the "microliver" phenotype on 5 dpf had significantly higher mortality by 10 dpf (67%) than those that started with a normal-sized liver (7%; Figure 2E). Thus, high UHRF1 expression in hepatocytes causes DNA hypomethylation, microliver, and larval death.

We next investigated the relationship between DNA hypomethylation and the microliver phenotype by asking whether further reducing DNA methylation could enhance this phenotype or restoring Dnmt1 could suppress it. We previously reported that exposing embryos to 50 µM of the Dnmt1 inhibitor, 5-azacytidine (5-Aza) from 0 to 5 dpf caused a profoundly small liver and DNA hypomethylation (Mudbhary and Sadler, 2011). By restricting the 5-Aza exposure time to 2.5–5 dpf, we reduced DNA methylation in the liver of control larvae by 40% (Figure S1C), which induced a moderately small liver in 16% of larvae ($p = 0.0035$; Figure 2F). This same treatment of *UHRF1-GFP High* larvae significantly increased the percent with small livers ($p < 0.0001$; Figure 2F). Whereas this could be attributed to DNA damage caused by 5-Aza, our finding that injecting *UHRF1-GFP High* embryos with mRNA-encoding Dnmt1 modestly suppressed

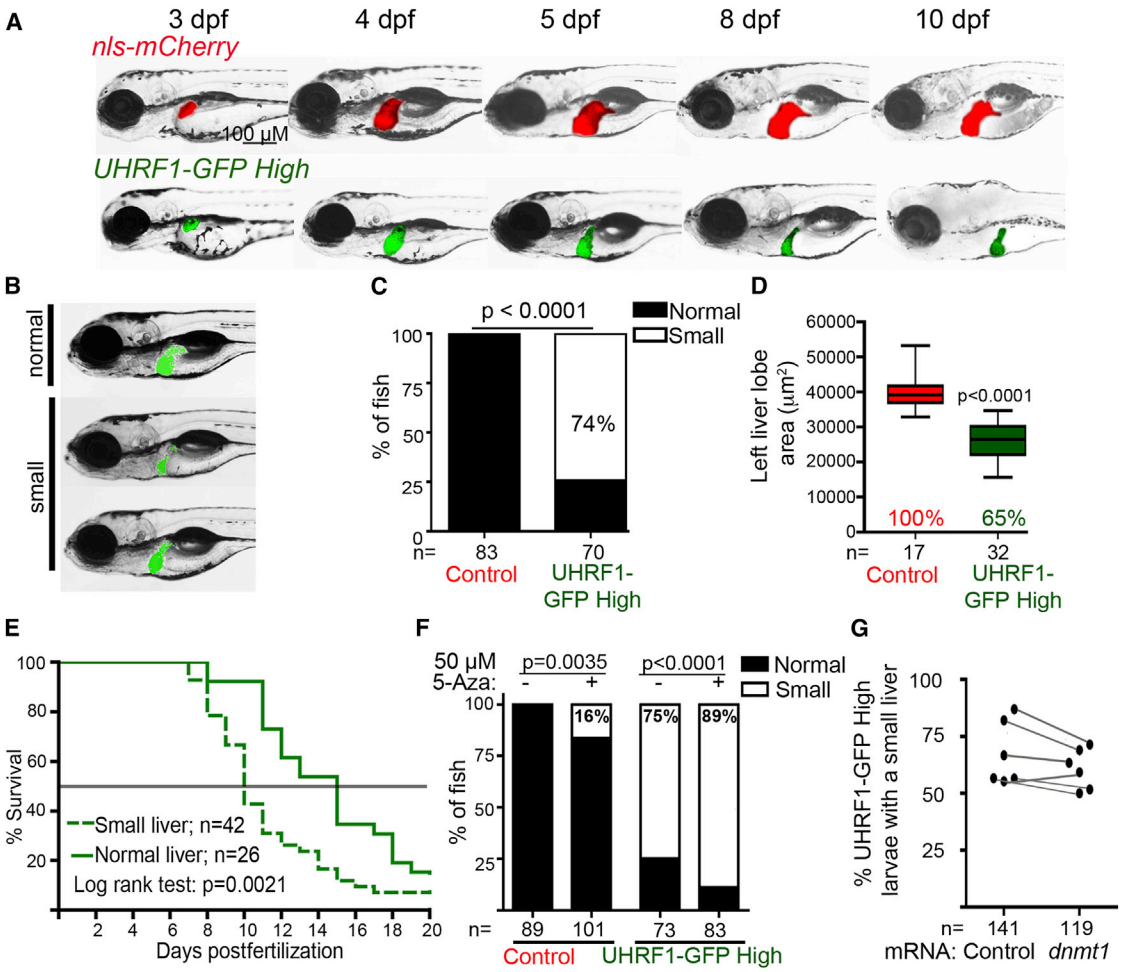

Figure 2. UHRF1-Induced Hypomethylation Reduces Liver Size

(A) Individual larvae were imaged daily from 3–10 dpf.

(B) Five dpf *UHRF1-GFP High* larvae display a range of liver sizes scored as "normal" or "small".

(C) Three clutches were scored according to criteria in (B); n, number of larvae. Fisher's exact test was used to determine p value.

(D) The area of the left liver lobe was measured in 5 dpf fish from two clutches. Boxes represent 75th and 25th percentile, horizontal line is the median, and whiskers mark lowest and highest values. Student's t test was used to determine p value.

(E) *UHRF1-GFP High* larvae were sorted by liver size on 5 dpf and tracked daily for survival to 20 dpf. Data are pooled from three clutches.

(F) *UHRF1-GFP High* and control larvae were treated with 50 μM 5-Aza from 2.5–5 dpf and scored for liver size in six clutches. Fisher's exact test was used to determine p values.

(G) *UHRF1-GFP High* embryos were injected with mRNA encoding *dnmt1* or Mpi before 1 hpf. The percent of fish with a normal liver size was scored at 5 dpf in six clutches.

See also Figure S2.

the percent of fish with a small liver (Figure 2G) and increased the average size of the left liver lobe by 10%–15% (Figure S2D) suggests that hypomethylation, at least in part, contributes to the small-liver phenotype of *UHRF1-GFP High* larvae.

UHRF1 Overexpression Triggers Tp53-Mediated Senescence

DNA hypomethylation can induce apoptosis, but we found no TUNEL-positive cells on 5 dpf in *UHRF1-GFP High* livers (Figure S3A). However, senescence-associated β-galactosidase (SA-β-gal) staining was detected throughout the liver of most *UHRF1-GFP High* 5 dpf larvae (n = 93; Figures 3A and 3B), but not other transgenic lines (Figure S3B). Additionally, the DNA in control hepatocytes was evenly distributed throughout the uniformly sized nuclei compared to the large nuclei where DNA resembled senescence-associated heterochromatic foci (inset, Figure 3C). Strikingly, the largest hepatocyte nuclei also had the brightest GFP (Figure 3C), suggesting the effect of UHRF1 overexpression cell autonomously affected nuclear morphology.

Senescent cells do not divide, and we found significantly less bromodeoxyuridine (BrdU) incorporation in the liver of 5 dpf *UHRF1-GFP High* larvae compared to controls ($p < 0.0001$; Figure 3D). Interestingly, in *nls-mCherry* larvae, most BrdU incorporation was detected in hepatocytes that express *nls-mCherry*, but the only BrdU-positive cells in *UHRF1-GFP High* larvae were negative for GFP (see inset in Figure 3D). RNA sequencing

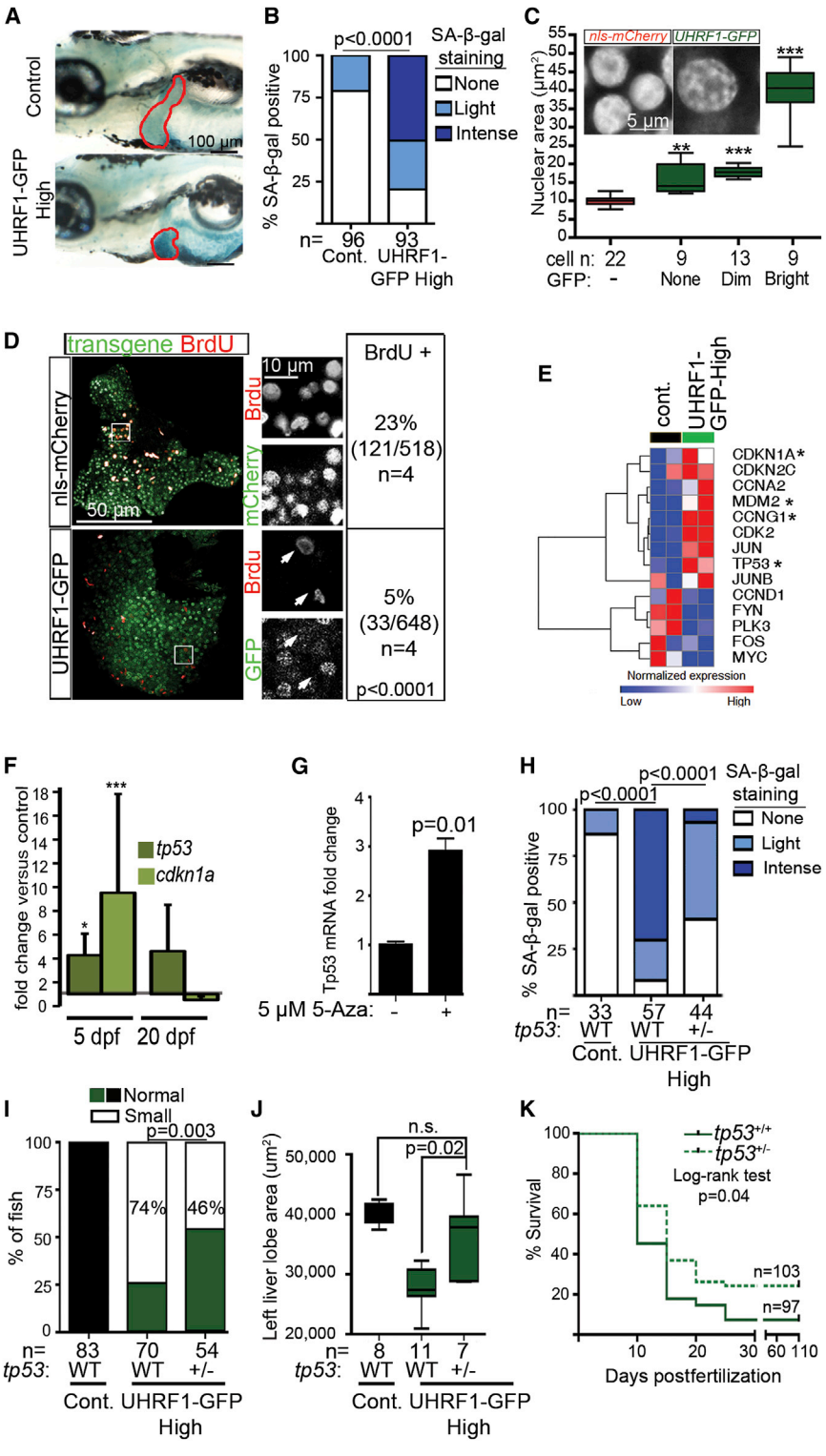

Figure 3. UHRF1 Overexpression in Hepatocytes Induces Tp53-Mediated Senescence

(A) Intense senescence-associated β-galactosidase (SA-β-gal) staining was detected in the liver (outlined) of 5 dpf *UHRF1-GFP High* larvae compared to light or no staining in controls.

(B) Five dpf fish from five clutches were scored for hepatic SA-β-gal staining. ***p < 0.0001 by Fisher's exact test.

(C) Nuclear size was measured in hepatocytes of a single control or *UHRF1-GFP High* 5 dpf liver, and cells were stratified according to GFP expression. Inset shows confocal stack of the DNA organized into foci. **p < 0.001 and ***p < 0.0001, compared to nuclear size in *nls-mCherry* larvae.

(D) BrdU-positive cells and the total number of transgene-expressing hepatocytes in *nls-mCherry* and *UHRF1-GFP High* larvae (bottom) 5 dpf larvae. A Fisher's exact test was used to calculate p value. In *nls-mCherry* larvae, most BrdU-positive cells also express the transgene, whereas the BrdU-positive cells in *UHRF1-GFP High* livers did not express GFP (white arrows in magnified regions, which are marked by the white box).

(E) Heatmap of log2 values from RNA-seq shows cell-cycle regulators are down and Tp53 target genes (marked by *) are up in *UHRF1-GFP High* 5 dpf livers.

(F) *tp53* and *cdkn1a* mRNA expression were induced on 5 dpf and downregulated on 20 dpf in *UHRF1-GFP High* livers. *p = 0.05; ***p = 0.001 calculated by one sample Student's t test. Error bars represent SD.

(G) 5-Aza induces *Tp53* expression in primary mouse hepatocytes. Student's t test was used to determine p value with SD indicated by the error bars across three replicates.

(H–K) $tp53^{+/-}$ in *UHRF1-GFP High* larvae significantly reduced SA-β-gal staining in the liver (two clutches) (H), and increased the percent of larvae with normal liver size (I), the area of the left liver lobe (J), and survival at 5 dpf (K). p values were calculated with a Fisher's test with Freeman-Halton extension (H), Fisher's exact test (I), and Student's t test. Boxes represent 75th and 25th percentile, horizontal line is the median, and whiskers mark lowest and highest values (J).

See also Figure S3.

(RNA-seq) analysis of liver samples from 5 dpf revealed downregulation of some proproliferative genes (*ccnd1* and *myc*) (Figure 3E), lending further support to the conclusion that senescence is the primary response to high UHRF overexpression in hepatocytes during hepatic outgrowth.

TP53 is a key mediator of senescence caused by DNA damage and oncogenic stress (Di Micco et al., 2011; McDuff and Turner, 2011; Ventura et al., 2007; Xue et al., 2007). RNA-seq (Figure 3E) and quantitative PCR (qPCR) analysis (Figure 3F) show that *tp53* and its target genes, especially *cdkn1a*, are significantly induced in the liver of 5 dpf *UHRF1-GFP High* larvae but then return to baseline by 20 dpf (Figure 3F). 5-Aza treatment of primary mouse hepatocytes induced *Tp53* expression (Figure 3G), similar to the effects of 5-Aza treatment or Dnmt1 depletion in other mammalian cell types (Jackson-Grusby et al., 2001;

Karpf et al., 2001) and in zebrafish embryos (V.J. and K.C.S., unpublished data; not shown). However, because significant alteration in methylation of the *tp53* promoter was not detected in these models (not shown), we hypothesize that DNA methylation does not directly regulate *Tp53* expression. Instead, DNA hypomethylation may induce *tp53* by an indirect mechanism, such as increased DNA damage or genomic instability.

A direct role for Tp53 in the phenotypes induced by UHRF1 overexpression was demonstrated by removing one copy of *tp53*. This reduced the incidence and intensity of SA-β-gal staining in the liver (Figure 3H), increased liver size (Figures 3I and 3J), and reduced mortality (Figure 3K) of *UHRF1-GFP High* fish. We thus propose a model whereby high UHRF1 causes DNA hypomethylation, induces Tp53-mediated senescence, which prevents expansion of the hepatic bud, resulting in hepatic insufficiency and larval death.

UHRF1 Overexpression Induces Liver Cancer in Zebrafish

To determine if UHRF1 overexpression was sufficient to cause HCC, 281 control and *UHRF1-GFP* transgenics were collected between 5 and 300 dpf, serial sectioned, and analyzed for atypical cells, dysplastic foci, and HCC using histological criteria devised by two expert pathologists (R.T.B. and M.I.F.), which included disrupted tissue architecture, cell size, shape, nuclear structure, and the presence of mitotic figures (Figures S4A and S4B). Evidence of increased hepatocyte proliferation was detected in all UHRF1-overexpressing lines on 20 and 40 dpf (Figure S4C), but this was insufficient to cause HCC, as *UHRF1-GFP Low* fish were tumor free at all time points (Table 1). In contrast, *UHRF1-GFP High* fish developed atypical hepatocytes as early as 5 dpf, with an 8% incidence of dysplastic foci and 46% incidence of HCC by 15 dpf. On 20 dpf, 76% of fish had HCC (Figures 4A and 4B; Table 1). *UHRF1-GFP Medium* fish also developed atypical hepatocytes and dysplastic foci at young ages, and one large HCC was detected in a 60 dpf fish (Table 1). In a classical transformation assay using NIH 3T3 cells, UHRF1 cooperated with RAS to promote growth on soft agar (Figure 4C). These conclusively demonstrate that UHRF1 is an oncogene.

We found that *UHRF1-GFP High* larvae older than 8 dpf had a lower incidence and intensity of hepatic SA-β-gal staining (Figure 4D). Interestingly, in many of these fish, intense staining was distributed in a punctate pattern. By 20 dpf, 75% of fish had either punctate or no staining (Figure 4D), which is a striking correlation with the 70% incidence of HCC at this time point. This was mirrored by increased proliferation of liver cells, detected by increased BrdU incorporation in *UHRF1-GFP High* livers (22% versus 4% in controls) at 11 dpf ($p < 0.001$; Figure 4E), and higher PCNA staining on 20 and 40 dpf in all lines (Figure S4C). Loss of senescence was not attributed to re-establishment of DNA methylation or transgene silencing, as reduced 5MeC staining persisted in tumor cells (Figure S4D) and transgene expression was detectable in all 20 dpf fish (Figures S4E and S4F), albeit reduced from levels detected in 5 dpf livers.

We asked whether Tp53 epistatically interacted with UHRF1 overexpression to contribute to HCC by removing one copy of *tp53* (Berghmans et al., 2005). The liver appeared normal in 13 $tp53^{+/-}$ fish without transgene expression (not shown), but in *UHRF1-GFP High* fish, tumor incidence on 15 dpf increased from 50% in wild-type (WT) to 87% in $tp53^{+/-}$ fish (Figure 4B). Interestingly, in a single *UHRF1-GFP High*;$p53^{+/-}$, 15 dpf fish, we found a tumor with immature cells resembling a cholangiocarcinoma. Thus, *tp53* functions to suppress tumor formation and may alter the spectrum of tumors caused by UHRF1 overexpression.

UHRF1 Is Upregulated in Human HCC

We next investigated the relevance of UHRF1 expression in human HCC. We assessed UHRF1 expression by qPCR in 16 normal liver samples and in two cohorts of patients with dysplastic nodules or HCC: the first cohort of 58 patients had hepatitis C infection (HCV) (Figure 5A; Wurmbach et al., 2007), and the second cohort of 69 patients had hepatitis B virus, alcohol, and other etiologies (Figure S5A; Villanueva et al., 2008). Additional publically available transcriptome data sets from three other cohorts of HCCs (Figure S5B) and from lung, gastric, colorectal, and breast cancer (Figure S5C) were also analyzed. All showed elevated *UHRF1* in tumors, with expression elevated >2-fold compared to controls in 17/18 dysplastic foci and 104/109 HCCs (Figures 5A and S5A). An average of 20- and 46-fold overexpression of *UHRF1* was detected in advanced and very advanced HCCs. UHRF1 protein was barely detectable in five normal liver samples but highly expressed in 38/52 (73%) of the tumors analyzed for *UHRF1* mRNA in Figure 5A ($p < 0.003$; Figure 5B). Thus, *UHRF1* is overexpressed in HCCs of diverse etiologies as well as in other tumor types, and high *UHRF1* expression is significantly associated with the most advanced tumors.

Targeting UHRF1 in liver cancer cells (HepG2) using small interfering RNA (siRNA) induced PARP cleavage (Figure 5C) and other markers of apoptosis (not shown), similar to results obtained using another HCC cell line (Hep3B; not shown) and colon cancer cells (Tien et al., 2011). Thus, blocking UHRF1 in cancers with high UHRF1 expression could be an effective means to induce tumor cell death.

Of the 109 HCCs analyzed for *UHRF1* expression by qPCR, 71 had multiple clinical and genomics parameters available (Chiang et al., 2008). These were rank-ordered based on *UHRF1* expression determined by qPCR (Figure 6A). Tumors with expression above and equal to or below the median log2-fold change value of 3.64 were designated as "high" (n = 35) and "low" (n = 36), respectively (Figure 6A). High-*UHRF1*-expressing tumors were associated with signs of poor clinical outcome: 80% had microvascular invasion (Figure 5D) and significantly higher alpha-fetoprotein (AFP) levels (Figure 5E), although AFP levels alone did not cooperate with UHRF1 to predict survival (data not shown). Importantly, high *UHRF1* expression significantly correlated with early (<2 years; Figure 5F), but not late (Figure 5G), tumor recurrence and was inversely correlated with survival (Figure 5H). This suggests that high *UHRF1* expression predicted recurrence of the primary tumor, causing decreased survival (Villanueva et al., 2011). Molecular signatures of aggressive HCC tumors compiled from several previous studies (Table S1) were concordantly and significantly enriched in high-*UHRF1*-expressing tumors (Figure 6A). Moreover, high-UHRF1-expressing tumors were distinguished by induction of pathways that drive the cell cycle, DNA replication, and repair (Figure S6A; Tables S2 and S3). *UHRF1* overexpression also significantly

Table 1. HCC Onset and Incidence in *Tg(fabp10:nls-mCherry)* and *Tg(fabp10:UHRF1-GFP)* Zebrafish

Transgene	dpf	5	10	15	20	25	30	40	50	60	90	180	300	Total n = 281	CI
nls-mCherry	normal	100%	100%	100%	100%			100%	100%	100%	100%	100%	100%	65	100%
	atypical cells	0%	0%	0%	0%			0%	0%	0%	0%	0%	0%	0	0%
	dysplastic foci	0%	0%	0%	0%			0%	0%	0%	0%	0%	0%	0	0%
	tumor	0%	0%	0%	0%			0%	0%	0%	0%	0%	0%	0	0%
	n =	8	8	8	11	nd	nd	5	5	5	5	5	5	65	
UHRF1-GFP Low	normal	100%	100%	100%	100%			100%			100%	100%	100%	60	100%
	atypical cells	0%	0%	0%	0%			0%			0%	0%	0%	0	0%
	dysplastic foci	0%	0%	0%	0%			0%			0%	0%	0%	0	0%
	tumor	0%	0%	0%	0%			0%			0%	0%	0%	0	0%
	n =	7	9	10	12	nd	nd	4	nd	nd	6	6	6	60	
UHRF1-GFP Medium	normal	90% (9)	100% (11)	50% (3)	28% (4)	66% (4)	80% (4)	50% (4)	50% (5)	81% (13)				57	66%
	atypical cells	10% (1)	0%	50% (3)	57% (8)	33% (2)	20% (1)	50% (4)	20% (2)	44% (7)				28	32%
	dysplastic foci	0%	0%	0%	7% (1)	0%	0%	25% (2)	30% (3)	0%				6	7%
	tumor	0%	0%	0%	0%	0%	0%	0%	0%	6% (1)				1	1%
	n =	10	11	6	14	6	5	8	10	16				86	
UHRF1-GFP High	normal	0%	0%	7% (1)	0%					0%				1	2%
	atypical cells	100% (13)	100% (7)	46% (6)	17% (3)					75% (3)				36	61%
	dysplastic foci	0%	0%	8% (1)	12% (2)					25% (1)				4	7%
	tumor	0%	0%	46% (6)	76% (13)					0%				18	30%
	n =	13	7	13	17					4				54	
UHRF1-GFP High/ p53$^{+/-}$	normal			0%										0	0%
	atypical cells			13% (2)										2	13%
	dysplastic foci			0%										0	0%
	tumor			88% (14)										14	88%
	n =			16										16	

The incidence (percent) and absolute number of fish (parentheses) with cancer-relevant histological phenotypes were scored in a total of 281 fish from four transgenic lines. The total n for each time point is indicated. Some fish were diagnosed with more than one lesion. nd, not done; CI, cumulative incidence.

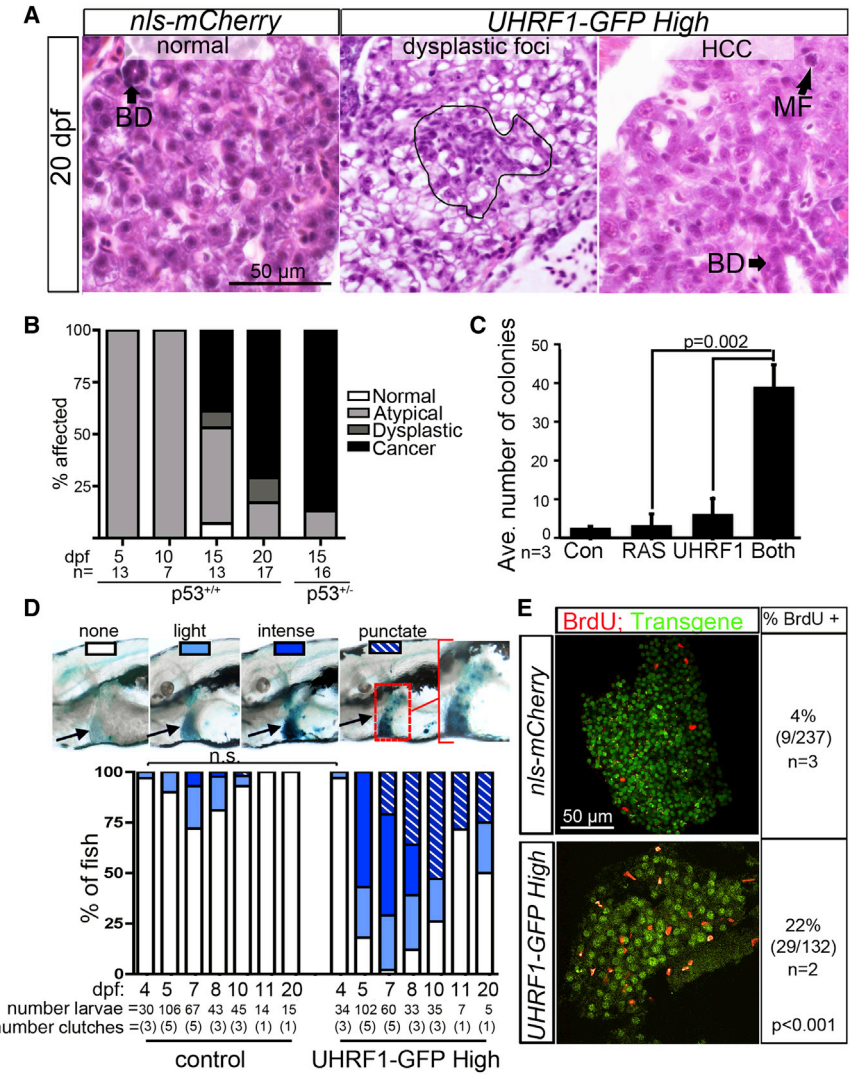

Figure 4. UHRF1 Is an Oncogene

(A) Atypical cells, dysplastic foci (outlined), and HCC are apparent in hematoxylin and eosin-stained *UHRF1-GFP High* livers. BD, bile duct; MF, mitotic figure.

(B) Incidence of normal and atypical hepatocytes, dysplastic foci, and cancer in the liver of *UHRF1-GFP High* fish on WT or *tp53*$^{+/-}$ background.

(C) NIH 3T3 cell growth in soft agar is enhanced when UHRF1 overexpression is combined with RAS (n = 3). The p value was calculated by Student's t test, and error bars represent the SD.

(D) Hepatic SA-β-gal-staining patterns in *UHRF1-GFP High* larvae change as fish age. Images of 8 dpf larvae illustrate the SA-β-gal-staining patterns that were scored in the time course shown in the graph. A significant increase in the number of *UHRF1-GFP High* fish with intense or punctate SA-β-gal compared to controls at all time points ($p < 0.01$ by Fisher's exact test) except at 4 dpf; n.s., not significant.

(E) BrdU incorporation in the liver on 11 dpf is five times higher in *UHRF1-GFP High* fish than in controls. Total number of cells counted is indicated with n = number of clutches assessed. Fisher's exact test was used to calculate p value. See also Figure S4.

correlated with advanced-stage prostate cancer, but not lung or colon (Figures S5D–S5G).

High *UHRF1* Expression Delineates a Subclass of HCCs that Have Downregulated TP53-Mediated Senescence

Our zebrafish studies demonstrated that bypass of Tp53-induced senescence is required for UHRF1 to act as an oncogene. Our analysis of human HCCs indicates that a similar paradigm occurs in these samples. First, inactivating mutations in *TP53* significantly correlated with high *UHRF1* expression (Figure 6A). Second, many of the core enriched genes high-*UHRF1*-expressing tumors are regulated by TP53 in senescent fibroblasts (Table S4; Tang et al., 2007), and high-UHRF1-expressing tumors downregulated the gene expression signature associated with TP53-induced senescence in fibroblasts (Table S5; Figure S6B; Tang et al., 2007) and in hepatic stellate cells (Table S6; Figure S6C; Lujambio et al., 2013). Fourth, significant correlation between *UHRF1* overexpression, *TP53* mutation, and genome integrity in human HCCs indicates that these pathways act together, where high *UHRF1* expression (Figures 6B and 6C) and *TP53* mutation (Figure 6D) are independently correlated with chromosomal loss, but tumors that have both features display even more chromosomal loss (Figure 6D). Finally, *UHRF1* expression was significantly higher in tumors with *TP53* mutation (Figure 6E). *UHRF1* overexpression did not correlate with copy-number variation at the *UHRF1* locus (Figure S6D) suggesting that a different mechanism drives UHRF1 overexpression.

Genome-wide DNA hypomethylation is found in most HCCs (Calvisi et al., 2007), and this rendered it difficult to correlate methylome changes with *UHRF1* expression. However, *DNMT1* expression was directly correlated with *UHRF1* expression in HCC samples (Figure 6F). This may be a consequence of the high proliferation rate in these tumors or an induction of the methylation machinery to compensate for hypomethylation. Together, these data indicate that high UHRF1 expression in HCC defines a subset of aggressive tumors that have inactivated the TP53-induced senescence program, suggesting that, in humans, as observed in zebrafish, TP53 acts as a tumor suppressor to restrict the oncogenic potential of UHRF1-overexpressing cells.

DISCUSSION

We show that UHRF1 overexpression is sufficient to cause two oncogene-associated phenotypes: senescence and cancer. This defines UHRF1 as an epigenetic regulator that causes cancer upon overexpression, and it is thus an oncogene. We

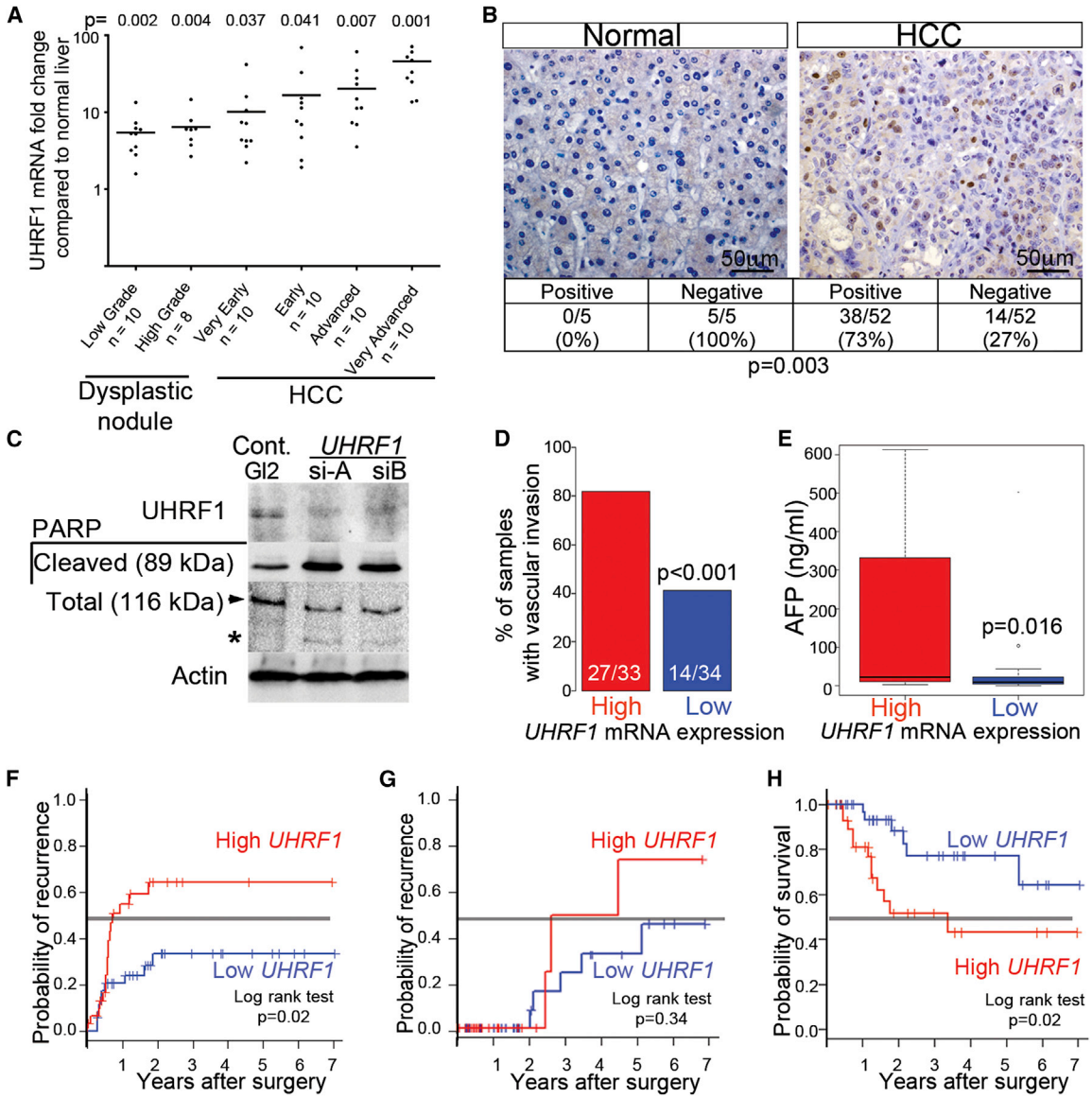

Figure 5. UHRF1 mRNA and Protein Are Overexpressed in HCC

(A) *UHRF1* detected by qRT-PCR in 18 preneoplastic lesions and 40 HCCs from hepatitis C virus (HCV)-infected patients compared to expression in nine normal livers. Horizontal line indicates median.

(B) Immunohistochemistry for UHRF1 protein (brown) was evaluated in 52 of the same HCCs examined in (A) plus five normal liver samples. Fisher's exact test was used to calculate p value. Seventy-one of the HCV-associated HCCs analyzed by qPCR were grouped into high (n = 35) and low (n = 36) UHRF1-expressing tumors based on the median log2-fold change of 3.64.

(C) HepG2 cells transfected with control siRNA (GL2) or two different siRNAs targeting *UHRF1* described in Tien et al. (2011) were blotted for UHRF1 and cleaved and total PARP (arrow indicates full length; * indicates cleaved protein).

(D–H) Vascular invasion (33 high and 34 low tumors; four missing values) (D), serum AFP (29 UHRF1-high and 29 low tumors; 13 missing values) (E), early (<2 years) (F) and late (>2 years; 32 UHRF1-high and 35 low tumors; four missing values) (G) tumor recurrence, and overall survival after surgery (32 high and 35 low tumors; four missing values) (H) were stratified according to *UHRF1* expression. Continuous and categorical variables were assessed by Wilcoxon rank-sum test and Fisher's exact test, respectively. Clinical outcome difference was evaluated by log rank test. In box and whisker plots, boxes represent the 75th and 25th percentiles, the whiskers represent the most extreme data points within interquartile range × 1.5, and the horizontal bar represents the median.

See also Figure S5.

hypothesize that UHRF1 overexpression is one mechanism by which cancer genomes can become hypomethylated, either via UHRF1-mediated Dnmt1 ubiquitination and degradation (Du et al., 2010; Qin et al., 2011) or by redistribution and/or sequestration of Dnmt1 away from DNA. Excess UHRF1 might also sequester the DNMT1-deubiquitinating enzyme, USP7 (Qin et al., 2011), to further promote DNMT1 ubiquitination and degradation.

The precise mechanism by which DNA hypomethylation causes cancer remains elusive. Both apoptosis and senescence

serve to limit the propagation of cells with aberrant DNA methylation (Decottignies and d'Adda di Fagagna, 2011; Fairweather et al., 1987); however, once epigenetically altered cells escape these tumor-suppressive mechanisms, they likely accumulate genetic lesions that predispose to cancer. Indeed, chromosomal instability and mitotic catastrophe occur following DNMT1 depletion (Chen et al., 2007; Karpf and Matsui, 2005; Weber and Schübeler, 2007), and transposons, which are heavily methylated in normal cells, could become activated and cause genomic instability upon UHRF1-induced DNA hypomethylation. Additionally, hypomethylated DNA is more likely to assume an open chromatin conformation, which may promote oncogene expression, although this possibility has not been fully evaluated. Whereas the oncogenic role of UHRF1 could also be mediated by the impact of UHRF1 on other epigenetic marks or on DNA replication (Taylor et al., 2013), our data combined with findings from others (Eden et al., 2003; Gaudet et al., 2003) suggest that DNA hypomethylation is a likely mechanism driving UHRF1-mediated transformation.

Our working model (Figure 7) proposes that UHRF1 overexpression causes DNA hypomethylation by reducing Dnmt1 levels and its access to hemimethylated DNA. Tp53 is then induced in response to either genomic instability or some other mechanism, causing hepatocyte senescence, which prevents hepatic expansion and results in larval death from hepatic insufficiency. We propose that Tp53 inactivation and senescence bypass by an as of yet unknown mechanism and allow for unhindered cell proliferation and malignant transformation. How this tumor-suppressive mechanism is overcome remains a central, unanswered question in cancer biology.

Studies in a mouse liver cancer model show that Tp53 reactivation causes senescence, and these cells are then cleared by the immune system (Xue et al., 2007) and the liver is then repopulated with senescence-resistant tumor-forming cells. Our finding that senescence decreases and BrdU incorporation increases in *UHRF1-GFP High* livers over time suggests a similar process at play. Moreover, BrdU incorporation in primarily GFP-negative cells suggests the expansion of either immune cells or immature hepatic progenitors in response to senescent hepatocytes. The finding of a cholangiocarcinoma in a *UHRF1-GFP High/p53*$^{+/-}$ fish may indicate a bipotential progenitor cell as the tumor-forming cell in this model. Additionally, our data indicate that there is a threshold effect of UHRF1 expression, in which the highest expressing cells undergo senescence and neighboring hepatocytes expressing UHRF1-GFP at levels below those detectable via microscopy undergo unhindered expansion.

HCC is the third cause of cancer-related deaths globally (Llovet et al., 2003), yet curative therapies are limited, with sorafenib as the only systemic therapy available for advanced cases (Llovet et al., 2008). Thus, there is an urgent and unmet need for novel therapies. HCC, like other cancers, is characterized by global DNA hypomethylation (Calvisi et al., 2007; Pogribny and Rusyn, 2014; Tischoff and Tannapfe, 2008), and high UHRF1 expression could be the cause. Our finding that UHRF1 depletion in HCC and other types of cancer cells causes apoptosis (Tien et al., 2011) presents UHRF1 as an attractive target for inducing cancer cell death induced by massive epigenetic changes incompatible with cell survival or by resetting the cancer cell methylome to reinstate the expression of genes that block cell proliferation.

EXPERIMENTAL PROCEDURES

Zebrafish Maintenance and Generation of Transgenics

Zebrafish were maintained on a 14:10 hr light:dark cycle at 28°C. mRNA-encoding zebrafish Dnmt1 (Rai et al., 2006) or mannose phosphate isomerase (Mpi) (Chu et al., 2013) as a control was injected into embryos just after fertilization.

Tg(fabp10:nls-mCherry) fish expressing nls-mCherry exclusively in hepatocytes were generated using Gateway cloning (Invitrogen) to produce vectors with *tol2* transposon sites (Kwan et al., 2007). *Tg(hsp70l:hsa.UHRF1-GFP)* and *Tg(fabp10:hsa.UHRF1-GFP)* were described in Chu et al. (2012). The high, medium, and low expressing alleles are listed at http://www.ZFIN.org with superscripts *mss1a*, *mss1b*, and *mss1c*, respectively. Transgenics were outcrossed to Tab14 (WT) or *tp53*$^{-/-}$ fish (Berghmans et al., 2005).

Tg(hsp70l:UHRF1-GFP) embryos were heat shocked at 37°C for 1 hr at 24 and 27 hr postfertilization (hpf). At 28 hpf, embryos were sorted visually for GFP expression and incubated with either 10 μM MG132 or DMSO and collected for immunoblotting at 34 hpf. 5-Aza (50 μM) was added to larvae from 2.5 to 5 dpf. The Mount Sinai Institutional Animal Care and Use Committee approved all protocols. Nomenclature guidelines for the species under discussion were followed, and when no species are specified, human nomenclature was used.

Gene-Expression Analysis

RNA was isolated from a pool of at least ten livers from 5 dpf fish and from one to five livers from 20 dpf fish using the RNeasy mini-kit (QIAGEN). cDNA was prepared by polyA priming using qScript SuperMix (Quanta). Quantitative RT-PCR (qRT-PCR) analysis was performed in the Light Cycler 480 (Roche) using gene-specific primers (see Supplemental Information) and PerfeCTa SYBRGreen FastMix (Quanta). C_t values from triplicate reactions were averaged and $2^{-Ct(target)}/2^{-Ct(reference)}$ was used to calculate expression, with *rpp0* and cyclophilin A used as reference genes of zebrafish and mouse samples, respectively.

RNA-seq analysis was carried out on RNA from pools of 50 livers dissected from two clutches of 5 dpf *UHRF1-GFP High* and *nls-mCherry* larvae, described in Supplemental Information.

Histology

Fish younger than 20 dpf were fixed overnight at 4°C in 4% paraformaldehyde (PFA), and older fish were fixed for 2–5 days at room temperature in Bouin's fixative. Four micromolar serial sections of paraffin-embedded fish were stained with hematoxylin and eosin as described (Imrie and Sadler, 2010) and imaged on an Olympus BX41 clinical microscope equipped with a Nikon DS-Ri1 digital camera. Histological criteria used for scoring tumors are described in Figures S4A and S4B.

Immunoblotting

Lysates prepared from 15 embryos dissolved in 150 μl protein lysis buffer were homogenized by sonication. One embryo equivalent was loaded per lane of an 8% or 12% SDS gel, transferred to nitrocellulose, and blotted. HepG2 cell lysates were prepared as described (Tien et al., 2011).

Antibodies

Antibodies recognizing DNMT1 (1:1,000 for blotting; 1:10 for immunofluorescence; Santa Cruz Biotechnology), UHRF1 (immunoblotting: 1:1,000; BD Biosciences; immunohistochemistry: 1:50; ab57083; Abcam), tubulin (1:5,000; Developmental Studies Hybridoma Bank), p89 PARP and total PARP (1:1,000; Cell Signaling Technology), B-actin (1:2,000; Sigma), 5MeC (1:500; Eurogentec), BrdU (1:200; BD Biosciences), and anti-rabbit or mouse conjugated to Alexa 555 or Alexa 488 (1:100; Invitrogen) were diluted in 10% fetal bovine serum (FBS) or 2% BSA in 1% Triton in PBS (PBST).

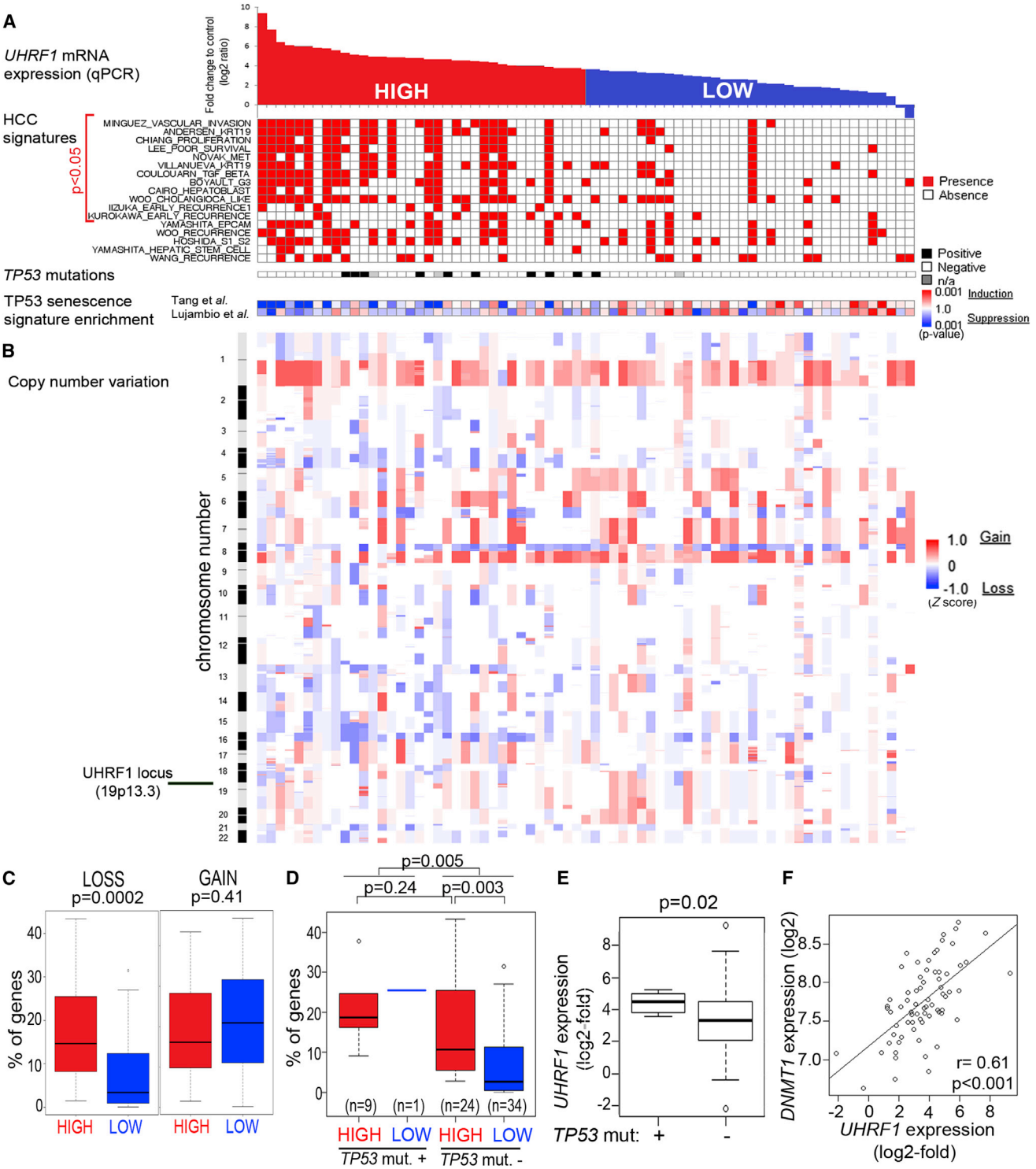

Figure 6. High *UHRF1* Expression Defines a Subclass of Tumors with Inactivated tp53, Repression of Senescence, and Chromosomal Instability

(A) The 71 human HCC tumors analyzed in Figures 5C–5G were rank-ordered according to *UHRF1* expression by qPCR and classified as high (<median, red; n = 35) or low (≥median, blue; n = 36). The presences of aggressive human HCC gene signatures from published studies and of *TP53*-inactivating mutations are indicated by red and black boxes, respectively. TP53-mediated senescence gene signatures (Lujambio et al., 2013; Tang et al., 2007) are displayed as a range from repressed (blue) to activated (red).

(B) Genome-wide profile of DNA copy number variation was obtained from Gene Expression Omnibus gene set GSE9829.

(C) Proportion of genes with DNA copy number loss and gain in tumors according to *UHRF1* expression.

(legend continued on next page)

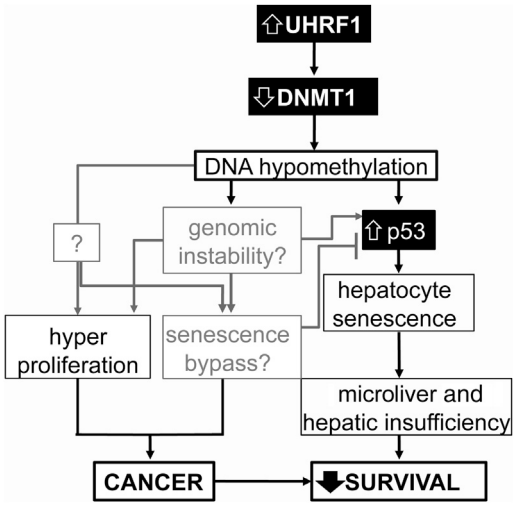

Figure 7. Model of the Relationship between UHRF1 Overexpression, DNA Hypomethylation, Tp53-Mediated Senescence, Cancer, and Survival

Factors investigated in this study are in solid black boxes with black lines indicating the correlations demonstrated in this work and gray lines indicating relationships that are speculative. Senescence reduces liver size and function and reduces larval survival, whereas cancer occurs when senescence is bypassed and also reduces survival.

Zebrafish Staining

Larvae fixed in 4% PFA were washed in PBST and stained using the Senescence β-Galactosidase Staining Kit (Cell Signal) or stained with CY3-streptavadin (1:300; Sigma) as described (Sadler et al., 2005). The left liver lobe area was measured using ImageJ.

Immunofluorescence was carried out on whole fish or on livers dissected from fixed larvae. BrdU was added to larvae water (10 mM) for 4–6 hr followed by immediate fixation, dehydration in methanol, rehydration to PBST, and permeabilization with 10 μg/ml Proteinase K. DNA was denatured in 1 or 2 N HCl, renatured, and blocked in 10% FBS or 1% BSA in PBST prior to immunofluorescence. DNA was stained with Hoechst 33342 (Sigma). A Leica SP5 DM confocal microscope was used for imaging.

Slot Blots

Genomic DNA was denatured in 0.4 M NaOH at 95°C for 10 min and neutralized in an equal volume of cold 2 M ammonium acetate, and 100 ng DNA was blotted in duplicate onto nitrocellulose membrane using a slot blot apparatus, washed in 2× saline sodium citrate, and vacuum baked at 80°C for 2 hr. Half was stained with 0.2% methylene blue in 0.3 M NaOAc and the other with anti-5MeC followed by horseradish peroxidase-conjugated anti-mouse (1:2,000) and visualized by Chemilumiescence (Roche). Image J was used to quantify 5MeC and methylene blue intensity, and 5MeC levels were determined by normalizing to total DNA.

Cell Culture

Primary mouse hepatocytes were isolated and plated in triplicate at 50% confluency and then treated with 5 μm 5-Aza or DMSO for 24 hr, and RNA was isolated.

NIH 3T3 cells were transfected in triplicate with pCDNA3.1 lacking an insert (control) or containing human RAS, UHRF1, or both and were retransfected 24 hr later. Forty-eight hours after the second transfection, 700 mg /ml neomycin was added for 7 days. Ten thousand cells per condition were plated on 0.3% soft agar layered on top of 0.6% soft agar. Media was changed every third day for 2 weeks, plates were stained with 0.005% crystal violet, and colony number was counted.

HepG2 cells cultured in DMEM supplemented with 10% (v/v) FBS and 5% (w/v) penicillin-streptomycin were transfected twice, 24 hr apart, with 20 nM siRNA-targeting firefly luciferase (GL2; Dharmacon) or UHRF1-targeting si-A and si-B using RNAiMAX (Invitrogen) as described (Tien et al., 2011).

Human Tissue Samples

Pathologically staged human tumors, dysplastic foci, and normal liver samples were obtained from the HCC Genomic Consortium (Mount Sinai Hospital, Instituto Nazionale dei Tumori, and Hospital Clinic). The study was approved by the institutional review board of each institution, and informed consent was obtained from all participants. TaqMan probes were used to analyze *UHRF1* expression by qPCR as described (Villanueva et al., 2008). Samples were grouped into a training set (nine normal liver, 18 low- and high-grade dysplastic nodules, and 40 pathologically staged HCCs; Llovet et al., 2006; Wurmbach et al., 2007) and a validation set (seven normal liver and 69 HCC; Villanueva et al., 2008). Integrative genomic and clinical data analysis was performed on 71 of the hepatitis-C-related, surgically treated HCC patients (National Center for Biotechnology Information [NCBI] Gene Expression Omnibus accession numbers GSE9829 and GSE44970). The liver pathologist, S.T., scored UHRF1 staining of 52 paraffin-embedded tumors from the training set.

Bioinformatics and Statistical Analysis

Seventy-one patients with HCC were grouped based on the median expression level of UHRF1 in the tumors determined by qPCR (UHRF1-high: n = 35 or low: n = 36). Presence of aggressive human HCC gene signatures (Table S1) were evaluated in the transcriptome data set using nearest-template prediction method (Hoshida, 2010) implemented by the GenePattern genomic analysis tool kit (http://www.broadinstitute.org/genepattern) based on prediction confidence $p < 0.05$. The senescence-related TP53 target genes were obtained from Molecular Signature Database (MSigDB; http://www.broadinstitute.org/msigdb; TANG_SENESCENCE_TP53_TARGETS_UP and _DN; Tang et al., 2007) and from NCBI Gene Expression Omnibus (GSE39469; Lujambio et al., 2013). Mouse genes from normalized microarray data were converted to human orthologs based on a mapping table (http://www.informatics.jax.org). Differentially expressed genes between senescent and proliferative cells were identified by using Bayesian t test implemented in Cyber-T software (http://molgen51.biol.rug.nl/cybert) at the significance threshold of posterior probability of differential expression >0.998 after excluding less variable genes with coefficient of variation ≤0.1 across the samples. Expression pattern of each signature was assessed by nearest-template prediction algorithm. Significance of induction or suppression of each signature was quantitatively measured by nominal p value of cosine distance. Pearson correlation test determined the significance between induction and suppression of gene signatures with *UHRF1* mRNA expression level as measured by qPCR. Statistical difference between groups was assessed by Wilcoxon rank-sum test and Fisher's exact test for continuous and categorical variables, respectively. Bonferroni correction for multiple hypothesis testing was applied when appropriate.

Survival analysis was performed by using Kaplan-Meier estimator and log rank test. All analyses were performed using R statistical package (http://www.r-project.org) and GenePattern genomic analysis tool kit (http://www.broadinstitute.org/genepattern). Gene expression levels and liver size were compared using Student's t or Mann Whitney U tests.

(D) Proportion of genes with DNA copy number loss according to *UHRF1* expression and *TP53* mutation status.
(E) *UHRF1* expression is significantly higher in tumors with *TP53* mutations.
(F) *DNMT1* expression by microarray analysis is significantly correlated with *UHRF1* expression assessed by qPCR in HCCs. In box and whisker plots, boxes represent the 75th and 25th percentiles, the whiskers represent the most extreme data points within interquartile range × 1.5, and the horizontal bar represents the median.
See also Figure S6 and Tables S1, S2, S3, S4, S5, and S6.

ACCESSION NUMBERS

Data from RNA-seq was deposited in the NCBI Gene Expression Omnibus with accession number GSE52605.

SUPPLEMENTAL INFORMATION

Supplemental Information includes Supplemental Experimental Procedures, six figures, and six tables and can be found with this article online at http://dx.doi.org/10.1016/j.ccr.2014.01.003.

AUTHOR CONTRIBUTIONS

R.M., Y.H., Y.C., A.V., C.U., J.M.L. and K.C.S. conceived of the experiments; R.M., Y.H., Y.C., V.J., A.V., A.L., A.D., and S.S. carried out experiments and analyzed data; M.I.F., X.C., K.K., S.T., R.T.B., K.R., C.A., R.S., C.U., J.M.L., and K.C.S. analyzed and interpreted data; and R.M. and K.C.S. wrote the paper. Y.H. and Y.C. contributed equally.

ACKNOWLEDGMENTS

Financial support was provided by The Breast Cancer Alliance and the March of Dimes (to K.C.S.), a Pilot Project from the DFCI NCI Cancer Center (5P30CA006516-45) and The Sidney A. Swensrud Foundation (to C.U.), the NIH (5R01DK080789-02 to C.U. and K.C.S., 1R01DK099558 to Y.H., 1R01DK076986 to J.M.L., F30DK094503 to V.J., and T32CA078207-14 to Y.C.), the European Commission Seventh Framework Programme FP7-Health 2010 (Heptromic number 259744 to Y.H. and J.M.L.), The Samuel Waxman Cancer Research Foundation, The Spanish National Health Institute (SAF-2010-16055), and the Asociación Española Contra el Cáncer (to J.M.L.). Liz Loughlin, Brandon Kent, Meghan Walsh, Alex Mir, Laia Cabellos, Helena Cornellà Vives, and Sara Toffanin provided expert technical assistance. We are grateful to Sam Sidi for *tp53*$^{-/-}$ fish, stimulating discussions, and critical reading of the manuscript.

Received: March 9, 2013
Revised: August 29, 2013
Accepted: January 6, 2014
Published: January 30, 2014

REFERENCES

Anderson, R.M., Bosch, J.A., Goll, M.G., Hesselson, D., Dong, P.D., Shin, D., Chi, N.C., Shin, C.H., Schlegel, A., Halpern, M., and Stainier, D.Y. (2009). Loss of Dnmt1 catalytic activity reveals multiple roles for DNA methylation during pancreas development and regeneration. Dev. Biol. *334*, 213–223.

Arita, K., Ariyoshi, M., Tochio, H., Nakamura, Y., and Shirakawa, M. (2008). Recognition of hemi-methylated DNA by the SRA protein UHRF1 by a base-flipping mechanism. Nature *455*, 818–821.

Avvakumov, G.V., Walker, J.R., Xue, S., Li, Y., Duan, S., Bronner, C., Arrowsmith, C.H., and Dhe-Paganon, S. (2008). Structural basis for recognition of hemi-methylated DNA by the SRA domain of human UHRF1. Nature *455*, 822–825.

Babbio, F., Pistore, C., Curti, L., Castiglioni, I., Kunderfranco, P., Brino, L., Oudet, P., Seiler, R., Thalman, G.N., Roggero, E., et al. (2012). The SRA protein UHRF1 promotes epigenetic crosstalks and is involved in prostate cancer progression. Oncogene *31*, 4878–4887.

Berdasco, M., and Esteller, M. (2010). Aberrant epigenetic landscape in cancer: how cellular identity goes awry. Dev. Cell *19*, 698–711.

Berghmans, S., Murphey, R.D., Wienholds, E., Neuberg, D., Kutok, J.L., Fletcher, C.D., Morris, J.P., Liu, T.X., Schulte-Merker, S., Kanki, J.P., et al. (2005). tp53 mutant zebrafish develop malignant peripheral nerve sheath tumors. Proc. Natl. Acad. Sci. USA *102*, 407–412.

Biniszkiewicz, D., Gribnau, J., Ramsahoye, B., Gaudet, F., Eggan, K., Humpherys, D., Mastrangelo, M.A., Jun, Z., Walter, J., and Jaenisch, R. (2002). Dnmt1 overexpression causes genomic hypermethylation, loss of imprinting, and embryonic lethality. Mol. Cell. Biol. *22*, 2124–2135.

Bostick, M., Kim, J.K., Estève, P.O., Clark, A., Pradhan, S., and Jacobsen, S.E. (2007). UHRF1 plays a role in maintaining DNA methylation in mammalian cells. Science *317*, 1760–1764.

Calvisi, D.F., Ladu, S., Gorden, A., Farina, M., Lee, J.S., Conner, E.A., Schroeder, I., Factor, V.M., and Thorgeirsson, S.S. (2007). Mechanistic and prognostic significance of aberrant methylation in the molecular pathogenesis of human hepatocellular carcinoma. J. Clin. Invest. *117*, 2713–2722.

Cheah, M.S., Wallace, C.D., and Hoffman, R.M. (1984). Hypomethylation of DNA in human cancer cells: a site-specific change in the c-myc oncogene. J. Natl. Cancer Inst. *73*, 1057–1065.

Chen, T., Hevi, S., Gay, F., Tsujimoto, N., He, T., Zhang, B., Ueda, Y., and Li, E. (2007). Complete inactivation of DNMT1 leads to mitotic catastrophe in human cancer cells. Nat. Genet. *39*, 391–396.

Chiang, D.Y., Villanueva, A., Hoshida, Y., Peix, J., Newell, P., Minguez, B., LeBlanc, A.C., Donovan, D.J., Thung, S.N., Solé, M., et al. (2008). Focal gains of VEGFA and molecular classification of hepatocellular carcinoma. Cancer Res. *68*, 6779–6788.

Chu, J., Loughlin, E.A., Gaur, N.A., SenBanerjee, S., Jacob, V., Monson, C., Kent, B., Oranu, A., Ding, Y., Ukomadu, C., and Sadler, K.C. (2012). UHRF1 phosphorylation by cyclin A2/cyclin-dependent kinase 2 is required for zebrafish embryogenesis. Mol. Biol. Cell *23*, 59–70.

Chu, J., Mir, A., Gao, N., Rosa, S., Monson, C., Sharma, V., Steet, R., Freeze, H.H., Lehrman, M.A., and Sadler, K.C. (2013). A zebrafish model of congenital disorders of glycosylation with phosphomannose isomerase deficiency reveals an early opportunity for corrective mannose supplementation. Dis. Model. Mech. *6*, 95–105.

Decottignies, A., and d'Adda di Fagagna, F. (2011). Epigenetic alterations associated with cellular senescence: a barrier against tumorigenesis or a red carpet for cancer? Semin. Cancer Biol. *21*, 360–366.

Di Micco, R., Sulli, G., Dobreva, M., Liontos, M., Botrugno, O.A., Gargiulo, G., dal Zuffo, R., Matti, V., d'Ario, G., Montani, E., et al. (2011). Interplay between oncogene-induced DNA damage response and heterochromatin in senescence and cancer. Nat. Cell Biol. *13*, 292–302.

Du, Z., Song, J., Wang, Y., Zhao, Y., Guda, K., Yang, S., Kao, H.Y., Xu, Y., Willis, J., Markowitz, S.D., et al. (2010). DNMT1 stability is regulated by proteins coordinating deubiquitination and acetylation-driven ubiquitination. Sci. Signal. *3*, ra80.

Eden, A., Gaudet, F., Waghmare, A., and Jaenisch, R. (2003). Chromosomal instability and tumors promoted by DNA hypomethylation. Science *300*, 455.

Fairweather, D.S., Fox, M., and Margison, G.P. (1987). The in vitro lifespan of MRC-5 cells is shortened by 5-azacytidine-induced demethylation. Exp. Cell Res. *168*, 153–159.

Feng, S., Cokus, S.J., Zhang, X., Chen, P.Y., Bostick, M., Goll, M.G., Hetzel, J., Jain, J., Strauss, S.H., Halpern, M.E., et al. (2010). Conservation and divergence of methylation patterning in plants and animals. Proc. Natl. Acad. Sci. USA *107*, 8689–8694.

Gaudet, F., Hodgson, J.G., Eden, A., Jackson-Grusby, L., Dausman, J., Gray, J.W., Leonhardt, H., and Jaenisch, R. (2003). Induction of tumors in mice by genomic hypomethylation. Science *300*, 489–492.

Gaudet, F., Rideout, W.M., 3rd, Meissner, A., Dausman, J., Leonhardt, H., and Jaenisch, R. (2004). Dnmt1 expression in pre- and postimplantation embryogenesis and the maintenance of IAP silencing. Mol. Cell. Biol. *24*, 1640–1648.

Hashimoto, H., Horton, J.R., Zhang, X., Bostick, M., Jacobsen, S.E., and Cheng, X. (2008). The SRA domain of UHRF1 flips 5-methylcytosine out of the DNA helix. Nature *455*, 826–829.

Hoshida, Y. (2010). Nearest template prediction: a single-sample-based flexible class prediction with confidence assessment. PLoS ONE *5*, e15543.

Howard, G., Eiges, R., Gaudet, F., Jaenisch, R., and Eden, A. (2008). Activation and transposition of endogenous retroviral elements in hypomethylation induced tumors in mice. Oncogene *27*, 404–408.

Imrie, D., and Sadler, K.C. (2010). White adipose tissue development in zebrafish is regulated by both developmental time and fish size. Dev. Dyn. *239*, 3013–3023.

Jackson-Grusby, L., Beard, C., Possemato, R., Tudor, M., Fambrough, D., Csankovszki, G., Dausman, J., Lee, P., Wilson, C., Lander, E., and Jaenisch, R. (2001). Loss of genomic methylation causes p53-dependent apoptosis and epigenetic deregulation. Nat. Genet. *27*, 31–39.

Jin, W., Chen, L., Chen, Y., Xu, S.G., Di, G.H., Yin, W.J., Wu, J., and Shao, Z.M. (2010). UHRF1 is associated with epigenetic silencing of BRCA1 in sporadic breast cancer. Breast Cancer Res. Treat. *123*, 359–373.

Jirtle, R.L. (2004). IGF2 loss of imprinting: a potential heritable risk factor for colorectal cancer. Gastroenterology *126*, 1190–1193.

Karpf, A.R., and Matsui, S. (2005). Genetic disruption of cytosine DNA methyltransferase enzymes induces chromosomal instability in human cancer cells. Cancer Res. *65*, 8635–8639.

Karpf, A.R., Moore, B.C., Ririe, T.O., and Jones, D.A. (2001). Activation of the p53 DNA damage response pathway after inhibition of DNA methyltransferase by 5-aza-2′-deoxycytidine. Mol. Pharmacol. *59*, 751–757.

Kwan, K.M., Fujimoto, E., Grabher, C., Mangum, B.D., Hardy, M.E., Campbell, D.S., Parant, J.M., Yost, H.J., Kanki, J.P., and Chien, C.B. (2007). The Tol2kit: a multisite gateway-based construction kit for Tol2 transposon transgenesis constructs. Dev. Dyn. *236*, 3088–3099.

Li, E., Beard, C., and Jaenisch, R. (1993). Role for DNA methylation in genomic imprinting. Nature *366*, 362–365.

Liu, X., Gao, Q., Li, P., Zhao, Q., Zhang, J., Li, J., Koseki, H., and Wong, J. (2013). UHRF1 targets DNMT1 for DNA methylation through cooperative binding of hemi-methylated DNA and methylated H3K9. Nat. Commun. *4*, 1563.

Llovet, J.M., Burroughs, A., and Bruix, J. (2003). Hepatocellular carcinoma. Lancet *362*, 1907–1917.

Llovet, J.M., Chen, Y., Wurmbach, E., Roayaie, S., Fiel, M.I., Schwartz, M., Thung, S.N., Khitrov, G., Zhang, W., Villanueva, A., et al. (2006). A molecular signature to discriminate dysplastic nodules from early hepatocellular carcinoma in HCV cirrhosis. Gastroenterology *131*, 1758–1767.

Llovet, J.M., Ricci, S., Mazzaferro, V., Hilgard, P., Gane, E., Blanc, J.F., de Oliveira, A.C., Santoro, A., Raoul, J.L., Forner, A., et al.; SHARP Investigators Study Group (2008). Sorafenib in advanced hepatocellular carcinoma. N. Engl. J. Med. *359*, 378–390.

Lujambio, A., Akkari, L., Simon, J., Grace, D., Tschaharganeh, D.F., Bolden, J.E., Zhao, Z., Thapar, V., Joyce, J.A., Krizhanovsky, V., and Lowe, S.W. (2013). Non-cell-autonomous tumor suppression by p53. Cell *153*, 449–460.

McDuff, F.K., and Turner, S.D. (2011). Jailbreak: oncogene-induced senescence and its evasion. Cell. Signal. *23*, 6–13.

Mudbhary, R., and Sadler, K.C. (2011). Epigenetics, development, and cancer: zebrafish make their mark. Birth Defects Res. C Embryo Today *93*, 194–203.

Nishiyama, A., Yamaguchi, L., Sharif, J., Johmura, Y., Kawamura, T., Nakanishi, K., Shimamura, S., Arita, K., Kodama, T., Ishikawa, F., et al. (2013). Uhrf1-dependent H3K23 ubiquitylation couples maintenance DNA methylation and replication. Nature *502*, 249–253.

Pogribny, I.P., and Rusyn, I. (2014). Role of epigenetic aberrations in the development and progression of human hepatocellular carcinoma. Cancer Lett. *342*, 223–230.

Qin, W., Leonhardt, H., and Spada, F. (2011). Usp7 and Uhrf1 control ubiquitination and stability of the maintenance DNA methyltransferase Dnmt1. J. Cell. Biochem. *112*, 439–444.

Rai, K., Nadauld, L.D., Chidester, S., Manos, E.J., James, S.R., Karpf, A.R., Cairns, B.R., and Jones, D.A. (2006). Zebra fish Dnmt1 and Suv39h1 regulate organ-specific terminal differentiation during development. Mol. Cell. Biol. *26*, 7077–7085.

Rai, K., Sarkar, S., Broadbent, T.J., Voas, M., Grossmann, K.F., Nadauld, L.D., Dehghanizadeh, S., Hagos, F.T., Li, Y., Toth, R.K., et al. (2010). DNA demethylase activity maintains intestinal cells in an undifferentiated state following loss of APC. Cell *142*, 930–942.

Sadler, K.C., Amsterdam, A., Soroka, C., Boyer, J., and Hopkins, N. (2005). A genetic screen in zebrafish identifies the mutants vps18, nf2 and foie gras as models of liver disease. Development *132*, 3561–3572.

Sadler, K.C., Krahn, K.N., Gaur, N.A., and Ukomadu, C. (2007). Liver growth in the embryo and during liver regeneration in zebrafish requires the cell cycle regulator, uhrf1. Proc. Natl. Acad. Sci. USA *104*, 1570–1575.

Sharif, J., Muto, M., Takebayashi, S., Suetake, I., Iwamatsu, A., Endo, T.A., Shinga, J., Mizutani-Koseki, Y., Toyoda, T., Okamura, K., et al. (2007). The SRA protein Np95 mediates epigenetic inheritance by recruiting Dnmt1 to methylated DNA. Nature *450*, 908–912.

Tang, X., Milyavsky, M., Goldfinger, N., and Rotter, V. (2007). Amyloid-beta precursor-like protein APLP1 is a novel p53 transcriptional target gene that augments neuroblastoma cell death upon genotoxic stress. Oncogene *26*, 7302–7312.

Taylor, E.M., Bonsu, N.M., Price, R.J., and Lindsay, H.D. (2013). Depletion of Uhrf1 inhibits chromosomal DNA replication in Xenopus egg extracts. Nucleic Acids Res. *41*, 7725–7737.

Tien, A.L., Senbanerjee, S., Kulkarni, A., Mudbhary, R., Goudreau, B., Ganesan, S., Sadler, K.C., and Ukomadu, C. (2011). UHRF1 depletion causes a G2/M arrest, activation of DNA damage response and apoptosis. Biochem. J. *435*, 175–185.

Tischoff, I., and Tannapfe, A. (2008). DNA methylation in hepatocellular carcinoma. World J. Gastroenterol. *14*, 1741–1748.

Tittle, R.K., Sze, R., Ng, A., Nuckels, R.J., Swartz, M.E., Anderson, R.M., Bosch, J., Stainier, D.Y., Eberhart, J.K., and Gross, J.M. (2011). Uhrf1 and Dnmt1 are required for development and maintenance of the zebrafish lens. Dev. Biol. *350*, 50–63.

Unoki, M., Daigo, Y., Koinuma, J., Tsuchiya, E., Hamamoto, R., and Nakamura, Y. (2010). UHRF1 is a novel diagnostic marker of lung cancer. Br. J. Cancer *103*, 217–222.

Ventura, A., Kirsch, D.G., McLaughlin, M.E., Tuveson, D.A., Grimm, J., Lintault, L., Newman, J., Reczek, E.E., Weissleder, R., and Jacks, T. (2007). Restoration of p53 function leads to tumour regression in vivo. Nature *445*, 661–665.

Villanueva, A., Chiang, D.Y., Newell, P., Peix, J., Thung, S., Alsinet, C., Tovar, V., Roayaie, S., Minguez, B., Sole, M., et al. (2008). Pivotal role of mTOR signaling in hepatocellular carcinoma. Gastroenterology *135*, 1972–1983.

Villanueva, A., Hoshida, Y., Battiston, C., Tovar, V., Sia, D., Alsinet, C., Cornella, H., Liberzon, A., Kobayashi, M., Kumada, H., et al. (2011). Combining clinical, pathology, and gene expression data to predict recurrence of hepatocellular carcinoma. Gastroenterology *140*, 1501–1512.

Wang, F., Yang, Y.Z., Shi, C.Z., Zhang, P., Moyer, M.P., Zhang, H.Z., Zou, Y., and Qin, H.L. (2012). UHRF1 promotes cell growth and metastasis through repression of p16(ink4a) in colorectal cancer. Ann. Surg. Oncol. *19*, 2753–2762.

Weber, M., and Schübeler, D. (2007). Genomic patterns of DNA methylation: targets and function of an epigenetic mark. Curr. Opin. Cell Biol. *19*, 273–280.

Wurmbach, E., Chen, Y.B., Khitrov, G., Zhang, W., Roayaie, S., Schwartz, M., Fiel, I., Thung, S., Mazzaferro, V., Bruix, J., et al. (2007). Genome-wide molecular profiles of HCV-induced dysplasia and hepatocellular carcinoma. Hepatology *45*, 938–947.

Xue, W., Zender, L., Miething, C., Dickins, R.A., Hernando, E., Krizhanovsky, V., Cordon-Cardo, C., and Lowe, S.W. (2007). Senescence and tumour clearance is triggered by p53 restoration in murine liver carcinomas. Nature *445*, 656–660.

Yamada, Y., Jackson-Grusby, L., Linhart, H., Meissner, A., Eden, A., Lin, H., and Jaenisch, R. (2005). Opposing effects of DNA hypomethylation on intestinal and liver carcinogenesis. Proc. Natl. Acad. Sci. USA *102*, 13580–13585.

You, J.S., and Jones, P.A. (2012). Cancer genetics and epigenetics: two sides of the same coin? Cancer Cell *22*, 9–20.

Cancer Cell
Article

Disrupting the Interaction of BRD4 with Diacetylated Twist Suppresses Tumorigenesis in Basal-like Breast Cancer

Jian Shi,[1,4] Yifan Wang,[1,4,5] Lei Zeng,[6] Yadi Wu,[2,4] Jiong Deng,[7] Qiang Zhang,[6] Yiwei Lin,[1,4] Junlin Li,[1,4] Tiebang Kang,[5] Min Tao,[8] Elena Rusinova,[6] Guangtao Zhang,[6] Chi Wang,[4] Haining Zhu,[1] Jun Yao,[9] Yi-Xin Zeng,[5] B. Mark Evers,[1,3,4] Ming-Ming Zhou,[6,*] and Binhua P. Zhou[1,4,5,*]

[1]Department of Molecular and Cellular Biochemistry, College of Medicine, University of Kentucky, Lexington, KY 40506, USA
[2]Department of Molecular and Biomedical Pharmacology, College of Medicine, University of Kentucky, Lexington, KY 40506, USA
[3]Department of Surgery, College of Medicine, University of Kentucky, Lexington, KY 40506, USA
[4]Markey Cancer Center, College of Medicine, University of Kentucky, Lexington, KY 40506, USA
[5]Sun Yat-sen University Cancer Center, State Key Laboratory of Oncology in South China, and Collaborative Innovation Center of Cancer Medicine, Guangzhou 510060, China
[6]Department of Structural and Chemical Biology, Icahn School of Medicine at Mount Sinai, New York, NY 10029, USA
[7]Department of Pathophysiology, Shanghai Key Laboratory for Tumor Microenvironment and Inflammation, and Translation Medicine Center, Shanghai Chest Hospital, Shanghai Jiao Tong University School of Medicine, Shanghai 200025, China
[8]Department of Oncology, the First Affiliated Hospital of Soochow University, Suzhou 215006, China
[9]Department of Molecular and Cellular Oncology, University of Texas M.D. Anderson Cancer Center, Houston, TX 77030, USA
*Correspondence: ming-ming.zhou@mssm.edu (M.-M.Z.), peter.zhou@uky.edu (B.P.Z.)
http://dx.doi.org/10.1016/j.ccr.2014.01.028

SUMMARY

Twist is a key transcription activator of epithelial-mesenchymal transition (EMT). It remains unclear how Twist induces gene expression. Here we report a mechanism by which Twist recruits BRD4 to direct *WNT5A* expression in basal-like breast cancer (BLBC). Twist contains a "histone H4-mimic" GK-X-GK motif that is diacetylated by Tip60. The diacetylated Twist binds the second bromodomain of BRD4, whose first bromodomain interacts with acetylated H4, thereby constructing an activated Twist/BRD4/P-TEFb/RNA-Pol II complex at the *WNT5A* promoter and enhancer. Pharmacologic inhibition of the Twist-BRD4 association reduced *WNT5A* expression and suppressed invasion, cancer stem cell (CSC)-like properties, and tumorigenicity of BLBC cells. Our study indicates that the interaction with BRD4 is critical for the oncogenic function of Twist in BLBC.

INTRODUCTION

Recruitment and activation of RNA-Pol II at gene promoters are two key steps required for a productive transcription (Zhou et al., 2012). After RNA-Pol II recruitment to a gene promoter, TFIIH phosphorylates serine 5 of the heptapeptide repeats in the C-terminal domain (CTD) of RNA-Pol II, resulting in initial synthesis of short RNA species. However, RNA-Pol II pauses in the proximal promoter and requires a second phosphorylation event on serine 2 of the CTD that is carried out by the pause release factor P-TEFb, a complex composed of CDK9 and cyclin T1/2. Importantly, the recruitment of P-TEFb to RNA-Pol II is mediated, in part, by BRD4 (Jang et al., 2005).

BRD4 is a member of the BET (bromodomain and extra terminal domain) family proteins that are characteristic of two tandem bromodomains (BDs) located in the N terminus. The BDs of BET proteins recognize acetylated-lysine residues in nucleosomal histones (Filippakopoulos et al., 2012), facilitating the

Significance

BLBC is associated with an aggressive clinical history, development of recurrence, distant metastasis, and shorter patient survival. BLBC contains abundant EMT transcription factor Twist and possesses many CSC-like characteristics, suggesting that the Twist-activated EMT program confers growth advantages to BLBC. However, the absence of a clear ligand-binding domain in Twist creates a formidable hurdle toward developing inhibitors that can suppress its function. We found that Twist interacts with and recruits the BRD4/P-TEFb/RNA-Pol II transcription complex to the *WNT5A* superenhancer for gene activation. BET-specific inhibitors disrupted the Twist-BRD4 interaction and resulted in significant Wnt5a reduction, leading to inhibition of invasion and tumorigenicity of BLBC in vitro and in vivo. Our study indicates that targeting the Twist-BRD4 interaction provides an effective approach for treating BLBC.

recruitment of transcriptional proteins to chromatin. Recent studies have shown that pharmacologic inhibition of BRD4 with BET-specific BD inhibitors effectively blocks *MYC* expression in multiple myeloma (Delmore et al., 2011), Burkitt's lymphoma, and acute myeloid leukemia (Dawson et al., 2011; Zuber et al., 2011). However, many mechanistic questions about BRD4 functions as a chromatin regulator in gene transcription are still unanswered, including (1) how BRD4 interacts and works with transcription factors at the target gene promoter and enhancer sites and (2) whether and how the two BDs in BRD4 function differently in gene transcription.

Breast cancer is a heterogeneous disease that can be divided into four major subtypes based on gene expression profiling: luminal A, luminal B, ErbB2, and basal like. Basal-like breast cancer (BLBC) is characterized by the lack of expression of estrogen receptor (ER), progesterone receptor (PR), and epidermal growth factor receptor 2 (HER2) and positive expression of basal markers (Cytokeratin 5/6 [CK5/6] and CK14) (Rakha et al., 2008). The absence of effective targeted therapies and poor response to standard chemotherapy often results in a rapidly fatal clinical outcome for this disease. Notably, BLBC has activated the epithelial-mesenchymal transition (EMT) program, which provides cells with increased plasticity and stem-cell-like properties required during embryonic development, tissue remodeling, wound healing, and metastasis (Thiery et al., 2009).

Twist and Snail are two key members of EMT-activating transcriptional factors. During mesoderm development in *Drosophila*, Snail functions as a transcriptional repressor to prevent expression of genes that belong to ectoderm, whereas Twist serves as a transcriptional activator to induce mesodermal gene expression (Leptin, 1991). A complete loss of all mesodermal characteristics occurs only when both Snail and Twist are absent. These results suggest that Snail and Twist work synergistically, controlling distinct sets of genes, to coordinate EMT induction and mesoderm formation (Zeitlinger et al., 2007). We previously showed that Snail interacts with several transcriptional repressive complexes to suppress gene expression. However, the mechanism underlying gene transcriptional activation by Twist has remained elusive. In this study, we sought to identify Twist-interacting proteins and determine the mechanism by which Twist controls gene transcriptional activation in EMT and BLBC.

RESULTS

BRD4-BD2 Interacts with Lysine-Acetylated Twist

We sought to identify Twist-interacting proteins from a stable HeLa S3 cell line expressing Flag-Twist. Affinity protein purification, followed by SDS-PAGE and analysis by mass spectrometry, revealed the presence of BRD4 and TRRAP/EP400 (data not shown). To validate the interaction between Twist and BRD4, we coexpressed hemagglutinin (HA)-Twist and Flag-BRD4 in HEK293 cells in the presence or absence of the histone deacetylase inhibitor Trichostatin (TSA). After immunoprecipitating Twist, we detected the associated BRD4, and vice versa (Figure 1A and Figure S1A available online). Although similar amounts of Twist were immunoprecipitated from cells with and without TSA treatment, Twist was more acetylated and interacted with more BRD4 in cells treated with TSA. In addition, immunoprecipitation with a pan-acetylated-lysine (pan-AcK) antibody pulled down Twist and BRD4 in cells treated with TSA. Similar observations were made in Twist-expressing HeLa S3 cells (Figures 1B and S1B). We further confirmed the interaction between the endogenous Twist and BRD4 and acetylation of the endogenous Twist in four BLBC cell lines, both of which were substantially enhanced with TSA treatment (Figures 1C and S1C). The Twist-BRD4 interaction is specific because Twist did not associate with other BET members (BRD2, BRD3, and BRDT) or lysine specific demethylase 1 (LSD1), and BRD4 did not associate with TCF4 (Figure S1D). The increased Twist-BRD4 interaction by TSA could not be due to an altered subcellular localization of these two proteins as TSA did not affect their localization (Figure S1E).

We next generated BRD4 deletion constructs and coexpressed them with Twist in HEK293 cells. We found that only N-terminal fragments containing both BDs, but not other regions of BRD4, retained the ability to interact with Twist (Figure 1D). When BD1 or BD2 was coexpressed with Twist in HEK293 cells, only $BD2^{WT}$, but not $BD1^{WT}$, bound to Twist (Figures 1E and S1F). Mutation of the conserved tyrosine and asparagine residues in the acetyllysine binding pocket of BD2 to alanine ($BD2^{YN}$) reduced its binding to Twist. The Twist-BRD4 interaction was readily disrupted when JQ1, a BET-specific BD inhibitor, was added to the immunoprecipitation reaction (Figures 1F, 1G, S1G, and S1H). Similarly, MS417, a BET-specific BD inhibitor with approximately 10-fold higher binding affinity than JQ1 (Zhang et al., 2012), effectively blocked the Twist-BRD4 interaction in four BLBC cell lines (Figures S1I and S1J). These results indicate that the Twist-BRD4 interaction is mediated by the BD2 of BRD4 binding to lysine-acetylated Twist.

Twist Diacetylation at K73 and K76 by Tip60 Is Required for Twist-BRD4 Interaction

The N-terminal half of Twist contains an acidic segment and two lysine/arginine-rich basic motifs that share high sequence similarity to histones H2B and H4, respectively (Figure S2A). We generated Twist deletion constructs DL1 (residues 15–202), DL2 (residues 31–202), and DL3 (residues 47–202) and coexpressed them individually with Flag-BRD4 in HEK293 cells. DL1 retained, whereas DL2 and DL3 lost, interaction with BRD4 (Figures 2A and S2B). Surprisingly, in contrast to DL1, DL2 and DL3 also completely lost acetylation (Figures 2B and S2C). Because the first 30 N-terminal residues in Twist do not contain lysine, the loss of acetylation in DL2 and DL3 suggests that the N-terminal region is critical for Twist acetylation. In our mass spectrometry analysis, the NuA4 histone acetyltransferase complex proteins, including TRRAP and EP400 (Doyon and Côté, 2004), were identified as Twist association partners. We postulated that Tip60, the acetyltransferase of NuA4 complex, was responsible for Twist acetylation. Indeed, when $Twist^{WT}$, DL1, DL2, and DL3 were coexpressed with Tip60 in HEK293 cells, we found that $Twist^{WT}$ and DL1, but not DL2 or DL3, interacted with Tip60 (Figures 2C and S2D). Endogenous Twist-Tip60 interaction was confirmed in three BLBC cell lines, which was markedly enhanced by TSA treatment (Figure S2E). We further observed that ectopic expression of Tip60 in BT549 and SUM1315 cells resulted in enhanced acetylation of Twist and the association of Twist with BRD4 even in the absence of

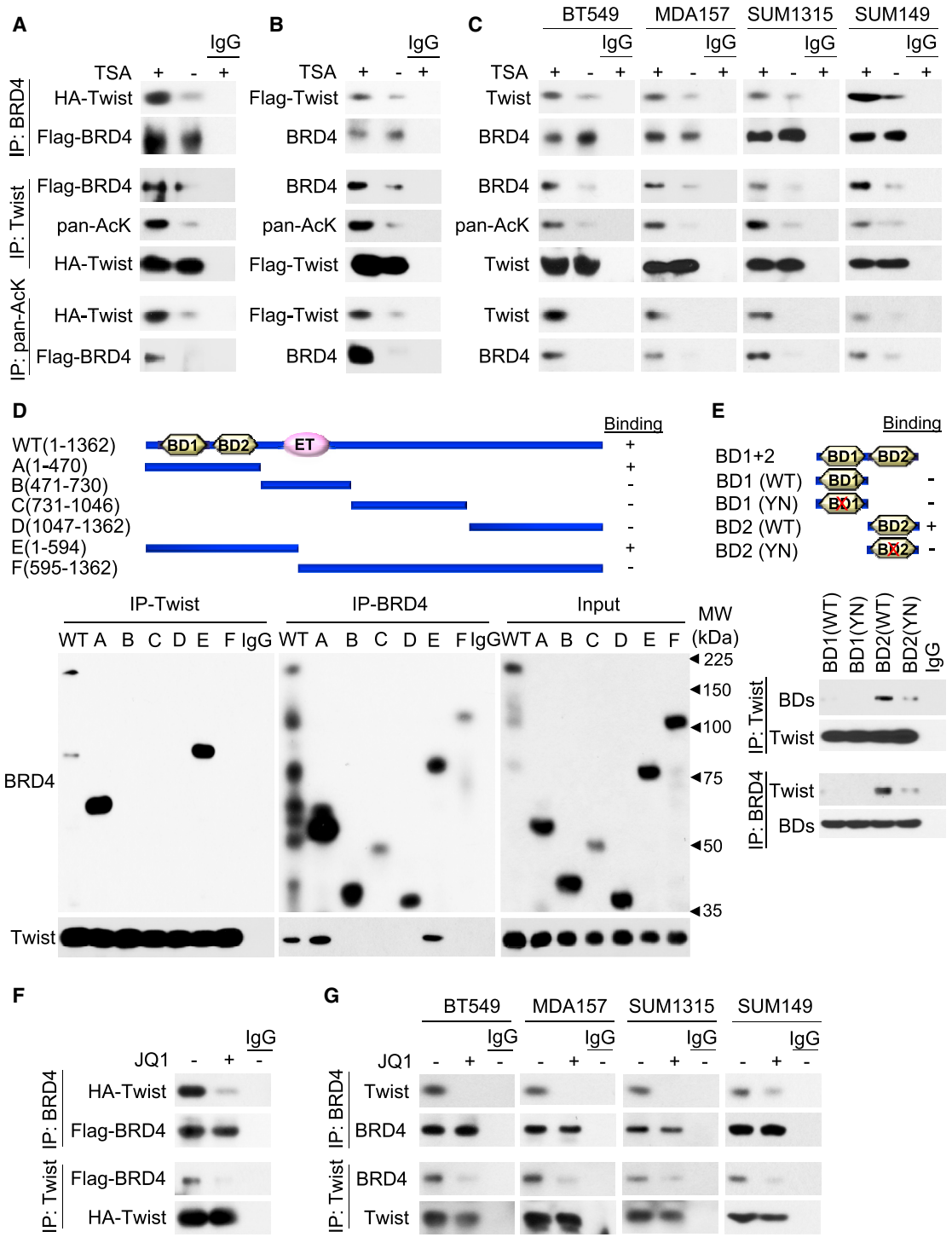

Figure 1. BD2 of BRD4 Is Required for Its Interaction with Acetylated Twist

(A) HA-Twist and Flag-BRD4 were coexpressed in HEK293 cells. After treatment of cells with TSA (2 μM) for 12 hr, Twist, BRD4, and acetylated Twist were immunoprecipitated with HA, Flag, and pan-acetylated-lysine (pan-AcK) antibodies, respectively, and analyzed by western blotting.

(B) HeLa cells stably expressing Flag-Twist were treated with TSA as in (A). Flag-Twist, endogenous BRD4, and acetylated Twist were immunoprecipitated and examined by western blotting.

(C) Cells were treated as described in (A). Endogenous Twist, BRD4, and acetylated Twist were immunoprecipitated and examined by western blotting.

(D) Schematic depiction of the functional domains of BRD4 and deletion constructs used (top). ET, extraterminal domain. Flag-tagged wild-type (WT) or deletion mutants of BRD4 were coexpressed with HA-Twist in HEK293 cells. After being immunoprecipitated with HA or Flag antibody, the bound BRD4 or Twist was examined by western blotting (bottom).

(legend continued on next page)

TSA, whereas knockdown of Tip60 yielded opposite effects even in the presence of TSA (Figures 2D and S2F).

Twist contains five lysine residues (K33, K38, K73, K76, and K77) in its N-terminal region, which are highly conserved among different species (Figure S2A). Point mutation of K33R, K73R, and K76R showed a reduced level of acetylation compared to that of Twist^{WT} (Figures 2E and S2G). Twist^{WT}, K33R, K38R, and K77R showed a similar interaction with BD2, whereas K73R and K76R exhibited clearly weaker binding to BD2 (Figures 2F and S2H). The K73R/K76R double mutant showed an almost complete loss of acetylation and interaction with BD2 (Figures 2G and S2I). We further confirmed the Tip60-mediated Twist acetylation on K73/K76 by mass spectrometry analysis (Figures 2H and S2J). There are 12 nuclear histone acetyltransferases (HATs), divided into three major groups: (1) the GNAT family (e.g., PCAF), (2) the MYST family (e.g., Tip60), and (3) the p300/CBP family (e.g., p300 and CBP) (Rekowski and Giannis, 2010). To examine whether other HATs can also acetylate Twist, we knocked down the expression of p300, CBP, PCAF, or Tip60 individually in BT549 and SUM1315 cells (Figure S2K). We found that knockdown of Tip60, but not p300, CBP, or PCAF, suppressed Twist acetylation at K73/K76. Taken together, these data support our contention that Tip60 is the major HAT responsible for the K73/K76 acetylation on Twist and that diacetylation of Twist is required for its association with BRD4-BD2.

Histone H4 Mimicry in Twist Is Responsible for Its Interaction with BRD4

Diacetylations of the N-terminal tail of H4 at K5 and K8 are often required for the interaction of H4 with BDs of BET family proteins (Filippakopoulos et al., 2012; Morinière et al., 2009). The Twist sequence at K73 and K76 shares high similarity to the N-terminal tail of H4 at K5 and K8 (Figure 3A). To investigate this "histone mimicry" in the interaction between Twist and BRD4, we performed a pull-down study using biotinylated H4 and Twist peptides and lysate of HEK293 cells expressing BRD4-BD2. We observed that biotinylated H4-K5ac/K8ac peptide (residues 1–21) was bound to BD2 and that this interaction was disrupted by nonbiotinylated H4-K5ac/K8ac peptide (Figure 3B, lane 2 versus lane 1). This interaction was also markedly reduced by a Twist-K73ac/K76ac peptide (residues 61–80) but not by the unacetylated corresponding peptide (Figure 3B, lanes 3 and 4 versus lane 1). Similarly, the interaction of a biotinylated Twist-K73ac/K76ac peptide with BD2 was disrupted by a Twist-K73ac/K76ac, but not unacetylated, peptide (Figure 3B, lanes 7 and 8 versus lane 5). Notably, acetylated H4 peptide also disrupted the acetylated Twist and BD2 association (Figure 3B, lane 6 versus lane 5), indicating that diacetylated K5/K8 in H4 and diacetylated K73/K76 in Twist function similarly as a recognition motif for BRD4-BD2.

We then developed a specific antibody against Twist-K73ac/K76ac. Twist recognition by this antibody was disrupted by a Twist-K73ac/K76ac peptide, but not the corresponding nonacetylated peptide (Figures 3C and S3A). This antibody recognized immunoprecipitated Twist^{WT}, but not Twist$^{K73R/K76R}$ that harbored mutated K73 and K76 (Figures 3D and S3B). In line with our contention that Tip60 acetylates Twist at K73/K76, both Twist and H4 acetylated by purified Tip60 in vitro were recognized by this Twist-K73ac/K76ac antibody and a pan-acetylated antibody (Figure 3E). Furthermore, this antibody readily detected endogenous Twist-K73ac/K76ac that was immunoprecipitated from four BLBC cell lines (Figures 3D and S3B). Although immunoprecipitation of the endogenous Twist by this antibody was weak, it was robustly increased by the addition of JQ1 to the binding buffer, indicating that the K73ac/K76ac site is masked by binding to BRD4 in cells (Figure 3F).

We further characterized the functional importance of this diacetylation-dependent Twist-BRD4 interaction in human mammary epithelial (HMLE) cells. Ectopic expression of Twist^{WT} resulted in an induction of EMT, as indicated by the downregulation of E-cadherin and upregulation of vimentin (Figures 3G and S3C). While localized in the nucleus (Figure S3D), Twist$^{K73R/K76R}$ expression failed to induce EMT, indicating that the interaction with BRD4 is critical for the function of Twist.

Molecular Basis of BRD4 Binding to Lysine-Acetylated Twist

To determine the molecular basis of diacetylation-dependent Twist-BRD4 association, we characterized binding of the two BDs of BRD4 to a series of Twist peptides (residues 68–79) bearing no, single-acetylated, or diacetylated lysine at K73 and K76 by nuclear magnetic resonance (NMR) titration. As shown in 2D ^{1}H-^{15}N HSQC spectra (Figure S4A), BRD4-BD2 exhibited substantially more extended chemical shift perturbations upon binding to the single-acetylated, and even more to the diacetylated, Twist peptides than those produced by BRD4-BD1, confirming that BRD4-BD2 is largely responsible for BRD4 association with the diacetylated Twist. The preferred recognition of Twist-K73ac/K76ac by BRD4-BD2 was supported in a fluorescence anisotropy competition binding study using a fluorescein-labeled H4K5ac/K8ac peptide as an assay probe, yielding a K_i of 800 μM and >3,000 μM for BRD4-BD2 and BRD4-BD1, respectively (Figure S4B). Furthermore, BRD4-BD1 and other BDs, including those from CBP and PCAF, showed almost no interaction with the single- or diacetylated Twist peptides (data not shown).

We next solved the 3D structure of BRD4-BD2 bound to Twist-K73ac/K76ac peptide using NMR spectroscopy to determine the molecular basis of this selective interaction (Figures 4A, 4B, and S4C and Table S1). As revealed in the 3D structure, the Twist-K73ac/K76ac peptide is bound in the protein across

(E) Schematic diagram showing the double bromodomain (BD1+BD2) of BRD4 and individual BD constructs used (top). Flag-BD1^{WT}, BD1^{YN}, BD2^{WT}, and BD2^{YN} were coexpressed with HA-Twist in HEK293 cells treated with TSA as in (A). Twist and BDs were immunoprecipitated with HA and Flag antibodies, respectively, and analyzed by western blotting (bottom).
(F) HA-Twist and Flag-BRD4 were coexpressed in HEK293 cells treated with TSA as in (A). Twist and BRD4 were immunoprecipitated with HA and Flag antibodies, respectively, in the presence or absence of JQ1 (1 μM) and analyzed by western blotting.
(G) Cells were treated with TSA as in (A). Endogenous Twist and BRD4 were immunoprecipitated with Twist and BRD4 antibodies, respectively, in the presence or absence of JQ1 (1 μM) and examined by western blotting.
See also Figure S1.

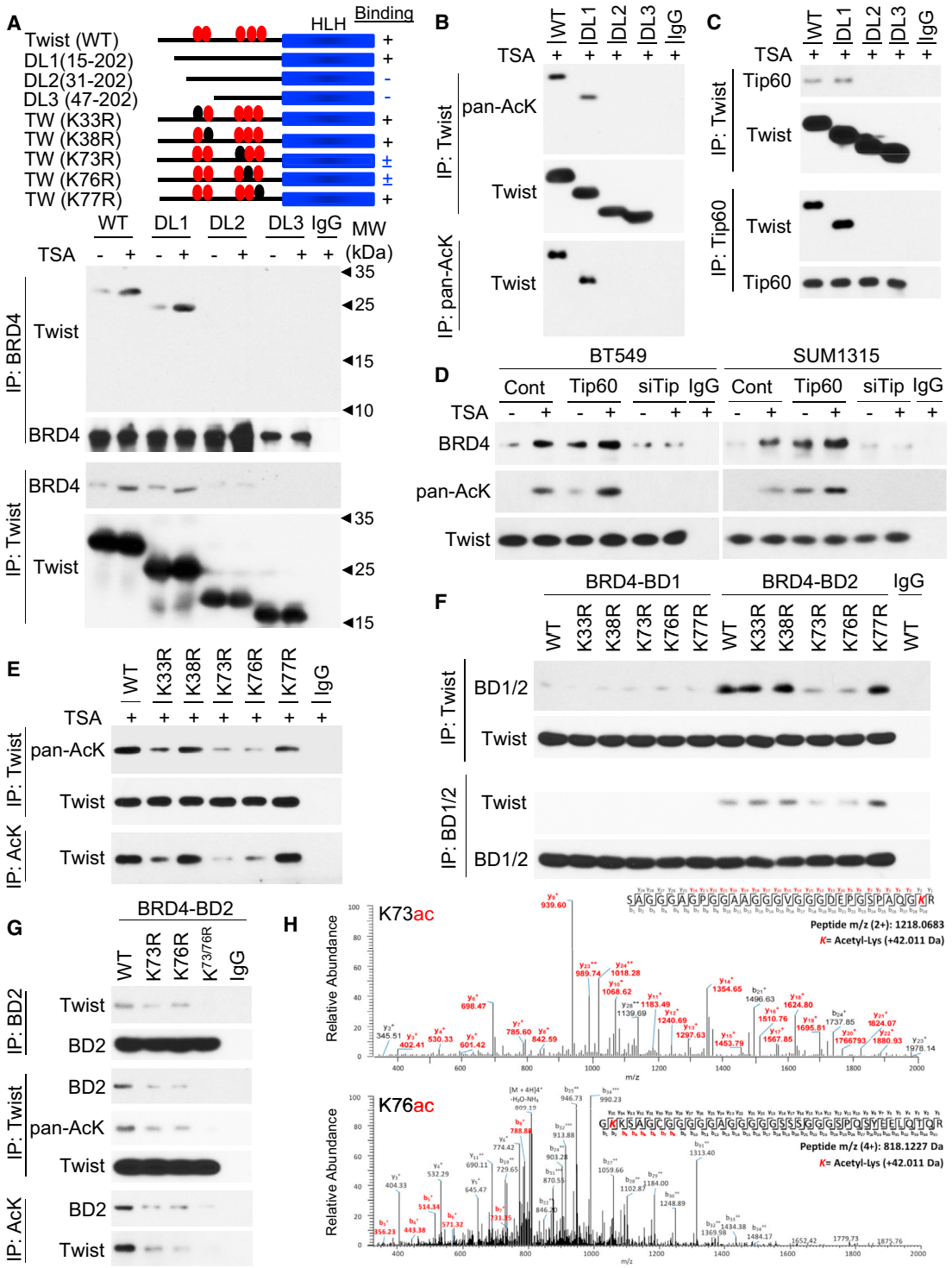

Figure 2. Twist Diacetylation at K73/K76 by Tip60 Is Required for Interaction with BRD4

(A) Schematic diagram showing the domain organization of Twist, with deletion and mutation constructs used (top). HA-tagged WT or deletion mutants of Twist were coexpressed with Flag-BRD4 in HEK293 cells treated with or without TSA. Twist and BRD4 were immunoprecipitated with HA and Flag antibodies, respectively, and analyzed by western blotting (bottom).

(B) HA-tagged WT or deletion mutants of Twist were expressed in HEK293 cells treated with TSA. Twist and acetylated Twist were immunoprecipitated with HA and pan-AcK antibodies, respectively, and analyzed by western blotting.

(C) Flag-tagged WT or deletion mutants of Twist were coexpressed with HA-Tip60 in HEK293 cells treated with TSA. Twist and Tip60 were immunoprecipitated with Flag and HA antibodies, respectively, and analyzed by western blotting.

(legend continued on next page)

an elongated cavity formed between the ZA and BC loops of this left-handed four-helical bundle structure. Specifically, acetylated K73 is bound in the canonical acetyllysine binding site, forming a hydrogen bond between its carbonyl oxygen and the side-chain nitrogen of the conserved Asn433. Acetylated K76 is recognized, next to K73ac, by the BD2 in a small hydrophobic cavity that is lined with Trp374, Val380, Leu385, and Val439. While the overall recognition of the diacetylated K73/K76 in Twist by BD2 is similar to that of the diacetylated K5/K8 in H4 by the BD1 of BRD4, several additional interactions observed in the former complex explain its selectivity. For instance, the imidazole nitrogen atom of His437 of BD2 is within hydrogen bond distance to the backbone carbonyl oxygen of the K73ac (Figures 4A and 4B). Notably, within this highly conserved acetyllysine binding pocket, His437 in BRD4-BD2, which corresponds to Asp144 in BRD4-BD1, is unique. Asp144 was not engaged in any interaction with the H4 peptide as shown in the crystal structure of the BD1/H4-K5ac/K8ac peptide complex (Filippakopoulos et al., 2012), explaining the failed binding of BRD4-BD1 to Twist-K73ac/K76ac. To further examine the role of His437 in BRD4/Twist association, we engineered two point mutants by switching His437 and Asp144 in the two BDs, generating BD2-H437D and BD1-D144H mutants. Remarkably, we found that BD2-H437D almost completely lost its ability to bind to the diacetylated Twist, whereas BD1-D144H gained binding ability for the acetylated Twist (Figure 4C), confirming the important function of His437 in the Twist-K73ac/K76ac recognition.

We observed additional intermolecular interactions in the complex structure that contribute to the selectivity of BRD4-BD2/Twist recognition. For instance, the methyl group of Ala70 of Twist interacts with the aromatic side chain of the conserved Tyr432 in BRD4-BD2, whereas side chains of Ser78 of Twist and Glu438 of the BD2 form electrostatic interactions. Importantly, both Ala70 and Ser78 in Twist are located outside the diacetylation GK-X-GK motif and are not conserved in H4. Ala70 has no corresponding residue in H4, whereas the corresponding residue for Ser78 in H4 is Leu10, which could not form a favorable interaction with Glu438 in BD2, or even Asp145 in BD1. Collectively, our structural insights provide a detailed understanding of the molecular basis for the selective recognition of Twist-K73ac/K76ac by BRD4-BD2.

Histone H4 and Twist Synergistically Interact with BRD4

Because single BD2 of BRD4 can interact with H4 or Twist, we examined their interactions in a cellular context by expressing Twist or Twist$^{K73R/K76R}$ with single or double BDs of BRD4 in HEK293 cells. After immunoprecipitation of Twist, BDs, or H4 individually, the association and acetylation of the other two molecules were analyzed by western blotting (Figures 4D and S4D). First, we immunoprecipitated Twist and examined the presence of other two molecules (Figure 4D, left panel). We found that Twist$^{K73R/K76R}$ did not associate with any of the BDs (Figure 4D, left panel, lanes 7–9), whereas Twist associated with BD2 and BD1+BD2 but not BD1. Notably, the associated BD1+BD2 also contained H4 (Figure 4D, left panel, lanes 4–6). Second, we immunoprecipitated BD1, BD2, or BD1+BD2 and examined the presence and acetylation of Twist and H4 (Figure 4D, middle panel). BD1 associated with H4 but not Twist, whereas BD2 interacted with both Twist and H4, indicating that Twist and H4 can compete for interaction with BD2 (Figure 4D, middle panel, lanes 4–6). BD1+BD2 also associated with Twist and H4. Intriguingly, the amount of H4 associated with single BD (BD1 or BD2) is similar to that with double BDs in BD1+BD2 (Figure 4D, middle panel, lanes 2 and 3 versus lane 1), suggesting that only one BD in BD1+BD2 binds to H4. In the presence of Twist, the binding of BD1+BD2 to H4 did not alter (Figure 4D, middle panel, lane 4 versus lane 1). Because Twist interacts with BD2 but not BD1, H4 likely only interacts with BD1 when BD1+BD2, Twist, and H4 are all present. Consistent with this contention, the amount of Twist associated with BD1+BD2 was more than that with BD2 (Figure 4D, middle panel, lane 4 versus lane 5), where Twist and H4 competed for the binding to the BD2. Lastly, we immunoprecipitated H4 and examined the association of Twist and BDs (Figure 4D, right panel). We found that levels of BD1, BD2, and BD1+BD2 appeared to be equivalent, suggesting that H4 interacted equally with BD1, BD2, and BD1+BD2 and that only one BD interacted with H4 in BD1+BD2. In the presence of Twist, the immunoprecipitated BD2 was reduced (Figure 4D, right panel, lane 5 versus lane 2), suggesting that Twist and H4 compete for the interaction with single BD2. However, when the double BDs (BD1+BD2) were present, only one BD was engaged in interaction with H4, since the intensity of immunoprecipitated BD1+BD2 was about equal to that of Twist (Figure 4D, right panel, lane 1 versus lane 4). Consistent with the results from immunoprecipitated Twist, the immunoprecipitated BD1+BD2 by H4 contained Twist, reaffirming the association of three protein molecules in cells. Taken together, these results indicate that Twist and H4 can simultaneously interact with the double BDs of BRD4, in which BD1 binds to H4, whereas BD2 associates with Twist. This distinct binding selectivity of the two BDs of BRD4 is supported by our structural analysis.

Twist-BRD4 Interaction Is Required for *WNT5A* Expression

To identify the transcriptional target of the Twist-BRD4 complex, we performed cDNA microarray analysis of HMLE and luminal

(D) Ectopic expression of Tip60 or knockdown of endogenous Tip60 was performed in BT549 and SUM1315 cells. After endogenous Twist was immunoprecipitated, acetylation of Twist and the bound BRD4 were examined by western blotting.
(E) HA-tagged WT and mutant Twist were expressed in HEK293 cells, acetylated Twist was immunoprecipitated with HA and pan-AcK antibodies, respectively, and examined by western blotting.
(F) HA-tagged WT or mutant Twist was coexpressed with Flag-tagged BD1 and BD2 in HEK293 cells treated with TSA. Twist and BDs were immunoprecipitated with HA and Flag antibodies, respectively, and examined by western blotting.
(G) HA-tagged WT or mutant Twist was coexpressed with Flag-tagged BD2 in HEK293 cells treated with TSA. Twist, BRD4, and acetylated Twist were immunoprecipitated with HA, Flag, and pan-AcK antibodies, respectively, and analyzed by western blotting.
(H) Determination of Tip60 catalyzed acetylation sites in Twist by mass spectrometry. Peptides contain K73 and K76 acetylations are shown at the top and bottom, respectively.
See also Figure S2.

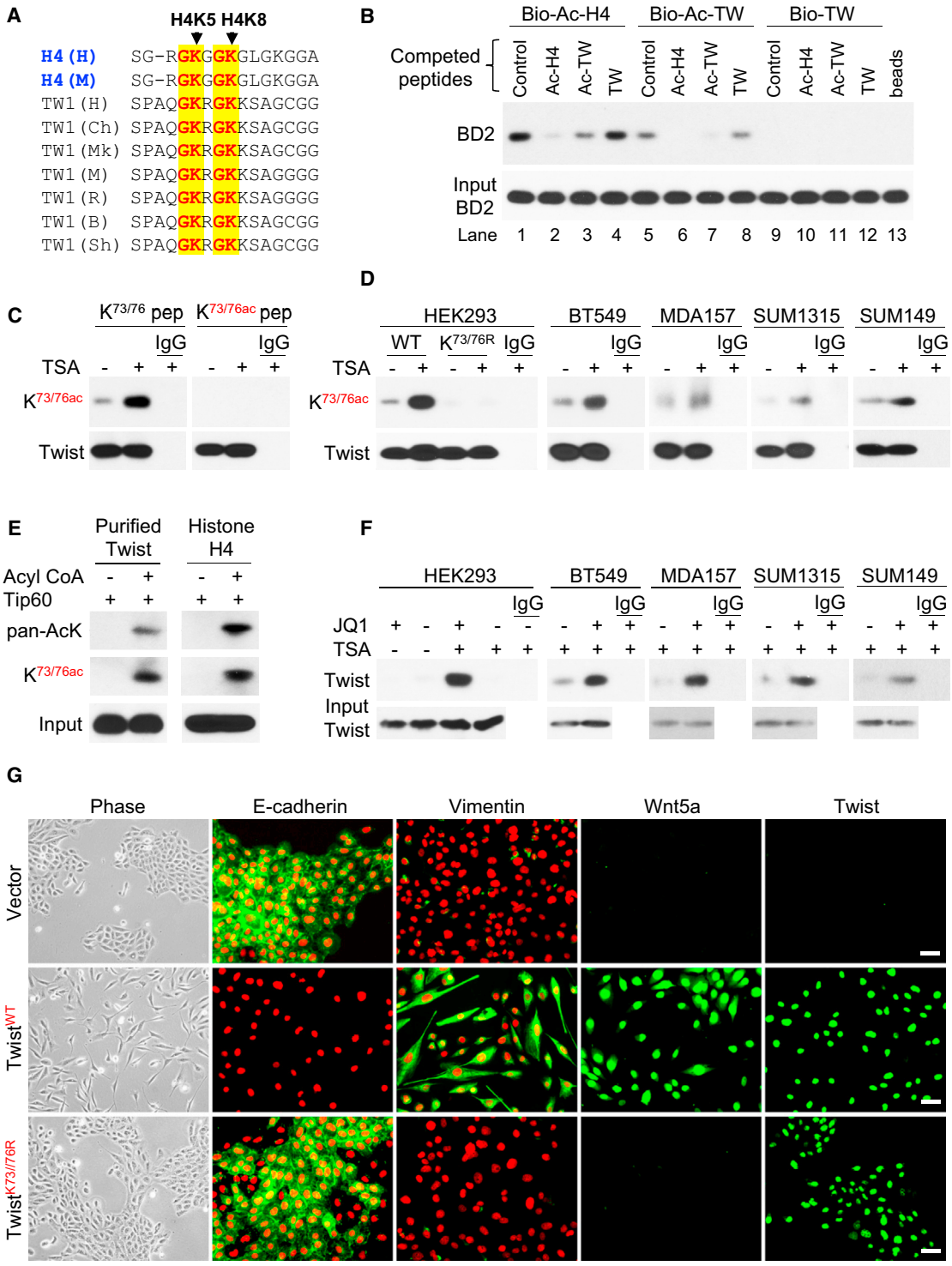

Figure 3. K73ac/K76ac Twist and BRD4 Interaction Is Critical for the Function of Twist

(A) Sequence alignment between K5/8 of histone H4 and K73/76 of Twist. H, human; M, mouse; Ch, chimpanzee; Mk, monkey; R, rat; B, bovine; Sh, sheep.

(B) The indicated biotinylated peptides were mixed with lysates from HEK293 cells expressing BD2 without or with indicated nonbiotinylated competing peptides. The bound BD2 was analyzed by western blotting after pull-down of the biotinylated peptides.

(C) HA-Twist was expressed in HEK293 cells treated with or without TSA. The immunoprecipitated Twist was analyzed on western blots using indicated antibody in the presence of Twist-K73/K76 or Twist-K73ac/K76ac peptides.

(D) HA-tagged or endogenous Twist was immunoprecipitated from cells treated with or without TSA using HA and Twist antibodies, respectively, and analyzed by K73ac/K76ac antibody.

(legend continued on next page)

T47D cells that have undergone Twist-mediated EMT (Figures 3G and S5A). We reasoned that genes that are transcriptionally active in Twist/HMLE and Twist/T47D cells but are downregulated by JQ1 in these cells but not in vector control cells are likely targets of the Twist-BRD4 complex (Figure 5A). Among the 29 overlapping genes, *WNT5A* is noted to encode a critical ligand of both canonical (controlling pluripotency) and noncanonical (regulating motility and planar cell polarity) Wnt pathways. Upregulation of Wnt5a is correlated with an aggressive phenotype in melanoma, as well as breast, lung, and prostate tumors (Witze et al., 2008). We thus selected *WNT5A* as an example to characterize the transcriptional mechanism of Twist. We noticed that $Twist^{WT}$ but not $Twist^{K73R/76R}$ induced Wnt5a expression (Figures 3G and S3C). Similarly, $Twist^{WT}$ induced EMT and Wnt5a expression in T47D cells (Figure S5A). In addition, *TWIST* expression positively correlates with *WNT5A* expression in eight microarray data sets from human breast cancer (Figure S5B). Using Twist and Wnt5a antibodies that detect Twist and Wnt5a, respectively, in xenograft tumors derived from SUM1315 cells, which express high levels of Twist and Wnt5a, but not MCF7 cells, which express low levels of Twist and Wnt5a (Figure S5C), we found that Twist is also positively correlated with Wnt5a expression in breast cancer specimens, with both increased expression found predominantly in estrogen receptor negative (ER^-) breast cancer (Figure S5D). Further, in 14 breast cell lines (Figure 5B), both the mRNA and protein levels of Twist and Wnt5a were found to be largely correlated, with elevated expressions found in BLBC cell lines. BRD4 expression is relatively constant among normal breast, luminal, and BLBC cell lines (Figure 5B). Consistently, no significant difference in BRD4 mRNA was found between ER^+ and ER^- breast cancers from a 477 sample microarray data set (Figure S5E).

We generated a clone of SUM1315 cells with stable knockdown of Twist. Twist knockdown reduced the mesenchymal phenotype as these cells were clustered together; cells also gained expression of epithelial markers and reduced the expression of mesenchymal markers (Figures 5C and S5F). Ectopic expression of $Twist^{WT}$, but not $Twist^{K73R/K76R}$, restored the mesenchymal phenotype in these cells. Twist knockdown also resulted in suppression of Wnt5a expression. Ectopic expression of $Twist^{WT}$, but not $Twist^{K73R/K76R}$, recovered Wnt5a expression (Figure 5C) and restored the invasiveness and mammosphere formation in these cells (Figure S5G). These results are in line with observations in HMLE cells (Figure 3G) and indicate that the Twist-BRD4 interaction is critical in maintaining mesenchymal phenotype/characteristics in BLBC cells. Consistently, JQ1 suppressed Wnt5a expression in both Twist/HMLE and Twist/T47D EMT cells (Figure S5H). In addition, knockdown of Twist or BRD4 in five BLBC cell lines resulted in reduced Wnt5a expression; double knockdown of these two molecules almost completely abolished Wnt5a expression (Figure 5D). The downregulation of Wnt5a by BRD4-knockdown is specific, because knockdown of other BET members did not alter Wnt5a expression (Figure S5I). In addition, knockdown of BRD4 did not change the expression of either epithelial or mesenchymal markers (Figure S5J). The downregulation of Wnt5a correlated with inhibition of invasiveness in BLBC cells; addition of recombinant Wnt5a partially restored invasiveness (Figure S5K). Collectively, these results indicate that the Twist-BRD4 interaction is most likely conserved in HMLE and BLBC cells for EMT and that this interaction is required for the expression of Wnt5a, which may represent as a bona fide target of Twist for promoting tumorigenicity in BLBC.

Twist-BRD4 Interaction Is Required for the Recruitment of BRD4 at the *WNT5A* Superenhancer

To delineate how the Twist-BRD4 complex activates *WNT5A* expression, we constructed a Twist-Gal4 fusion protein by fusing Twist N-terminal residues 1–100 to Gal4 DNA-binding domain (DBD). We also generated several N-terminal deletion mutants of Twist fused with Gal4-DBD, including DL1-Gal4, DL2-Gal4, DL3-Gal4, and KR-Gal4 (Figure S6A). When these Twist-Gal4 constructs were coexpressed with the Gal4-luciferase reporter, Gal4-luciferase activity was moderately increased by about 2-fold compared to the control; coexpression of BRD4 with the Twist-Gal4 fusion constructs that contain the N-terminal region required for Tip60-mediated acetylation (i.e., TW and DL1) greatly enhanced luciferase activity to approximately 8-fold, suggesting that the N-terminal half of Twist contains transactivation activity and its interaction with BRD4 boosts this activity.

The *WNT5A* promoter contains two Twist-responsive E boxes, conserved in human and mouse, and located at −160 bp and −67 bp from transcription start site (TSS) (Figure 6A). We cloned the human *WNT5A* promoter (−2,000 bp upstream of the translation start site) and generated several deletion and E box mutants of the promoter-luciferase constructs, including Luc1 (−2,000 bp), Luc2 (−760) and LucEM (−760, two E box mutations). As expected, Twist alone induced Luc1 and Luc2 promoter luciferase activity; coexpression of BRD4 further enhanced the Twist-induced Luc1 and Luc2 promoter luciferase activities (Figure 6A, left panel). In addition, mutation of each E box (E1M and E2M) in this region reduced, whereas mutation of both E boxes (EM) completely abolished, Twist-BRD4-mediated activation of the *WNT5A* promoter luciferase activity, suggesting that both E boxes are required for Twist-BRD4-induced transcriptional activation. $Twist^{K73R/K76R}$ mutant partially decreased *WNT5A* promoter luciferase activity and was completely insensitive to BRD4-mediated transcriptional activation (Figure 6A, right panel). BRD4-mediated enhancement of Twist transcriptional activity is specific because other BET members did not possess this capability, and treatment with JQ1 or MS417 disrupted this BRD4-mediated enhancement (Figure S6B).

(E) Purified human Twist or histone H4 was incubated with purified Tip60 in the absence or presence of acetyl-CoA. The acetylation of Twist and histone H4 was examined by pan-AcK and anti-K73ac/K76ac antibodies.
(F) K73ac/K76ac Twist was immunoprecipitated with K73ac/K76ac antibody in the presence or absence of JQ1. The bound Twist was examined by western blotting.
(G) HMLE cells expressing the vector or the WT or K73/76R Twist were examined for morphological changes indicative of EMT by phase microscopy and the expression of E-cadherin, vimentin, Wnt5a, and Twist (green) by immunofluorescence staining. Nuclei were stained with DAPI (red). Scale bars, 50 μM.
See also Figure S3.

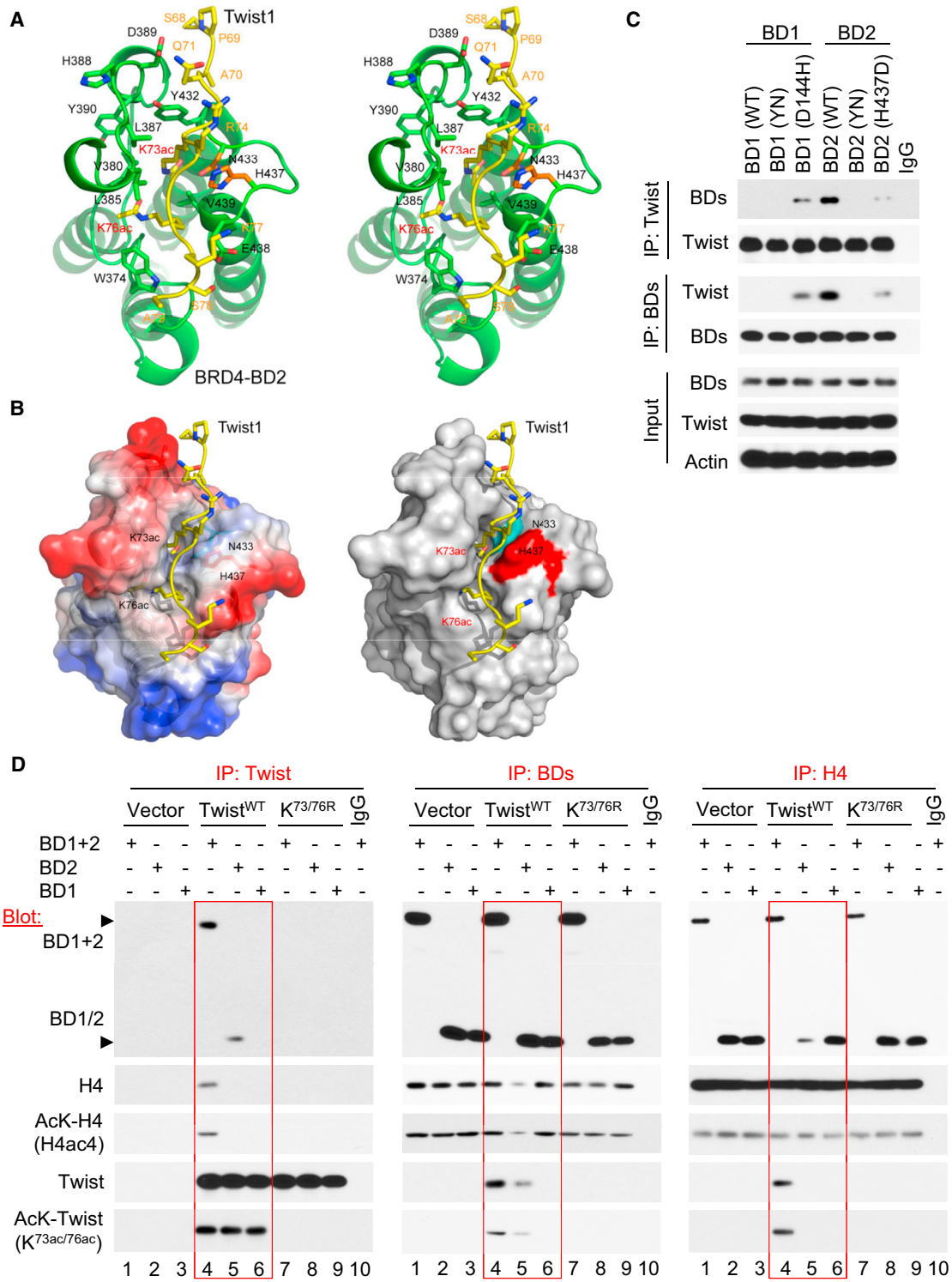

Figure 4. The Structural and Molecular Basis of Twist-K73ac/K76ac Recognition by BRD4

(A) Stereo ribbon diagram of the 3D solution structure of the BRD4-BD2 bound to a diacetylated K73ac/K76ac Twist peptide (yellow). Side chains of key residues engaged at the protein/peptide interactions are depicted and color coded by atom type.

(B) Surface electrostatic potential (left) or space-filled (right) representation of the BRD4-BD2/Twsit-K73ac/K76ac complex structure highlights His437 (red) at the acetyllysine binding site that is responsible for the BRD4-BD2′ specificity of this molecular recognition.

(legend continued on next page)

Chromatin immunoprecipitation (ChIP) analysis revealed that Twist, BRD4, and acetylated H4 associated at the *WNT5A* promoter in BT549 and SUM1315 cells, together with P-TEFb and RNA-Pol II (Figure 6B). A recent study indicated that BRD4 preferentially occupied a small subset of superenhancers in transcriptional active key oncogenes that are critical for proliferation and survival of tumor cells (Lovén et al., 2013). Intriguingly, *WNT5A* is one of these key oncogenes that contain BRD4-associated superenhancer, which covers exon1, promoter, and a region up to 30 kb upstream of the TSS in the *WNT5A* genomic sequence in chromosome 3. To examine whether Twist and BRD4 also bind the *WNT5A* superenhancer in BLBC, we designed two sets of ChIP primers that are 22 and 28 kb upstream of the TSS. ChIP experiments indicated that Twist and BRD4 indeed occupied the *WNT5A* enhancer together with H3K27ac, a mark of active enhancer (Figure 6C). Knockdown of Twist or JQ1 treatment inhibited the association of BRD4 at the *WNT5A* enhancer (data not shown). Knockdown of Twist or JQ1 treatment also reduced the presence of BRD4, P-TEFb, and RNA-Pol II at the *WNT5A* promoter (Figure 6D). However, JQ1 treatment did not affect the association of Twist at the *WNT5A* promoter, suggesting that Twist is required for the recruitment of the BRD4/P-TEFb/RNA-Pol II complex to the *WNT5A* promoter. Consistent with these observations, $Twist^{KR}$, which could not interact with BRD4 and failed to rescue Wnt5a expression (Figure 5C), was unable to recruit the BRD4/P-TEFb/RNA-Pol II complex to the *WNT5A* promoter (data not shown). In addition, ectopic expression of BRD4 increased Twist interaction with P-TEFb and RNA-Pol II, whereas knockdown of BRD4 reduced the association of Twist with P-TEFb and RNA-Pol II (Figure 6E). Our results indicate that Twist recruits BRD4 and acts together with P-TEFb and RNA-Pol II at the *WNT5A* promoter/enhancer to activate transcription.

The direct transcriptional activation of *WNT5A* by the Twist-BRD4 complex prompted us to investigate the stimuli responsible for Twist acetylation and *WNT5A* expression. We found that several stimuli, including TNFα and EGF plus insulin, could induce Twist acetylation at K73/K76 (Figure S6C). TNFα and EGF/insulin treatments greatly enhanced the interaction of Twist with BRD4 and with Tip60, increased K73ac/K76ac of Twist, and promoted Wnt5a expression (Figure 6F, left panel); JQ1 blocked the interaction of Twist with BRD4 and thus suppressed Wnt5a expression (Figure 6F, right panel). Consistent with these findings, TNFα or EGF/insulin treatment greatly enhanced the association of Twist, BRD4, P-TEFb, and RNA-Pol II at the *WNT5A* promoter (Figure S6D). Knockdown of Twist suppressed the association of BRD4 and Twist at the *WNT5A* promoter; however, JQ1 treatment did not inhibit the binding of Twist at the *WNT5A* promoter (Figure S6E). These data suggest that the association of BRD4 at the *WNT5A* promoter is mediated by Twist.

Although JQ1 was reported to reduce c-Myc expression, we noticed that JQ1 (1 μM) caused a decrease of c-Myc expression only in one of five examined BLBC cell lines (Figure 6G). However, JQ1 reduced Wnt5a expression in all cell lines. The low sensitivity to JQ1 in Hs578T cells is likely due to the remarkably high expression levels of Twist and Wnt5a in this particular cell line (Figure 5B). Increased JQ1 concentration resulted in Wnt5a downregulation in a dose-dependent manner in this cell line (Figure S6F). The downregulation of Wnt5a by JQ1 correlated with its inhibition of invasion and tumorsphere formation of these cells; addition of recombinant Wnt5a could partially restore this inhibitory effect (Figures 6H, S6F, and S6G). Together, these data indicate that the Twist-BRD4 interaction, enhanced by extracellular signals, is required for the recruitment of P-TEFb/RNA-Pol II complex to the *WNT5A* superenhancer for transcription of *WNT5A*, which executes, at least in part, the oncogenic function of Twist. JQ1 disrupts this interaction and thereby suppresses *WNT5A* expression in BLBC.

The Twist-BRD4-Wnt5a Axis Is Critical for Tumorigenicity in Breast Cancer

To further examine the oncogenic role of the Twist-BRD4-Wnt5a axis and explore the therapeutic potential of BET-specific inhibitors for targeting this axis in BLBC in vivo, we established two Wnt5a knockdown clones in SUM1315 cells. Knockdown of Wnt5a inhibited the noncanonical Wnt pathway, exemplified by the downregulation of JNK phosphorylation (Figure 7A). Wnt5a knockdown also suppressed the canonical Wnt/β-catenin pathway, indicated by the downregulation of β-catenin and the suppression of Akt/GSK-3β phosphorylation. These effects were further confirmed by β-catenin reporter assay (Figure S7A). Although Wnt5a knockdown did not alter the expression of epithelial or mensenchymal markers, it did reduce the expression of several pluripotent molecules (CD44, Sox2, and Oct4). Consistently, Wnt5a knockdown suppressed invasion and tumorsphere formation in these cells (Figure 7B).

In vivo studies were performed by injection of SUM1315 vector control cells or Wnt5a knockdown clones into the mammary fat pads of NOD-SCID mice. When control tumors were approximately 100 mm^3, mice were divided into three groups to receive daily treatments of JQ1 (50 mg/kg), MS417 (20 mg/kg), or solvent control for 2 weeks. We found that knockdown of Wnt5a completely inhibited tumor growth in SUM1315 cells and that both JQ1 and MS417 treatments significantly inhibited tumor growth (Figure 7C). The growth inhibitory effect of JQ1 and MS417 correlated with suppression of Wnt5a expression and downregulation of proliferative marker Ki67 in these tumors (Figure S7B). These results suggest that Wnt5a is critical for the tumorigenicity of BLBC. BET-specific inhibitors suppress the tumorigenicity of BLBC by inhibiting the Twist-BRD4 interaction and *WNT5A* expression.

DISCUSSION

Our study provides several mechanistic insights into how Twist and BRD4 function cooperatively to activate gene transcription in EMT and BLBC. First, we show that Twist uses a unique

(C) HA-tagged Twist was coexpressed with Flag-tagged WT or mutant BD1 and BD2 in HEK293 cells. Twist and BDs were immunoprecipitated with HA and Flag antibodies, respectively, and the bound BDs and Twist were analyzed by western blotting.
(D) HA-tagged Twist was coexpressed with Flag-tagged BD1, BD2, and BD1+BD2 in HEK293 cells. After immunoprecipitation of Twist, BDs, and H4, the association and acetylation of these molecules were examined by western blotting.
See also Figure S4 and Table S1.

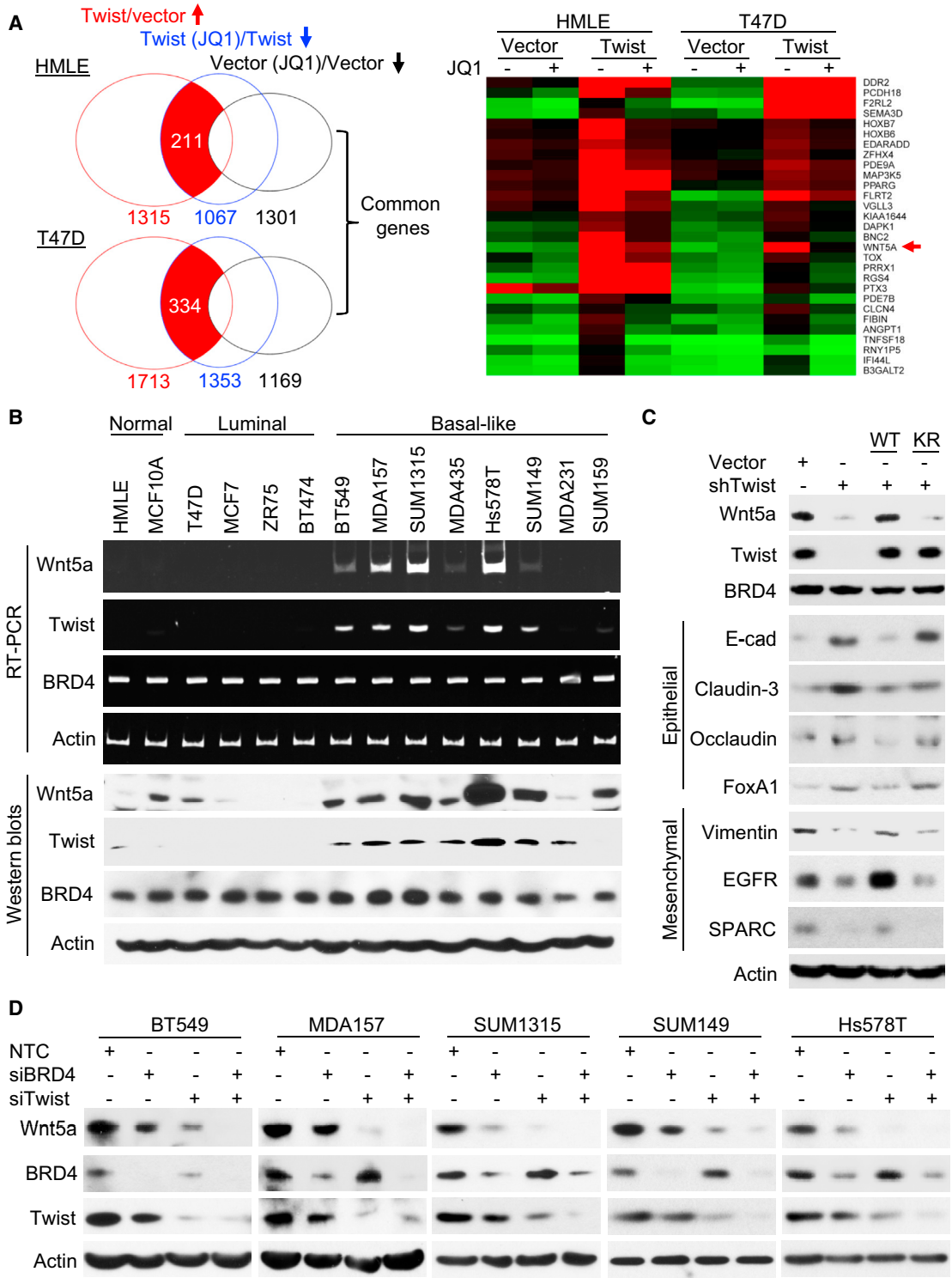

Figure 5. Twist Positively Correlates with Wnt5a Expression in Breast Cancer

(A) Gene expression profiling analysis (left) was used to identify potential Twist target genes. Common Twist target genes between HMLE and T47D cells are shown in the heatmap (right).

(B) The mRNA and protein levels of Twist, Wnt5a, and BRD4 were analyzed by RT-PCR and western blotting.

(C) The effects of stable small hairpin RNA knockdown of endogenous Twist in SUM1315 cells that were transiently transfected with WT or mutant (KR) Twist on the expression of Wnt5a and various molecules was evaluated by western blotting.

(D) Wnt5a expression in five BLBC cell lines with knockdown of Twist and/or BRD4 was analyzed by western blotting. NTC, nontarget control small interfering RNA. See also Figure S5.

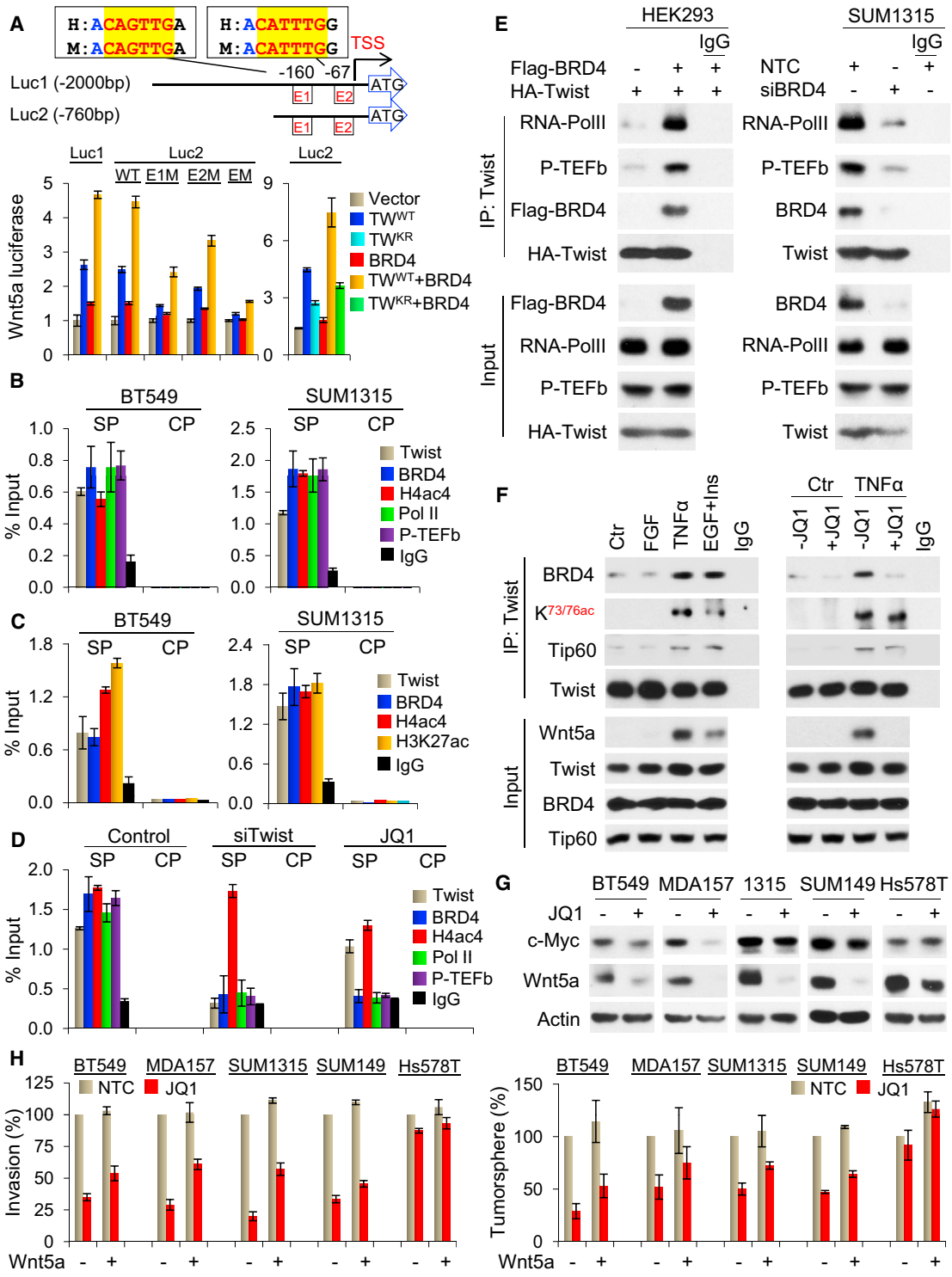

Figure 6. The Twist-BRD4 Complex Directly Activates *WNT5A* Transcription

(A) Schematic depiction of the *WNT5A* promoter and *WNT5A* reporter luciferase constructs used (top). Enhancement of Wnt5a luciferase activity by coexpression of Twist and BRD4 in HEK293 cells is shown (bottom).

(B) Twist, BRD4, H4ac4, RNA-Pol II, and P-TEFb (CDK9) association at the *WNT5A* promoter as assessed by ChIP. SP, specific primer; CP, control primer (5 kb downstream of the 3′ untranslated region).

(C) Twist, BRD4, H4ac, and H3K27ac association at the *WNT5A* enhancer as assessed by ChIP. SP, specific primer (22 kb upstream of the TSS); CP, control primer (5 kb downstream of the 3′ untranslated region).

(legend continued on next page)

mechanism for recruiting BRD4 in gene transcription (Figure 7D). Although BRD4 is the key transcriptional regulator, it lacks specific DNA binding motif. How BRD4 and its associated transcriptional complex are recruited to gene-specific promoters/enhancers remains elusive. We found that Twist contains an "H4-mimic" GK-X-GK motif and becomes diacetylated by Tip60, which also acetylates multiple lysine residues in histone H4 including K5 and K8. By binding to BRD4-BD2 via the K73ac/K76ac motif, Twist recruits BRD4 to target gene promoters/enhancers through the recognition of and interaction with E boxes by its bHLH domain. Once localized in the chromatin, BRD4-BD1 binds with acetylated H4-K5ac/K8ac to facilitate the docking of the BRD4 complex on promoters/enhancers and thereby activates pause release factor P-TEFb to phosphorylate and release RNA-Pol II for *WNT5A* transcription.

Our study demonstrates that the two BDs of BRD4 have distinct functions and binding specificities for acetylated proteins in transcription. Although a single BD1 or BD2 of BRD4 is individually capable of interacting with acetylated H4 in vitro, only BD1 is engaged in the binding with acetylated H4 in the tandem BD1+BD2. This is consistent with the observation that a single BD1 of Brdt binds to acetylated histone H4 nearly as well as Brdt (full length; contains BD1+BD2) (Morinière et al., 2009) and that BRD4-BD1 specifically recognizes acetylation marks on H4, whereas BRD4-BD2 has broad binding specificity for diacetylated substrates (Filippakopoulos et al., 2012). In line with this contention, only BRD4-BD2 interacts with Twist-K73ac/K76ac. We found that charged amino acid residues (D144 in BD1, H437 in BD2) surrounding the acetyllysine-binding pocket of BDs contributed to the binding specificity of BD1 and BD2. Additional residues beyond the diacetylation motif further contribute to Twist's association with BRD4-BD2. Notably, it has recently been reported that BRD4 is phosphorylated by CK2 on several Ser residues in the C-terminal region of BD2 and that these phosphorylations were suggested to affect the interaction of BRD4 with acetylated histones and transcriptional cofactors (Wu et al., 2013). Although a single BD2 of BRD4 can interact with either acetylated H4 or Twist-K73ac/K76ac individually, the tandem BD1+BD2 of BRD4 apparently form a ternary complex with two acetylated proteins in that diacetylated H4 is bound to BD1 and diacetylated Twist is bound to BD2. These results suggest that BRD4 utilizes its tandem BDs as an integration platform to cooperatively interact with H4 and Twist in assembling the integrated transcriptional complex containing P-TEFb and RNA-Pol II at target gene promoters/enhancers. Notably, several transcription-associated proteins that contain tandem binding modules have been shown to engage in combinatorial recognition of different posttranslational modifications (PTMs) in histones for the assembly of transcriptional complexes (Zeng et al., 2010). For example, the tandem PHD-BD module in BPTF specifically recognizes a combination of H3K4me3 and H4K16ac in gene activation (Ruthenburg et al., 2011). Our results not only support this notion, but also extend the functionality of these tandem binding modules in directing gene transcriptional activation as exemplified by the tandem BDs of BRD4 in bridging histone and nonhistone transcription factor.

Notably, these histone-mimic sequences contain lysine/arginine-rich resides, which are often viewed conventionally as a nuclear-localization signal (NLS), as in the case of Twist. However, Twist^{KR} mutant, which cannot be acetylated but still resides in the nucleus, fails to interact with BRD4 and is unable to induce EMT and *WNT5A* expression. Our results suggest that theses lysine/arginine-rich "potential" NLS motifs in transcription factors may have previously unrecognized histone-mimic functions. Consistent with our findings, histone-mimic sequences are deployed by influenza nonstructural protein 1 (NS1) in inhibiting human transcription elongation complex in the antivirus response and by HP1 in forming HP1-chromatin complex (Canzio et al., 2013; Marazzi et al., 2012). We believe that PTMs on histone-mimic sequences present in nonhistone proteins likely play an important role, via conserved molecular mechanisms as seen with those PTMs in histone, in governing the assembly and function of transcriptional complexes in chromatin.

Second, our study demonstrates that Twist is a transcriptional activator responsible for *WNT5A* expression in BLBC. Twist has been shown to bind to the E-cadherin promoter to repress transcription in a way similar to that of Snail. However, this contradicts the role of Twist in development, where it acts as a transcriptional activator to upregulate mesoderm-specific genes in *Drosophila*. When the bHLH domain of Twist was replaced with Gal4-DBD, we found that the Twist-Gal4-DBD fusion was sufficient to activate gene expression, indicating that Twist functions as a transcriptional activator. We further show that Twist recruits BRD4 and the associated P-TEFb and RNA-Pol II to the *WNT5A* promoter/enhancer to directly activate *WNT5A* expression, which is required for invasion and the maintenance of CSC-like properties of BLBC. Notably, Wnt5a is induced in epithelial cells during EMT and required for maintenance of CSC-like properties in the resulting mesenchymal cells (Scheel et al., 2011). In addition, Wnt5a expression is required for the loss of cell-cell contacts, allowing cells to migrate to the edge

(D) Effects of Twist knockdown or JQ1 treatment on the association of Twist, BRD4, RNA-Pol II, and P-TEFb (CDK9) and H4ac4 at the *WNT5A* promoter as assessed by ChIP in SUM1315 cells. SP and CP primers are same as in (B).
(A–D) Statistical analysis (mean ± SD) from three separate experiments in triplicates is shown.
(E) Assessment of the effects of transient expression of HA-Twist and/or Flag-BRD4 on their association with RNA-Pol II and P-TEFb (CDK9) in HEK293 cells (left) and assessment of the effect of endogenous BRD4 knockdown on the association of Twist, BRD4, RNA-Pol II, and P-TEFb (CDK9) in SUM1315 cells (right) are shown.
(F) SUM1315 cells were serum starved for overnight followed by stimulation with FGF, TNFα, or EGF plus insulin for 3 hr in the absence or presence of JQ1 (right). Twist was immunoprecipitated and K73ac/K76ac of Twist and the association of Tip60 and BRD4 were analyzed. Expression of Wnt5a, Twist, BRD4 and Tip60 were also examined by western blotting (left).
(G) BLBC cells were treated with JQ1. Expression of c-Myc and Wnt5a was analyzed by western blotting.
(H) Invasion (left) and tumorsphere formation (right) assays of cells treated as in (G) were examined in the absence or present of recombinant Wnt5a (100 ng/ml). Statistical analysis (mean ± SD) from three independent experiments with duplicates is shown.
See also Figure S6.

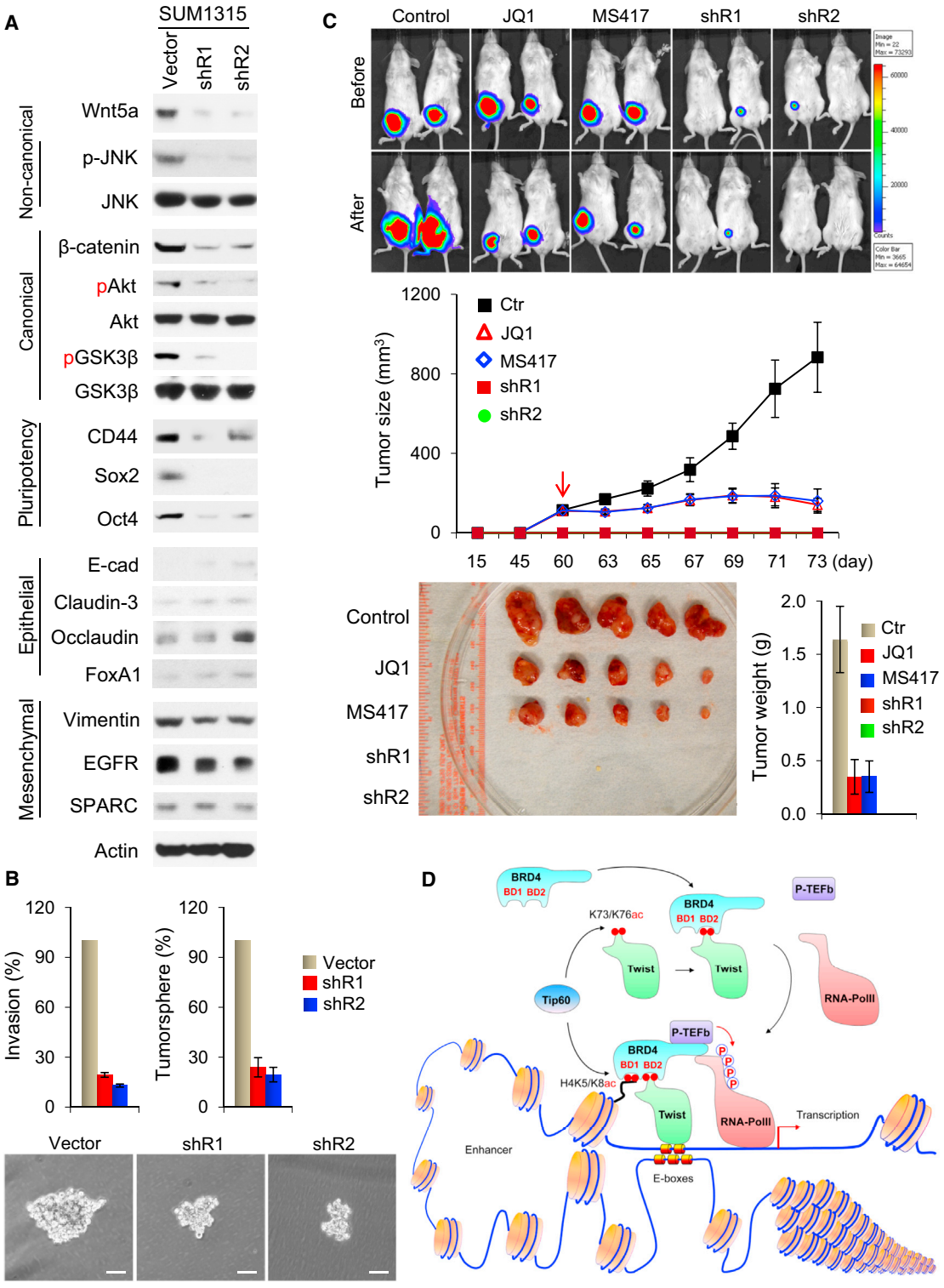

Figure 7. The Twist-BRD4-Wnt5a Axis Is Critical for Tumorigenicity In Vitro and In Vivo

(A) Expression of various molecules in SUM1315 cells with Wnt5a knockdown.

(B) Invasion and tumorsphere formation in SUM1315 cells with Wnt5a knockdown. Data are presented as a percentage of vector control values (mean ± SD in three separate experiments in duplicates). Representative pictures of tumorspheres are shown at the bottom. Scale bar, 100 μM.

(C) Vector control and Wnt5a knockdown SUM1315 cells were injected into the mammary fat pad of NOD-SCID mice. When tumors from mice injected with control cells reached 100 mm^3, mice were divided into three groups and treated with JQ1 (50 mg/Kg), MS417 (20 mg/Kg), or solvent control, respectively. The size

(legend continued on next page)

of wounds, and is also necessary for intestinal epithelial stem cells to regenerate damage tissues during wound healing and tissue repair (Miyoshi et al., 2012). The correlated expression of Twist and Wnt5a in BLBC supports our contention that the Twist-BRD4-Wnt5a signaling axis plays a critical role in the development and progression of BLBC.

Third, our study indicates that the Twist-BRD4 interaction represents a druggable target for treating BLBC. Although Twist is highly expressed in BLBC, the absence of a clear ligand-binding domain in Twist creates a formidable obstacle toward developing small molecules that inhibit its activity as a transcription factor. We found that BET-specific BD inhibitors disrupted the Twist-BRD4 interaction and resulted in significant Wnt5a reduction, leading to inhibition of invasion and tumorigenicity of BLBC cells in vitro and in vivo. Based on our mechanistic understanding of Twist-BRD4 interaction in gene transcription, we predict that selective chemical inhibition of BRD4/H4 interaction would result in a broad inhibition of BRD4 functions as chromatin regulator in gene transcription, whereas selective inhibition of the BRD4/transcription factor association might affect specific transcription factor's ability in their target gene activation. BD inhibitors selectively target BD2 over BD1 of BRD4 are needed to address these questions; they will also further functionally validate the effectiveness and therapeutic benefits of targeting BRD4 for treating BLBC.

EXPERIMENTAL PROCEDURES

Protein Purification and Mass Spectrometry Analysis

We generated a clone of HeLa S3 cells with stable expression of Flag-Twist (Li and Zhou, 2011). After enriching the nuclear extracts from 40 l of suspension culture, we carried out affinity protein purification with Flag affinity columns. The final eluted immunocomplexes were separated on SDS-PAGE, and the bound proteins were excised from the gel and subjected to nano-liquid chromatography-tandem mass spectrometry (nano-LC-MS/MS) analysis (Applied Biomics). For identification of the acetylated lysine residues on Twist, the acetylated Twist was digested with trypsin, and the tryptic peptides were analyzed by LC-MS/MS using an LTQ Velos Orbitrap mass spectrometer (Thermo Fisher Scientific) coupled with a nano-LC Ultra/CHiPLC Nanoflex high-performance liquid chromatography system (Eksigent) through a nanoelectrospray ionization source (Li et al., 2013). MS/MS data were acquired using CID fragmentation of selected peptides during the information-dependent acquisition. The LC-MS/MS results were subjected to protein identification and acetylation sites determination using ProteomeDiscoverer 1.3 software (Thermo Fisher Scientific) and MASCOT server.

Protein Structure Analysis by NMR

The NMR spectral collection, analysis, and structure determination of the BRD4-BD2 with Twist-K73ac/K76ac were performed as previously reported (Zhang et al., 2012). In brief, NMR samples contained a protein/peptide complex of 0.5 mM in a 100 mM sodium phosphate buffer (pH 6.5) that contains 5 mM perdeuterated dithiothreitol and 0.5 mM EDTA in $H_2O/^2H_2O$ (9/1) or ^2H_2O. All NMR spectra were collected at 30°C on NMR spectrometers of 800, 600, or 500 MHz. The ^1H, ^{13}C, and ^{15}N resonances of the protein in the complex were assigned by triple-resonance NMR spectra collected with a $^{13}C/^{15}N$-labeled and 75% deuterated BRD4-BD2 bound to an unlabeled Twist peptide (Clore and Gronenborn, 1994). The distance restraints were obtained from 3D ^{13}C-NOESY or ^{15}N-NOESY spectra. Protein structures were calculated with a distance geometry-simulated annealing protocol using X-PLOR (Brunger, 1993) that was aided with iterative automated NOE assignment by ARIA for refinement (Nilges and O'Donoghue, 1998). Structure quality was assessed by PROCHECK-NMR (Laskowski et al., 1996). The structure of the protein/ligand complex was determined using intermolecular NOE-derived distance restraints that were obtained from ^{13}C-edited (F_1), $^{13}C/^{15}N$-filtered (F_3) 3D NOESY spectra.

Immunoprecipitation, Immunoblotting, Immunofluorescence, Immunohistochemical Staining, RT-PCR, and ChIP

Detailed methods are provided in the Supplemental Experimental Procedures.

Tumorigenesis Assay

All procedures were approved by the Institutional Animal Care and Use Committee at the University of Kentucky College of Medicine and conform to the legal mandates and federal guidelines for the care and maintenance of laboratory animals. Animals were maintained and treated under pathogen-free conditions. Female NOD-SCID mice (6–8 weeks old; Taconic) were injected with breast cancer SUM1315 (2×10^6 cells/mouse) cells via mammary fat pad, and mice had three groups: vector control and two stable clones with Wnt5a-knockdown expression. Tumor growth was monitored with caliper measurements. When tumors were approximately 1.0 cm in size, mice were euthanized and tumors excised. Data were analyzed by Student's t test; $p < 0.05$ was considered significant.

Statistical Analysis

Data are presented as mean ± SD. A Student's t test (two-tailed) was used to compare two groups ($p < 0.05$ was considered significant) unless otherwise indicated.

ACCESSION NUMBERS

Microarray data of Twist expression in HMLE and T47D cells with or without JQ1 treatment were deposited at the Gene Expression Omnibus database with the accession number GSE53222. Structure factors and coordinates for the second bromodomain of BRD4 in complex with K73ac/K76ac diacetylated Twist peptide were deposited at the Protein Data Bank under ID code 2MJV, and the NMR spectral data were deposited at the BioMagResBank (BMRB) under BMRB accession number 19738.

SUPPLEMENTAL INFORMATION

Supplemental Information includes Supplemental Experimental Procedures, seven figures, and one table and can be found with this article online at http://dx.doi.org/10.1016/j.ccr.2014.01.028.

ACKNOWLEDGMENTS

We thank Cathy Anthony for critical reading and editing of this manuscript. We also thank Dr. Jing Chen for technical assistance on mass spectrometry analysis. We are grateful to Dr. James E. Bradner for providing JQ1, Dr. Robert A. Weinberg for HMLE cells, Dr. Michael Rosenblatt for SUM1315 cells, and Dr. Bruno Amati for Tip60 antibodies as valuable reagents for this study. This work was supported in part by grants from the National Institute of Health (CA125454 to B.P.Z., P20CA153043 to B.M.E., and HG004508 and CA87658 to M.-M.Z.), the American Cancer Society (RSG13187 to Y.W.), and the Nature Science Foundation of China (91129303 to J.D.). We acknowledge the University of Kentucky Proteomics Core, which is partially supported

of tumor was recorded by bioluminescence imaging before or after 2 week treatment. Tumor weight was also measured. Data are represented as a mean ± SEM from five mice.

(D) A proposed model illustrating the interaction of Twist and BRD4 at the enhancer/promoter of *WNT5A*, which leads to the transcriptional activation of *WNT5A* expression in EMT and BLBC.

See also Figure S7.

by grants from the National Cancer Institute (P30CA177558) and the National Institute of General Medical Sciences (P20GM103486).

Received: June 9, 2013
Revised: September 23, 2013
Accepted: January 24, 2014
Published: February 10, 2014

REFERENCES

Brunger, A.T. (1993). X-PLOR version 3.1: A system for X-ray Crystallography and NMR (version 3.1 edit.). (New Haven: Yale University Press).

Canzio, D., Liao, M., Naber, N., Pate, E., Larson, A., Wu, S., Marina, D.B., Garcia, J.F., Madhani, H.D., Cooke, R., et al. (2013). A conformational switch in HP1 releases auto-inhibition to drive heterochromatin assembly. Nature *496*, 377–381.

Clore, G.M., and Gronenborn, A.M. (1994). Multidimensional heteronuclear nuclear magnetic resonance of proteins. Methods Enzymol. *239*, 349–363.

Dawson, M.A., Prinjha, R.K., Dittmann, A., Giotopoulos, G., Bantscheff, M., Chan, W.I., Robson, S.C., Chung, C.W., Hopf, C., Savitski, M.M., et al. (2011). Inhibition of BET recruitment to chromatin as an effective treatment for MLL-fusion leukaemia. Nature *478*, 529–533.

Delmore, J.E., Issa, G.C., Lemieux, M.E., Rahl, P.B., Shi, J., Jacobs, H.M., Kastritis, E., Gilpatrick, T., Paranal, R.M., Qi, J., et al. (2011). BET bromodomain inhibition as a therapeutic strategy to target c-Myc. Cell *146*, 904–917.

Doyon, Y., and Côté, J. (2004). The highly conserved and multifunctional NuA4 HAT complex. Curr. Opin. Genet. Dev. *14*, 147–154.

Filippakopoulos, P., Picaud, S., Mangos, M., Keates, T., Lambert, J.P., Barsyte-Lovejoy, D., Felletar, I., Volkmer, R., Müller, S., Pawson, T., et al. (2012). Histone recognition and large-scale structural analysis of the human bromodomain family. Cell *149*, 214–231.

Jang, M.K., Mochizuki, K., Zhou, M., Jeong, H.S., Brady, J.N., and Ozato, K. (2005). The bromodomain protein Brd4 is a positive regulatory component of P-TEFb and stimulates RNA polymerase II-dependent transcription. Mol. Cell *19*, 523–534.

Laskowski, R.A., Rullmannn, J.A., MacArthur, M.W., Kaptein, R., and Thornton, J.M. (1996). AQUA and PROCHECK-NMR: programs for checking the quality of protein structures solved by NMR. J. Biomol. NMR *8*, 477–486.

Leptin, M. (1991). twist and snail as positive and negative regulators during Drosophila mesoderm development. Genes Dev. *5*, 1568–1576.

Li, J., and Zhou, B.P. (2011). Activation of β-catenin and Akt pathways by Twist are critical for the maintenance of EMT associated cancer stem cell-like characters. BMC Cancer *11*, 49.

Li, X., Zhou, Q., Sunkara, M., Kutys, M.L., Wu, Z., Rychahou, P., Morris, A.J., Zhu, H., Evers, B.M., and Huang, C. (2013). Ubiquitylation of phosphatidylinositol 4-phosphate 5-kinase type I γ by HECTD1 regulates focal adhesion dynamics and cell migration. J. Cell Sci. *126*, 2617–2628.

Lovén, J., Hoke, H.A., Lin, C.Y., Lau, A., Orlando, D.A., Vakoc, C.R., Bradner, J.E., Lee, T.I., and Young, R.A. (2013). Selective inhibition of tumor oncogenes by disruption of super-enhancers. Cell *153*, 320–334.

Marazzi, I., Ho, J.S., Kim, J., Manicassamy, B., Dewell, S., Albrecht, R.A., Seibert, C.W., Schaefer, U., Jeffrey, K.L., Prinjha, R.K., et al. (2012). Suppression of the antiviral response by an influenza histone mimic. Nature *483*, 428–433.

Miyoshi, H., Ajima, R., Luo, C.T., Yamaguchi, T.P., and Stappenbeck, T.S. (2012). Wnt5a potentiates TGF-β signaling to promote colonic crypt regeneration after tissue injury. Science *338*, 108–113.

Morinière, J., Rousseaux, S., Steuerwald, U., Soler-López, M., Curtet, S., Vitte, A.L., Govin, J., Gaucher, J., Sadoul, K., Hart, D.J., et al. (2009). Cooperative binding of two acetylation marks on a histone tail by a single bromodomain. Nature *461*, 664–668.

Nilges, M., and O'Donoghue, S. (1998). Ambiguous NOEs and automated NOE assignment. Prog. Nucl. Magn. Reson. Spectrosc. *32*, 107–139.

Rakha, E.A., Reis-Filho, J.S., and Ellis, I.O. (2008). Basal-like breast cancer: a critical review. J. Clin. Oncol. *26*, 2568–2581.

Rekowski, Mv., and Giannis, A. (2010). Histone acetylation modulation by small molecules: a chemical approach. Biochim. Biophys. Acta *1799*, 760–767.

Ruthenburg, A.J., Li, H., Milne, T.A., Dewell, S., McGinty, R.K., Yuen, M., Ueberheide, B., Dou, Y., Muir, T.W., Patel, D.J., and Allis, C.D. (2011). Recognition of a mononucleosomal histone modification pattern by BPTF via multivalent interactions. Cell *145*, 692–706.

Scheel, C., Eaton, E.N., Li, S.H., Chaffer, C.L., Reinhardt, F., Kah, K.J., Bell, G., Guo, W., Rubin, J., Richardson, A.L., and Weinberg, R.A. (2011). Paracrine and autocrine signals induce and maintain mesenchymal and stem cell states in the breast. Cell *145*, 926–940.

Thiery, J.P., Acloque, H., Huang, R.Y., and Nieto, M.A. (2009). Epithelial-mesenchymal transitions in development and disease. Cell *139*, 871–890.

Witze, E.S., Litman, E.S., Argast, G.M., Moon, R.T., and Ahn, N.G. (2008). Wnt5a control of cell polarity and directional movement by polarized redistribution of adhesion receptors. Science *320*, 365–369.

Wu, S.Y., Lee, A.Y., Lai, H.T., Zhang, H., and Chiang, C.M. (2013). Phospho switch triggers Brd4 chromatin binding and activator recruitment for gene-specific targeting. Mol. Cell *49*, 843–857.

Zeitlinger, J., Zinzen, R.P., Stark, A., Kellis, M., Zhang, H., Young, R.A., and Levine, M. (2007). Whole-genome ChIP-chip analysis of Dorsal, Twist, and Snail suggests integration of diverse patterning processes in the Drosophila embryo. Genes Dev. *21*, 385–390.

Zeng, L., Zhang, Q., Li, S., Plotnikov, A.N., Walsh, M.J., and Zhou, M.M. (2010). Mechanism and regulation of acetylated histone binding by the tandem PHD finger of DPF3b. Nature *466*, 258–262.

Zhang, G., Liu, R., Zhong, Y., Plotnikov, A.N., Zhang, W., Zeng, L., Rusinova, E., Gerona-Nevarro, G., Moshkina, N., Joshua, J., et al. (2012). Down-regulation of NF-κB transcriptional activity in HIV-associated kidney disease by BRD4 inhibition. J. Biol. Chem. *287*, 28840–28851.

Zhou, Q., Li, T., and Price, D.H. (2012). RNA polymerase II elongation control. Annu. Rev. Biochem. *81*, 119–143.

Zuber, J., Shi, J., Wang, E., Rappaport, A.R., Herrmann, H., Sison, E.A., Magoon, D., Qi, J., Blatt, K., Wunderlich, M., et al. (2011). RNAi screen identifies Brd4 as a therapeutic target in acute myeloid leukaemia. Nature *478*, 524–528.

Cancer Cell
Article

SYK Is a Critical Regulator of FLT3 in Acute Myeloid Leukemia

Alexandre Puissant,[1] Nina Fenouille,[2] Gabriela Alexe,[1,3,4] Yana Pikman,[1] Christopher F. Bassil,[1] Swapnil Mehta,[1] Jinyan Du,[3] Julhash U. Kazi,[5] Frédéric Luciano,[6] Lars Rönnstrand,[5] Andrew L. Kung,[7] Jon C. Aster,[8] Ilene Galinsky,[9] Richard M. Stone,[9] Daniel J. DeAngelo,[9] Michael T. Hemann,[2] and Kimberly Stegmaier[1,3,*]

[1]Department of Pediatric Oncology, Dana-Farber Cancer Institute and Boston Children's Hospital, Harvard Medical School, Boston, MA 02215, USA
[2]Koch Institute for Integrative Cancer Research at Massachusetts Institute of Technology, Massachusetts Institute of Technology, Cambridge, MA 02139, USA
[3]The Broad Institute of Harvard University and Massachusetts Institute of Technology, Cambridge, MA 02139, USA
[4]Bioinformatics Graduate Program, Boston University, Boston, MA 02215, USA
[5]Experimental Clinical Chemistry, Department of Laboratory Medicine, Lund University, Medicon Village, 221 00 Lund, Sweden
[6]C3M/ INSERM U1065 Team Cell Death, Differentiation, Inflammation and Cancer, 06204 Nice, France
[7]Pediatric Department, Columbia University Medical Center, New York, NY 10032, USA
[8]Department of Pathology, Brigham and Women's Hospital, Harvard Medical School, Boston, MA 02215, USA
[9]Department of Medical Oncology, Dana-Farber Cancer Institute, Harvard Medical School, Boston, MA 02215, USA
*Correspondence: kimberly_stegmaier@dfci.harvard.edu
http://dx.doi.org/10.1016/j.ccr.2014.01.022

SUMMARY

Cooperative dependencies between mutant oncoproteins and wild-type proteins are critical in cancer pathogenesis and therapy resistance. Although spleen tyrosine kinase (SYK) has been implicated in hematologic malignancies, it is rarely mutated. We used kinase activity profiling to identify collaborators of SYK in acute myeloid leukemia (AML) and determined that FMS-like tyrosine kinase 3 (FLT3) is transactivated by SYK via direct binding. Highly activated SYK is predominantly found in *FLT3-ITD* positive AML and cooperates with FLT3-ITD to activate *MYC* transcriptional programs. FLT3-ITD AML cells are more vulnerable to SYK suppression than FLT3 wild-type counterparts. In a FLT3-ITD in vivo model, SYK is indispensable for myeloproliferative disease (MPD) development, and SYK overexpression promotes overt transformation to AML and resistance to FLT3-ITD-targeted therapy.

INTRODUCTION

Sequencing of acute myeloid leukemia (AML) genomes has revealed a heterogeneous disease characterized by mutations altering proliferation, differentiation programs, and the epigenetic landscape, resulting in an accumulation of immature hematopoietic cells (Ley et al., 2013). Though these mutations can result in exquisite dependency on mutant proteins, they can also lead to aberrant dependency on nonmutant proteins. For example, the histone 3 lysine 79 (H3K79) methyltransferase DOT1L has been implicated in the development of leukemias bearing translocations of the *Mixed Lineage Leukemia* (*MLL*) gene, although *DOT1L* itself is not mutated. DOT1L small-molecule inhibitors have been demonstrated in preclinical studies to selectively kill *MLL*-rearranged leukemia (Bernt et al., 2011; Daigle et al., 2011). Similarly, a small hairpin RNA (shRNA) screen targeting known chromatin regulators identified the transcriptional regulator BET bromodomain BRD4 as an epigenetic dependency in an MLL-AF9/Nras^{G12D} AML mouse model (Zuber et al., 2011). By recruiting the MLL-fusions into a transcription elongation complex, BET bromodomain proteins appear to be critical mediators for leukemogenesis involving MLL-fusion proteins (Deshpande et al., 2012).

We previously used chemical genomic, proteomic, and shRNA screening to identify SYK as a target in AML (Hahn et al., 2009). *SYK*-targeting shRNA induced AML cell differentiation in vitro,

Significance

Although imatinib therapy has been paradigm shifting for treating patients with *BCR-ABL*-rearranged chronic myelogenous leukemia (CML), the application of targeted kinase inhibitors to treating AML has been a more complex undertaking. In this study, we identified an oncogenic partnership between the most commonly mutated kinase in AML, FLT3, and the cytoplasmic kinase SYK. SYK transactivates FLT3 by a direct physical interaction, is critical for the development of FLT3-ITD-induced myeloid neoplasia, and is more highly activated in primary human FLT3-ITD-positive AML. These studies also raise the possibility of SYK activation as a mechanism of resistance to FLT3 inhibitors, suggest *FLT3* mutant AML as a subtype for SYK inhibitor testing, and nominate the clinical testing of SYK and FLT3 inhibitor combinations.

and SYK inhibition was shown to have anti-leukemia activity in AML mouse models. SYK is a cytoplasmic tyrosine kinase critical in normal B cell development and hematopoietic signaling (Mócsai et al., 2010) that was recently found to be aberrantly activated through translocations in T cell lymphoma (*ITK-SYK*) (Pechloff et al., 2010) and myelodysplastic syndrome (MDS) (*TEL-SYK*) (Kuno et al., 2001). Thus far, however, next-generation sequencing efforts have failed to identify frequent mutational events in *SYK* in AML or in B cell malignancies, where SYK dependency has also been demonstrated. In B cell malignancies, signaling from the B cell receptor (BCR) through SYK has been implicated in the pathogenesis of disease, and small molecules inhibiting SYK have had promising early clinical activity (Friedberg et al., 2010). In AML, however, little is known about the cooperative interactions of SYK in its contribution to the disease.

RESULTS

FLT3 Is a Target of SYK in AML

To identify SYK interactors in AML, we used a bead-based screening technology to profile the phosphorylation state of 80 receptor and nonreceptor tyrosine kinases, 18 tyrosine kinase signaling adaptors/regulators, and 7 tyrosine kinase signaling-linked serine/threonine kinases in the presence of activated SYK. We generated four AML cell lines stably expressing a *SYK-TEL* construct encoding a fusion protein with a constitutively active SYK kinase due to the TEL moiety that promotes homodimerization and intrinsic activation. Kinome activity in the presence of activated SYK is depicted in Figure 1A. SYK and two of its reported targets, PIK3R1 (Moon et al., 2005) and SHC1 (Umehara et al., 1998), as well as ZAP70, a member of the SYK kinase family possibly transphosphorylated by constitutively active SYK, were identified among the most hyperactivated proteins. Surprisingly, FLT3 receptor and two other platelet-derived growth factor receptor (PDGFR) family receptors, KIT and PDGFRα, also scored as top hits. Kinome activity profiling in 12 AML cell lines was next used to establish the tyrosine kinases or tyrosine kinase-regulated proteins whose activation was most highly correlated ($\rho \geq 0.5$) with basal SYK activation (Figure 1B). As in the prior screen, ZAP70, PIK3R1, and SHC1 appeared in the top correlated hits, as did FLT3 and KIT.

Our group previously demonstrated induction of myeloid differentiation in AML cells upon SYK inhibition (Hahn et al., 2009). To discover which of the PDGFR family receptors scoring in our kinase activity profiling mediates differentiation, as seen with SYK knockdown, we developed a flow-based assay to measure $CD11b^+/CD14^+$ differentiation. We transduced a panel of AML cell lines with shRNAs targeting either *SYK* or each of the identified PDGFR family kinases. Only FLT3 knockdown recapitulated the phenotypic consequence of SYK knockdown despite high knockdown efficiency in each of the kinases evaluated (Figure 1C and Figure S1 available online).

SYK Enhances FLT3 WT and Mutant Activation by Phosphorylation of Residues Y768 and Y955

Based on the kinome activity profiling results, we evaluated the phosphorylation status of the intracellular domain of the activated FLT3 receptor (GST-FLT3, 571–end) in the presence of active GST-SYK and ATP [γ-^{32}P] (Figure 2A). We found FLT3 to be directly phosphorylated by SYK, as observed by increased incorporation of γ-^{32}P.

Next, we used a phospho-mapping approach by mass spectrometry to nominate sites on the FLT3 receptor directly phosphorylated by SYK. Y726, Y768, Y842, Y899, and Y955, located in the TK1-TK2 interdomain or in the tyrosine kinase TK2 region of FLT3, were identified (Figure 2B, top). In contrast, the phosphorylation level of residue Y969, located at the extreme C-terminal region of FLT3, was not increased in the presence of SYK. In cells, a similar phospho-mapping analysis identified the same tyrosine sites to be regulated by SYK, with Y899 as the only exception (Figure 2B, bottom). These results were confirmed by an in vitro kinase assay using phosphospecific antibodies; GST-SYK increased FLT3 phosphorylation at Y768, Y842, and Y955 sites but not at site Y969 (Figure 2C). GST-SYK also promoted hyperphosphorylation of the FLT3 Y591 site, a predictor of FLT3 activity (Griffith et al., 2004).

Although this phospho-mapping approach nominated candidate FLT3 sites phosphorylated by SYK, it was not adequate to confirm direct SYK-targeted tyrosine residues because of the fact that certain FLT3 tyrosine sites, such as Y591, are also subject to autotransphosphorylation. To prevent transactivation cascades, we created a cell-based system with a kinase dead (KD; K644R) FLT3 receptor incapable of autotransphosphorylation. However, this FLT3 KD did require "prephosphorylation" to recapitulate the basal-activated state of the wild-type form of FLT3. As shown in Figures S2A and S2B, a construct encoding for V5-tagged kinase dead FLT3 [FLT3 KD (V5)] was first cotransfected with a DDK-tagged FLT3 WT (FLT3-DDK) construct to ensure the prephosphorylation of FLT3 KD (V5). The FLT3 KD (V5) was then V5-tag immunoprecipitated to separate it from the FLT3-DDK protein and incubated with GST-SYK in an in vitro kinase assay. Because FLT3 KD (V5) was now activated (phosphorylated) but unable to autotransphosphorylate, we could discriminate between sites directly phosphorylated by SYK and those autotransphosphorylated as an indirect effect of SYK-mediated FLT3 activation.

This approach was validated by V5-tag immunoprecipitation of FLT3 WT (V5) (Figure 2D). As expected, FLT3 WT was highly phosphorylated in the presence of GST-SYK. In contrast, the FLT3-KD (V5) mutant was poorly phosphorylated without prephosphorylation by FLT3-DDK. After incubation with FLT3-DDK, however, FLT3-KD (V5) was responsive to SYK phosphorylation, but because FLT3-KD (V5) was unable to autotransphosphorylate, its phosphorylation level remained lower than that of FLT3 WT (V5). This requirement for prephosphorylation of FLT3 before SYK can activate FLT3 WT (V5) further was also observed with FLT3-ITD (V5) (Figure S2C). In accordance with these results, the mutant FLT3-KD YY589/591AA, nontransphosphorylable by FLT3-DDK, was also resistant to SYK-dependent phosphorylation. We next mutated all FLT3 tyrosine residues identified by mass spectrometry into nonphosphorylatable alanines (FLT3-KD Y726A, Y768A, Y842A, Y899A, Y955A, and Y969A) to identify sites directly phosphorylated by SYK. Only two mutants, FLT3-KD (V5) Y768A and Y955A, were resistant to SYK-mediated FLT3 phosphorylation, suggesting that SYK directly phosphorylates FLT3 at sites Y768 and Y955

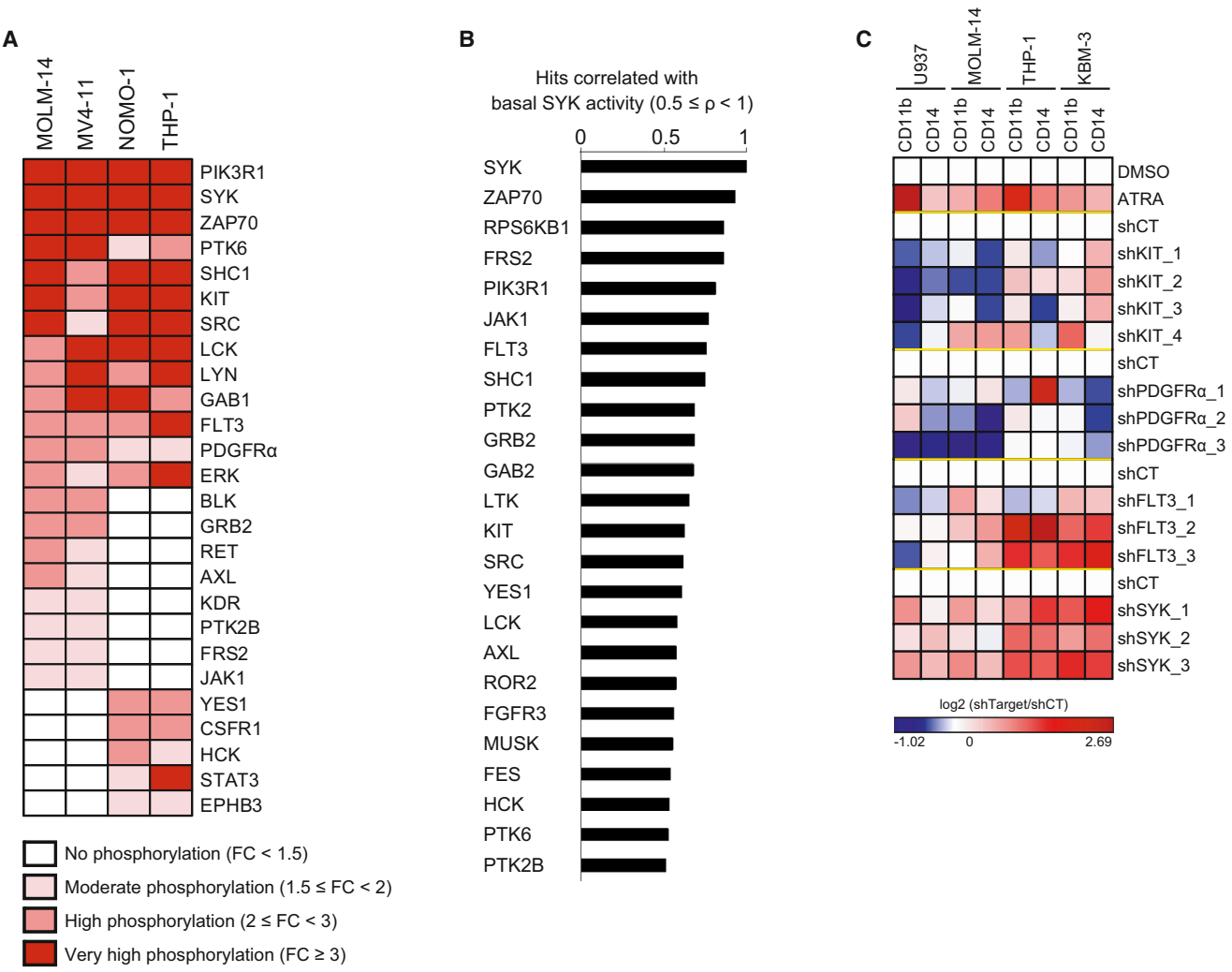

Figure 1. FLT3 Activation Correlates with SYK Activation in AML

(A) Lysates from AML cell lines stably transduced with either a constitutively activated form of SYK (SYK-TEL) or an empty vector (CT) were evaluated by kinase activity profiling. The log_2-transformed ratio (SYK-TEL versus CT) of tyrosine phosphorylation is depicted as a heatmap where each protein is ranked by its phosphorylation level across the cell lines. FC, fold change.

(B) Spearman correlation between basal phosphorylation of SYK compared to all other detected candidates in the kinase activity profiling assay across 12 AML cell lines. The most highly correlated hits ($\rho \geq 0.5$) are represented on the histogram.

(C) Heatmap showing level of CD14 and CD11b-positive myeloid differentiation in AML cell lines treated with ATRA or transduced with a control shRNA (shCT) or *KIT*-, *PDGFRα*-, *FLT3*-, or *SYK*-targeting shRNAs. Normalized data are presented as a log_2-ratio (shTarget versus shCT).

See also Figure S1.

(Figure 2D). These two mutations completely abrogated SYK-mediated FLT3 activation, with a consequent downregulation of FLT3 activation at site Y591 (Figure 2E).

FLT3 mutations are the most common genetic alterations in AML. Internal tandem duplication (ITD) mutations within the FLT3 juxtamembrane domain occur in 20%–30%, and other point mutations (i.e., D835Y or D835V) in the tyrosine-kinase domain (FLT3-TKD) occur in an additional 7%–9% of AML (Swords et al., 2012). By an in vitro kinase assay, we determined that the well-described *FLT3* mutants *FLT3-ITD* and D835Y were also SYK phosphorylated (Figure 2F). WT and mutant FLT3 showed increased SYK phosphorylation at Y768 and Y955, which is strongly associated with increased FLT3 activation at Y591 as well as activation of known FLT3 targets STAT5 and ERK1/2 (Figure 2G). Of note, overexpression of inactive SYK KD induced neither FLT3 phosphorylation nor the activation of ERK1/2.

FLT3 Activation by SYK Depends on a Physical Interaction

We used two approaches to investigate the effects of SYK on FLT3 activation in a cellular context. First, using recently generated small-molecule inhibitors of SYK, PRT062607 (Spurgeon et al., 2013) and Merck SYKi (Moy et al., 2013), we determined both in AML cell lines and primary patient samples that SYK inhibition diminished FLT3 activation in a few hours, as reflected

by the downregulation of FLT3 phosphorylation at site Y591 and at the SYK-phosphorylated sites Y768 and Y955. This was accompanied by an inhibition of downstream STAT5 and ERK1/2 signaling (Figures 3A, 3B and S3A). Next, to confirm that this effect was on target for SYK, we used a doxycycline-inducible microRNA (miRNA)-based short hairpin RNA (miR30-shRNA) system to produce knockdown approximating that of a null allele. Expression of two different miR30-shRNAs targeting *SYK* (shSYK_4 and shSYK_5) induced a time-dependent downregulation of SYK expression, loss of FLT3 phosphorylation at Y768, Y955, and Y591, and a decrease in STAT5 activation (Figure 3C).

To further validate these results, we overexpressed a constitutively activated SYK (*SYK-TEL*) to assess its effects on FLT3 activation and its downstream effectors (Figure S3B). We also generated a *TEL-SYK* chimera, a fusion between a truncated form of *SYK* lacking its SH2 domains (SH2 Nter + SH2 Cter) and a *TEL* sequence substituting for these SH2 domains (Kuno et al., 2001). Transduction of wild-type *SYK* (SYK WT) into two AML cell lines with low basal levels of SYK activation, THP-1 and NOMO-1, enabled expression of moderately activated SYK, whereas the *SYK-TEL* construct encoded for a highly activated form (Figure 3D). When these two constructs were expressed, FLT3 phosphorylation at Y768 and Y955 increased, and FLT3 activation was enhanced, as demonstrated by Y591 phosphorylation and hyperactivation of the downstream STAT5, AKT, and ERK1/2 pathways. FLT3 phosphorylation was even more pronounced with *SYK-TEL* than *SYK* WT expression, an effect that was abrogated in the presence of KD (K402R) mutants. These results were confirmed in 293E cells transfected with *SYK* WT and *SYK-TEL* constructs. Surprisingly, however, *TEL-SYK*, which, like *SYK-TEL*, enabled overexpression of a constitutive active SYK, did not fully recapitulate the effects of *SYK-TEL* on FLT3 activation (Figure 3E).

We thus hypothesized that the SH2-binding region expressed on SYK-TEL but absent on TEL-SYK supports an essential interaction between SYK and FLT3 needed for phosphorylation of FLT3 by SYK. To test this, we coexpressed V5-tagged FLT3 WT with either SYK WT or the chimeric proteins TEL-SYK and SYK-TEL WT or KD in 293E cells (Figure 3F). We determined that the SYK WT, SYK-TEL WT, and KD expressed proteins, along with a SYK mutant (Y130E) reported to be activated in the presence of BCR (Keshvara et al., 1997), coimmunoprecipitated with FLT3, whereas the TEL-SYK fusion protein did not. However, as confirmed in Figure S3C, the TEL moiety did not markedly alter the binding capacity to FLT3 WT or mutant. To confirm that SYK interacted with FLT3 through its SH2-binding region, we generated several SYK mutants by deleting the SH2 N-terminal, C-terminal, or both domains (ΔSH2 Nter, ΔSH2 Cter, and ΔSH2 Nter + Cter) or by inactivation of these domains by point mutation (SH2 Nter$^{mut\ (42RQS\ >\ GGI)}$, SH2 Cter$^{mut\ (195RAR\ >\ GAL)}$ and SH2 Nter + Cter^{mut}) (Figure 3G). Only SYK mutants lacking the SH2 Cter domain or mutated in the SH2 Cter domain failed to coimmunoprecipitate with FLT3, demonstrating that the SYK SH2 C-terminal domain is involved in FLT3 binding. Notably, cytoplasmic sequestration of a SYK mutant with deletion of the nuclear localization sequence (SYK ΔNLS) enhanced the association of that mutant with FLT3. Mutagenesis of *FLT3* revealed a tetrad of tyrosine residues Y589, Y591, Y597, and Y599 located in the juxtamembrane region of FLT3 as essential for this physical interaction (Figures S3D and S3E). To see if SYK interacted more avidly with FLT3-ITD than WT, we immunoprecipitated SYK in cells expressing isogenic pairs of FLT3 constructs. As observed in Figure 3H, SYK showed greater affinity for FLT3-ITD than FLT3 WT. Finally, we validated the endogenous interaction between SYK and FLT3 in a panel of 12 AML cell lines expressing various levels of either FLT3 WT or ITD (Figure 3I). A fraction of SYK associated with FLT3 is activated, as shown by phosphorylation of SYK at Y525/Y526. Using confocal microscopy on primary AML patient samples, we identified that the proteins interacted predominantly at the cellular membrane, suggesting that FLT3 (APC) trapped SYK (FITC) at FLT3′s primary site of localization (Figure 3J).

SYK Is Required for FLT3-ITD-Induced Myeloid Disease

We next investigated whether SYK was required for FLT3-ITD-dependent myeloproliferative disease (MPD). We used miR30-shRNA to stably and efficiently knockdown *Sykb* (homologous to human *SYK*) in murine myeloid progenitors. As depicted in Figure 4A, murine myeloid progenitors (common myeloid progenitor [CMP] and granulocyte/monocyte progenitor [GMP] cells) expressed high levels of *Sykb* compared to more immature LSK cells. The Sca-1^{-}/c-KIT^{+} myeloid progenitor fraction from donor mice whole bone marrow was transduced first with one nontargeting control (CT) miR30-shRNA or the two most effective hairpins directed against *Sykb* (miR30-shSykb1 and miR30-shSykb4) before sorting and transduction with the MSCV-EGFP empty (MIG) or *FLT3-ITD* vector (Figure S4A). Transduction efficiency was analyzed by flow cytometry to confirm that GFP expression occurred only in the tomato-positive cell fraction (Figure S4B) and knockdown confirmed by western blot (Figure S4C).

Animals receiving miR30-shCT + *FLT3-ITD* developed marked splenomegaly, with spleens two to seven times larger than those of the miR30-shCT + MIG mice (Figure 4B). These mice also developed a striking leukocytosis and an approximately 2-fold decrease in both hematocrit (HCT) and platelet (PLT) count compared to miR30-shCT + MIG-transplanted mice, an effect abrogated with Sykb knockdown (Figures 4B and S4D). Similarly, miR30-shCT + *FLT3-ITD* mice developed a lethal hematopoietic disease with a median latency of approximately 75 days, whereas animals transplanted with *FLT3-ITD* and either miR30-shSykb1 or miR30-shSykb4 cells exhibited almost normal overall survival at 150-day follow up (Figure 4C).

In *FLT3-ITD* + miR30-shCT spleen and blood, flow cytometric analysis showed a marked increase in cells positive for the late myeloid markers GR-1 and Mac-1, respectively, indicative of granulocytes (GR-1^{+}/Mac-1^{+}) and monocytes (GR-1^{-}/Mac-1^{+}), compared to the spleen and blood cells of control mice (Figure 4D). The majority of these mature myeloid cells were both tomato and GFP positive, demonstrating that they arose from *FLT3-ITD* + miR30-shCT-transduced marrow. In contrast, the *Sykb*-depleted *FLT3-ITD* mice displayed a minimal increase in granulocytes in blood and spleen, largely tomato and GFP negative. Finally, *FLT3-ITD*-mediated myeloid expansion was accompanied by a reduction in lymphoid maturation, as assessed by a decrease in the number of B220 or CD3-positive

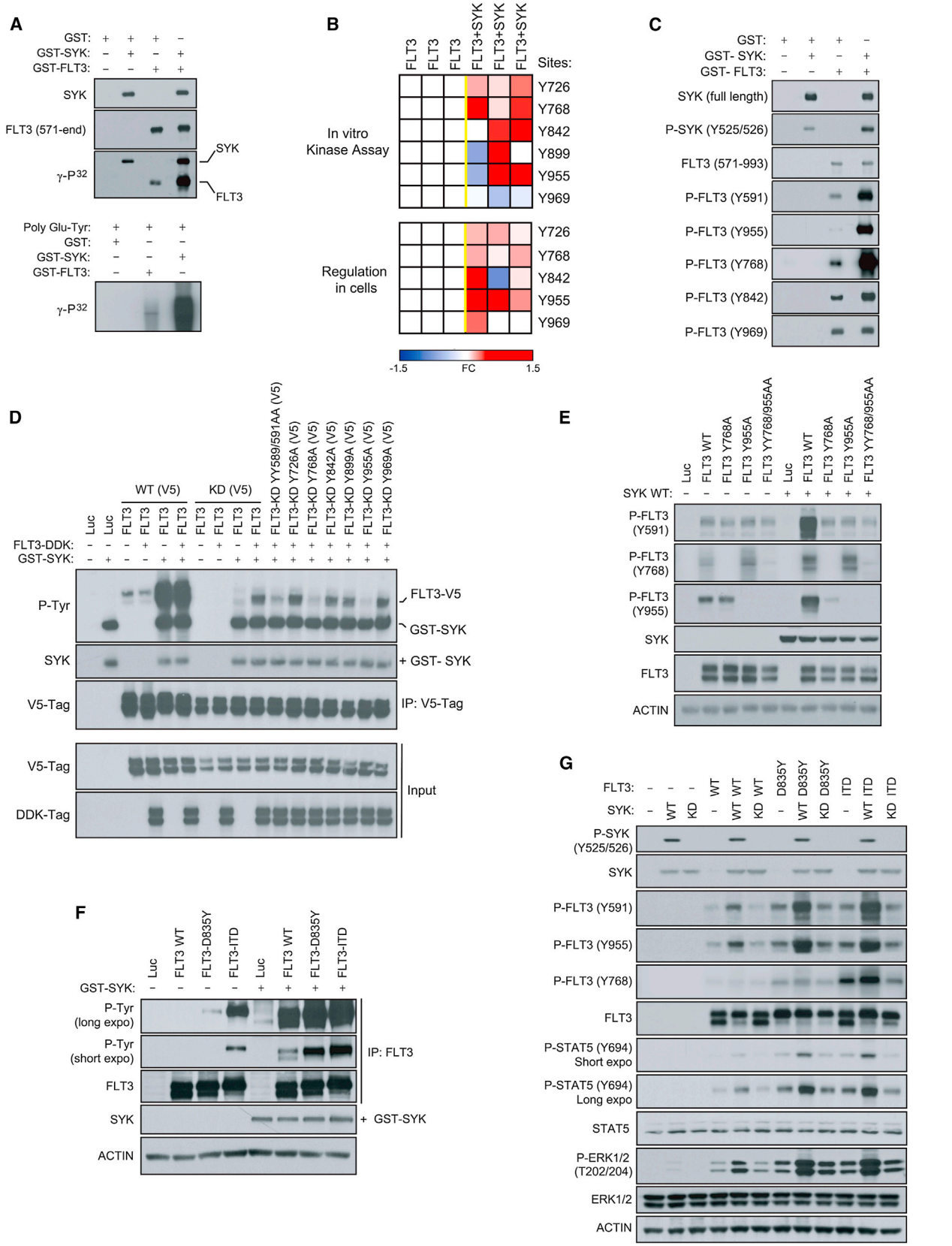

(legend on next page)

cells in spleen and blood from *FLT3-ITD* + shCT mice. As expected, *Sykb* knockdown restored a normal proportion of these lymphoid cells (Figure S4E).

Finally, we detected by fragment analyzer the presence of *FLT3-ITD* sequence in genomic DNA extracted from bone marrow and spleen cells to ensure stable insertion of the mutation (Figure S4F). Although the *FLT3-ITD* sequence was highly represented in the bone marrow and spleen of mice transplanted with miR30-shCT infected cells, its abundance was strongly decreased in *Sykb*-depleted counterparts, suggesting suppression of *FLT3-ITD* positive cells.

To rule out the possibility that this phenotype resulted from failed engraftment of *FLT3-ITD*-positive cells, we used a complementary approach: doxycycline-induction of *Sykb* knockdown in murine myeloid cells already transformed by *FLT3-ITD* (Figure S4G). From the TRMPVIR doxycycline-inducible vector, we engineered a TRMPCIR vector by substitution of the yellow-green Venus reporter for a far-red fluorescent Crimson sequence suitable for cotransduction with the *FLT3-ITD* GFP vector (Figure S4H). Transduction efficiency was analyzed by flow cytometry to confirm that GFP expression occurred only in crimson-positive cells (Figure S4I). The normalization of the white blood cell (WBC) count and a marked decrease in FLT3-ITD-positive cells were observed following induction of *Sykb* knockdown at the onset of disease, an effect sustained after doxycycline withdrawal (Figures 4E and 4F). This resulted in a significant improvement in the overall survival of *FLT3-ITD* + miR30-shSykb1 and *FLT3-ITD* + miR30-shSykb4 mice in comparison to *FLT3-ITD* + miR30-shCT mice (Figure 4G). In vitro, we confirmed that doxycycline-induced suppression of *Sykb* decreased FLT3 activity at Y591 and profoundly altered growth of the *FLT3-ITD*-transduced myeloid cells from 5 to 12 days after doxycycline (Figures 4H and 4I). Finally, to investigate whether FLT3-ITD AML cells are more vulnerable to SYK inhibition than FLT3 WT AML, we screened several genetically defined AML cell lines (Figures 4J and 4K) and patient AML samples (Figures 4L and 4M) for sensitivity to doxycycline-mediated SYK knockdown or SYK-specific inhibitors PRT062607 and Merck SYKi. FLT3-ITD positive AML cell lines and patient primary cells were strikingly more sensitive to SYK targeting by shRNA or small-molecule inhibitors than were their FLT3 WT counterparts (Figures 4J–4M).

Highly Activated SYK Cooperates with FLT3-ITD in Primary Patient AML

To assess the representation of highly versus minimally activated SYK across cohorts of patient samples, we profiled three AML cell lines transduced with either control or *SYK*-targeting shRNAs using genome-wide transcriptional profiling. SYK knockdown prompted a dynamic change in transcription, with 115 genes significantly upregulated and 95 genes significantly downregulated based on permutation $p < 0.05$ and FDR < 0.05 for signal-to-noise ratio (SNR). The top differentially 45 upregulated and 36 downregulated genes are depicted in Figure 5A. The full list is reported in Table S1. As expected, SYK expression was significantly downregulated across all AML cell lines in response to the two *SYK*-targeting shRNAs (Figure S5A). Next, we used this complete SYK gene set (Table S1) to query by single sample gene set enrichment analysis (ssGSEA) three cohorts of AML patient samples (GSE14468, GSE10358, and TCGA LAML), revealing that patients with a SYK-high signature were predominantly present in French-American-British (FAB) classification M1, whereas FAB M4 AML was enriched in patients with the SYK-low signature (Figure S5B). An analogous investigation applied to the two largest cohorts of FLT3-ITD AMLs, GSE14468 and TCGA LAML, showed that the SYK-high signature frequency is significantly higher in the *ITD* mutant than in the wild-type *FLT3* subgroup (Figure 5B). An extension of this analysis to other known mutations in AML (*NPM1*, *DNMT3A*, *IDH1/2*, *RUNX1*, *TET2*, *TP53*, *KRAS*, *NRAS*, *CEBPA*, *WT1*, and *KIT*; data not shown) revealed no significant positive correlation between the SYK-high signature and any of these mutations. However, in the GSE14468 and GSE10358 cohorts, the frequency of patients with the SYK-low signature is higher in *NPM1* mutants than in the wild-type *NPM1* subgroup. This trend was also observed in patients with double *FLT3-ITD* and *NPM1* mutations (Figure S5C).

We then used a complementary flow cytometry approach to assess an independent group of primary patient AML samples with either wild-type *FLT3* (n = 25) or *FLT3-ITD* (n = 23) for SYK and FLT3 activation levels using P-SYK (Y525/526) or P-FLT3 (Y591) directed antibodies (Figures 5C and 5D). As observed when using SYK transcriptional signatures as surrogates for SYK activation, primary patient AML samples with high P-SYK levels appeared more frequently in the *ITD* than in the wild-type

Figure 2. SYK Phosphorylates FLT3 WT and Mutants at Sites Y768 and Y955

(A) In vitro kinase assay showing incorporation of γ-^{32}P in response to the incubation of active GST-FLT3 (571–end) with active GST-SYK. The poly Glu-Tyr universal substrate peptide is used to validate FLT3 and SYK kinase activity.

(B) FLT3 phosphorylation state from an in vitro kinase assay performed with active GST-SYK (top) or immunoprecipitated from 293E cells transfected with FLT3-V5 and SYK WT (bottom) was analyzed by targeted mass spectrometry and phosphorylation ratios determined from chromatographic peak intensities. Heatmap showing the level of tyrosine phosphorylation of three biological replicates. Fold change (FC) is presented as a $\log_2$ ratio [exp(FLT3+SYK)/exp(FLT3)].

(C) In vitro kinase assay performed by incubating active GST-FLT3 (571–end) with active GST-SYK and immunoblotted using phosphospecific FLT3 and SYK antibodies.

(D) V5-tagged *FLT3* WT [*FLT3* WT (V5)] or kinase dead [*FLT3*-KD (V5)] with tyrosines either wild-type or mutated to alanine were cotransfected into 293E cells along with a DDK-tagged *FLT3* WT (*FLT3*-DDK) vector. V5-tagged constructs were then V5-tag immunoprecipitated to purify out the FLT3-DDK protein before incubation with GST-SYK for an in vitro kinase assay. Global FLT3 phosphorylation level was detected by immunoblot using an anti-phospho-tyrosine (P-Tyr) antibody.

(E) Western blot for FLT3 specific phosphosites from 293E cells coexpressing FLT3 WT or FLT3 Y768A, Y955A and YY768/955AA mutants, and SYK WT.

(F) FLT3 WT, D835Y, and ITD immunoprecipitated from 293E cells expressing each of these constructs and incubated with GST-SYK for an in vitro kinase assay. Detection of global FLT3 phosphorylation level using anti-phospho-tyrosine (P-Tyr) antibody.

(G) Western blot for FLT3 specific phosphosites from 293E cells coexpressing FLT3 WT, D835Y or ITD, and SYK WT or kinase dead (KD).

See also Figure S2.

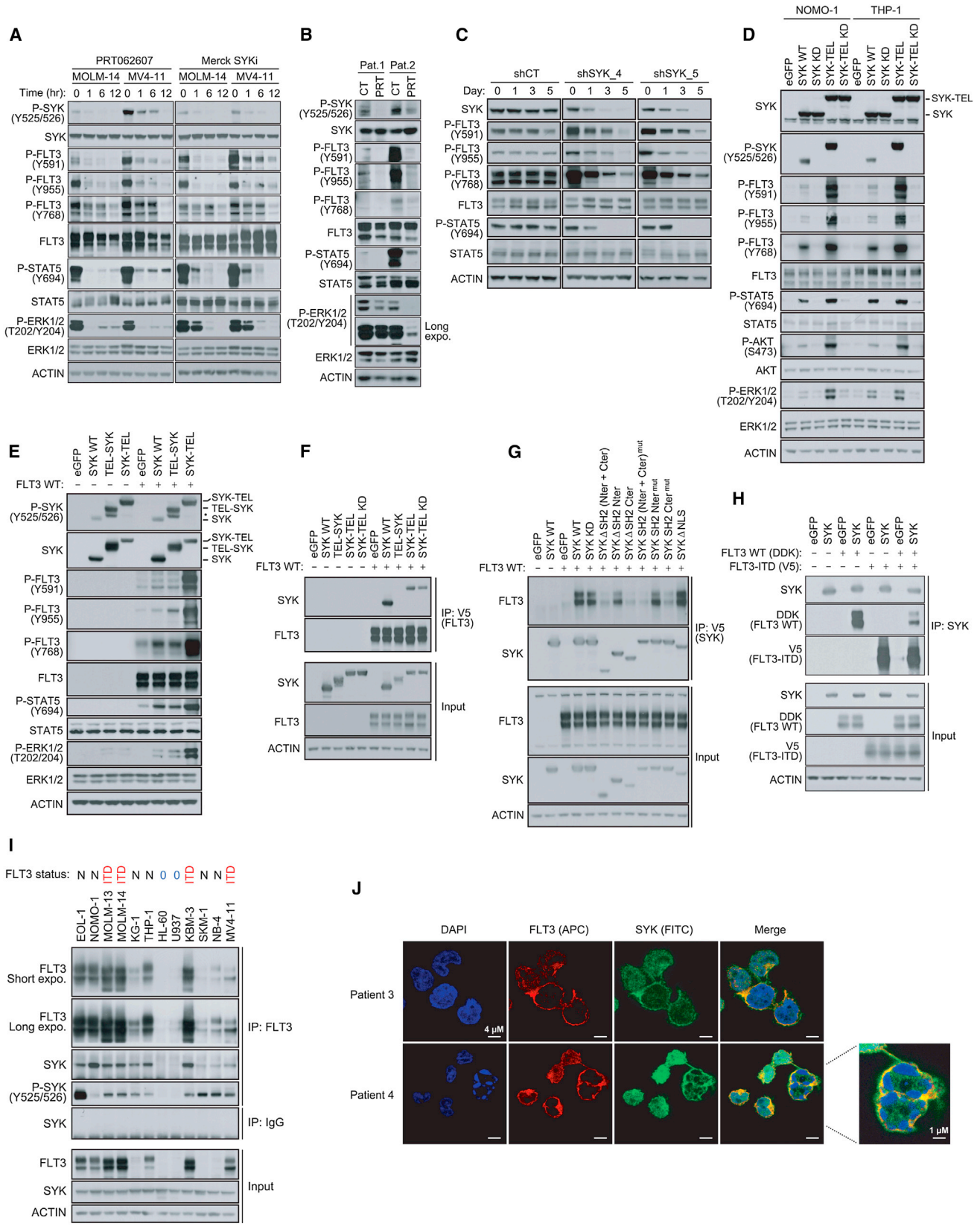

(legend on next page)

FLT3 subgroup (Figure 5C). To further characterize this association, each subgroup of patients was scaled on X-Y graphs based on their P-SYK/SYK and P-FLT3/FLT3 *Z* scores (Figures 5D and S5D). As expected, FLT3 was more highly activated in patients with *FLT3-ITD*, and P-SYK and P-FLT3 activation levels were more strikingly correlated in patients with *FLT3-ITD* (ρ score = 0.7) than with wild-type *FLT3* (ρ score = 0.5). Interestingly, SYK and FLT3 activation were most highly correlated in patients with relapsed AML expressing the *FLT3-ITD* mutation (ρ score = 0.8).

We divided FLT3-ITD patient samples from three AML data sets into two groups based on SYK signature (high versus low) and interrogated the data with published, validated gene signatures (available from Molecular Signature Data Base [MSig] and Differentiation Map [DMAP]) for enrichment by ssGSEA. As shown in Figures 5E and S5E and Tables S2 and S3, gene sets associated with hematopoietic progenitor maintenance and MYC-dependent transcriptional programs were significantly enriched in the FLT3-ITD samples displaying a high SYK signature and depleted in those displaying a low SYK signature. High P-SYK activation combined with FLT3-ITD mutation is associated with overexpression of MYC at both mRNA and protein levels (Figures 5F and 5G). Finally, using top genes from human and murine MYC target-related gene sets, we designed a MYC consensus transcriptional target mini signature. We used quantitative RT-PCR (qRT-PCR) to assess alteration of these signature genes in Ba/F3 or U937 cells coexpressing FLT3-ITD and SYK or SYK-TEL constructs (Figure 5H). These results suggest that a pro-leukemogenic, cooperative interaction between FLT3-ITD and SYK may select for higher levels of SYK activation in FLT3-driven disease and that SYK may promote MYC expression and activation as a mechanism of leukemogenesis.

SYK Activation Promotes Progression of FLT3-ITD-MPD to AML

We generated a second bone marrow transplantation model using sorted myeloid progenitors cotransduced with MSCV-EGFP-FLT3-ITD in combination with MSCV-tomato vectors (MIT) encoding for either wild-type SYK (SYK WT), a constitutively activated SYK-TEL, or TEL-SYK (Figure S6A). Before retransplantation, transduction efficiency was analyzed by flow cytometry to confirm that GFP expression occurred in the tomato-positive cell fraction (Figure S6B).

Although mice that received myeloid cells cotransduced with *FLT3-ITD* and MIT developed a lethal disease (median latency 73 days) (Figure 6A), mice transplanted with cells expressing *FLT3-ITD* and either *SYK* or *SYK-TEL* constructs developed a disease with a more rapid onset and a reduced median latency (64 and 43 days, respectively) (Figure 6A). However, animals injected with cells expressing both *FLT3-ITD* and *TEL-SYK* constructs did not show signs of more accelerated disease, suggesting that both the level of SYK activation and the capacity for binding and transactivation of FLT3 are essential to modulate FLT3-ITD disease progression. Importantly, groups receiving *SYK-TEL*- or *TEL-SYK*-expressing cells contracted a lethal disease by 180 days posttransplantation, as compared to control mice showing no lethality for up to 220 days (data not shown).

The decreased overall survival of mice injected with cells coexpressing either *SYK* or *SYK-TEL* and *FLT3-ITD* was associated with marked splenomegaly, as compared to mice transduced only with *FLT3-ITD* (Figure 6B). These mice also exhibited elevated WBC counts, anemia, and thrombocytopenia (Figure S6C). *FLT3-ITD* sequence levels were more elevated in spleens of mice coexpressing *SYK* and *SYK-TEL* based on fragment analyzer (Figure S6D). In addition, qRT-PCR using primers specific for a common region of *SYK*, *SYK-TEL*, and *TEL-SYK* confirmed homogeneous expression of each construct on an equivalent number of infected spleen-sorted cells (Figure S6E).

Consistent with the myeloproliferative phenotype described earlier, an increase in a myeloid cell population positive for GR-1 and Mac-1 was observed in spleen cells from *FLT3-ITD* + MIT mice compared to those from control MIT + MIG mice (Figure 6C). However, this cell fraction was more highly represented in the spleens of mice transplanted with either *SYK* or *SYK-TEL* constructs combined with *FLT3-ITD* than in those injected with cells coexpressing *TEL-SYK* and *FLT3-ITD*. H&E staining of *FLT3-ITD* + MIT spleen and bone marrow showed a marked predominance of maturing myeloid lineage cells, consistent with MPD, whereas spleens and bone marrow harvested from mice expressing either *SYK* or *SYK-TEL* constructs combined with *FLT3-ITD* showed extensive infiltration

Figure 3. Activation of FLT3 and Its Downstream Effectors Is Dependent on a Physical Interaction with SYK.

(A) Western blot for indicated proteins from MOLM-14 and MV4-11 cells treated with 3 μM PRT062607 or 5 μM Merck SYKi. The phosphosite Y768 was detected on FLT3 total immunoprecipitate.

(B) Western blot for indicated proteins from FLT3-ITD positive primary patient AML cells treated for 6 hr with 3 μM PRT062607.

(C) Western blot for SYK and FLT3 specific phosphosites from MOLM-14 cells stably transduced with either a control or two *SYK*-targeting doxycycline-inducible miR30-shRNAs and treated with doxycycline for 1, 3, or 5 days. The phosphosite Y768 was detected on FLT3 total immunoprecipitate.

(D) Western blot for indicated proteins from NOMO-1 and THP-1 AML cells expressing different forms of SYK. The phosphosite Y768 was detected on FLT3 total immunoprecipitate.

(E) Western blot for FLT3, STAT5, and ERK specific phosphosites from 293E cells expressing FLT3 WT and different forms of SYK.

(F) Using anti-V5 antibody, FLT3 immunoprecipitation from 293E cells coexpressing FLT3 and different forms of untagged SYK and western blot using anti-SYK antibody.

(G) Using anti-V5 antibody, immunoprecipitation of several truncated and mutated forms of SYK from 293E cells coexpressing these constructs and untagged FLT3 WT and western blot using anti-FLT3 antibody.

(H) Using anti-SYK antibody, immunoprecipitation of SYK from 293E cells coexpressing isogenic pairs of FLT3 WT and ITD constructs and western blot using anti-SYK, anti-V5, and anti-DDK antibodies.

(I) FLT3 immunoprecipitation from 12 AML cell lines expressing low levels of FLT3 WT (0) and various levels of FLT3 WT (N) or mutated (ITD) and western blot using anti-SYK and anti-P-SYK (Y525/526) antibodies. Anti-IgG antibody was used as a control.

(J) Staining for SYK (green), FLT3 (red), and DAPI (blue) in blast cells from two FLT3-ITD positive primary patient AML samples.

See also Figure S3.

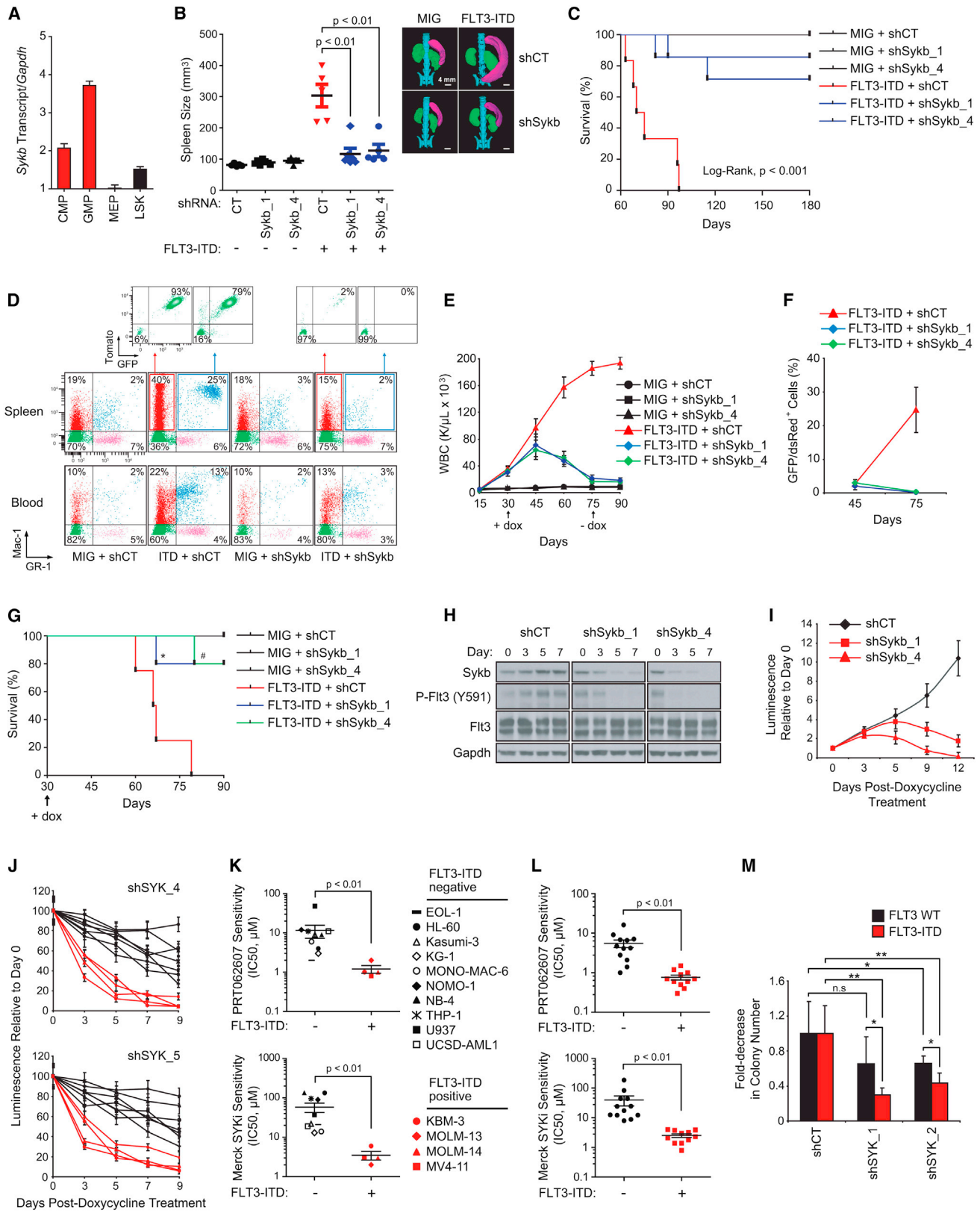

(legend on next page)

by sheets of immature myeloid blasts, consistent with AML, in about 65% to 75% of cases, respectively (Figure 6D). Furthermore, a population of tomato- and GFP-positive cells positive for the hematopoietic progenitor marker c-KIT was also found in spleens from all *FLT3-ITD* + *SYK* and *FLT3-ITD* + *SYK-TEL* moribund animals, but not in spleens of other *FLT3-ITD* groups (Figure 6E). These results suggest that the MPD observed with *FLT3-ITD* alone has a more immature phenotype when *FLT3-ITD* is combined with *SYK* or *SYK-TEL* activation consistent with AML.

Several FLT3-ITD + SYK or SYK-TEL moribund animals showed a recurrent expansion of the Lin^{Low}/Sca-1^{-}/c-KIT^{+}/$CD16/32^{+}$/$CD34^{+}$ GMP compartment (n = 5/7 and n = 4/6, respectively; representative examples in Figure 6F). Whereas FLT3-ITD alone enhanced the expansion of the GMP population by 1.5-fold, the proportion of GMP cells expressing either *FLT3-ITD* + *SYK* or *FLT3-ITD* + *SYK-TEL* was increased by 2.5- and 4.5-fold, respectively. Simultaneous expression of *FLT3-ITD* and either *SYK* or *SYK-TEL* results in a growth advantage of this fraction at the expense of megakaryocyte/erythrocyte progenitor (MEP) and CMP fractions, because, in both cases, double tomato/GFP-positive GMP clones emerged from the whole GMP population. Finally, *SYK* and, even more dramatically, *SYK-TEL* expression enhanced the growth capacity of *FLT3-ITD*-expressing $tomato^{+}$/GFP^{+} myeloid cells in vitro over 9 days (Figure 6G). We also assessed the effect of SYK and FLT3-ITD cooperation on the clonogenic potential of normal purified $CD34^{+}$ human cells. As shown in Figure 6H, the number of $CD34^{+}$ colonies significantly increased with cotransduction of *FLT3-ITD* and either *SYK* WT or *SYK-TEL* in comparison to FLT3-ITD only controls. This increase relies on SYK activity, because it was not observed in the presence of the KD mutant of SYK-TEL (SYK-TEL KD). Further mutation of FLT3-ITD's SYK phosphorylation sites, Y768 and Y955, into alanines undermined the cooperation of SYK with FLT3-ITD in promoting colony formation (Figure 6I). An analogous experiment was conducted in vivo (Figure 6J). Unfortunately, YY768/955AA and Y768A mutants impeded *FLT3-ITD*'s ability to induce a lethal MPD. However, although the FLT3-ITD Y955 mutant generated a low-penetrance lethal disease, it did block acceleration of the disease induced by SYK-TEL coexpression.

To determine the degree to which a potentially promiscuous kinase such as SYK would have a similar effect on other mutated tyrosine kinase oncogenes, we evaluated a BCR-ABL-driven leukemia model. By kinome profiling and in vitro kinase assay, we determined that ABL was neither an indirect nor a direct target of SYK (data not shown and Figure S6F). We used an acute lymphocytic leukemia model of murine $p19^{Arf\ -/-}$ pre-B cells driven by *Bcr-Abl* transplantable into immune-competent syngeneic C57/BL6 mice (Williams et al., 2006). As shown in Figures S6G and S6H, SYK-TEL overexpression neither amplified growth of BCR-ABL-positive cells in bone marrow or spleen nor influenced survival. Furthermore, SYK-TEL overexpression did not significantly enhance the number of colonies of either $CD34^{+}$ cells transduced with BCR-ABL or CD34+ BCR-ABL positive cells purified from a patient with chronic myeloid leukemia (CML) (Figures S6I and S6J). These results suggest that activated SYK does not exert the same pro-oncogenic effect on other tyrosine kinase oncogenes, such as BCR-ABL, as it does on FLT3-ITD.

SYK Activation Promotes Resistance to Targeted Kinase Inhibitors

We next asked whether the *FLT3-ITD/SYK* models could be transplanted into secondary recipients. $Tomato^{+}$/GFP^{+} myeloid cells expressing *FLT3-ITD* in combination with MIT empty, *SYK* WT, or *SYK-TEL* were sorted from spleens of moribund donor mice and reinjected into sublethally irradiated recipient mice. Although FLT3-ITD + MIT-expressing cells did not alter mice survival, purified FLT3-ITD + SYK or SYK-TEL cells generated a lethal disease in secondary recipients with median latencies of 64 and 19–28 days, respectively (Figure 7A) and induced previously observed features, including increased WBC, decreased PLT count and HCT, and marked splenomegaly (Figures

Figure 4. SYK Knockdown Impairs Development of FLT3-ITD-Driven Myeloid Disease

(A) qRT-PCR showing relative expression levels of *Sykb* in purified progenitor hematopoietic stem and progenitor subsets. Error bars represent mean ± SD.

(B) Spleen size measurement by microtomography of five mice per group. One representative picture is shown for one mouse per indicated group. $p < 0.01$ calculated using a Mann-Whitney test. Error bars represent mean ± SEM.

(C) Kaplan-Meier curves showing overall survival of mice (n = 6) transplanted with myeloid cells expressing each combination of MSCV and miR30-shRNA vectors. Statistical significance determined by log-rank (Mantel-Cox) test.

(D) FACS analysis of Mac-1 and GR-1 expressing populations in spleen and blood. A representative FACS plot from each group is shown.

(E) WBC count in the blood harvested from three mice per group. The p value was calculated using a Mann-Whitney test. Arrow indicates beginning and end of doxycycline treatment. Error bars represent mean ± SEM.

(F) FACS analysis of GFP/dsRed-positive cells in bone marrow with error bars representing the mean ± SEM of three bleedings per time point.

(G) Kaplan-Meier curves showing overall survival of mice (n = 4 for MIG and FLT3-ITD + shCT groups; n = 6 for FLT3-ITD + shSykb groups) transplanted with myeloid cells expressing each combination of MSCV and doxycycline-inducible vectors (TRMPCIR). Statistical significance determined by log-rank (Mantel-Cox) test. $^{*}p = 0.02$ and $^{\#}p = 0.003$ by comparison with FLT3-ITD + shCT group. Arrow indicates beginning of doxycycline treatment.

(H) Western blot indicating the expression level of SYK and FLT3 activity over 7 days after doxycycline.

(I) Growth after treatment with doxycycline is shown relative to day 0 (time of seeding), with error bars representing the mean ± SD.

(J) AML cell lines were infected with two *SYK*-directed shRNAs. Growth after doxycycline is normalized to the control shRNA and shown relative to day 0 (time of seeding), with error bars representing the mean ± SD.

(K and L) Distribution of IC_{50} for *FLT3* wild-type versus *FLT3-ITD* AML cell lines (K) or patient primary cells (L) in response to treatment with PRT062607 or Merck SYKi. The p value was calculated using nonparametric Mann-Whitney test.

(M) $CD34^{+}$ primary cells from *FLT3* WT (n = 4) or *ITD* (n = 5) patients with AML were purified and infected with shCT or two *SYK*-targeting shRNAs. Colony number was evaluated after MTT staining. $^{**}p < 0.01$, $^{*}p \leq 0.05$ calculated using a Mann-Whitney test. n.s, non significant ($p > 0.05$).

Error bars represent mean ± SEM (K–M).

See also Figure S4.

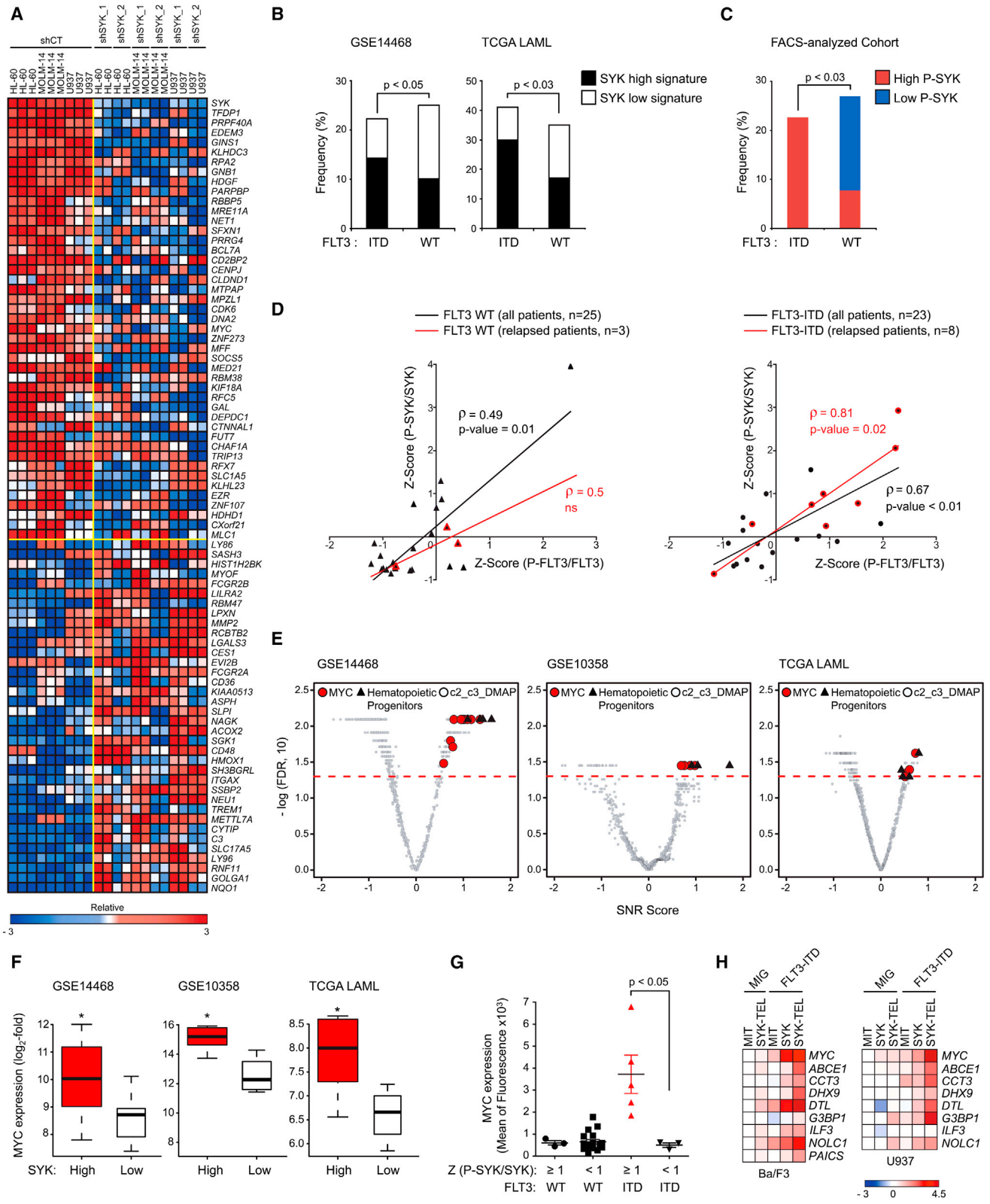

Figure 5. Highly Activated SYK Is Enriched in FLT3-ITD Patient AML Samples and Is Associated with MYC-Related Transcriptional Programs

(A) Heatmap of the top down and upregulated genes following transduction of AML cell lines with CT or two *SYK*-targeting shRNAs based on an SNR score and $p < 0.05$. Data are presented as row normalized.

(legend continued on next page)

S7A–S7D). Finally, H&E staining confirmed that these cells infiltrated the bone marrow and other sites (e.g, liver) (Figure 7B).

We used these secondary transplantable cells to explore the impact of activated SYK on resistance to FLT3 inhibition with the FLT3 inhibitor AC220 (Quizartinib). Although FLT3-ITD-expressing cells were highly sensitive to AC220, those expressing either SYK or SYK-TEL as well as FLT3-ITD showed increased resistance (Figure 7C). This effect was also observed in Ba/F3 cells coexpressing both FLT3-ITD and SYK or SYK-TEL. Interestingly, in vitro and in vivo, these cells were also more resistant to the dual SYK/FLT3 inhibitor, R406, reported to have 5-fold greater potency for SYK than FLT3 (Braselmann et al., 2006) (Figures 7D–7I). AC220 resistance was confirmed in the AML cell lines MOLM-14 and MV4-11 expressing either SYK WT or SYK-TEL and was associated with sustained FLT3 phosphorylation, even in the presence of an otherwise active dose of AC220 (Figures S7E and S7F). Resistance was not observed in vitro with coexpression of FLT3-ITD and the noninteracting partner TEL-SYK, SH2 domain-deleted SYK, KD SYK or SYK-TEL mutants (Figure 7D). These results indicate that the level of SYK activation is correlated with resistance to both molecules and that the physical interaction between SYK and FLT3 is necessary for resistance to the dual inhibitor.

To assess a combination strategy, AC220 and PRT062607 were combined across a range of concentrations and synergy and assessed in vitro using excess over Bliss additive synergy analysis (Figures S7G and S7H). Both compounds synergized to impair the viability of the two cell types as observed by a high excess over Bliss additive. In vivo, in both the SYK WT and SYK-TEL cooperative models with FLT3-ITD, the combination of PRT062607 and AC220 significantly increased survival of mice developing AML (Figures 7E and 7F) and resulted in a marked reduction of leukocytosis, decrease of double GFP/tomato-positive leukemic blasts and profound inhibition of FLT3-ITD and SYK activation (Figures 7G–7I).

DISCUSSION

FLT3-ITD mutations occur in approximately 20% of patients with AML and result in a blockade of differentiation and hyperproliferation of hematopoietic cells (Patel et al., 2012). Early single agent trials were notable for some clinical activity (DeAngelo et al., 2006; Fischer et al., 2010; Knapper et al., 2006; Pratz et al., 2009), but the low complete remission rate as well as the development of progressive disease despite an initial clinical response dampened enthusiasm for using FLT3 inhibitors as a single agent in AML (Weisberg et al., 2010). Newer agents with greater potency and sustained inhibition have been developed with exciting results in recent clinical trials, including the observation of terminal differentiation of AML blasts in patients treated with AC220 (Sexauer et al., 2012). Moreover, mutations within the kinase domain of *FLT3-ITD*, conferring AC220 acquired clinical resistance, were recently reported (Smith et al., 2012), providing additional validation that *FLT3-ITD* is an important oncogenic driver of AML.

In this study, we identify an unexpected functional role for SYK in modulating FLT3 activation and demonstrate FLT3-ITD dependency on SYK for driving myeloid neoplasia in mice despite the constitutive activation of the FLT3 receptor. A role for the SYK-FLT3 collaboration is also highlighted by our in silico and flow-based analysis showing that *FLT3-ITD*-positive patient AML blasts exhibit higher levels of SYK activation than *FLT3*-wild-type patient AML blasts. Although our data reveal the activation of FLT3 by SYK, the mechanism of SYK activation in FLT3-ITD-positive AML remains uncertain. Neither mutation of *SYK* (with the exception of a case report of a *TEL-SYK* rearrangement in a patient with MDS) (Kuno et al., 2001) nor association of SYK activation with other known mutations has previously been described in myeloid neoplasms. Recent manuscripts describe a link between SYK activation and both integrin β2 and β3 signaling (Miller et al., 2013; Oellerich et al., 2013), suggesting two potential mechanisms for SYK activation. Crosstalk between integrin β1 signaling, PYK2, and FLT3-ITD has also been reported (Katsumi et al., 2011), perhaps pointing toward possible feedback of FLT3-ITD on SYK activation.

We engineered a tractable myeloid transplantation model to delineate the effects of various levels of SYK activation on FLT3-ITD-induced disease. This model revealed a link between SYK activation and FLT3-ITD disease progression, with SYK activation leading to acceleration of disease development and transformation from MPD to AML. This is likely dependent on the FLT3-ITD and SYK partnership, rather than exclusively a FLT3-independent effect of SYK, because both the level of SYK activation and the capacity for FLT3 transactivation are essential for the observed effects. The stratification of the FLT3-ITD+ patient group based on high versus low SYK activation highlighted a MYC-driven transcriptional program in the cooperation of SYK with FLT3. In light of this observation, and

(B) Bar graph showing the frequency of primary patient AML samples with *FLT3* WT versus *FLT3-ITD* displaying SYK high versus low signatures in two cohorts GSE14468 (n = 526) and TCGA LAML (n = 179). The p value was calculated using Fisher exact test.
(C) Bar graph showing the frequency of primary patient AML samples with *FLT3* WT (n = 25) versus *FLT3-ITD* (n = 23) exhibiting a high (Z score ≥ 1) versus low (Z score ≤ -1) level of (P-SYK/SYK) evaluated by phospho-flow cytometry on CD13/33-gated population. The p value was calculated using Fisher exact test.
(D) Spearman correlation (ρ-score) between (P-SYK/SYK) and (P-FLT3/FLT3) following Z score normalization across two subgroups of *FLT3* WT and *ITD* patients. Highlighted in red are samples from patients at time of relapse.
(E) Quantitative comparison of gene sets available from the MSig and DMAP database by ssGSEA for patient AML samples with *FLT3-ITD* from three different cohorts (GSE 14468, 10358, and TCGA LAML) displaying a SYK high versus low signature. Red dots indicate sets for *MYC*, black triangles for hematopoietic progenitors, and gray for all other available gene sets.
(F) Comparison of MYC expression levels for patient samples with *FLT3-ITD* from three different cohorts (GSE 14468, 10358, and TCGA LAML) displaying a SYK high versus low signature. The p value was calculated using Fisher exact test. Error bars represent mean ± SD.
(G) MYC protein level evaluated by intracellular flow cytometry on a cohort of *FLT3* WT or *ITD* patient samples (n = 25) exhibiting either high (Z score [P-SYK/SYK] ≥ 1) or medium to low (Z score [P-SYK/SYK] < 1) SYK activation. The p value was calculated using a Mann-Whitney test. Error bars represent mean ± SEM.
(H) Heatmap showing expression level of MYC transcriptional target genes evaluated by qRT-PCR. Normalized data are presented as a $\log_2$-ratio versus MIT.
See also Figure S5 and Tables S1, S2, and S3.

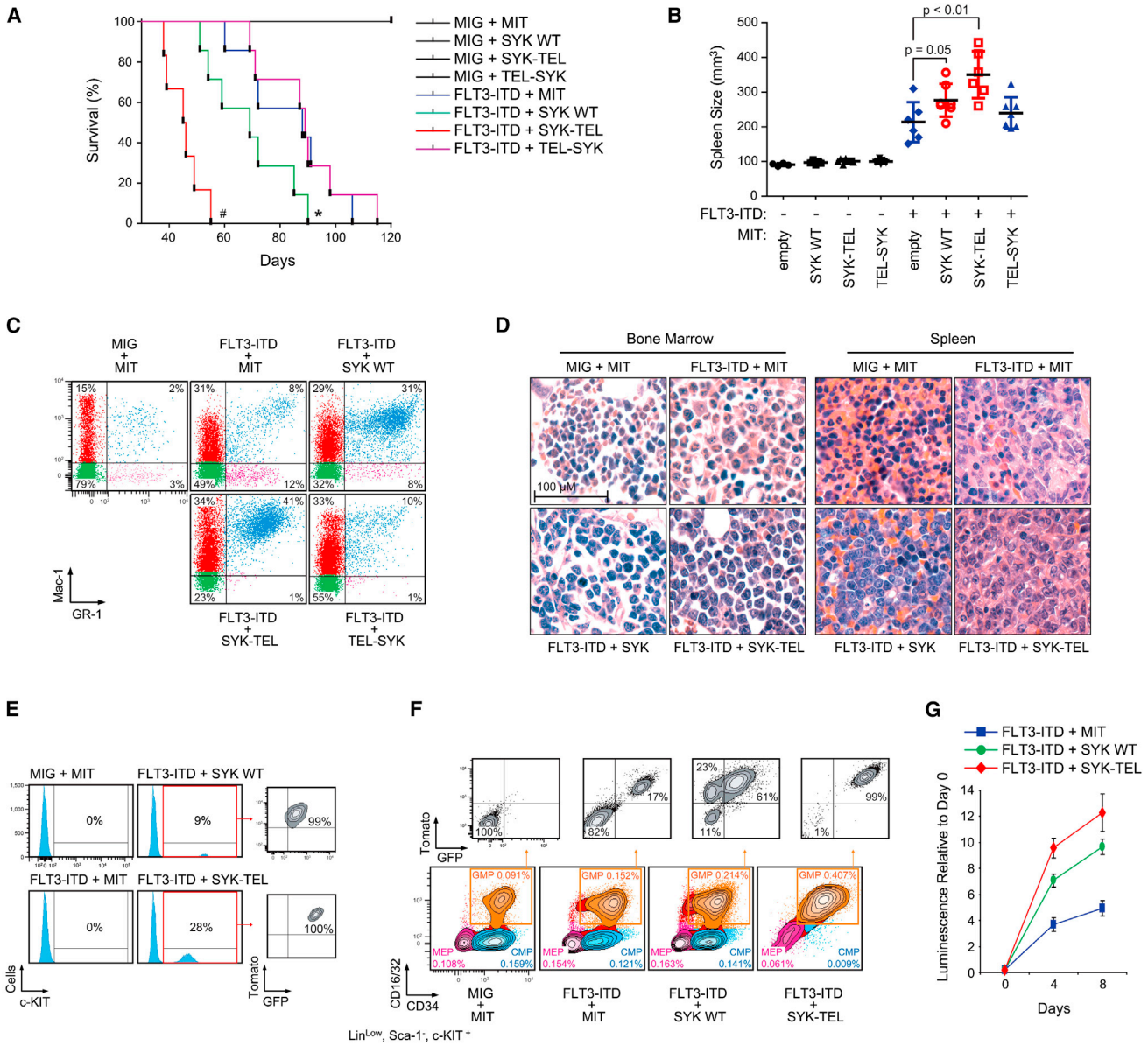

(legend on next page)

because the overexpression of this transcription factor has the capacity to induce AML (Luo et al., 2005), MYC has been nominated as one candidate for explaining the mechanism for the transition from MPD to an AML-like disease emerging from the SYK-FLT3 synergistic signal.

Our study has important clinical implications. First, we identify an increased sensitivity to SYK inhibition in the specific FLT3-ITD-positive AML subtype, suggesting the testing of SYK inhibitors in this patient population. We also identified a strong positive correlation between SYK and FLT3 activation in a subgroup of relapsed FLT3-ITD patient samples, nominating the SYK/FLT3-ITD cooperation as a potential mechanism of chemoresistance and inviting further study of the relationship between SYK activation and prognosis in FLT3 mutated AML. Moreover, our study reveals that the secondary transplantable AML, driven by the coexpression of highly activated SYK and FLT3-ITD, exhibits moderate resistance to the single FLT3 inhibitor AC220 and strong resistance to the dual SYK/FLT3 inhibitor fostamatinib (R406). Among the possible mechanisms to explain this surprising resistance to fostamatinib are inadequate pharmacokinetics with a failure to sufficiently inhibit SYK and FLT3 or an altered binding/inhibiting capacity of the compound due to the physical association between SYK and FLT3. A similar observation has been made in CML where another tyrosine kinase, LYN, can cooperate with BCR-ABL to overcome BCR-ABL small-molecule inhibition by mediating BCR-ABL phosphorylation even in the presence of inhibitor (Wu et al., 2008). The finding that the SYK mutant lacking the ability to transactivate FLT3 failed to promote resistance supports a similar mechanism of action for SYK-mediated FLT3 resistance. In this context, whereas SYK or FLT3 inhibition alone had some activity in vivo, the combined treatment with the SYK and FLT3 specific inhibitors was highly efficacious, suggesting this combination for clinical testing.

In summary, we report that the level of SYK activation is critical for outcome in mice developing a FLT3-ITD-driven myeloid neoplasia, illustrating the notion that additional interacting partners are essential in the oncogenic effects of FLT3 in promoting disease. This study also reveals the important clinical translational finding that *FLT3-ITD* AML cells have increased sensitivity to SYK suppression, raises the possibility that SYK hyperactivation may attenuate the response to FLT3 inhibitors, and supports the testing of FLT3 inhibitors in combination with SYK inhibitors in patients with FLT3 mutant AML.

EXPERIMENTAL PROCEDURES

See Supplemental Experimental Procedures for detailed methods.

High-Throughput Kinase Activity Profiling

A Luminex immunosandwich assay was performed in AML cells stably transduced with a pWZL empty or *SYK-TEL* vector encoding for a constitutively activated form of SYK. One hundred micrograms of whole-cell lysates from each cell line and positive control lysates were quantified, and equal concentrations of protein were incubated with a mixture of antibody-coupled Luminex beads directed against 105 protein candidates and then with a secondary anti-phospho-tyrosine biotin-labeled 4G10 antibody (Millipore).

Growth Measurement

Cells were plated in 384-well plates. ATP content was measured using CellTiter Glo (Promega) per the manufacturer's instructions.

Flow-Based Myeloid Differentiation Screening

U937, MOLM-14, THP-1, and KBM-3 cells were arrayed in two series of three replicates per shRNA in round bottom 96-well tissue culture plates. The next day, cells were infected, incubated for 5 days, and stained. Heatmap projections on differentially expressed CD11b and CD14 across each hairpin-transduced cell line were created based on the GENE-E software (http://www.broadinstitute.org/cancer/software/GENE-E/).

In Vivo Transplantation

The Massachusetts Institute of Technology Committee on Animal Care reviewed and approved all mouse experiments. The 4-week-old BALB/c male donor mice were primed with an intraperitoneal injection of 5′-fluorouracil (150 mg/kg) and sacrificed after 6 days. Bone marrow was harvested from the femur, tibia, and humerus, and red blood cells were lysed (RBCL buffer, Sigma). Myeloid cells were sorted and infected with the different combination of vectors and reinjected into recipient irradiated mice.

Figure 6. High SYK Activation Synergizes with FLT3-ITD to Promote Progression to AML

(A) Kaplan-Meier curves showing overall survival of mice (n = 7 for each group except for *FLT3-ITD* + *SYK-TEL* group, for which n = 6) transplanted with myeloid cells expressing each combination of indicated constructs. Statistical significance determined by log-rank (Mantel-Cox) test. *p = 0.05 and #p < 0.01 by comparison with *FLT3-ITD* + MIT group.

(B) Spleen size measurement by microtomography of six mice per group when *FLT3-ITD* + *SYK-TEL* mice became moribund. The p value was calculated using a Mann-Whitney test. Error bars represent mean ± SEM.

(C) FACS analysis of Mac-1 and GR-1 expressing populations in spleen. A representative FACS plot from each group is shown. Analysis was performed after *FLT3-ITD* + *SYK-TEL* mice became moribund.

(D) H&E staining of bone marrow and spleen of a representative moribund mouse from each indicated group.

(E) FACS analysis of *c-KIT* expressing cells in spleen after 5 days in culture. One representative moribund mouse from each indicated group is shown.

(F) Proportion of CMP ($CD16/32^{-}/CD34^{+}$), GMP ($CD16/32^{+}/CD34^{+}$), and MEP ($CD16/32^{-}/CD34^{-}$) cell populations on gated $Lin^{Low}/Sca\text{-}1^{-}/c\text{-}KIT^{+}$ myeloid progenitors. Tomato and GFP expression were evaluated on each GMP cell population. One representative moribund mouse from each group is shown.

(G) Double tomato and GFP positive $Lin^{Low}/Sca\text{-}1^{-}/c\text{-}KIT^{+}$ myeloid cells were sorted from the whole bone marrow harvested from moribund mice transplanted with each combination of *FLT3-ITD* and *SYK* vectors. Growth after sorting is shown relative to the day 0 (time of seeding) values, with error bars representing the mean ± SD.

(H and I) Purified normal $CD34^{+}$ human primary cells were infected with *FLT3-ITD* in combination with different forms of *SYK* (wild-type, constitutively active *SYK-TEL*, or inactive *SYK-TEL* KD) (H) or *SYK-TEL* in combination with either *FLT3-ITD* or the two mutants *FLT3-ITD* Y768A and Y955A (I). Colony number was evaluated after MTT staining. $p < 0.01$ and $p < 0.05$, calculated using a Mann-Whitney test. Error bars represent mean ± SD.

(J) Kaplan-Meier curves showing overall survival of mice (n = 5 for each group) transplanted with myeloid cells expressing each indicated combination of *FLT3-ITD* or *FLT3-ITD* mutants (Y > A) in combination with *SYK-TEL*. Statistical significance determined by log-rank (Mantel-Cox) test. *p = 0.05 by comparison with *FLT3-ITD* group.

See also Figure S6.

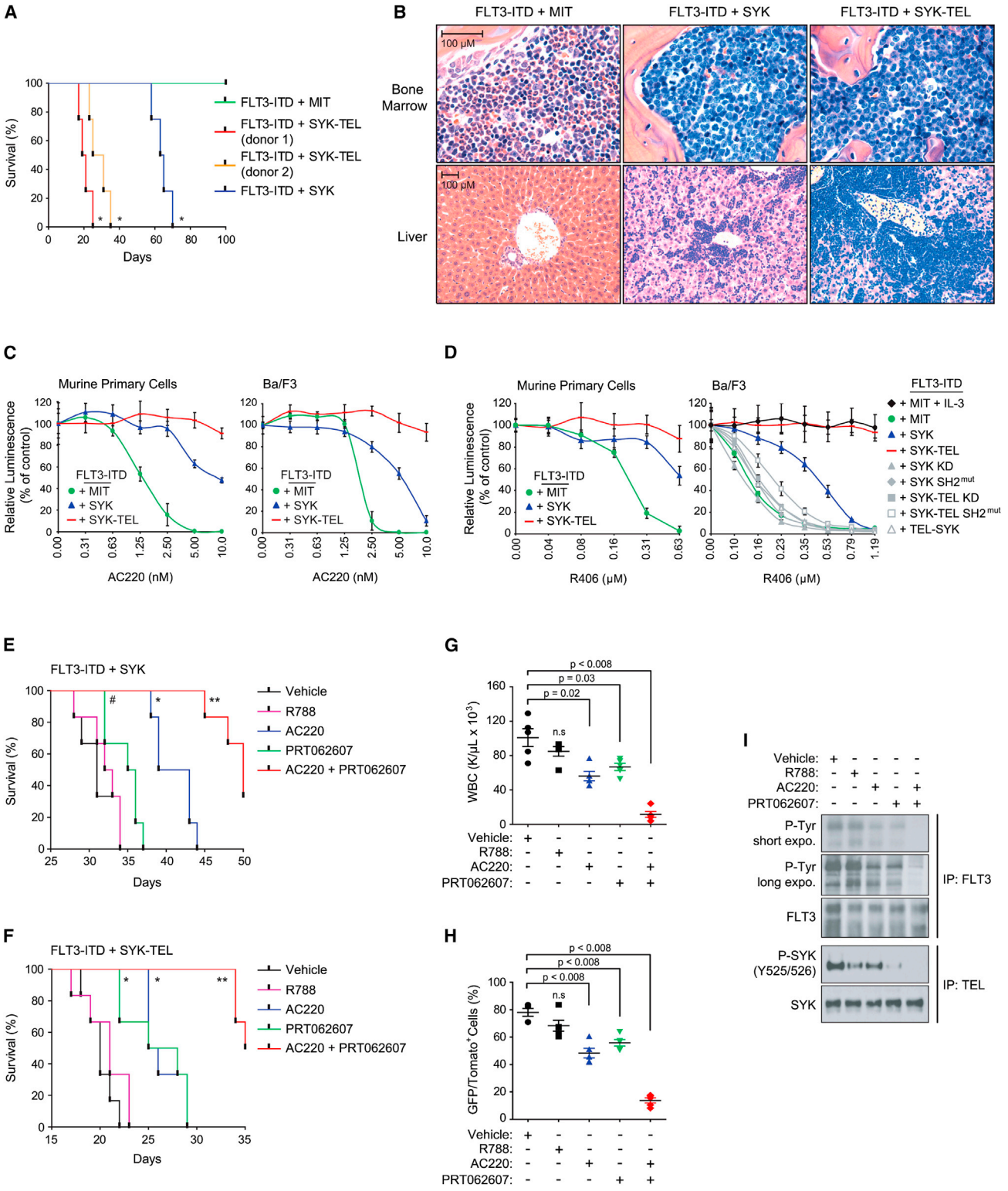

Figure 7. High SYK Activation Impairs the Targeting of FLT3-ITD-Driven AML with Small-Molecule Inhibitors In Vitro and In Vivo

(A) Kaplan-Meier curves showing overall survival of mice (n = 4) secondary transplanted with double tomato and GFP-positive myeloid cells expressing *FLT3-ITD* in combination with MIT empty, *SYK* WT, or *SYK-TEL* (clones from two different donor mice). Statistical significance determined by log-rank (Mantel-Cox) test.

(B) H&E staining of the bone marrow and liver of a representative moribund mouse from each indicated group.

(C and D) Growth inhibition of secondary transplantable murine primary and Ba/F3 cells coexpressing *FLT3-ITD* and indicated *SYK* constructs and treated with increasing doses of either AC220 (C) or R406 (D). Values are shown relative to day 0 (time of seeding), with error bars representing the mean ± SD.

(legend continued on next page)

Primary Cell Studies

Normal purified CD34$^+$ human cells were obtained from Lonza. Use of these materials is considered exempt as Human Subjects by the Dana-Farber Cancer Institute Internal Review Board. Primary patient AML blasts were collected after obtaining patient informed consent under Dana-Farber Cancer Institute Internal Review Board-approved protocols.

ACCESSION NUMBERS

The Gene Expression Omnibus (GEO) accession number for the genome-wide expression analysis reported in this paper is GSE54065.

SUPPLEMENTAL INFORMATION

Supplemental Information includes Supplemental Experimental Procedures, seven figures, and three tables and can be found with this article online at http://dx.doi.org/10.1016/j.ccr.2014.01.022.

ACKNOWLEDGMENTS

We thank Merck for providing their small-molecule inhibitor of SYK. This research was supported by grants from the National Cancer Institute (R01 CA140292), the American Cancer Society, the Starr Cancer Consortium, Project Cupid and One Mission (to K.S.), and the Swedish Research Council and Swedish Cancer Society (to L.R. and J.U.K.). A.P. is a Leukemia and Lymphoma Society (LLS) Fellow, and K.S. is an LLS Scholar.

Received: April 24, 2013
Revised: November 14, 2013
Accepted: January 22, 2014
Published: February 10, 2014

REFERENCES

Bernt, K.M., Zhu, N., Sinha, A.U., Vempati, S., Faber, J., Krivtsov, A.V., Feng, Z., Punt, N., Daigle, A., Bullinger, L., et al. (2011). MLL-rearranged leukemia is dependent on aberrant H3K79 methylation by DOT1L. Cancer Cell *20*, 66–78.

Braselmann, S., Taylor, V., Zhao, H., Wang, S., Sylvain, C., Baluom, M., Qu, K., Herlaar, E., Lau, A., Young, C., et al. (2006). R406, an orally available spleen tyrosine kinase inhibitor blocks fc receptor signaling and reduces immune complex-mediated inflammation. J. Pharmacol. Exp. Ther. *319*, 998–1008.

Daigle, S.R., Olhava, E.J., Therkelsen, C.A., Majer, C.R., Sneeringer, C.J., Song, J., Johnston, L.D., Scott, M.P., Smith, J.J., Xiao, Y., et al. (2011). Selective killing of mixed lineage leukemia cells by a potent small-molecule DOT1L inhibitor. Cancer Cell *20*, 53–65.

DeAngelo, D.J., Stone, R.M., Heaney, M.L., Nimer, S.D., Paquette, R.L., Klisovic, R.B., Caligiuri, M.A., Cooper, M.R., Lecerf, J.M., Karol, M.D., et al. (2006). Phase 1 clinical results with tandutinib (MLN518), a novel FLT3 antagonist, in patients with acute myelogenous leukemia or high-risk myelodysplastic syndrome: safety, pharmacokinetics, and pharmacodynamics. Blood *108*, 3674–3681.

Deshpande, A.J., Bradner, J., and Armstrong, S.A. (2012). Chromatin modifications as therapeutic targets in MLL-rearranged leukemia. Trends Immunol. *33*, 563–570.

Fischer, T., Stone, R.M., Deangelo, D.J., Galinsky, I., Estey, E., Lanza, C., Fox, E., Ehninger, G., Feldman, E.J., Schiller, G.J., et al. (2010). Phase IIB trial of oral Midostaurin (PKC412), the FMS-like tyrosine kinase 3 receptor (FLT3) and multi-targeted kinase inhibitor, in patients with acute myeloid leukemia and high-risk myelodysplastic syndrome with either wild-type or mutated FLT3. J. Clin. Oncol. *28*, 4339–4345.

Friedberg, J.W., Sharman, J., Sweetenham, J., Johnston, P.B., Vose, J.M., Lacasce, A., Schaefer-Cutillo, J., De Vos, S., Sinha, R., Leonard, J.P., et al. (2010). Inhibition of Syk with fostamatinib disodium has significant clinical activity in non-Hodgkin lymphoma and chronic lymphocytic leukemia. Blood *115*, 2578–2585.

Griffith, J., Black, J., Faerman, C., Swenson, L., Wynn, M., Lu, F., Lippke, J., and Saxena, K. (2004). The structural basis for autoinhibition of FLT3 by the juxtamembrane domain. Mol. Cell *13*, 169–178.

Hahn, C.K., Berchuck, J.E., Ross, K.N., Kakoza, R.M., Clauser, K., Schinzel, A.C., Ross, L., Galinsky, I., Davis, T.N., Silver, S.J., et al. (2009). Proteomic and genetic approaches identify Syk as an AML target. Cancer Cell *16*, 281–294.

Katsumi, A., Kiyoi, H., Abe, A., Tanizaki, R., Iwasaki, T., Kobayashi, M., Matsushita, T., Kaibuchi, K., Senga, T., Kojima, T., et al. (2011). FLT3/ITD regulates leukaemia cell adhesion through $\alpha4\beta1$ integrin and Pyk2 signalling. Eur. J. Haematol. *86*, 191–198.

Keshvara, L.M., Isaacson, C., Harrison, M.L., and Geahlen, R.L. (1997). Syk activation and dissociation from the B-cell antigen receptor is mediated by phosphorylation of tyrosine 130. J. Biol. Chem. *272*, 10377–10381.

Knapper, S., Burnett, A.K., Littlewood, T., Kell, W.J., Agrawal, S., Chopra, R., Clark, R., Levis, M.J., and Small, D. (2006). A phase 2 trial of the FLT3 inhibitor lestaurtinib (CEP701) as first-line treatment for older patients with acute myeloid leukemia not considered fit for intensive chemotherapy. Blood *108*, 3262–3270.

Kuno, Y., Abe, A., Emi, N., Iida, M., Yokozawa, T., Towatari, M., Tanimoto, M., and Saito, H. (2001). Constitutive kinase activation of the TEL-Syk fusion gene in myelodysplastic syndrome with t(9;12)(q22;p12). Blood *97*, 1050–1055.

Ley, T., Miller, C., Ding, L., Raphael, B., Mungall, A., Robertson, A., Hoadley, K., Triche, T.J., Laird, P., Baty, J., et al.; Cancer Genome Atlas Research Network (2013). Genomic and epigenomic landscapes of adult de novo acute myeloid leukemia. N. Engl. J. Med. *368*, 2059–2074.

Luo, H., Li, Q., O'Neal, J., Kreisel, F., Le Beau, M.M., and Tomasson, M.H. (2005). c-Myc rapidly induces acute myeloid leukemia in mice without evidence of lymphoma-associated antiapoptotic mutations. Blood *106*, 2452–2461.

Miller, P.G., Al-Shahrour, F., Hartwell, K.A., Chu, L.P., Järås, M., Puram, R.V., Puissant, A., Callahan, K.P., Ashton, J., McConkey, M.E., et al. (2013). In Vivo RNAi screening identifies a leukemia-specific dependence on integrin beta 3 signaling. Cancer Cell *24*, 45–58.

Mócsai, A., Ruland, J., and Tybulewicz, V.L. (2010). The SYK tyrosine kinase: a crucial player in diverse biological functions. Nat. Rev. Immunol. *10*, 387–402.

Moon, K.D., Post, C.B., Durden, D.L., Zhou, Q., De, P., Harrison, M.L., and Geahlen, R.L. (2005). Molecular basis for a direct interaction between the Syk protein-tyrosine kinase and phosphoinositide 3-kinase. J. Biol. Chem. *280*, 1543–1551.

Moy, L.Y., Jia, Y., Caniga, M., Lieber, G., Gil, M., Fernandez, X., Sirkowski, E., Miller, R., Alexander, J.P., Lee, H.H., et al. (2013). Inhibition of spleen tyrosine

(E and F) Kaplan-Meier curves showing overall survival of mice (n = 6) secondary transplanted with double tomato and GFP positive myeloid cells expressing *FLT3-ITD* in combination with *SYK* WT (E), or *SYK-TEL* (F) and treated with vehicle, R788 (R406 prodrug, Fostamatinib), PRT062607, AC220, or a combination of PRT062607 + AC220. Statistical significance determined by log-rank (Mantel-Cox) test. $^{\#}p < 0.02$, $^{*}p < 0.002$, and $^{**}p \leq 0.0008$ by comparison with vehicle-treated group.

(G and H) WBC count in the blood harvested from five mice per group at day 10 posttreatment (G). Proportion of double tomato and GFP positive secondary transplanted *FLT3-ITD* + *SYK-TEL* cells in spleen of five mice sacrificed at day 15 posttreatment (H). The p value was calculated using a Mann-Whitney test in comparison with vehicle condition. n.s, nonsignificant ($p > 0.05$). Error bars represent mean ± SEM.

(I) Western blot showing the levels of FLT3 and SYK phosphorylation on *FLT3-ITD* + *SYK-TEL* cells sorted from spleen of mice treated for 3 days with indicated compounds.

See also Figure S7.

kinase attenuates allergen-mediated airway constriction. Am. J. Respir. Cell Mol. Biol. *49*, 1085–1092.

Oellerich, T., Oellerich, M.F., Engelke, M., Munch, S., Mohr, S., Nimz, M., Hsiao, H.H., Corso, J., Zhang, J., Bohnenberger, H., et al. (2013). β_2 integrin-derived signals induce cell survival and proliferation of AML blasts by activating a Syk/STAT signaling axis. Blood *121*, 3889–3899.

Patel, J.P., Gönen, M., Figueroa, M.E., Fernandez, H., Sun, Z., Racevskis, J., Van Vlierberghe, P., Dolgalev, I., Thomas, S., Aminova, O., et al. (2012). Prognostic relevance of integrated genetic profiling in acute myeloid leukemia. N. Engl. J. Med. *366*, 1079–1089.

Pechloff, K., Holch, J., Ferch, U., Schweneker, M., Brunner, K., Kremer, M., Sparwasser, T., Quintanilla-Martinez, L., Zimber-Strobl, U., Streubel, B., et al. (2010). The fusion kinase ITK-SYK mimics a T cell receptor signal and drives oncogenesis in conditional mouse models of peripheral T cell lymphoma. J. Exp. Med. *207*, 1031–1044.

Pratz, K.W., Cortes, J., Roboz, G.J., Rao, N., Arowojolu, O., Stine, A., Shiotsu, Y., Shudo, A., Akinaga, S., Small, D., et al. (2009). A pharmacodynamic study of the FLT3 inhibitor KW-2449 yields insight into the basis for clinical response. Blood *113*, 3938–3946.

Sexauer, A., Perl, A., Yang, X., Borowitz, M., Gocke, C., Rajkhowa, T., Thiede, C., Frattini, M., Nybakken, G.E., Pratz, K., et al. (2012). Terminal myeloid differentiation in vivo is induced by FLT3 inhibition in FLT3/ITD AML. Blood *120*, 4205–4214.

Smith, C.C., Wang, Q., Chin, C.S., Salerno, S., Damon, L.E., Levis, M.J., Perl, A.E., Travers, K.J., Wang, S., Hunt, J.P., et al. (2012). Validation of ITD mutations in FLT3 as a therapeutic target in human acute myeloid leukaemia. Nature *485*, 260–263.

Spurgeon, S.E., Coffey, G., Fletcher, L.B., Burke, R., Tyner, J.W., Druker, B.J., Betz, A., DeGuzman, F., Pak, Y., Baker, D., et al. (2013). The selective SYK inhibitor P505-15 (PRT062607) inhibits B cell signaling and function in vitro and in vivo and augments the activity of fludarabine in chronic lymphocytic leukemia. J. Pharmacol. Exp. Ther. *344*, 378–387.

Swords, R., Freeman, C., and Giles, F. (2012). Targeting the FMS-like tyrosine kinase 3 in acute myeloid leukemia. Leukemia *26*, 2176–2185.

Umehara, H., Huang, J.Y., Kono, T., Tabassam, F.H., Okazaki, T., Gouda, S., Nagano, Y., Bloom, E.T., and Domae, N. (1998). Co-stimulation of T cells with CD2 augments TCR-CD3-mediated activation of protein tyrosine kinase p72syk, resulting in increased tyrosine phosphorylation of adapter proteins, Shc and Cbl. Int. Immunol. *10*, 833–845.

Weisberg, E., Sattler, M., Ray, A., and Griffin, J.D. (2010). Drug resistance in mutant FLT3-positive AML. Oncogene *29*, 5120–5134.

Williams, R.T., Roussel, M.F., and Sherr, C.J. (2006). Arf gene loss enhances oncogenicity and limits imatinib response in mouse models of Bcr-Abl-induced acute lymphoblastic leukemia. Proc. Natl. Acad. Sci. USA *103*, 6688–6693.

Wu, J., Meng, F., Lu, H., Kong, L., Bornmann, W., Peng, Z., Talpaz, M., and Donato, N.J. (2008). Lyn regulates BCR-ABL and Gab2 tyrosine phosphorylation and c-Cbl protein stability in imatinib-resistant chronic myelogenous leukemia cells. Blood *111*, 3821–3829.

Zuber, J., Shi, J., Wang, E., Rappaport, A.R., Herrmann, H., Sison, E.A., Magoon, D., Qi, J., Blatt, K., Wunderlich, M., et al. (2011). RNAi screen identifies Brd4 as a therapeutic target in acute myeloid leukaemia. Nature *478*, 524–528.

Cancer Cell
Article

Wild-Type H- and N-Ras Promote Mutant K-Ras-Driven Tumorigenesis by Modulating the DNA Damage Response

Elda Grabocka,[1] Yuliya Pylayeva-Gupta,[1] Mathew J.K. Jones,[2] Veronica Lubkov,[1] Eyoel Yemanaberhan,[1] Laura Taylor,[1] Hao Hsuan Jeng,[1] and Dafna Bar-Sagi[1,*]
[1]Department of Biochemistry and Molecular Pharmacology, New York University School of Medicine, New York, NY 10016, USA
[2]Molecular Biology Program, Memorial Sloan-Kettering Cancer Center, New York, NY 10065, USA
*Correspondence: dafna.bar-sagi@nyumc.org
http://dx.doi.org/10.1016/j.ccr.2014.01.005

SUMMARY

Mutations in *KRAS* are prevalent in human cancers and universally predictive of resistance to anticancer therapeutics. Although it is widely accepted that acquisition of an activating mutation endows *RAS* genes with functional autonomy, recent studies suggest that the wild-type forms of Ras may contribute to mutant Ras-driven tumorigenesis. Here, we show that downregulation of wild-type H-Ras or N-Ras in mutant K-Ras cancer cells leads to hyperactivation of the Erk/p90RSK and PI3K/Akt pathways and, consequently, the phosphorylation of Chk1 at an inhibitory site, Ser 280. The resulting inhibition of ATR/Chk1 signaling abrogates the activation of the G2 DNA damage checkpoint and confers specific sensitization of mutant K-Ras cancer cells to DNA damage chemotherapeutic agents in vitro and in vivo.

INTRODUCTION

Three closely related *RAS* oncogenes, *HRAS*, *NRAS*, and *KRAS*, have been identified in mammals. These genes encode small GTPases that function as molecular switches governing the activation of a vast network of signaling pathways. Growth factor signaling activates Ras by recruiting guanine nucleotide exchange factors (GEFs) that catalyze the exchange of guanosine diphosphate (GDP) for guanosine triphosphate (GTP) (Bos et al., 2007). In turn, Ras activity is terminated through GTP hydrolysis, which is greatly enhanced by GTPase-accelerating proteins (GAPs). Hyperactivation of Ras, which largely occurs through the acquisition of mutations that hinder GTP hydrolysis, has been implicated in the etiology of a wide number of human cancers. Overall, mutations in the *RAS* genes have been associated with ~30% of all human tumors. Such mutations are generally limited to one of the *RAS* genes, with *KRAS* being the most frequently mutated and with the highest incidence in adenocarcinomas of the pancreas (57%), colon (33%), and lung (17%) (Pylayeva-Gupta et al., 2011).

The critical role of oncogenic K-Ras as a driving mutation in the pathogenesis of cancer is supported by several genetically engineered mouse models. Accordingly, expression of mutant K-Ras alone is sufficient to drive malignant progression, whereas elimination of mutant K-Ras from established tumors leads to tumor regression (Chin et al., 1999; Fisher et al., 2001; Haigis et al., 2008; Jackson et al., 2001; Li et al., 2011; Ying et al., 2012). Because of its capacity to constitutively engage downstream effector pathways, oncogenic K-Ras was initially thought to drive the tumorigenic process independently of the wild-type forms. However, it is becoming increasingly evident that the biological outputs of oncogenic K-Ras are subject to a complex and context-dependent modulation by wild-type Ras proteins. Studies in chemically induced models of lung or skin tumorigenesis have demonstrated that the acquisition of an activating mutation in a *KRas* or *HRas* allele is associated with loss of the *KRas* wild-type or *HRas* wild-type allele, respectively (Bremner and Balmain, 1990; Hegi et al., 1994; Zhang et al., 2001). Zhang et al. (2001) further demonstrated that loss of the wild-type *KRas* allele enhanced mutant K-Ras-driven tumorigenesis. Together, these results suggest a tumor suppressive effect of

Significance

This study defines a functional dependence of K-Ras-driven tumors on wild-type H- and N-Ras for the DNA damage response and reveals a promising therapeutic strategy for the treatment of mutant K-Ras tumors. We demonstrate that mutant K-Ras cancer cells require wild-type H-Ras and N-Ras for the activation of the ATR-Chk1-mediated DNA damage checkpoint and that this dependence can be exploited to specifically sensitize K-Ras-driven cancers to DNA damage-inducing agents.

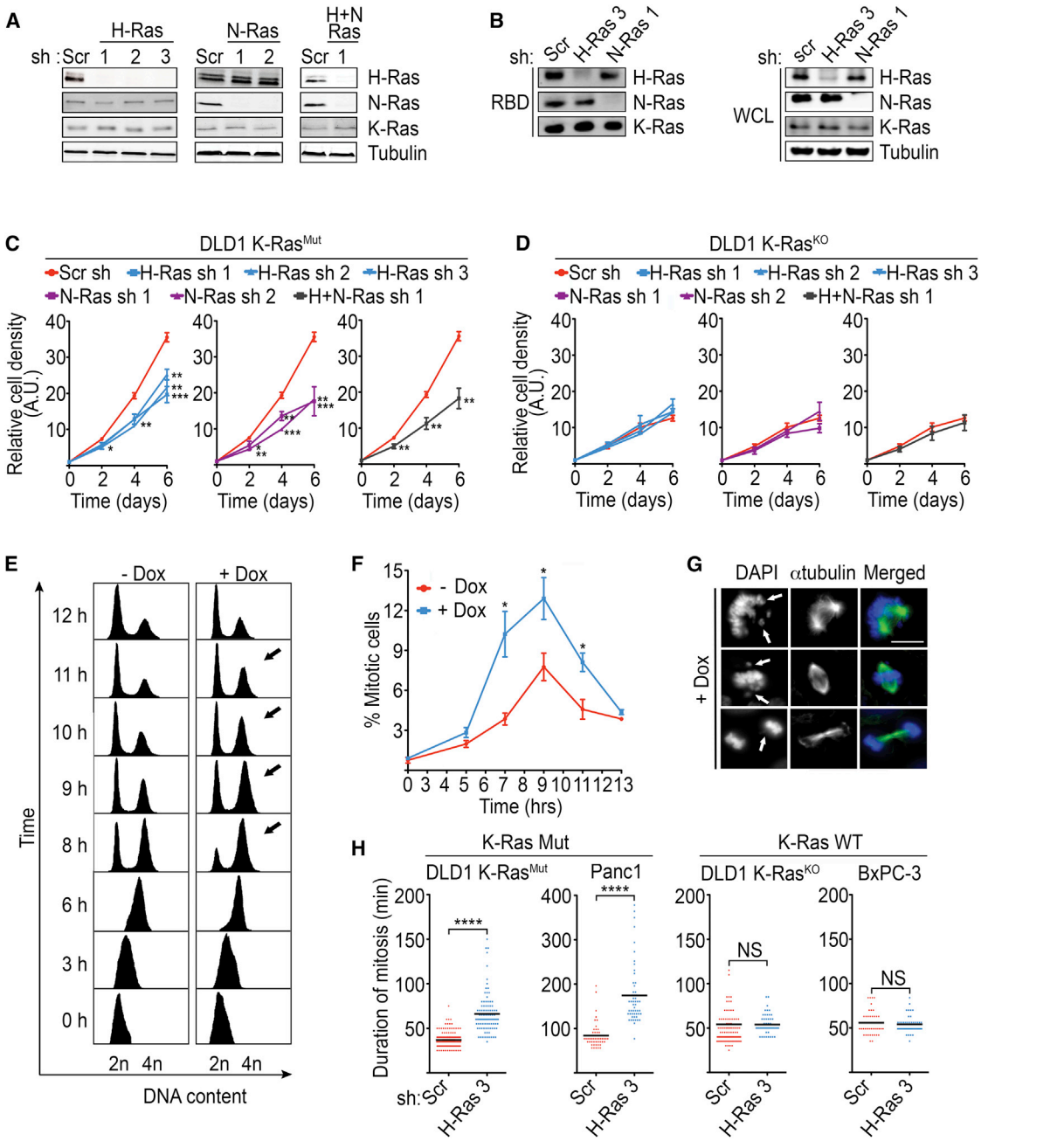

Figure 1. WT-H-Ras Knockdown Perturbs the Mitotic Progression of K-Ras Mutant Cancer Cells

(A) Isoform-specific knockdown of WT-H-Ras, WT-N-Ras, or WT-H- and N-Ras combined. DLD1 K-Ras^{Mut} cells that harbor doxycycline-inducible shRNAs directed at H-Ras (H-Ras sh 1, 2, 3), N-Ras (N-Ras sh 1, 2), H-Ras and N-Ras combined (H-Ras sh 1 and N-Ras sh 1), or scramble shRNA (Scr sh) were treated with doxycycline for 96 hr. Whole-cell lysates (WCL) were immunoblotted for H-Ras, N-Ras, K-Ras, and tubulin (loading control).

(B) Effect of WT-H-Ras or WT-N-Ras suppression on the GTP-bound status of the remaining Ras isoforms. WCLs were subjected to GST-bound CRAF Ras-binding domain (RBD) pull-downs and immunoblotted with the indicated antibodies.

(C and D) Effect of suppression of WT-H-Ras, WT-N-Ras, or WT-H- and N-Ras combined on the proliferation of DLD1 K-Ras^{Mut} cells (C) and DLD1 K-Ras^{KO} cells (D). The relative cell density was measured using a Syto60 stain and is expressed in arbitrary units (a.u.).

(E) Representative FACS histograms showing cell-cycle progression of synchronized control (−Dox) and H-Ras-suppressed (+Dox) DLD1 K-Ras^{Mut} cells that harbor inducible H-Ras sh 3. Cells were released from a double thymidine block, fixed at the indicated time points, and FACS sorted for DNA content. Arrows indicate the G2/M fraction at relevant time points. Data are representative of at least three independent experiments.

(F) Detection of mitotic fraction by FACS analysis of phosphorylated histone H3 (P-HH3)-positive cells in double-thymidine-release experiments as in (E).

(G) Representative images of mitotic aberrations (arrows) seen in WT-H-Ras-depleted DLD1 K-Ras^{Mut} cells following a double-thymidine-release experiment as in (E). Immunofluorescence images of cells stained for α-tubulin and DNA. Scale bar, 10 μm.

(legend continued on next page)

the wild-type *Ras* allele. Conversely, a recent study reported that in mutant K-Ras-driven colorectal cancer, wild-type K-Ras plays a tumor promoting role through counteracting mutant K-Ras-induced apoptosis by mediating signaling from mutant K-Ras-dependent autocrine-activated EGFR (Matallanas et al., 2011).

Mutant K-Ras-driven cancers also retain the wild-type products of the remaining *RAS* genes, *H-* and *NRAS*, which appear to synergize with mutant K-Ras in tumors of various tissues. For example, enhanced levels of GTP-bound H-Ras and N-Ras, due to mutant K-Ras-dependent nitrosylation of wild-type H- and N-Ras, were shown to be required for the proliferation of mutant K-Ras cancer cells (Lim et al., 2008). A role for wild-type H-Ras and N-Ras proteins in mediating RTK signaling and proliferation of cancer cells that harbor mutant K-Ras has also been demonstrated (Young et al., 2012). Moreover, Son of Sevenless (Sos), a guanine nucleotide exchange factor (GEF) for Ras and Rho GTPases, has been implicated in mutant Ras-driven tumorigenesis (Jeng et al., 2012).

In the current study, we sought to determine the mechanisms by which wild-type H-Ras and N-Ras proteins promote the mutant K-Ras-driven tumorigenic phenotype.

RESULTS

Mutant K-Ras Cancer Cells Require Wild-Type H-Ras for Proliferation and Progression through Mitosis

To investigate the functional relationship between mutant K-Ras and wild-type (WT) H/N-Ras, we took the approach of specifically suppressing the expression of WT-H-Ras and/or WT-N-Ras, in cancer cells positive or negative for mutant K-Ras. To this end, we initially employed the isogenic colon cancer cells DLD-1 K-Ras$^{WT/G12D}$ (DLD1 K-Ras^{Mut}) and DLD1 K-Ras$^{WT/-}$ (DLD1 K-Ras^{KO}), where the *K-RAS*^{G12D} allele has been knocked out by homologous recombination (Luo et al., 2009b; Shirasawa et al., 1993). These cell lines were engineered to harbor doxycycline (Dox)-inducible small hairpin RNAs (shRNAs) directed at H-Ras, N-Ras, or both H- and N-Ras. Accordingly, doxycycline treatment specifically suppressed expression and activity of the targeted isoforms, with no effect on the remaining isoforms (Figures 1A and 1B; Figure S1A available online). As shown in Figure 1C, individual knockdown of WT-H-Ras or WT-N-Ras in DLD1 K-Ras^{Mut} cells led to slower growth. Of note, no synergy was observed upon knockdown of both WT-H-Ras and WT-N-Ras, suggesting that the two WT-isoforms converge on the same signaling module that regulates growth of DLD1 K-Ras^{Mut} cells (Figure 1C). In contrast, knockdown of either WT-H-Ras or WT-N-Ras, or the two combined, in DLD1 K-Ras^{KO} cells, had no effect on cell growth, indicating that the dependence on WT-H- and/or N-Ras for cell growth is a specific property of mutant K-Ras cancer cells (Figures 1D and S1A).

We next investigated whether the attenuated cell growth observed upon WT-H-Ras and/or N-Ras knockdown in DLD1 K-Ras^{Mut} cells could be the result of a slower progression through the cell cycle. Initially, we examined the cell-cycle progression of WT-H-Ras-suppressed DLD1 K-Ras^{Mut} cells that were synchronized at the G1/S border by double thymidine treatment. Six hours after release, both WT-H-Ras-suppressed (+Dox) and WT-H-Ras-intact (−Dox) DLD1 K-Ras^{Mut} cells had completed replication and were predominantly in G2 as determined by the accumulation of cells with 4N DNA content (Figures 1E, 1F, and S1B). However, whereas the majority of WT-H-Ras-intact cells completed mitosis and cell division and reached G1 over the next 4 hr, WT-H-Ras-suppressed cells showed a delayed transition through G2/M, as evident by the persistence of cells with 4N DNA content (Figure 1E, arrows). Fluorescence-activated cell sorting (FACS) analysis of phosphohistone H3-positive cells revealed an increased mitotic index of WT-H-Ras-suppressed cells relative to control (7–11 hr), suggesting that the elevated fraction of 4N DNA content cells associated with WT-H-Ras knockdown was due to a mitotic delay (Figures 1E and 1F). Consistent with this interpretation, WT-H-Ras-suppressed DLD1 K-Ras^{Mut} cells showed mitotic defects that would preclude the timely satisfaction of the spindle checkpoint, including misaligned and damaged chromosomes (Figure 1G). To quantitatively measure the mitotic delay within individual cells and rule out the possibility that the observed mitotic aberrations were due to the synchronization technique, we analyzed the duration of mitosis in asynchronous cells by time-lapse phase-contrast microscopy. We observed that WT-H-Ras knockdown delayed mitotic progression in DLD1 K-Ras^{Mut} cells (duration of mitosis was ~2 times longer compared to control), but not in DLD1 K-Ras^{KO} cells (Figures 1H, S1C, and S1D). Similar results were obtained when this analysis was extended to the pancreatic cell line pair Panc-1 (K-Ras mutant) and BxPC-3 (K-Ras WT) (Figure 1H; Movies S1 and S2; Figures S1C and S1D). Taken together, these data indicate that K-Ras mutant cells specifically require WT-H-Ras for the timely progression of mitosis.

Wild-Type H- and N-Ras Knockdown Enhance DNA Damage in Mutant K-Ras Cancer Cells

In principle, the delay in mitosis and damaged chromosomes, induced by WT-H-Ras knockdown, can be explained by misregulation of the DNA damage response (DDR) (Rieder and Maiato, 2004; Brown and Baltimore, 2000; Lam et al., 2004; Löffler et al., 2006; Zachos and Gillespie, 2007). A defective DDR would compromise the ability of the cell to repair DNA damage, thereby leading to an enhancement in the levels of DNA strand breaks (Syljuåsen et al., 2005; Toledo et al., 2011b). Evaluation of DNA strand breaks by monitoring γH2AX staining revealed a significant accumulation of γH2AX-positive cells upon knockdown of WT-H-Ras in the DLD1-K-Ras^{Mut} cells and a panel of K-Ras mutant (Mut) pancreatic cancer cells (Panc-1, AsPC-1, PL45, and MIA PaCa-2) (Figures 2A–2C). In contrast, γH2AX levels remain unaltered when WT-H-Ras was knocked down in the DLD1-K-Ras^{KO} and K-Ras WT pancreatic cancer cell lines (BxPC-3 and Hs-700T), consistent with K-Ras Mut cancer cells

(H) Scatter plots show the duration of mitosis, as determined by phase-contrast time-lapse microscopy, in asynchronous K-Ras Mut (DLD1 K-Ras^{Mut} cells and Panc-1) and K-Ras WT (DLD1 K-Ras^{KO} and BxPC-3) cancer cells expressing scramble or H-Ras shRNAs. ****$p < 0.0001$ by Student's t test; NS, no significant difference.

All experiments: error bars, mean ± SEM, n = 3, *$p < 0.05$, **$p < 0.005$, ***$p < 0.0005$. See also Movies S1 and S2 and Figure S1.

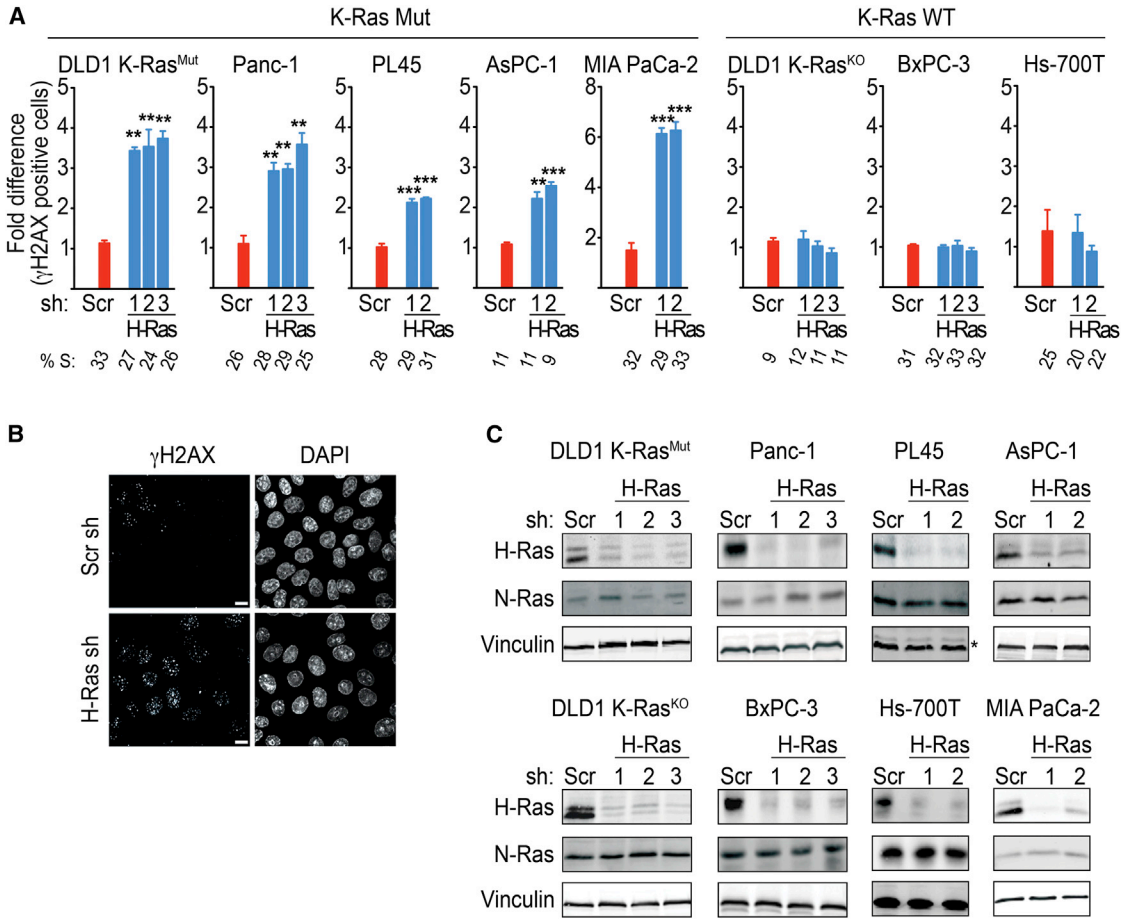

Figure 2. WT-H-Ras Knockdown Enhances DNA Damage in K-Ras Mut, but Not in K-Ras WT, Cancer Cells

(A) Quantification of γH2AX-positive cells in K-Ras Mut and K-Ras WT cancer cells upon WT-H-Ras knockdown. K-Ras Mut and K-Ras WT cells from cancers of the colon (DLD1) and pancreas (Panc-1, AsPC-1, PL45, MIA PaCa-2, BxPC-3, and Hs-700T), depleted of WT-H-Ras, were costained for γH2AX and DAPI, and the percentage of cells positive for γH2AX foci (>10 per cell) was determined. At least 500 cells were scored per condition. Data are presented relative to the values obtained for scramble shRNA cells in each cell line, respectively. Error bars, mean ± SEM, n = 3, $^{**}p < 0.005$, $^{***}p < 0.0005$. S-phase percentages as determined by flow cytometry analysis of the percentage of BrdU-incorporating cells are indicated below the bar graphs.

(B) Representative images showing γH2AX levels in WT-H-Ras-suppressed DLD1 K-Ras^{Mut} cells. Cells were costained for γH2AX and DAPI. Scale bars, 5 μm.

(C) Isoform-specific knockdown of H-Ras in the cancer cells lines shown in (A). * indicates Erk2 as a loading control instead of vinculin.

See also Figure S2.

being selectively dependent on WT-H-Ras for modulating DNA damage and cell-cycle progression (Figures 2A–2C). A similar dependency was observed upon knockdown of WT-N-Ras, and no synergistic effect was observed when both WT-H-Ras and WT-N-Ras were knocked down (Figures S2A–S2C). The elevated γH2AX levels were not due to an accumulation of cells in S-phase because there was no significant difference in the S-phase profiles between control and WT-H-Ras, WT-N-Ras, or WT-H- and N-Ras-suppressed cells (Figures 2A and S2B). Of note, we have observed no correlation between enhanced γH2AX levels due to WT-H- and/or N-Ras knockdown and the proliferative rate or basal γH2AX levels of the cancer cells analyzed (Figure S1D; data not shown). This suggests that the elevated DNA damage induced by WT-H- and/or N-Ras knockdown is not due to a faster proliferation rate or higher basal DNA damage of K-Ras mutant cells but instead is a consequence of a perturbed DDR. Moreover, knockdown of WT-H-Ras in melanoma cells that harbor an activating N-Ras mutation (NRas Q61L) also enhanced γH2AX levels, indicating that WT-Ras could be required for the regulation of the basal levels of DNA damage in cancer cells with activating mutations in any of the Ras isoforms (Figure S2E).

Dependence of Mutant K-Ras Cancer Cells on Wild-Type H- and N-Ras for the Activation of the G2 DNA Damage Checkpoint

To directly evaluate whether WT-H-Ras knockdown impacted the activation of the DNA damage checkpoint, we subjected K-Ras Mut cells to UV-C irradiation and monitored mitotic entry at 1, 2, and 3 hr intervals after UV-C-induced damage. Panc-1 and DLD1-K-Ras^{Mut} cells expressing scramble shRNA displayed a block in mitotic entry in response to UV-C-induced DNA damage, indicating a functional G2 DNA damage checkpoint (Figures 3A, 3B, and S3A). In contrast, progression into mitosis following

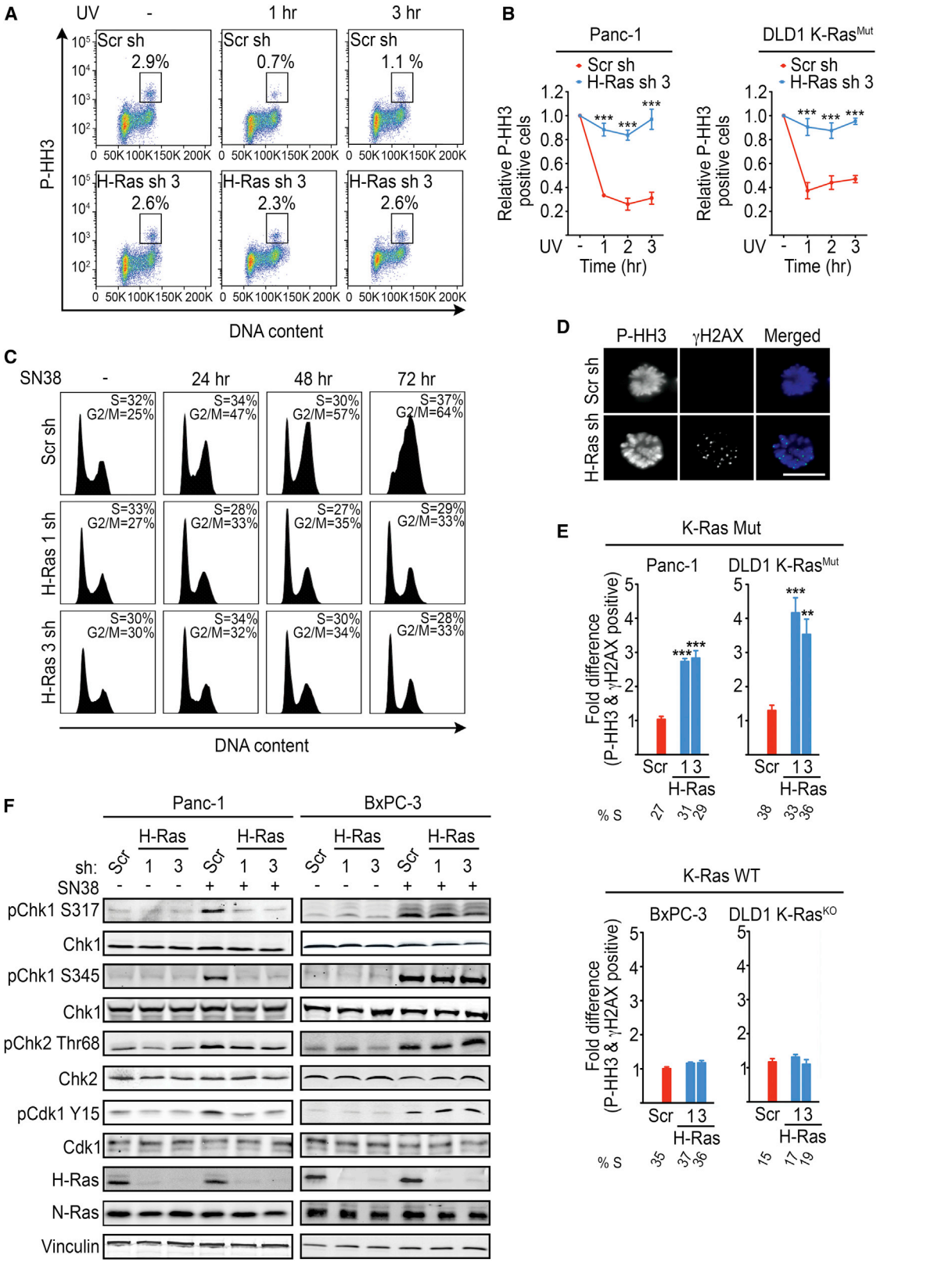

(legend on next page)

UV-C treatment was unperturbed in Panc-1 and DLD1-K-Ras^{Mut} cells depleted of WT-H-Ras, indicating a defective G2 DNA damage checkpoint (Figures 3A and 3B). This defect was not specific to UV-C-induced damage as Panc-1 (Figure 3C) and DLD1-K-Ras^{Mut} cells (Figure S3B) depleted of WT-H-Ras failed to initiate and maintain cell-cycle arrest in response to the topoisomerase I inhibitor SN38. A similar defect was observed in Panc-1 cells depleted of WT-N-Ras (Figure S3C).

A predictable outcome of a defective G2 DNA damage checkpoint is entry into mitosis with unresolved DNA breaks following damage (Jiang et al., 2009). In agreement with this prediction, a significant fraction of WT-H- and/or N-Ras-depleted Panc-1 and DLD1-K-Ras^{Mut} cancer cells that entered mitosis following UV-C exposure also stained positive for γH2AX (Figures 3D, 3E, and S3D). Notably, no such differences were observed in K-Ras WT cancer cell lines (Figures 3E and S3D). These data demonstrate that WT-H- and/or N-Ras are critical for the establishment of a functional G2 DNA damage checkpoint selectively in K-Ras Mut cancer cells.

Wild-Type H- and N-Ras Knockdown Impairs Chk1 Activation in K-Ras Mutant Cancer Cells

To gain insight into the molecular basis for the perturbation of the G2 DNA damage checkpoint by WT-H/N-Ras knockdown, we examined the DNA-damage-specific activation of ATR/Chk1 and ATM/Chk2 in response to SN38 or UV-C treatment (Bartek and Lukas, 2003; Zhou and Elledge, 2000). Notably, WT-H-Ras knockdown was accompanied by a defective Chk1 activation in response to either SN38 or UV-C treatment in K-Ras Mut cell lines Panc-1 and DLD1-K-Ras^{Mut} (Figures 3F, S3E, and S3F), and MIA PaCa-2 (Figure S4A) as evidenced by impaired phosphorylation of Chk1 at Ser 317 and Ser 345. The requirement for WT H-Ras for ATR/Chk1 activation was a specific property of K-Ras mutant cells as WT-H-Ras knockdown had no effect on Chk1 activation in the K-Ras WT cell lines BxPC-3 and DLD1-K-Ras^{KO} (Figures 3F, S3E, and S3F). The defect in Chk1 activation upon WT H-Ras knockdown in K-Ras mutant cells was also reflected in the impaired inhibitory phosphorylation of Cdk1 at Tyr 15 (Figures 3F and S3E). By comparison, Chk2 activation, as monitored by phosphorylation of Chk2 at threonine 68 (Thr68), was not affected by WT-H-Ras knockdown in either K-Ras Mut (Panc-1) or K-Ras WT (BxPC-3) cancer cell lines (Figures 3F and S3E). Of note, Chk2 protein levels in DLD1 cells were too low to reliably measure its activation status. WT-N-Ras knockdown also led to a selective and similar impairment of ATR/Chk1 activation in K-Ras mutant cells (Figure 4). Taken together, these results indicate that the defective G2 DNA damage checkpoint caused by WT-H/N-Ras knockdown in K-Ras mutant cells is due to the failure to properly activate Chk1.

Wild-Type H- and N-Ras Negatively Regulate MAPK and Akt Signaling to Control Chk1 Phosphorylation

The Ras effector signaling pathways, Raf/Erk and PI3K/Akt, have been shown to play a key role in Chk1 activation and the G2/M phase of the cell cycle. PI3K/Akt was reported to override DNA-damage-induced G2 arrest through repression of Chk1 activation via Akt-mediated inhibitory phosphorylation of Chk1 at Ser 280 (King et al., 2004; Puc and Parsons, 2005; Shtivelman et al., 2002). More recently, the Raf/MAPK pathway has been shown to impair Chk1 activity through Chk1 Ser 280 phosphorylation by MAPK-activated protein kinase RSK (p90 ribosomal S6 kinase) (Li et al., 2012; Ray-David et al., 2012). As wild-type Ras proteins have been reported to antagonize Ras effector signaling output in cancer cells that harbor mutant Ras (Young et al., 2012), we next investigated whether impaired Chk1 activation upon WT-H- or N-Ras knockdown was due to enhanced activation of Ras effector pathways. Knockdown of WT-H- or N-Ras in mutant K-Ras cancer cells was associated with elevated Erk/p90RSK and Akt activation, which correlated with enhanced inhibitory phosphorylation of Chk1 at Ser 280, both in the basal state and following SN38-induced DNA damage (Figures 4A and 4B). Conversely, suppression of Erk or Akt signaling via treatment with MAPK or Akt inhibitors overturned the hyperphosphorylation of Chk1 at Ser 280 in WT-H- or N-Ras-depleted mutant K-Ras cancer cells. Importantly, under these conditions, the activation of Chk1 in response to SN38-induced DNA damage was restored as shown by Chk1 Ser 317 phosphorylation (Figure 4C). Altogether, these results support a model whereby in K-Ras mutant cells, the downregulation WT-H/N-Ras leads to the enhancement of Erk/p90RSK and Akt signaling, which in turn represses Chk1 activation through Chk1 Ser 280 phosphorylation.

To rule out the possibility that WT-H/N-Ras may also specifically prevent Chk1 Ser 280 phosphorylation, we generated an isogenic derivative of the DLD1-K-Ras^{Mut} cell line that can

Figure 3. K-Ras Mutant Cancer Cells Selectively Depend on WT-H-Ras for the Activation of the ATR-Chk1-Mediated G2 DNA Damage Checkpoint

(A) Representative FACS plots showing the P-HH3-positive population in untreated ($^-$) and ($^+$) UV-C treated (at 1 and 3 hr posttreatment) Panc-1 cells expressing scramble (Scr) or WT-H-Ras shRNA (n = 3). The boxed area represents the % P-HH3-positive cells.

(B) Quantifications of the experiments described in (A) for K-Ras Mut cell lines. Data are presented as relative to the values obtained for the respective (scramble or WT-H-Ras shRNA) untreated cells.

(C) FACS histograms showing the cell-cycle profile of WT-H-Ras-suppressed Panc-1 cells following SN38 (4 nM) treatment. The S and G2/M fractions are indicated. Data are representative of three independent experiments.

(D and E) K-Ras Mut and K-Ras WT cancer cells expressing the indicated shRNAs were treated with UV-C, placed in nocodazole containing media for 4 hr to trap mitotic cells, and costained for P-HH3 (blue) and γH2AX (green). Representative immunofluorescence images of mitotic DLD1 K-Ras^{Mut} cells treated as indicated are shown in (D). Scale bar, 10 μm. Quantifications of the fraction of mitotic cells (P-HH3) expressing the indicated shRNAs that are positive for γH2AX foci (>10 per cell) are shown in (E). Data are presented as relative to the values obtained for the scramble shRNA (Scr sh) cells. At least 50 mitotic cells were analyzed per experiment. S-phase percentages are indicated below the bar graphs.

(F) Representative immunoblots for the indicated proteins in mock or SN38 treated (4 nM SN38 for 2 hr) Panc-1 (K-Ras Mut) and BxPC-3 (K-Ras WT) cancer cells are shown.

All experiments: error bars, mean ± SEM, n = 3, $^{**}p < 0.005$, $^{***}p < 0.0005$. See also Figure S3.

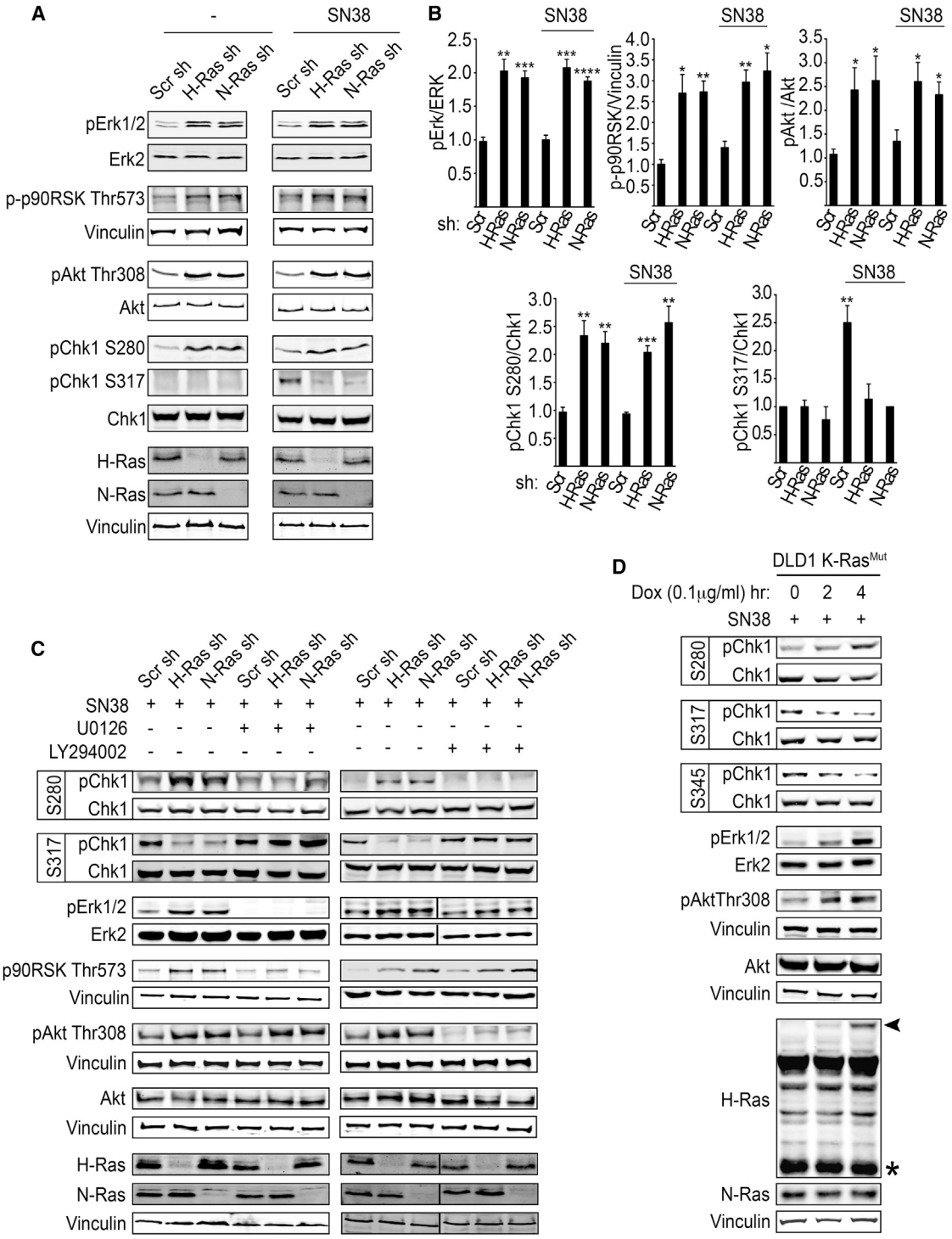

Figure 4. WT-H- and N-Ras Knockdown Enhances Erk/p90RSK and PI3K/Akt Activation to Promote Phosphorylation of Chk1 at Ser 280 and Inhibit its Activity

(A) Activation status of Erk, p90RSK, Akt, and Chk1 in WT-H/N-Ras-suppressed Panc-1 cells in the basal state or upon SN38-induced damage (8 nM SN38 for 2 hr).

(B) The fold change in the amount of pErk1/2, p-p90RSK Thr573, pAkt Thr308, pChk1 S280, and pChk1 S317 in WT-H/N-Ras shRNA as compared to scramble shRNA-expressing cells is indicated. Quantification of pErk1/2, pAkt Thr308, pChk1 S280, pChk1 S317, and p-p90RSK Thr573 was carried out by densitometry scanning and normalized to the total levels of Erk, Akt, and Chk1, respectively, and vinculin for p-p90RSK Thr573. Error bars, mean ± SD, n = 3, *p < 0.05, **p < 0.005, ***p < 0.0005, ****p < 0.00005.

(legend continued on next page)

inducibly express GFP-H-RasG12V upon doxycycline administration (DLD1-K-Ras^{Mut} Flip-IN TREX GFP-H-RasV12) (Girdler et al., 2006). As illustrated in Figure 4D, expression of GFP-H-RasG12V at sub-endogenous levels led to a concomitant increase in Erk and AKT signaling despite the presence of WT-H/N-Ras in these cells. Moreover, this was accompanied by the phosphorylation of Chk1 at the inhibitory site Ser 280 and an impairment of Chk1 phosphorylation at the activation sites Ser 317 and Ser 345 (Figure 4D). Altogether, our data are consistent with a model in which the enhanced phosphorylation of Chk1 at Ser 280 and inhibition of Chk1 activity observed under conditions of WT-H-Ras deficiency in mutant K-Ras cells is a consequence of an increase in Erk/Akt signaling.

If the activation of Chk1 is directly linked to the presence of mutant K-Ras, then the acute expression of mutant K-Ras in an otherwise K-Ras wild-type cancer cell line should render Chk1 activation in these cells dependent on WT-H/N-Ras. To test this idea, we silenced WT-H-Ras in BxPC-3 cells (K-Ras WT) that had been engineered to inducibly express K-RasG12V (BxPC-3 K-RasV12) (Figure S4C). Whereas, knockdown of WT-H-Ras in the parental BxPC-3 cell line had no effect on Chk1 Ser 280 phosphorylation and Chk1 activation (Figures 3F and S4B), knockdown of WT-H-Ras in BxPC-3 cells induced to express K-RasG12V led to elevated Erk activation, induction of Chk1 Ser 280 phosphorylation, and impairment of Chk1 phosphorylation at Ser 317 (Figure S4D). These results suggest that the hyperactivation of Erk/Akt pathways, the enhancement of Chk1 Ser 280 phosphorylation, and the impairment of Chk1 activation induced by WT-H-Ras knockdown represent a set of responses that are specifically dictated by the mutational status of K-Ras.

Mutant K-Ras Cancer Cells Depleted of Wild-Type H- and N-Ras Are Highly Sensitive to DNA Damage-Inducing Agents

The underlying premise for the therapeutic use of DNA-damaging agents is that susceptibility of cancer cells is linked to the lack of G1/S and G2 checkpoints (Ma et al., 2011; Zhou and Bartek, 2004). Therefore, we reasoned that the abrogation of the ATR/Chk1-induced DNA damage checkpoint in K-Ras mutant cells by WT-H- and/or N-Ras knockdown could enhance the therapeutic efficacy of DNA damaging agents. Assessment of cell viability following treatment with SN38 indicated that the K-Ras mutant cells DLD1 K-Ras^{Mut} and Panc-1-expressing shRNAs targeting H-Ras were on average ~90-fold and ~50-fold more sensitive to SN38, respectively, as compared to DLD1 K-Ras^{Mut} and Panc-1 cells expressing scramble shRNA (Figure 5A). Similarly, WT-H-Ras knockdown sensitized these cells (~13-fold for DLD1 K-Ras^{Mut} and ~25-fold for Panc-1) to the DNA intrastrand crosslinker oxaliplatin (Figure 5B). Notably, knockdown of WT-H-Ras or N-Ras in K-Ras WT cancer cells did not lead to a sensitization to SN38 or oxaliplatin treatment (Figures 5A and 5B). Analysis of the apoptotic index, as measured by FACS detection of cleaved caspase 3-positive cells, demonstrates an exacerbation of cell death by WT-H-Ras knockdown in response to SN38 treatment (Figures 5C and 5D). Knockdown of WT-N-Ras also sensitized these cells to SN38 and oxaliplatin (Figure S5). Together, these results show that WT-H-Ras or N-Ras knockdown specifically sensitizes K-Ras Mut cancer cells to DNA damaging agents. A similar sensitization pattern was observed upon the treatment of cells with the Chk1/Chk2 inhibitor AZD7726 (Figures 6A, 6B, and S6), supporting the hypothesis that WT-H/N-Ras downregulation selectively sensitizes K-Ras mutant cells to DNA damage-inducing agents by abrogating Chk1 activity.

Knockdown of Wild-Type H-Ras Sensitizes K-Ras Mutant Tumors to DNA Damage-Inducing Chemotherapy and Leads to Tumor Regression

To test the in vivo effects of WT-H-Ras knockdown on the sensitivity of K-Ras mutant tumors to DNA damaging agents, we established xenografts of DLD1-K-Ras mutant cells that inducibly express WT-H-Ras shRNA upon exposure to doxycycline in athymic nu/nu mice. Administration of doxycycline or vehicle was initiated after tumors had reached ~100 mm^3. Seven days postinduction (tumor size ~250 mm^3), efficient knockdown of WT-H-Ras was confirmed in the established tumors, and treatment with irinotecan (CPT), a topoisomerase I inhibitor that is FDA-approved for the treatment of colorectal cancer, was initiated (Figure S7A). In the absence of treatment with irinotecan, tumors arising from the WT-H-Ras-suppressed cells grew similarly to those arising from uninduced control cells (Figures 7A and 7B). Thus, distinct from our in vitro studies, WT-H-Ras knockdown in vivo was not associated with any delay in growth or mitotic progression under these conditions (Figures 7A, 7D, and 7E). However, similar to our observations in the synchronization studies, we did note an elevation in aberrant mitotic figures (chromosome misalignment and lagging chromosomes), which is an indication of perturbed mitosis (Figure 1G; data not shown). Hence, the lack of a higher mitotic index despite aberrant mitosis may reflect clearance of the aberrant mitotic cells in the in vivo setting. In agreement with previously reported studies, treatment with irinotecan alone resulted in a reduction of tumor growth (Figures 7A and 7B) (Harris et al., 2005; Zabludoff et al., 2008). Notably, 5 days following the termination of irinotecan administration, WT-H-Ras-suppressed tumors had undergone regression, which was maintained for the duration of the study, up to 18 days posttreatment (Figures 7A and 7B). In contrast, the control irinotecan-treated tumors showed in large part a modest growth over the same time period (Figure S7B). Consistent

(C) Panc-1 cells expressing the indicated shRNAs were treated with 8 nM SN38 for 2 hr and in the presence or absence of the MAPK inhibitor (U0126, 10 μM) or the PI3K inhibitor (LY294002, 5 μM). WCLs were analyzed to determine ERK/p90RSK or Akt inhibition and their respective effect on Chk1 phosphorylation and activation status.

(D) Isogenic derivatives of DLD1 K-Ras^{Mut} cells engineered to inducibly express GFP-H-RasG12V (DLD1 K-Ras^{Mut} Flp-IN TREX GFP-H-RasV12) upon addition of doxycycline were induced for 0, 2, or 4 hr and subjected to SN38 (8 nM) for 2 hr (for the 2 hr Dox induction, Dox and SN38 were added simultaneously; for the 4 hr Dox induction, SN38 was added 2 hr postinduction and the cells were incubated for an additional 2 hr). Representative immunoblots for the indicated proteins are shown. Arrowhead indicates GFP-H-RasG12V, and * indicates endogenous H-Ras.

See also Figure S4.

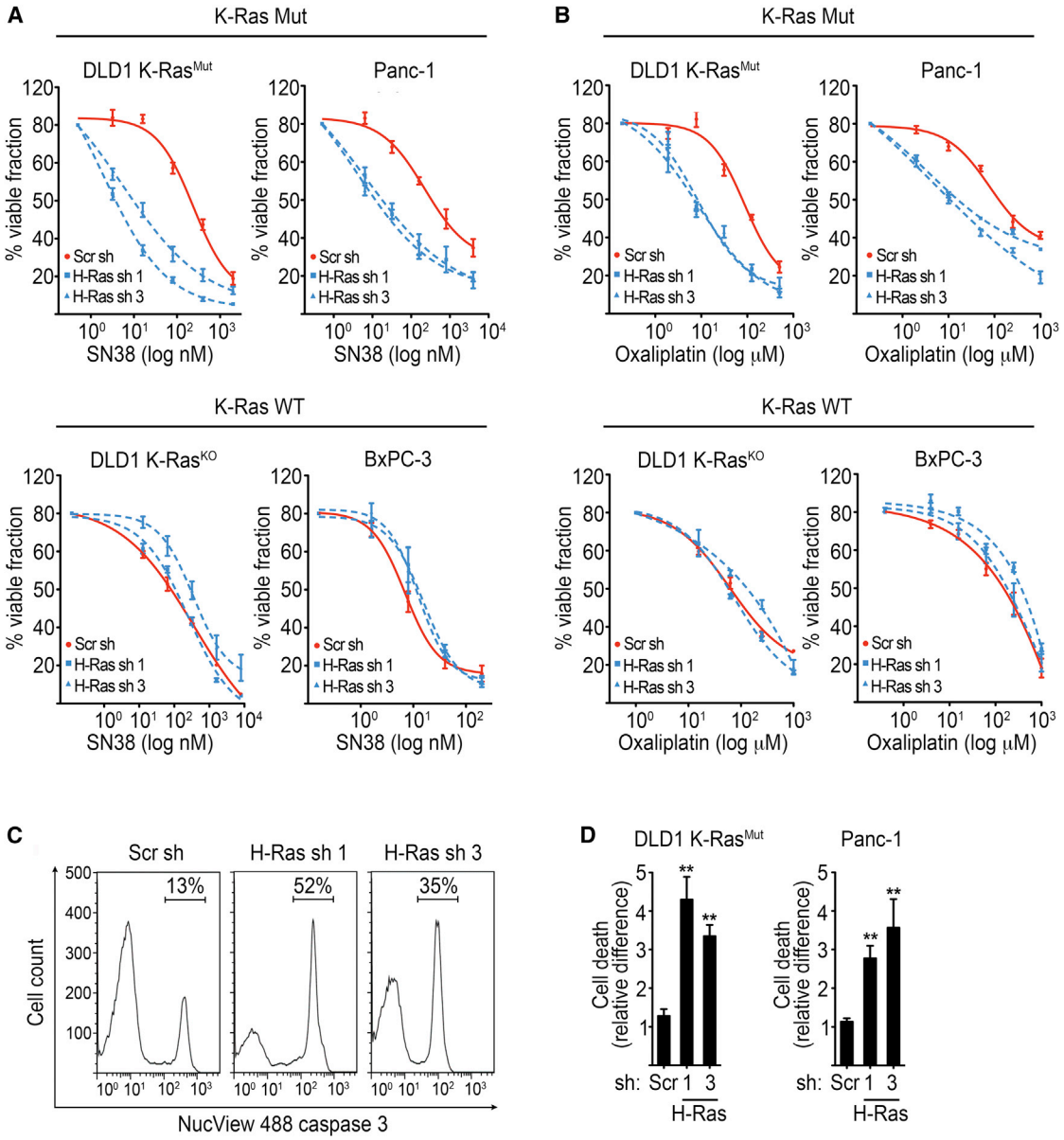

Figure 5. Knockdown of WT-H-Ras Selectively Sensitizes Mutant K-Ras Cancer Cells to DNA Damage

(A and B) MTT cell viability assays of K-Ras Mut cancer cells (DLD1 K-Ras^{Mut} and Panc-1) and K-Ras WT cancer cells (DLD1 K-Ras^{KO} and BxPC-3) induced to express scramble or WT-H-Ras shRNAs, and following a 72 hr treatment with SN38 (A) or oxaliplatin (B). Viable fraction is expressed as a percentage of the viability values obtained for the respective untreated conditions. $p < 0.005$ for H-Ras sh 1 or H-Ras sh 3 plus SN38 or oxaliplatin versus Scr sh plus SN38 or oxaliplatin in K-Ras mutant cells, respectively.

(C) Detection of cell death by FACS analysis of the Nucview Alexa-488 caspase 3-positive population in SN38-treated K-Ras Mut cells. Representative profiles of Nucview Alexa-488 caspase 3 fractions in DLD1 K-Ras^{Mut} cells inducibly expressing scramble or WT-H-Ras shRNAs and treated with SN38 (16 nM) for 72 hr.

(D) Quantification of cell death as determined by the Nucview Alexa-488 caspase 3-positive fraction in WT-H-Ras-depleted K-Ras mutant cells treated with SN38 as in (C). Data are presented relative to the values obtained for the respective scramble shRNA-expressing cells. Error bars, mean ± SEM, n = 3, $^{**}p < 0.005$. See also Figure S5.

with our cell-based studies, abrogation of WT-H-Ras in mutant K-Ras tumors led to Erk and Akt hyperactivation and the inhibition of Chk1 activation, as reflected by an elevated Chk1 Ser 280 phosphorylation and an impaired Chk1 Ser 317 phosphorylation in both mock and irinotecan-treated tumors (Figure 7C). Assessment of the extent of apoptosis revealed that the combination of WT-H-Ras knockdown and irinotecan treatment induced a significant increase in tumor cell apoptosis compared to WT-H-Ras knockdown or irinotecan treatment alone (Figures 7D and 7E). Importantly, irinotecan treatment failed to induce cell-cycle arrest of WT-H-Ras-suppressed tumors as evident by the significant increase in the number of cells staining positive for phosphorylated histone H3 compared to WT-H-Ras-intact tumors (Figures 7D and 7E). These results indicate that

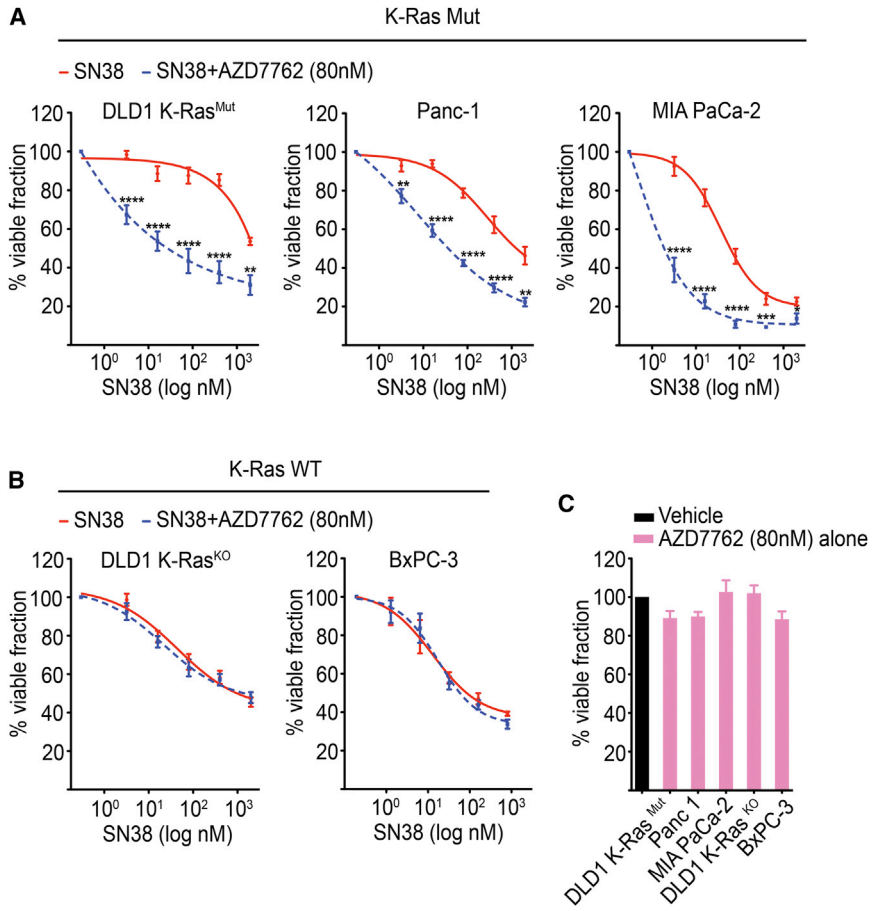

Figure 6. The Chk1/Chk2 Inhibitor AZD7762 Potentiates SN38 Cytotoxicity Selectively in K-Ras Mutant Cancer Cells

Viable fraction is expressed as a percentage mean ± SEM of the viability values obtained for respective vehicle-only treated conditions from three independent experiments each performed in triplicate.

(A and B) K-Ras mutant cancer cells (DLD1 K-Ras^{Mut}, Panc-1, and MIA PaCa-2) (A) or K-Ras WT cancer cells (DLD1 K-Ras^{KO} and BxPC-3) (B) were treated with SN38 alone or a combination of SN38 and AZD7762 (SN38 + AZD7762) for 48 hr at the indicated concentrations and analyzed for cell viability by the MTT assay. *$p < 0.05$, **$p < 0.01$, ***$p < 0.001$, ****$p < 0.0001$ for SN38 + AZD7762-treated versus SN38-treated alone.

(C) K-Ras mutant and K-Ras WT cells were treated with AZD7762 alone for 48 hr and assessed for cell viability by the MTT assay.

See also Figure S6.

WT-H-Ras knockdown in K-Ras mutant cells compromises the DNA damage checkpoint-mediated cell-cycle arrest in vivo.

To further substantiate the in vivo analyses of the consequences of WT-H-Ras knockdown, we administered irinotecan or vehicle to xenograft tumors derived from either MIA PaCa-2 (K-Ras Mutant) or BxPC-3 (K-Ras WT) cells that were engineered to inducibly (+Dox) express WT-H-Ras shRNA (Figures S7C and S7D). Similar to DLD1-K-Ras^{Mut} xenografts, combination of WT-H-Ras knockdown and irinotecan treatment led to MIA PaCa-2 tumor regression, but irinotecan alone led to a growth delay and WT-H-Ras knockdown alone had no effect (Figure S7C). Importantly, we found no synergy between WT-H-Ras knockdown and irinotecan treatment in BxPC-3 xenograft tumors (Figure S7D). Collectively, these observations establish a role for WT-H-Ras in maintaining a functional Chk1-dependent DNA damage checkpoint in established K-Ras mutant tumors.

DISCUSSION

Effective targeting of oncogenic K-Ras-driven tumors has remained a major challenge in cancer therapy. Considerable evidence indicates that cancer cells develop dependencies on normal functions of certain genes that can potentially be exploited to improve therapeutic strategies (De Raedt et al., 2011; Kumar et al., 2012; Luo et al., 2009a, 2009b). In the present study, we demonstrate that K-Ras mutant cancers display a dependency on WT-H/N-Ras for the activation of the ATR/Chk1-mediated DNA damage response (DDR) and therefore can be sensitized to DNA-damaging chemotherapeutics through the suppression of WT-H/N-Ras. The activation of DDR has been shown to play distinct context-dependent roles in the course of malignant transformation (Toledo et al., 2011a). In premalignant lesions, DDR activation is triggered by oncogenic stress and commonly leads to cell death or senescence, thereby functioning as an intrinsic barrier to malignancy (Bartkova et al., 2005; Gilad et al., 2010; Schoppy et al., 2012). Full malignant transformation, however, is accompanied by a weakening of the DDR barrier through the selective acquisition of mutations within critical DDR signaling modules (for example, p53 mutations and abrogation of ATM/Chk2/p53 signaling). As such, advanced tumors become highly reliant on the remaining functional DDR pathway (ATR/Chk1) for coping with the high levels of oncogene-induced genotoxic stress. In this context, the role of WT-H/N-Ras in coordinating the activation of ATR/Chk1 is critical for supporting the tumorigenic phenotype of K-Ras mutant tumors by preventing catastrophic DNA damage and enhancing tumorigenic fitness and survival. Consistent with this model, wild-type Ras has been shown to play a tumor-promoting role in cell lines from established tumors (Young et al., 2012).

Our results identify a role for WT-H/N-Ras in facilitating Chk1 activation by suppressing the Erk/p90RSK and PI3K/Akt pathways that inhibit Chk1 via Ser 280 phosphorylation. The capacity of WT-Ras to negatively regulate effector pathway signaling in mutant Ras cancer cells is consistent with earlier reports showing that the levels of WT-Ras proteins in mutant Ras cancer cell lines are inversely correlated to the activation status of Ras-effector molecules (Young et al., 2012; Zhang et al., 2001). It is noteworthy that the knockdown of wild-type isoform alone is sufficient to hyperactivate Erk and Akt and inhibit Chk1 activity and

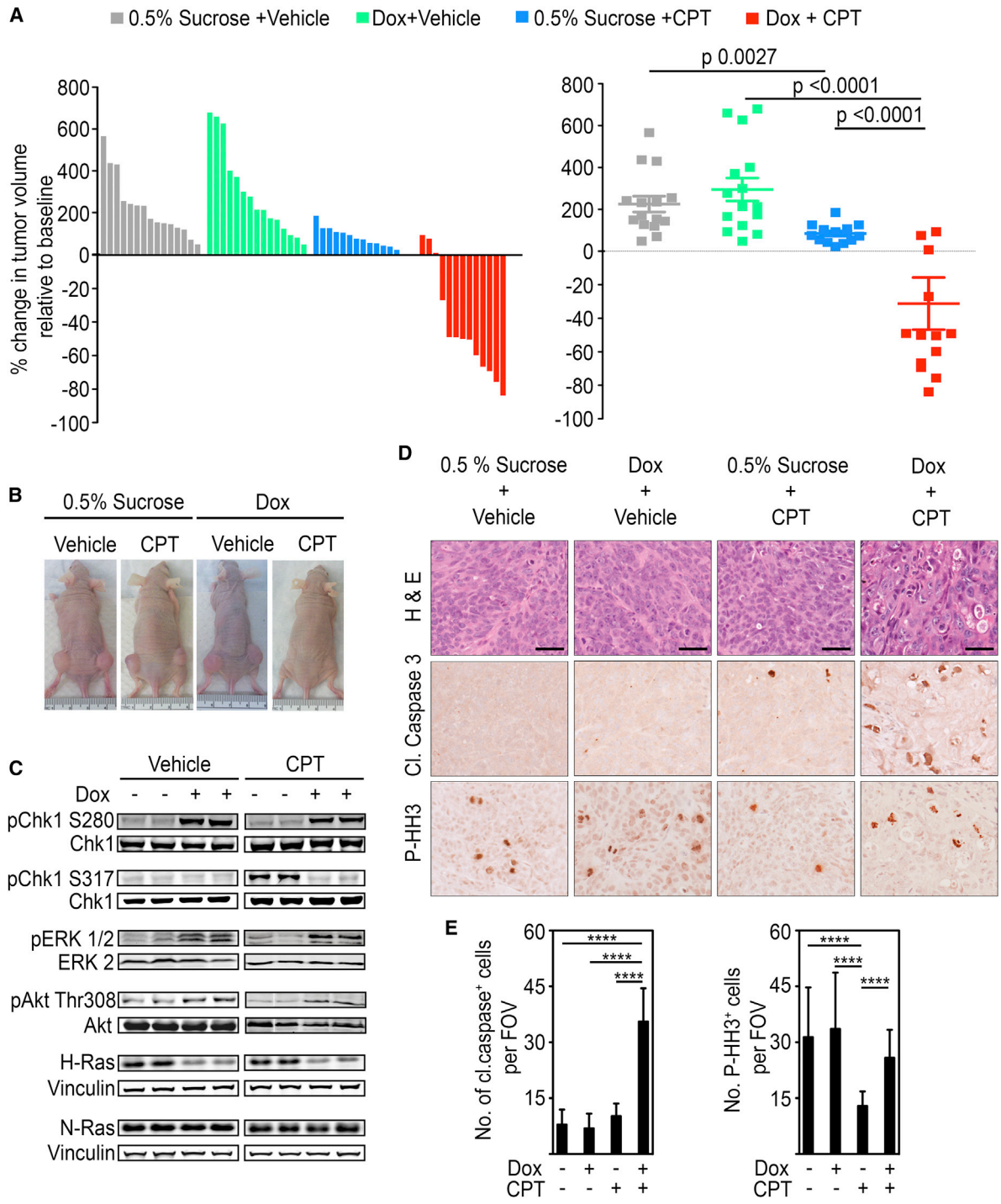

Figure 7. WT-H-Ras Knockdown in Established Mutant K-Ras Tumors Impairs Cell-Cycle Arrest Induced by DNA Damaging Chemotherapeutic Agents and Leads to Tumor Regression

(A) Waterfall plot and scatter plot showing percentage change in the volume of subcutaneous DLD1 K-Ras^{Mut} tumors in nude mice 5 days after the last dose of irinotecan (CPT) administration. Percentage change was determined relative to the tumor volume at the start of irinotecan (CPT) treatment for each individual tumor. Mice engrafted with 2 × 10^6 DLD1 K-Ras^{Mut} cells stable for the doxycycline-inducible H-Ras 1 sh were given either doxycycline or vehicle-only (0.5% sucrose) as a control via their drinking water once tumors attained ~100 mm^3. Irinotecan (CPT) administration (50 mg/kg every other day for 6 days [q2 dx3]) was initiated when tumors reached ~250 mm^3. Error bars, mean ± SEM.

(B) Representative xenograft tumors are shown.

(C) WCLs of tumor tissue obtained from the indicated animals 24 hr after the initiation of irinotecan (CPT) administration were immunoblotted with antibodies for the indicated proteins.

(legend continued on next page)

checkpoint function. This suggests a tightly controlled threshold for the WT-H/N-Ras-mediated attenuation of Ras-effector signaling in mutant K-Ras cancers. The mechanisms underlying the WT-H/N-Ras-mediated antagonism of Ras effector signaling in mutant K-Ras cancers remain to be delineated. Of potential relevance to this question are the seemingly contradictory observations that whereas the knockdown of WT-H/N-Ras in mutant K-Ras cancer cells induces Erk and Akt hyperactivation, the knockdown of Sos1, a guanine nucleotide exchange factor for Ras GTPases, instead impairs Erk and Akt activity (Jeng et al., 2012). A fundamental difference between these two scenarios is that whereas Sos knockdown would affect the levels of GTP-bound Ras, the knockdown of WT-H/N-Ras would inevitably lessen both GDP and GTP-bound Ras levels. Because the WT-isoforms exist predominantly in the GDP-bound form, knockdown of WT-H/N-Ras is likely to significantly alter the stoichiometry of GDP- to GTP-Ras molecules. This may provide a plausible explanation for the observed hyperactivation of Erk and Akt, as GDP-bound Ras molecules have been suggested to play an inhibitory role in Ras signaling (Singh et al., 2005). Furthermore, in the case of Raf, activation depends on Ras-mediated homo- and/or heterodimerization of Raf proteins, which likely require at least two Ras-GTP molecules (Heidorn et al., 2010; Inouye et al., 2000; Poulikakos et al., 2011; Rushworth et al., 2006; Weber et al., 2001). Because Ras dimerization appears to be constitutive and nonselective for GDP or GTP-bound Ras, depletion of GDP-bound Ras, as in the case of knockdown of WT-H-Ras or N-Ras, would stoichiometrically favor Ras-GTP dimer formation and consequently lead to Raf hyperactivation (Heidorn et al., 2010; Inouye et al., 2000).

There is now a large body of pre-clinical evidence showing that inhibition of the ATR/Chk1 pathway enhances the efficacy of standard chemotherapy. Indeed, several Chk1 inhibitors are being tested in clinical trials (Ma et al., 2012). As such, the ability of WT-H/N-Ras to determine Chk1 activation in mutant K-Ras tumors may warrant further exploration into the development of a therapeutic approach that utilizes inhibition of wild-type Ras-ATR/Chk1 signaling in combination with DNA damaging agents for the selective targeting of K-Ras-driven cancers.

EXPERIMENTAL PROCEDURES

Cell Culture and Lentiviral Transduction

Human pancreatic cancer cell lines Panc-1, PL45, AsPC-1, CFPAC-1, MIA PaCa-2, BxPC-3, and Hs700T were obtained from the American Type Culture Collection. The isogenic colon cancer cells DLD1-K-Ras^{Mut} and DLD1-K-Ras^{KO} were a kind gift from Dr. Mark Philips. Lentiviral particles were generated in accordance with standard protocols. For knockdown experiments, cells were transduced with lentiviral particles (multiplicity of infections [moi] for Hs700T, 15; all other cell lines, 7) containing pTripz scramble shRNA, H-Ras shRNA, or N-Ras shRNA and selected with puromycin (Calbiochem; for AsPC-1, 4 μg/ml; for all others, 2 μg/ml) for 3 days. Unless otherwise indicated, all experiments were performed on day 4 of doxycycline (1 μg/ml) induction. DLD1 K-Ras^{Mut} Flip-IN TREX GFP-H-RasV12 cells were generated through Flp recombinase-mediated homologous recombination between the FRT sites in the DLD1 K-Ras^{Mut} cell line and the pcDNA3/FRT/TO/GFP-HRasG12V expression vector. To generate BxPC-3-K-RasV12 cells, BxPC-3 cells were transduced with a TET-inducible lentiviral vector to express K-RasG12V, pLenti-TO-K-RasG12V (moi = 1). Following puromycin selection, cells that had efficiently integrated the K-RasG12V lentiviral construct (BxPC-3-K-RasV12) were expanded and subsequently transduced with a pTRIPZ-H-Ras sh construct. As both vectors are Dox inducible, induction of the expression of K-RasV12 also induces the knockdown of WT-H-Ras. Following a 48 hr induction, BxPC-3-K-RasV12 cells that also expressed the H-Ras sh were obtained by fluorescent sorting (RFP: pTRIPZ-H-Ras sh also expresses RFP upon Dox induction). The obtained cells were then cultured for an additional 48 hr in the presence of Dox and assayed for Chk1 activation upon treatment with SN38.

Cell Viability Assays

For viability assays, cells were treated with doxycycline to induce shRNA expression for 4 days and then seeded at a density of 4,000 cells/well in a 96-well plate in doxycycline containing media. Twenty-four hours postplating, SN-38 (Tocris Biosciences), oxaliplatin (Tocris Biosciences), or vehicle was added. Following a 72 hr treatment, cell viability was assessed by the MTT (3-[4,5-dimethylthiazol-2-yl]-2,5-diphenyl tetrazolium bromide; Sigma-Aldrich) assay in accordance with the manufacturer's protocol. Viable fraction is expressed as the percentage of vehicle-treated control cells. EC_{50} was calculated using Graphpad Prism (v. 4.0) software.

Cell Synchronization and Flow Cytometry

Cells were synchronized at the G1/S transition by a double thymidine block. Cells were treated with 2 mM thymidine for 22 hr and released from thymidine block by washing twice with PBS, followed by incubation in fresh medium. Fourteen hours after release, thymidine was added for another 20 hr. Induction of H-Ras shRNA expression was initiated with the first thymidine block. For the G2/M checkpoint analysis in response to UV-C, cells were irradiated with UV-C (25 J/m^2) during the exponential growth phase. Cells were harvested 1, 2, and 3 hr later, fixed with ice-cold 80% ethanol/PBS, and incubated overnight at −20°C. Fixed cells were washed with PBS and permeabilized with 0.25% Triton X-100/PBS on ice for 10 min. Cells were stained with anti-phospho histone H3 to detect mitotic cells and TO-PRO 3 for DNA content. For G2/M checkpoint activation in response to SN-38, cells were treated with 4 nM SN-38 and fixed at the indicated time points. Staining for cleaved caspase 3-positive cells was performed using the Nucview-488 Caspase 3 Kit (Biotium). Flow cytometry was performed on an LSRII (BD Biosciences) at NYU School of Medicine Flow Cytometry Core Facility, and data were analyzed using FlowJo software.

Animal Studies

For xenograft studies, we subcutaneously implanted 2 × 10^6 DLD1 K-Ras^{Mut}, MIA PaCa-2, or BxPC-3 cells stable for pTripz-H-Ras shRNA (1:1 in Matrigel, BD Biosciences) in both flanks of 8-week-old female athymic nude (NCRNU, Taconic) mice. When tumor size reached ~100 mm^3, mice were given drinking water containing either doxycycline (0.2 mg/ml)/0.5% sucrose or 0.5% sucrose alone. Water was replaced every 3 days. Tumor volume was determined using electronic calipers to measure length (l), width (w), and the formula (w^2 × l)/2. Tumor volume was measured twice a week. We treated mice bearing H-Ras-depleted (dox/sucrose) or H-Ras-intact (sucrose) DLD1 K-Ras^{Mut} tumors with either irinotecan or vehicle, once tumors reached 250 mm^3. Irinotecan hydrochloride (CPT) powder was dissolved into solution as previously described (Harris et al., 2005; Zabludoff et al., 2008). This solution was diluted with 5% dextrose for intraperitoneal (i.p.) injection at a dose of 50 mg/kg every other day for 3 rounds of treatment (q2 dx3). Irinotecan, or the combinatorial H-Ras knockdown and irinotecan treatments, were well tolerated as no weight loss above 10% body mass was observed. Body mass was measured using an electronic scale every 2 days. The percent change in tumor volume from day 0 of irinotecan treatment to tumor volume

(D and E) Tumor sections from mice in (A) treated as indicated were stained for hematoxylin and eosin (H&E), anti-cleaved caspase 3, or anti-P-HH3 antibody. Representative images are shown in (D), and quantifications are shown in (E). Scale bars, 40 μm. Cleaved caspase 3 or P-HH3-positive cells were counted per field of view (FOV) at 20× magnification. Error bars, mean ± SD, n = 3 mice per group, four FOV per mouse. ****p < 0.0001.
See also Figure S7.

5 days after the last dose of irinotecan administration was measured. Mice were euthanized by carbon dioxide-induced narcosis. To prepare lysates, tumor tissue was homogenized in RIPA buffer and sonicated to shear genomic DNA. All animal work was approved by New York University Langone Medical Center Institutional Animal Care and Use Committee.

Statistical Analyses

Data were analyzed by the Graphpad Prism built-in test (unpaired, two-tailed), and results were considered significant at $p < 0.05$.

SUPPLEMENTAL INFORMATION

Supplemental Information includes Supplemental Experimental Procedures, seven figures, and two movies and can be found with this article online at http://dx.doi.org/10.1016/j.ccr.2014.01.005.

ACKNOWLEDGMENTS

We thank Dr. Cosimo Commisso for his critical reading of our manuscript and his helpful discussions. We are grateful to Dr. Stephen Taylor for providing the DLD1 Flip-IN TRex cell line. This work was supported by research grants from National Institutes of Health (GM078266 and CA 055360 to D.B.-S. and 1F32CA13922 to E.G.). The NYU Cancer Institute Cytometry and Cell Sorting and Immunohistochemistry Core Facilities were supported in part by a grant (5P30CA016087-32) from the National Cancer Institute.

Received: March 9, 2013
Revised: November 25, 2013
Accepted: January 10, 2014
Published: February 10, 2014

REFERENCES

Bartek, J., and Lukas, J. (2003). Chk1 and Chk2 kinases in checkpoint control and cancer. Cancer Cell *3*, 421–429.

Bartkova, J., Horejsí, Z., Koed, K., Krämer, A., Tort, F., Zieger, K., Guldberg, P., Sehested, M., Nesland, J.M., Lukas, C., et al. (2005). DNA damage response as a candidate anti-cancer barrier in early human tumorigenesis. Nature *434*, 864–870.

Bos, J.L., Rehmann, H., and Wittinghofer, A. (2007). GEFs and GAPs: critical elements in the control of small G proteins. Cell *129*, 865–877.

Bremner, R., and Balmain, A. (1990). Genetic changes in skin tumor progression: correlation between presence of a mutant ras gene and loss of heterozygosity on mouse chromosome 7. Cell *61*, 407–417.

Brown, E.J., and Baltimore, D. (2000). ATR disruption leads to chromosomal fragmentation and early embryonic lethality. Genes Dev. *14*, 397–402.

Chin, L., Tam, A., Pomerantz, J., Wong, M., Holash, J., Bardeesy, N., Shen, Q., O'Hagan, R., Pantginis, J., Zhou, H., et al. (1999). Essential role for oncogenic Ras in tumour maintenance. Nature *400*, 468–472.

De Raedt, T., Walton, Z., Yecies, J.L., Li, D., Chen, Y., Malone, C.F., Maertens, O., Jeong, S.M., Bronson, R.T., Lebleu, V., et al. (2011). Exploiting cancer cell vulnerabilities to develop a combination therapy for ras-driven tumors. Cancer Cell *20*, 400–413.

Fisher, G.H., Wellen, S.L., Klimstra, D., Lenczowski, J.M., Tichelaar, J.W., Lizak, M.J., Whitsett, J.A., Koretsky, A., and Varmus, H.E. (2001). Induction and apoptotic regression of lung adenocarcinomas by regulation of a K-Ras transgene in the presence and absence of tumor suppressor genes. Genes Dev. *15*, 3249–3262.

Gilad, O., Nabet, B.Y., Ragland, R.L., Schoppy, D.W., Smith, K.D., Durham, A.C., and Brown, E.J. (2010). Combining ATR suppression with oncogenic Ras synergistically increases genomic instability, causing synthetic lethality or tumorigenesis in a dosage-dependent manner. Cancer Res. *70*, 9693–9702.

Girdler, F., Gascoigne, K.E., Eyers, P.A., Hartmuth, S., Crafter, C., Foote, K.M., Keen, N.J., and Taylor, S.S. (2006). Validating Aurora B as an anti-cancer drug target. J. Cell Sci. *119*, 3664–3675.

Haigis, K.M., Kendall, K.R., Wang, Y., Cheung, A., Haigis, M.C., Glickman, J.N., Niwa-Kawakita, M., Sweet-Cordero, A., Sebolt-Leopold, J., Shannon, K.M., et al. (2008). Differential effects of oncogenic K-Ras and N-Ras on proliferation, differentiation and tumor progression in the colon. Nat. Genet. *40*, 600–608.

Harris, S.M., Mistry, P., Freathy, C., Brown, J.L., and Charlton, P.A. (2005). Antitumour activity of XR5944 in vitro and in vivo in combination with 5-fluorouracil and irinotecan in colon cancer cell lines. Br. J. Cancer *92*, 722–728.

Hegi, M.E., Devereux, T.R., Dietrich, W.F., Cochran, C.J., Lander, E.S., Foley, J.F., Maronpot, R.R., Anderson, M.W., and Wiseman, R.W. (1994). Allelotype analysis of mouse lung carcinomas reveals frequent allelic losses on chromosome 4 and an association between allelic imbalances on chromosome 6 and K-ras activation. Cancer Res. *54*, 6257–6264.

Heidorn, S.J., Milagre, C., Whittaker, S., Nourry, A., Niculescu-Duvas, I., Dhomen, N., Hussain, J., Reis-Filho, J.S., Springer, C.J., Pritchard, C., and Marais, R. (2010). Kinase-dead BRAF and oncogenic RAS cooperate to drive tumor progression through CRAF. Cell *140*, 209–221.

Inouye, K., Mizutani, S., Koide, H., and Kaziro, Y. (2000). Formation of the Ras dimer is essential for Raf-1 activation. J. Biol. Chem. *275*, 3737–3740.

Jackson, E.L., Willis, N., Mercer, K., Bronson, R.T., Crowley, D., Montoya, R., Jacks, T., and Tuveson, D.A. (2001). Analysis of lung tumor initiation and progression using conditional expression of oncogenic K-ras. Genes Dev. *15*, 3243–3248.

Jeng, H.H., Taylor, L.J., and Bar-Sagi, D. (2012). Sos-mediated cross-activation of wild-type Ras by oncogenic Ras is essential for tumorigenesis. Nat. Commun. *3*, 1168.

Jiang, H., Reinhardt, H.C., Bartkova, J., Tommiska, J., Blomqvist, C., Nevanlinna, H., Bartek, J., Yaffe, M.B., and Hemann, M.T. (2009). The combined status of ATM and p53 link tumor development with therapeutic response. Genes Dev. *23*, 1895–1909.

King, F.W., Skeen, J., Hay, N., and Shtivelman, E. (2004). Inhibition of Chk1 by activated PKB/Akt. Cell Cycle *3*, 634–637.

Kumar, M.S., Hancock, D.C., Molina-Arcas, M., Steckel, M., East, P., Diefenbacher, M., Armenteros-Monterroso, E., Lassailly, F., Matthews, N., Nye, E., et al. (2012). The GATA2 transcriptional network is requisite for RAS oncogene-driven non-small cell lung cancer. Cell *149*, 642–655.

Lam, M.H., Liu, Q., Elledge, S.J., and Rosen, J.M. (2004). Chk1 is haploinsufficient for multiple functions critical to tumor suppression. Cancer Cell *6*, 45–59.

Li, Q., Haigis, K.M., McDaniel, A., Harding-Theobald, E., Kogan, S.C., Akagi, K., Wong, J.C., Braun, B.S., Wolff, L., Jacks, T., and Shannon, K. (2011). Hematopoiesis and leukemogenesis in mice expressing oncogenic NrasG12D from the endogenous locus. Blood *117*, 2022–2032.

Li, P., Goto, H., Kasahara, K., Matsuyama, M., Wang, Z., Yatabe, Y., Kiyono, T., and Inagaki, M. (2012). P90 RSK arranges Chk1 in the nucleus for monitoring of genomic integrity during cell proliferation. Mol. Biol. Cell *23*, 1582–1592.

Lim, K.H., Ancrile, B.B., Kashatus, D.F., and Counter, C.M. (2008). Tumour maintenance is mediated by eNOS. Nature *452*, 646–649.

Löffler, H., Rebacz, B., Ho, A.D., Lukas, J., Bartek, J., and Krämer, A. (2006). Chk1-dependent regulation of Cdc25B functions to coordinate mitotic events. Cell Cycle *5*, 2543–2547.

Luo, J., Solimini, N.L., and Elledge, S.J. (2009a). Principles of cancer therapy: oncogene and non-oncogene addiction. Cell *136*, 823–837.

Luo, J., Emanuele, M.J., Li, D., Creighton, C.J., Schlabach, M.R., Westbrook, T.F., Wong, K.K., and Elledge, S.J. (2009b). A genome-wide RNAi screen identifies multiple synthetic lethal interactions with the Ras oncogene. Cell *137*, 835–848.

Ma, C.X., Janetka, J.W., and Piwnica-Worms, H. (2011). Death by releasing the breaks: CHK1 inhibitors as cancer therapeutics. Trends Mol. Med. *17*, 88–96.

Ma, C.X., Cai, S., Li, S., Ryan, C.E., Guo, Z., Schaiff, W.T., Lin, L., Hoog, J., Goiffon, R.J., Prat, A., et al. (2012). Targeting Chk1 in p53-deficient triple-negative breast cancer is therapeutically beneficial in human-in-mouse tumor models. J. Clin. Invest. *122*, 1541–1552.

Matallanas, D., Romano, D., Al-Mulla, F., O'Neill, E., Al-Ali, W., Crespo, P., Doyle, B., Nixon, C., Sansom, O., Drosten, M., et al. (2011). Mutant K-Ras activation of the proapoptotic MST2 pathway is antagonized by wild-type K-Ras. Mol. Cell *44*, 893–906.

Poulikakos, P.I., Persaud, Y., Janakiraman, M., Kong, X., Ng, C., Moriceau, G., Shi, H., Atefi, M., Titz, B., Gabay, M.T., et al. (2011). RAF inhibitor resistance is mediated by dimerization of aberrantly spliced BRAF(V600E). Nature *480*, 387–390.

Puc, J., and Parsons, R. (2005). PTEN loss inhibits CHK1 to cause double stranded-DNA breaks in cells. Cell Cycle *4*, 927–929.

Pylayeva-Gupta, Y., Grabocka, E., and Bar-Sagi, D. (2011). RAS oncogenes: weaving a tumorigenic web. Nat. Rev. Cancer *11*, 761–774.

Ray-David, H., Romeo, Y., Lavoie, G., Deleris, P., Tcherkezian, J., Galan, J.A., and Roux, P.P. (2012). RSK promotes G2 DNA damage checkpoint silencing and participates in melanoma chemoresistance. Oncogene *32*, 4480–4489.

Rieder, C.L., and Maiato, H. (2004). Stuck in division or passing through: what happens when cells cannot satisfy the spindle assembly checkpoint. Dev. Cell *7*, 637–651.

Rushworth, L.K., Hindley, A.D., O'Neill, E., and Kolch, W. (2006). Regulation and role of Raf-1/B-Raf heterodimerization. Mol. Cell. Biol. *26*, 2262–2272.

Schoppy, D.W., Ragland, R.L., Gilad, O., Shastri, N., Peters, A.A., Murga, M., Fernandez-Capetillo, O., Diehl, J.A., and Brown, E.J. (2012). Oncogenic stress sensitizes murine cancers to hypomorphic suppression of ATR. J. Clin. Invest. *122*, 241–252.

Shirasawa, S., Furuse, M., Yokoyama, N., and Sasazuki, T. (1993). Altered growth of human colon cancer cell lines disrupted at activated Ki-ras. Science *260*, 85–88.

Shtivelman, E., Sussman, J., and Stokoe, D. (2002). A role for PI 3-kinase and PKB activity in the G2/M phase of the cell cycle. Curr. Biol. *12*, 919–924.

Singh, A., Sowjanya, A.P., and Ramakrishna, G. (2005). The wild-type Ras: road ahead. FASEB J. *19*, 161–169.

Syljuåsen, R.G., Sørensen, C.S., Hansen, L.T., Fugger, K., Lundin, C., Johansson, F., Helleday, T., Sehested, M., Lukas, J., and Bartek, J. (2005). Inhibition of human Chk1 causes increased initiation of DNA replication, phosphorylation of ATR targets, and DNA breakage. Mol. Cell. Biol. *25*, 3553–3562.

Toledo, L.I., Murga, M., and Fernandez-Capetillo, O. (2011a). Targeting ATR and Chk1 kinases for cancer treatment: a new model for new (and old) drugs. Mol. Oncol. *5*, 368–373.

Toledo, L.I., Murga, M., Zur, R., Soria, R., Rodriguez, A., Martinez, S., Oyarzabal, J., Pastor, J., Bischoff, J.R., and Fernandez-Capetillo, O. (2011b). A cell-based screen identifies ATR inhibitors with synthetic lethal properties for cancer-associated mutations. Nat. Struct. Mol. Biol. *18*, 721–727.

Weber, C.K., Slupsky, J.R., Kalmes, H.A., and Rapp, U.R. (2001). Active Ras induces heterodimerization of cRaf and BRaf. Cancer Res. *61*, 3595–3598.

Ying, H., Kimmelman, A.C., Lyssiotis, C.A., Hua, S., Chu, G.C., Fletcher-Sananikone, E., Locasale, J.W., Son, J., Zhang, H., Coloff, J.L., et al. (2012). Oncogenic Kras maintains pancreatic tumors through regulation of anabolic glucose metabolism. Cell *149*, 656–670.

Young, A., Lou, D., and McCormick, F. (2012). Oncogenic and wild-type Ras play divergent roles in the regulation of mitogen-activated protein kinase signaling. Cancer Discov. *3*, 112–123.

Zabludoff, S.D., Deng, C., Grondine, M.R., Sheehy, A.M., Ashwell, S., Caleb, B.L., Green, S., Haye, H.R., Horn, C.L., Janetka, J.W., et al. (2008). AZD7762, a novel checkpoint kinase inhibitor, drives checkpoint abrogation and potentiates DNA-targeted therapies. Mol. Cancer Ther. *7*, 2955–2966.

Zachos, G., and Gillespie, D.A. (2007). Exercising restraints: role of Chk1 in regulating the onset and progression of unperturbed mitosis in vertebrate cells. Cell Cycle *6*, 810–813.

Zhang, Z., Wang, Y., Vikis, H.G., Johnson, L., Liu, G., Li, J., Anderson, M.W., Sills, R.C., Hong, H.L., Devereux, T.R., et al. (2001). Wildtype Kras2 can inhibit lung carcinogenesis in mice. Nat. Genet. *29*, 25–33.

Zhou, B.B., and Elledge, S.J. (2000). The DNA damage response: putting checkpoints in perspective. Nature *408*, 433–439.

Zhou, B.B., and Bartek, J. (2004). Targeting the checkpoint kinases: chemosensitization versus chemoprotection. Nat. Rev. Cancer *4*, 216–225.

Cancer Cell
Erratum

Sox4 Is a Key Oncogenic Target in C/EBPα Mutant Acute Myeloid Leukemia

Hong Zhang, Meritxell Alberich-Jorda, Giovanni Amabile, Henry Yang, Philipp B. Staber, Annalisa Di Ruscio, Robert S. Welner, Alexander Ebralidze, Junyan Zhang, Elena Levantini, Véronique Lefebvre, Peter J.M. Valk, Ruud Delwel, Maarten Hoogenkamp, Claus Nerlov, Jörg Cammenga, Borja Saez, David T. Scadden, Constanze Bonifer, Min Ye,* and Daniel G. Tenen*
*Correspondence: mye@bidmc.harvard.edu (M.Y.), csidgt@nus.edu.sg (D.G.T.)
http://dx.doi.org/10.1016/j.ccr.2014.01.011

(Cancer Cell *24*, 575–588; November 11, 2013)
Dr. Di Ruscio's name was printed incorrectly as ''DiRuscio'' in the original article. It appears correctly in this erratum and has been updated in the article online.